Towards patient-specific modelling as a pre-operative planning strategy and follow up assessment for the treatment of advanced heart failure with rotary blood pumps

By

Massimo Capoccia, MBBS, MD, MSc
Cardiac Surgeon

Supervisor: Prof. Terence Gourlay

This thesis is submitted in accordance with the regulations governing the award of the Degree of Doctor of Philosophy in Biomedical Engineering

Declaration

"This thesis is the result of the author's original research. It has been composed by the author and has not been previously submitted for examination which has led to the award of a degree."

Signed:

Date: 25th September 2023

Acknowledgments

I am grateful to my supervisor, Prof. Terry Gourlay, who has been willing to take a clinician like me on board. His confidence in my abilities and encouragement has meant a great deal to me.

I am also very grateful to Dr Asimina Kazakidi for her precious help and advice.

I am also grateful to Dr Monica Kerr for her precious help with 3D reconstruction.

I have been privileged to meet Robert Woolhouse, Ansys Engineer, who has always been very supportive and ready to answer my questions. Vishal Sharma, Ansys Application Engineer, and Jenny Brimsted, Ansys Development Team, deserve my attention and gratitude too.

Part of this work is closely related to the book I have authored and edited with Dr. Claudio De Lazzari, biomedical engineer from the CNR Institute of Physiology in Rome, Italy, with whom I have had a very successful cooperation for the past seven years.

Once again, I have to say thank you to my parents who still enjoy fairly good health in their eighties and who have been supportive as they have always been. Although, they still ask me when I am going to slow down given my busy clinical practice.

Finally, I remain forever indebted to my lovely and supportive wife Michelle, who quietly remains the key of my successful professional and personal life.

Figure permission: when figures from other sources have been included, permission has been sought for their use and authors acknowledged.

Abstract

Background

Ventricular Assist Devices (VADs) insertion is an established treatment for patients with end-stage heart failure waiting for a heart transplant or in need for long-term circulatory support (destination therapy).

Rotary blood pumps (RBP) are the most popular devices in view of their size and performance. Pre-operative planning strategy for the insertion of a left ventricular assist device (LVAD) requires a timely discussion at a Multi-Disciplinary Team Meeting (MDT). Clinical-decision making is based according to the needs of the patient and must be processed without delays. Nevertheless, thrombus formation remains a feared complication which affects outcome. VADs operate in a flow regime which is difficult to simulate: the transitional region at the boundary of laminar and turbulent flow (low Reynolds number). Different methods have been used but the best approach remains debatable. Computational Fluid Dynamics (CFD) is an attractive and invaluable tool for the study of the interactions between VADs and the cardiovascular system. The aim of this thesis is three-fold:

a) to investigate the use of pressure-volume analysis in a clinical setting through the review of six heart failure patients previously discussed at a MDT meeting with a view to predict or guide further management;
b) to review the theory behind modelling approaches to VADs and their interactions with the cardiovascular system for better understanding of their clinical use. Then, an overview of computational fluid dynamics (CFD) is considered as a prelude to its application to the analysis of VADs performance. Additionally, the development of a simplified model of centrifugal pump will be used in initial simulations as preliminary analysis;
c) to examine an example of a proof-of-concept pilot patient-specific model of an axial flow pump (HeartMate II) as pre-operative planning strategy in a patient-specific model with a view to identify potential critical areas that may affect pump function and outcome in a clinical setting.

Material and Methods

3D reconstruction from CT-scan images of patients who underwent the insertion of rotary blood pumps, namely HeartWare HVAD and HeartMate II. Ansys Fluent has been used for CFD analysis based on the fundamental governing equations of motion. Blood has been modelled as incompressible, Newtonian fluid with density ρ = 1060 kg/m^3 and viscosity μ = 0.0035 kg/m-s. The laminar and $k-\omega$ SST models have been used for comparison purposes. The rotational motion of the

impeller has been implemented using the moving reference frame (MRF) approach. The sliding mesh method has also been used to account for unsteady interaction between stationary and moving part. The no-slip condition has been applied to all walls, which were assumed to be rigid. Boundary conditions consisting of velocity inlet and pressure outlet of the pump based on different settings and constant rotational speed for the impeller. Pressure-velocity coupling has been based on the coupled scheme. Spatial discretisation consisted of the "least square cell based" gradient for velocity and "PRESTO" or second order for pressure. Second order upwind has been set for the momentum, turbulent kinetic energy and specific dissipation rate. First order implicit has been set for transient formulation. The pseudo transient algorithm (steady state), the high order relaxation term and the warped-face gradient correction have been used to add an unsteady term to the solution equations with the aim to improve stability and enhance convergence. Specific settings have been considered for comparison purposes.

Results

Pressure-volume simulation analysis in six advanced heart failure patients showed that an integrated model of the cardiovascular system based on lumped-parameter representation, modified time-varying elastance and pressure-volume analysis of ventricular function seems a feasible and suitable approach yielding a sufficiently accurate quantitative analysis in real time, therefore applicable within the time-constraints of a clinical setting. Lumped-parameter models consist of simultaneous ordinary differential equations complemented by an algebraic balance equation and are suitable for examination of global distribution of pressure, flow and volume over a range of physiological conditions with inclusion of the interaction between modelled components. Higher level lumped-parameter modelling is needed to address the interaction between the circulation and other systems based on a compromise between complexity and ability to set the required parameters to personalise an integrated lumped-parameter model for a patient-specific approach. CARDIOSIM© fulfils these requirements and does address the systems interaction with its modular approach and assembly of models with varying degree of complexity although 0-D and 1-D coupling may be required for the evaluation of long-term VAD support. The challenge remains the ability to predict outcome over a longer period of time. The preliminary CFD simulations with the HeartWare HVAD centrifugal pump demonstrated that it is possible to obtain an accurate analysis in a timely manner to complement the clinical review process. The simulations with the pilot patient-specific model of the HeartMate II axial flow pump revealed that a complex 3D reconstruction is feasible in a timely manner and can be used to generate sufficiently accurate results to be used in the context of a MDT

meeting for the purposes of clinical decision-making. Overall, these three studies demonstrate that the time frame of the simulations was within hours which may fit the time constraints of the clinical environment in the context of a MDT meeting. More specifically, it was shown that the laminar model may be used for an initial evaluation of the flow development within the pump. Nonetheless, the k-ω model offers higher accuracy if the timeline of the clinical setting allows for a longer simulation.

Conclusion

This thesis aimed at the understanding of the use of computational modelling as a pre-operative planning strategy and follow up assessment for the treatment of advanced heart failure with rotary blood pumps. The novelty lays in the use of both pressure-volume simulation analysis and 3D flow dynamics studies in VADs with a view to treatment optimisation and outcome prediction within the time constraints of a clinical setting in the context of a MDT meeting. The clinical significance and the contribution to the field is a more targeted approach for different groups of patients and a more quantitative evaluation in the clinical decision process based on a pro-active co-operation between clinicians and scientists reducing the potential for “guess work”. The results of this thesis are a proof-of-concept as a prelude to a potential future implementation of patient-specific modelling within a clinical setting on a daily basis demonstrating a clear clinical significance and contribution to the field. The proposed approach does not consider modelling and simulation as a substitute for clinical experience but an additional tool to guide therapeutic intervention and complement the clinical decision process in which the clinician remains the ultimate decision-maker. Such an approach may well add a different dimension to the problem of heart failure with potential for high return in terms of patient’s outcome and long-term surveillance. The same principles would be applicable to other cardiovascular problems in line with the current concept of “Team Approach” such as the Heart Team, the Structural Heart Team or the Aortic Team. The present work has taken this concept closer to clinical delivery and has highlighted its potential but further work remains to be done in refining the technique.

Thesis Outline

The following is a summary of the chapters that comprise this thesis. Chapter 1 gives an overview of currently available ventricular assist devices (VADs) with a brief mention about key clinical trials. Chapter 2 gives an overview of pressure-volume analysis of cardiac mechanics and dynamics. The concept of time-varying elastance and ventricular-arterial coupling are presented in details. The importance of pressure-volume loop analysis for the evaluation of the interactions between VADs and the cardiovascular system is highlighted. Important concepts such as ventricular interdependence during circulatory support and the role of aortic valve physiology are also addressed. Chapter 3 is dedicated to the use of key mathematical models to further understand device function and interaction with the cardiovascular system based on the time-varying elastance and the electric circuit theory although alternative approaches are also discussed. An introduction to speed modulation is also given to address the shortcomings of constant speed currently used in VADs. Chapter 4 gives an introduction to the use of computational fluid dynamics for the analysis of flow in VADs and its role in device development and design improvement. Chapter 5 is dedicated to the modelling approach used to understand blood damage (thrombus formation and haemolysis). Chapter 6 describes the objectives and hypothesis of the work. Chapter 7 describes the clinical application of a combined modelling approach using pressure-volume analysis, 0-D modelling and modified time-varying elastance. All the simulations have been carried out using CARDIOSIM©, which is a modular software for cardiovascular modelling. The potential of this approach is discussed in terms of treatment optimisation and outcome prediction. Chapter 8 and 9 describe the design of CFD simulations and their results based on ANSYS software package, which is widely used in other engineering branches and more recently successfully applied to the biomedical field. Chapter 10 gives me the opportunity to discuss my ideas in relation to my simulations findings and the need for future developments in the field.

List of Figures

List of Tables

List of Abbreviations

REMATCH Trial – Randomised Evaluation of Mechanical Assistance for the Treatment of Congestive Heart Failure

ENDURANCE Trial – The HeartWare Ventricular Assist System as Destination Therapy of Advanced Heart Failure

MOMENTUM-3 Trial – Multicentre Study of MagLev Technology in patients undergoing MCS Therapy with HeartMate 3

INTERMACS – Interagency Registry for Mechanically Assisted Circulatory Support

MCS – Mechanical Circulatory Support

TETS – Transcutaneous External Transmission System

CE – Conformité Européenne (European Conformity)

FDA – Food and Drug Administration

CFD – Computational Fluid Dynamics

HVAD – HeartWare Ventricular Assist Device

RBP – Rotary Blood Pump

LVAD – Left Ventricular Assist Device

RVAD – Right Ventricular Assist Device

BiVAD – Biventricular Assist Device

CF-LVAD – Continuous-Flow Left Ventricular Assist Device

PF-LVAD – Pulsatile-Flow Left Ventricular Assist Device

TAH – Total Artificial Heart

PVAD – Percutaneous Ventricular Assist Device

BTT – Bridge to Transplant

BTD – Bridge to Decision

HDE – Humanitarian Device Exception

IVAD – Implantable Ventricular Assist Device

ECMO – Extracorporeal Membrane Oxygenation

DT – Destination Therapy

MVAD – Miniaturised Ventricular Assist Device

IDE – Investigational Device Exemption

aVAD – axial-flow Ventricular Assist Device

CFTAH – Continuous-Flow Total Artificial Heart

IABP – Intra-Aortic Balloon Pump

ESPVR – End-Systolic Pressure Volume Relationship

EDPVR – End-Diastolic Pressure Volume Relationship

LV – Left Ventricle

RV – Right Ventricle

LA – Left Atrium

RA – Right Atrium

MV – Mitral Valve

AV – Aortic Valve
TV – Tricuspid Valve
PV – Pulmonary Valve
MAP – Mean Arterial Pressure
SVR – Systemic Vascular Resistance
PVR – Pulmonary Vascular Resistance
PCWP – Pulmonary Capillary Wedge Pressure
SWEDVR – Stroke Work and End-Diastolic Volume Relationship
PRSW – Preload Recruitable stroke Work
ESVI – End-Systolic Volume Index
EDVI – End-Diastolic Volume Index
SW – Stroke Work
EEP – Energy Equivalent Pressure
THE – Total Haemodynamic Energy
SHE – Surplus Haemodynamic Energy
PPI – Pulse Power Index
PI – Pulsatility Index
TOE – Trans-Oesophageal Echocardiogram
PFO – Patent Foramen Ovale
ACT – Activated Clotting Time
CT-scan – Computed Tomography scan
MRI – Magnetic Resonance Imaging
CPB – Cardiopulmonary Bypass
ECG – Electrocardiogram
DNS – Direct Numerical Simulation
RANS – Reynolds-averaged Navier-Stokes Equations
BSL – Baseline Model
SST – Shear Stress Transport Model
RSM – Reynolds Stress Model
SRS – Scale-Resolving Simulation Model
LES – Large Eddy Simulation Model
DES – Detached Eddy Simulation Model
SAS – Scale-Adaptive Simulation Model
SBES – Stress-Blended Eddy Simulation Model
RNG – Renormalisation Group Model
WMLES – Wall-Modelled Large Eddy Simulation
ODE – Ordinary Differential Equations
PDE – Partial Differential Equations
CDR – Convection Diffusion Reaction Equation
NS – Navier-Stokes Equations

AT – Antithrombin

TF – Tissue Factor

vWF – von Willebrand Factor

FCM – Force Coupling Method

ADR – Advection Diffusion Reaction

SA – Stress Accumulation

CPM – Cellular Potts Model

DTE – Device Thrombogenicity Emulation

EPB – Evidence Based Practice

RCT – Randomised Control Trial

MDT – Multi-Disciplinary Team Meeting

URANS – Unsteady Reynolds-averaged Navier-Stokes Equations

MRF – Multiple Reference Frame Method

Table of Contents

PART A:

Introduction,

Background Theory and

Extensive Literature

Review

Chapter 1

Mechanical Circulatory

Assist Devices:

Overview

1 Mechanical Circulatory Assist Devices: Overview

1.1 Introduction

Ventricular assist devices (VADs) are designed to support a failing heart with a view to recovery, bridge to transplant or long-term treatment. Mechanical circulatory support has become a widely accepted standard treatment option in patients with advanced heart failure. Indication, timing and selection of the appropriate device are critical. Additional issues include quality of life, reliability and cost-effectiveness. From an engineering point of view, the greatest challenge is the development of a permanent circulatory support system. The system should be anatomically adaptable, structurally stable to operate in a corrosive saline environment and its components should be compatible in order to be joined to the flexible structures of the body. Such systems should operate continuously for years without maintenance. Mechanical components must necessarily be small and should operate without failing under extreme conditions. These systems should be efficient to reduce power requirement, prolong battery life and reduce waste heat. Blood trauma and flow disturbance should be within clinically tolerable limits. Blood-contacting surfaces should minimize potential generation of blood clots leading to cerebro-vascular accidents. Most of these issues have been addressed but there is still great potential for further improvement.

1.2 Types of VADs

Broadly speaking, there are two main categories of mechanical blood pumps: volume-displacement pumps and rotary pumps.

Volume-displacement pumps consist of a chamber or a sac that fills passively or by suction and is compressed by an external pusher plate (Fig. 1.1). Energy is transferred to the blood by periodic changes in a working space generating pulsatile flow. Inflow and outflow prosthetic valves are required. Devices such as HeartMate I XVE and Novacor are based on this principle. The output requirement for a pulsatile configuration is a flow rate of 5-10 *L/min* at a mean pressure of 100-150 *mmHg* and a rate less than 120 *bpm* with a mean filling pressure of about 20 *mmHg* (Antaki, 2006). Volume-displacement pumps are known as first generation devices. They unload the left ventricle very efficiently with a capacity to pump up to 10 *L/min* of pulsatile flow to sustain the circulation. Nevertheless, there are clear disadvantages such as large size, complexity, noisy operating mode and limited durability because of many moving parts (Birks, 2004; Pagani,

2006). Volume displacement pumps are suitable to generate pressure against resistance. They maintain a constant flow against an increasing resistance by generating a greater pressure at the expense of increased work and energy consumption. In the presence of very high resistance or flow stop, the pump fails. The heart is a modified but more complex volume displacement pump, which generates variable output according to preload, afterload and contractility. In the presence of very high afterload, failure is due to progressive endocardial ischaemia shown by the descending limb of the Frank-Starling curve (Arnold and Bourque, 2013).

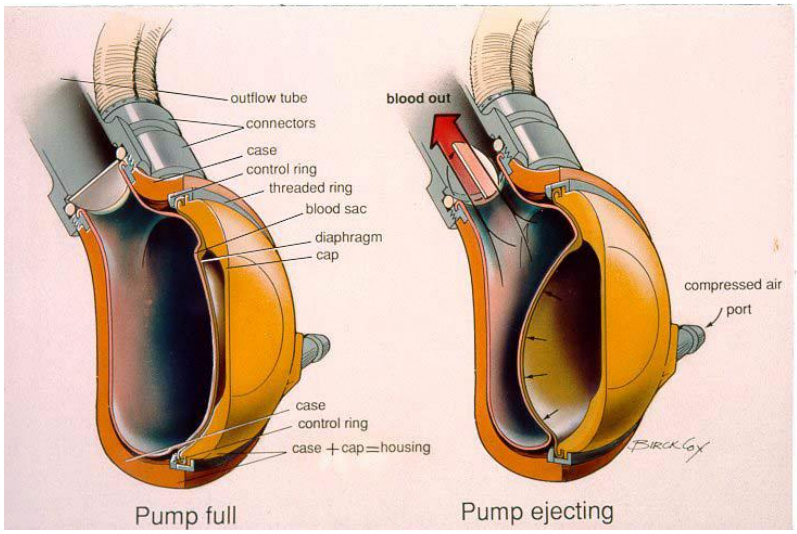

Figure 1.1 Volume displacement pump: compressed air is used to expand and contract a bladder with the aim to suck and eject blood in the circulation. A definite volume of fluid is delivered for each cycle of pump operation. From: Capoccia M, De Lazzari C. Concepts, Mathematical Modelling and Applications in Heart Failure, 2019, Nova Science Publishers.

Rotary blood pumps consist of an inlet and outlet with a single rotating element (impeller), which transfers energy to the blood in order to increase arterial blood flow and pressure. These devices can be axial, radial (centrifugal) and diagonal (mixed flow) according to the geometry of the impeller (Fig. 1.2). Energy is transferred to the blood by velocity changes within the impeller vanes generating non-pulsatile flow. The mechanism of the rotating element in an axial-flow pump can be viewed as a screw-driving manoeuvre along the x-axis. In contrast, the rotating element in a centrifugal-flow pump has a helicopter-like behaviour along the y-axis. Axial flow pumps (HeartMate II and Jarvik 2000) are driven by a spinning rotor around a central shaft. Centrifugal flow pumps (HeartWare, DuraHeart, HeartMate III) are driven by a hydrodynamic or electromagnetic suspended spinning rotor. Rotary blood pumps are suitable for high flows up to 20 *L/min*

at differential pressures lower than 500 *mmHg*. The radial design is capable of producing high pressures and low flows. An axial flow pump generates high flows at low pressure differences. A diagonal pump (Circulite Synergy) is a hybrid flow system capable of generating high pressures and high flows. Pump design is normalised to pump size taking into account that a 60-*mm*-diameter centrifugal pump can eject more fluid at significantly higher pressures than a 6-*mm*-diameter axial pump (Siess, 2000). An increased resistance in rotary blood pumps leads to decreased work and therefore available power (Arnold, 2013). Rotary blood pumps generate flow according to the amount of pressure dependent on resistance to flow. If the outflow graft of the HeartMate II (axial) or the HeatWare HVAD (centrifugal) is clamped, the true electrical and mechanical work done by the pump decreases although in theory the impeller may be pushing against an infinite resistance. In a clinical setting this would be paradoxical because myocardial oxygen demand and wall stress increase dramatically following aortic cross-clamp. The impeller rotates at high speed inside the pump housing with either forward (axial flow pump) or outward (centrifugal pump) fluid acceleration (Arnold, 2013). The impeller's ability to generate flow depends on the rotational speed and the blade features as described by Euler's pump theory.

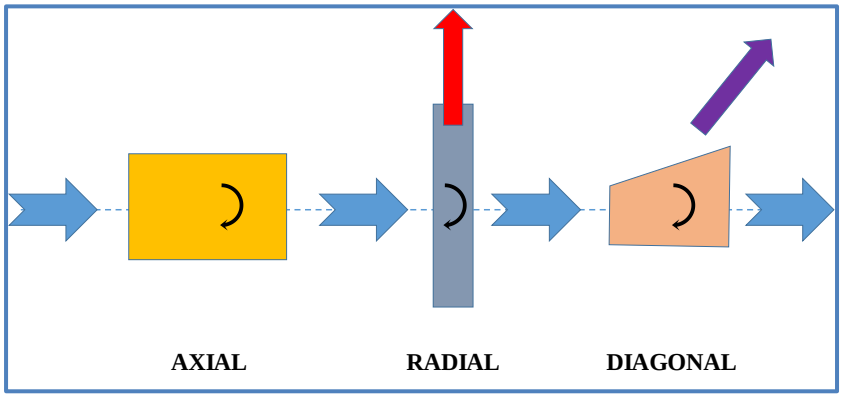

Figure 1.2 Direction of flow through the three types of rotary blood pumps. From: Capoccia M, De Lazzari C. Concepts, Mathematical Modelling and Applications in Heart Failure, 2019, Nova Science Publishers.

Rotary pumps with continuous axial flow requiring mechanical bearings and seals in contact with blood like the HeartMate II are known as second generation devices. They are smaller and safer to insert with more favourable durability because of only one moving part. Thrombus formation remains a feared complication and varies between pumps. Experience with this type of devices is well established (Miller, 2007; Pagani, 2009; Slaughter, 2009; Sheikh, 2011).

Rotary pumps with continuous flow based on magnetic levitation or non-contacting hydrodynamic bearings allowing the impeller to be suspended are known as third generation devices. These pumps are based on the concept of centrifugal flow and are even smaller than axial flow pumps. The use of magnetically levitated rotor systems is likely to improve durability. HeartWare, DuraHeart and HeartMate III are devices based on these principles (Tuzun, 2007; Morshuis, 2009; Wieselthaler, 2010; Strueber, 2011; Netuka, 2015; Rogers, 2017). The ENDURANCE trial has shown non inferiority of HeartWare compared to HeartMate II although with higher incidence of stroke requiring intensive blood pressure control (Rogers, 2017; Milano, 2018). The MOMENTUM-3 trial has shown superior performance of the HeartMate III with significant reduction in pump thrombosis, stroke and gastro-intestinal bleeding (Heatley, 2016; Mehra, 2017; Uriel, 2017; Mehra, 2018; Mehra, 2019).

Continuous-flow left ventricular assist devices (CF-LVADs), based on axial and centrifugal design, are currently the most popular devices in view of their smaller size, increased reliability and higher durability compared to pulsatile-flow left ventricular assist devices (PF-LVADs). The trend towards their use is increasing. Since the REMATCH (Randomized Evaluation of Mechanical Assistance for the Treatment of Congestive Heart Failure) Trial (Rose, 2001), the technological development from PF- to CF-LVADs has led to an increased survival of patients on prolonged circulatory support (Park, 2005; Slaughter, 2009; Boyle, 2011; Kirklin, 2012). CF-LVADs have proven their reliability in relation to outcome following elective surgery in chronic heart failure patients before the onset of cardiogenic shock (Boyle, 2011). In patients up to 70 years of age without cardiogenic shock, diabetes and renal failure, circulatory support with a CF-LVAD showed 1- and 2-year survival of 80% and 70%, which was comparable with heart transplantation (Kirklin, 2012; Kirklin, 2013; Kirklin, 2015). Although these results are encouraging, the impact of adverse events shows still limited advantage for patients with ambulatory heart failure suggesting a more effective control or prevention of major adverse events for left ventricular assist device (LVAD) insertion to be considered on a more frequent basis in this category of patients (Kirklin, 2017). Despite the greater durability for CF-LVADs in comparison with PF-LVADs (Holman, 2013) and the remarkable results achieved with the HeartMate III (Mehra, 2019), driveline infection, right heart failure, pump thrombosis and pump drive unit failure remain areas for further improvement. Despite the ongoing debate between transplantation and VADs, the two treatment options are closely related. Heart transplantation remains the first option for end-stage heart failure patients in view of

improved outcomes and better cost-effective profile (Aissaoui, 2018). Nevertheless, VADs are the necessary alternative option when transplant is contra-indicated or patient presentation is not optimal and in need of urgent attention. The more favourable outcomes with the HeartMate III may have shifted cost-effectiveness towards more acceptable levels (Mehra, 2018a; Sidhu, 2020). Improved haemocompatibility in terms of significant reduction in pump thrombosis, stroke and gastro-intestinal bleeding may have contributed to reduced hospital re-admission and therefore cost reduction (Sidhu, 2020).

1.3 Devices for Mechanical Circulatory Support

Current VADs range from short-term percutaneous devices to long-term permanently implantable systems and total artificial hearts (TAH). Appropriate device selection allows treatment to be tailored to the needs of each category of patients. Broadly speaking, mechanical circulatory support consists of short- and long-term treatment.

1.3.1 Pulsatile flow extra-corporeal

PVAD Thoratec

European Conformity (CE) mark approval in 1998. Food and Drug Administration (FDA) approval for BTT in 1995 and for post-cardiotomy recovery in 1998. Rarely used as LVAD; mainly as long-term right ventricular assist device (RVAD) or biventricular assist device (BiVAD); used as BTT for paediatric patients in selected cases.

Abiomed AB5000

FDA approval for short-term single or biventricular support with a view to recovery or BTD.

Abiomed BVS 5000

FDA approval for short-term or biventricular support; rarely used in post-cardiotomy support.

EXCOR Berlin Heart

Used as long-term biventricular support. CE mark approval in September 2021. Pending FDA approval as Humanitarian Device Exception (HDE) for BTT and bridge to recovery.

1.3.2 Pulsatile flow intra-corporeal

Novacor World Heart (Fig.1.4)
Long-term LVAD; CE mark approval in 2009; previously approved as BTT in North America, European Union and Japan. Subsequently BTT trial was stopped. Not used any longer; taken off the market.

HeartMate I XVE Thoratec (Fig.1.3)
CE mark approval in 2003; FDA approval as BTT in 2001 and subsequently for destination therapy in 2003. Long-term LVAD but rarely used now in view of newer technology.

IVAD Thoratec
CE mark approval in 2003; FDA approval as BTT in 2004. Authorised only for internal but not paracorporeal implantation due to reliability issues. Rarely used in view of newer technology.

Syncardia TAH Syncardia Systems
Pneumatically driven system used for long-term biventricular support. FDA and CE mark approval as BTT in Europe (70cc TAH in 1999; 50cc TAH in 2014), Canada (70cc TAH in 2005; 50cc TAH in 2016) and USA (70cc TAH in 2004; 50cc TAH in 2020) for patients at risk of imminent death from biventricular failure. The device is currently undergoing FDA clinical trial in the USA for destination therapy approval.

AbioCor TAH Abiomed
Completely self-contained implantable device based on TETS technology for long-term biventricular support. FDA approval in 2006 under HDE for destination therapy and implanted in a limited number of centres. Subsequently, further development abandoned due to insufficient evidence of its effectiveness.

Aeson® Carmat TAH (Carmat, Vélizy Villacoublay, France)
Electro-hydraulically driven pulsatile biventricular pump available in Europe only. CE mark approval for BTT in December 2020. FDA approval in February 2020 to undertake a feasibility study in the USA.

ReinHeart TAH (Aachen, Germany)
Passively filling pump unit driven by a low-wear linear drive between two artificial ventricles, an implantable control unit and a compliance chamber

and based on TETS technology. Currently under development with the aim to further validate its potential through prolonged in-vivo experiments after promising results in an acute setting.

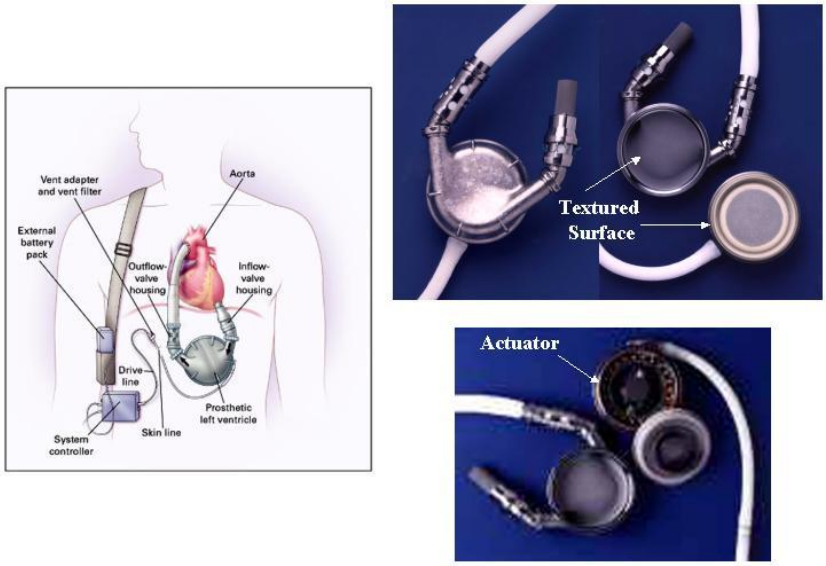

Figure 1.3 HeartMate I XVE Left Ventricular Assist System. From: Surg Clin N Am 2013; 93: 1343-1357.

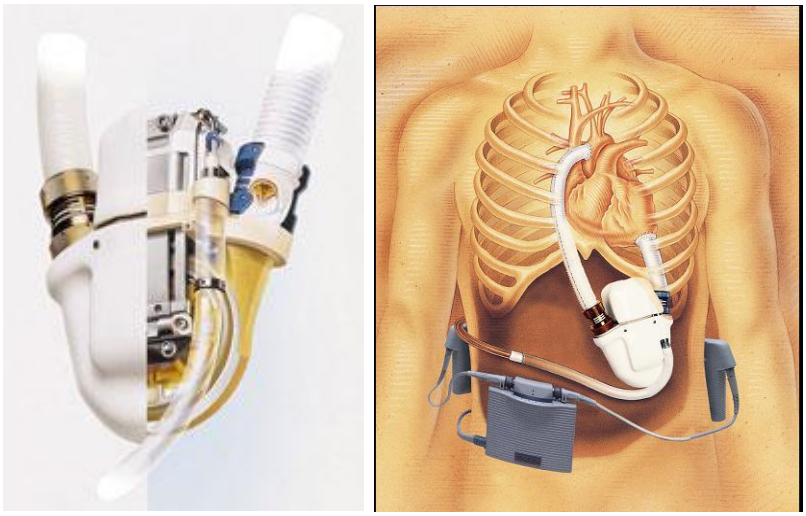

Figure 1.4 Novacor Left Ventricular Assist System. From: Semin Cardiothorac Vasc Anesth 2007; 11: 185-204.

1.3.3 Continuous-flow extra-corporeal

Centrimag (Levitronix) Thoratec

Magnetically levitated bearing-less centrifugal pump designed for short- to medium-term support (14 days to 3-6 months). CE mark approval in Europe

for short-term support. Versatile device suitable as veno-arterial (VA) extra-corporeal membrane oxygenation (ECMO), LVAD, RVAD and BiVAD.

Tandemheart CardiacAssist Inc.
Short-term biventricular support. FDA approved for extra-corporeal circulatory support for up to six hours for procedures not requiring full cardiopulmonary bypass.

Impella Abiomed
Short-term left ventricular support. FDA approved for circulatory support of periods up to six hours (April 2009).

HeartMate PHP
Percutaneous catheter-based trans-aortic pump. CE Mark approval (July 2015) for use in the European Union to support patients undergoing high-risk percutaneous coronary intervention (PCI).

1.3.4 Continuous-flow intra-corporeal

HeartMate II Thoratec (Fig.1.5)
Axial-flow pump for long-term left ventricular support: bridge to decision, bridge to transplant, destination therapy. Approved for use in North America and European Union. CE mark approval in 2005. FDA approval for BTT (April 2008) and DT (January 2010).

HeartMate III Thoratec (Fig.1.8)
Centrifugal-flow pump for long-term left ventricular support. Investigational device. CE Mark approval (September 2015).

HVAD HeartWare (Fig.1.6)
Centrifugal-flow for long-term left ventricular support. CE mark approval in Europe (January 2009). Completed USA BTT trial in 2009. FDA approval in 2012.

Jarvik-2000 Jarvik Heart
Axial-flow pump for long-term left ventricular support. CE mark approval in 2000 for BTT and DT in Europe. Child version is currently being developed. Under FDA clinical investigation for BTT approval in USA.

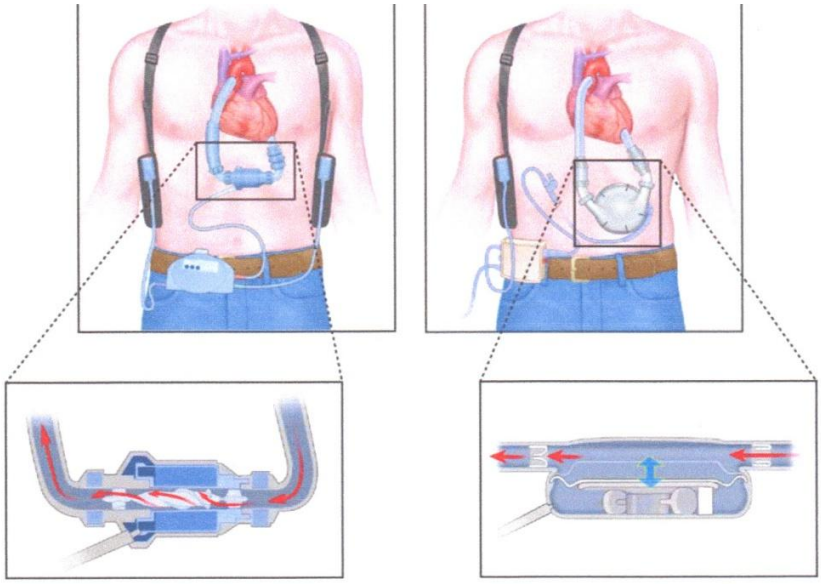

Figure 1.5 Difference between the mechanism of action of an axial flow pump (HeartMate II, left) and a volume displacement pump (HeartMate I, right). From: JACC 2009; 54: 1647-1659.

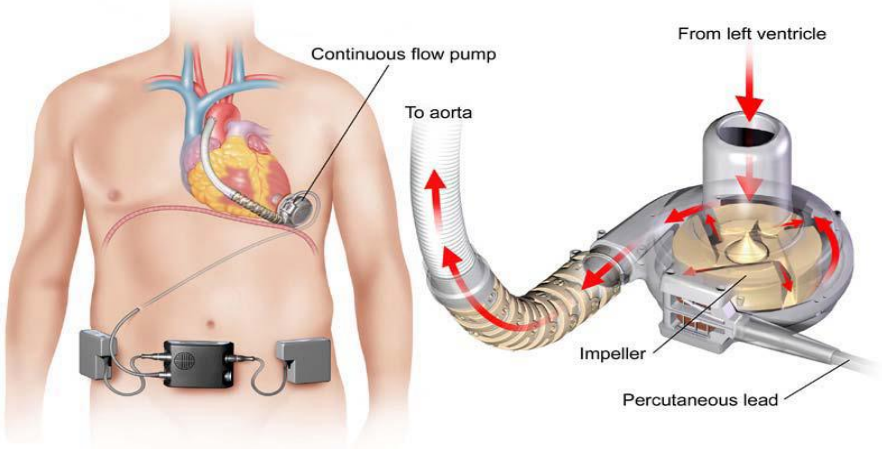

Figure 1.6 HeartWare HVAD centrifugal-flow pump. From: https://clinical.stjohnwa.com.au/medical-library/pathophysiology/cardiac-conditions/left-ventricular-assist-devices-(lvads)

MicroMed DeBakey VAD Micromed

Axial-flow pump for long-term left ventricular support. CE mark approval in 2006. Approved for use in Europe under HDE for BTT and BTD in children. FDA approval for use in children in USA. Under FDA consideration for BTT trial in USA.

Figure 1.7 Terumo DuraHeart^{TM} centrifugal-flow pump. From: Gregory SD, Stevens MC, Fraser JF. Mechanical Circulatory and Respiratory Support, 2018, Elsevier.

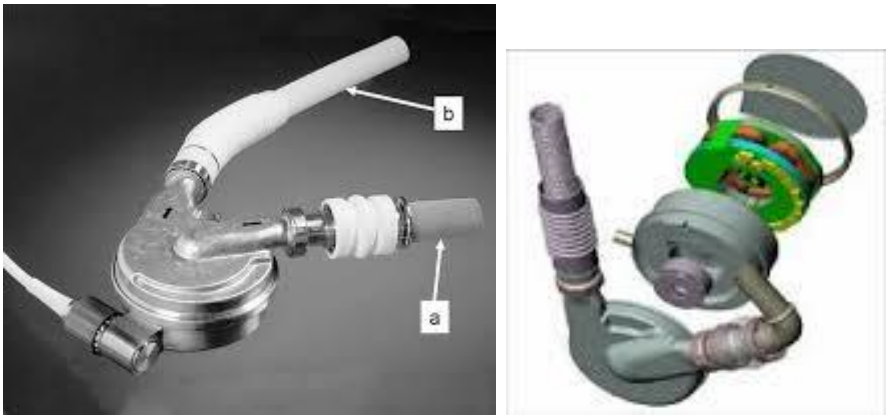

Figure 1.8 HeartMate III centrifugal pump. From: Cardiol Clin 2011; 29(4): 559-582 and https://www.lvad.nl/en/heartmate-3/

VentrAssist Ventracor

Centrifugal-flow pump for long-term left ventricular support. Approved for use in Europe and Australia. Company declared bankruptcy during clinical trials in 2009 for FDA approval.

Incor Berlin Heart

Axial-flow pump for long-term left ventricular support. CE mark approval in 2003. Approved for use in Europe. Clinical trials in USA in 2009. FDA approval for bridge to transplant.

MVAD HeartWare

Axial-flow pump. Good laboratory practices study completed. First implanted in 2015 and currently under clinical trials for CE mark and FDA approval.

DuraHeart Terumo (Fig.1.7)

Centrifugal-flow pump for left ventricular support. CE mark approval in 2007. Trials in USA for FDA approval (January 2010).

WorldHeart Levacor

Centrifugal-flow pump for long-term left ventricular support. Investigational device for BTT under investigational device exemptions (IDE) application in USA. Not available outside USA.

EVAHEART LVAS Evaheart

Centrifugal-flow pump for long-term left ventricular support. CE mark approval. FDA approval for clinical trial as BTT in USA in 2010.

Synergy Pocket Micro-Pump Circulite

Hybrid-flow pump for long-term left ventricular partial support. The device combines axial, centrifugal and orthogonal flow with a single-stage impeller powered by an integrated brushless micro-electric motor. Also considered for right ventricular support. CE mark approval in 2012.

HeartAssist5 ReliantHeart

Axial-flow pump for long-term left ventricular support. CE mark approval in 2014. In trial for BTT.

aVAD ReliantHeart

Light intraventricular axial flow LVAD that includes features like remote monitoring and flow measurement. CE Mark approval has been granted and implants started in September 2016.

CFTAH (Cleveland Clinic)

Single-piece, valveless, continuous-flow total artificial heart. The device uses a single, centrally located, rotating assembly with impellers for left and right centrifugal pumps.

BiVACOR TAH (Houston, Texas)

System of two centrifugal impellers placed on a single, magnetically levitated rotor located between opposing pump casings. Currently under development.

1.3.5 Counterpulsation devices

Intra-Aortic Balloon Pump (IABP)

The IABP consists of a cylindrical balloon placed in the descending thoracic aorta and connected to an external pump through a flexible catheter. In contrast to VADs, which replace the pumping function of the native heart, the IABP exerts its primary haemodynamic effects by inflating during diastole displacing blood proximally and distally, thereby raising the proximal arterial pressure and improving systemic perfusion, notably to the myocardium. When the balloon deflates at the end of diastole, a region of lower pressure akin to a "vascular void" is created within the aorta with reduction of left ventricular afterload.

Kantrowitz CardioVAD

The Kantrowitz CardioVAD was an ambulatory counterpulsation device developed to deliver chronic counterpulsation in an intermittent manner. It consisted of an elongated inflatable valve-less polyurethane patch sutured to the lateral aspect of the descending thoracic aorta and powered by an external compressor via a percutaneous pneumatic line. Despite an initial successful clinical application, the device did not achieve widespread acceptance.

C-Pulse® Heart Assist System (Sunshine Heart)

The C-Pulse® consists of a cuff that wraps around the ascending aorta with inflation and deflation of a membrane (balloon) against the vessel's external wall. The positive and negative pressure of the balloon synchronises aortic pulsation with the cardiac cycle, augmenting blood flow and reducing total cardiac work and strain. A battery-powered pump is connected to the device and worn outside the body. The C-Pulse® is currently an investigational device.

Symphony CPD

Symphony CPD is an implantable counterpulsation device developed for superficial implantation without the need to enter the chest. The surgical

approach is limited to an infraclavicular incision similar to that used for placement of a pacemaker. The device is implanted into a pocket below the pectoralis muscle on the anterior chest and attached to a vascular graft, which is anastomosed to the subclavian artery. A silicone diaphragm in the reservoir is inflated and deflated by an air driveline connected to an external pneumatic driver. The CPD reservoir fills during native ventricular systole and empties during native ventricular diastole. The operation mode of the device is by removal and return of blood to the circulation rather than volume displacement. Symphony CPD is currently an investigational device.

Para Aortic Blood Pump (PABP)

Para-aortic pumps operate on the same principle as IABP counterpulsation but are intended for long-term use to provide chronic contraction unloading and coronary perfusion augmentation.

PulseCath iVAC

The PulseCath consists of an extra-corporeal membrane pump connected to a large-bore catheter which is inserted across the aortic valve retrogradely into the left ventricle. A genuine IABP console drives the pulsatile pump.

1.4 Chapter Summary

The evolution from pulsatile to continuous-flow LVADs has played a key role for the treatment of advanced heart failure. A single moving part makes rotary blood pumps more reliable, durable and efficient. The absence of pulsatility is physiologically tolerable although not without drawbacks. The development of the HeartMate III has significantly reduced the potential for pump thrombosis, stroke and gastro-intestinal bleeding. The need for an external driveline through the skin remains the Achilles' heel although progress is being made towards wireless connection. Survival during the first two years is comparable to heart transplantation.

Chapter 2

Interactions between Rotary Blood Pumps and the Cardiovascular System

2 Interactions between Rotary Blood Pumps and the Cardiovascular System

2.1 Introduction

The time-varying elastance concept has been widely used to model the interaction between the cardiovascular system and mechanical circulatory support devices. Based on its load-independence property, the end-systolic pressure volume relationship (ESPVR) has been used to analyze the effect of aortic counterpulsation and other assist devices in experimental settings (Sun, 1991; Withington, 1991; Ratcliffe, 1991; De Lazzari 2006). The analysis has shown that circulatory assist devices may generate non-physiological pressures and improve heart function (Withington, 1991); a leftward shift of the ESPVR in hearts recovering from ischaemia suggest that circulatory support improves their contractility (Ratcliffe, 1991). Subsequently, further studies have shown that the ESPVR is either concave or convex toward the volume axis (Burkhoff, 2005). If the slope of the ESPVR does not remain constant, contractility varies with the end-systolic volume leading to nonlinear isochrones which result in load-dependence measure of contractility with significant variation of volume intercept (van der Velde, 1991; Claessens, 2006).

Although the time-varying elastance theory (Suga, 1973; Suga, 1974) has been proven sufficiently accurate (Stergiopulos, 1996; Segers, 2000; Segers, 2001) and adequate for realistic simulations of the instantaneous pressure-volume relationship (Lankhaar, 2009), its validity has been challenged when used to model the interactions between a left ventricular assist device (LVAD) and the cardiovascular system (Vandenberghe, 2006). During cardiac assistance with displacement blood pumps, the heart sustains extreme and rapidly changing loading conditions followed by simultaneous significant elastance changes. When the device is used in counterpulsation manner, significant unloading occurs during LV systole because all the blood is directed towards the LVAD. In view of these findings, it is questionable whether the original elastance theory is still valid for mechanically supported hearts (Vandenberghe, 2006). Changes in the elastance are also observed with continuous flow pumps: the end diastolic volume decreases and the maximum pressure increases possibly due to cardiac tissue damage caused by the presence of the device. In view of these considerations, a modified time-varying elastance approach (Capoccia, 2018; De Lazzari, 2019) or an alternative model (Kim and Capoccia, 2019; Kim and Capoccia, 2020) may be more appropriate to simulate the interactions between LVADs and the cardiovascular system.

2.2 Pressure-Volume Analysis

Cardiac mechanics and dynamics can be understood by means of pressure-volume analysis, which enables the evaluation of the working conditions imposed on the ventricle in terms of preload and afterload. The effective arterial elastance (E_a) can be coupled with ventricular elastance (E_v) to analyse ventricular-arterial interactions with particular reference to the optimal afterload for maximal stroke work, or maximal mechanical efficiency.

The assessment of the left ventricular systolic and diastolic function is critical in the understanding of the pathophysiology of heart failure and its treatment. Pressure-volume analysis describes global cardiac pump function and it remains a powerful approach to study the properties of the ventricular pump and its interaction with the vascular system (Sagawa, 1988). Although not commonly used in clinical practice, it allows a detailed and quantitative evaluation of the haemodynamics and ventricular-vascular coupling in health, in disease and in response to complex therapeutic interventions in heart failure that is not possible with other approaches (Burkhoff, 2005).

The ventricular pressure-volume (PV) loop describes the haemodynamic events during the cardiac cycle. It is obtained by plotting instantaneous ventricular pressure versus volume. This loop is repeated with each cardiac cycle and shows how the heart shifts from its end-diastolic to its end-systolic states and vice versa (Fig. 2.1).

For different filling volumes (preload) and different aortic pressures (afterload) the end-systolic and the end-diastolic pressure-volume values draw the end-systolic (ESPVR) and the end-diastolic (EDPVR) pressure-volume relationships. These curves constrain the operating range of both ventricles in the pressure-volume field: any PV loop is comprised between the ESPVR and the EDPVR. Diastolic and systolic pressure-volume relationships are obtained *in vivo* by simultaneous measurement of ventricular volume and pressure during changes in cardiac filling with constant contractility and heart rate. Filling changes *in vivo* are obtained with gradual occlusion of the vena cava (Westerhof, 2010).

ESPVR and EDPVR are not fixed for a given ventricle but they change according to the contractile state of the myocardium or with changes in the ratio of the wall thickness to the cavity radius. Sympathetic stimulation of the heart and left ventricular hypertrophy make the slope of ESPVR steeper while incomplete relaxation shifts EDPVR upward. At the same time, these alterations are observed in the ventricular state from the shifts of ESPVR and EDPVR (Sagawa, 1988).

The ESPVR is a linear function within the physiological range and is insensitive to preload and afterload conditions (Fig. 2.1) (Suga, 1973; Suga

and Sagawa, 1974). It defines the state of maximal activation of the chamber at a given contractile state. In mathematical terms, we have the following expression:

$$P_{es}(V) = E_{es}(V - V_0) \tag{2.1}$$

where P_{es} is the end-systolic pressure and V is the ventricular volume. V_0 is the volume axis intercept indicating that a certain amount of volume must be present in the ventricle before it can generate any pressure. Although this is not completely true, V_0 can be considered the same volume axis intercept for EDPVR and ESPVR. The slope of the linear relation (E_{es}) is the end-systolic elastance. Elastance is the equivalent of stiffness and is defined as the change in pressure for a given change in volume: the higher the elastance, the stiffer the ventricular wall.

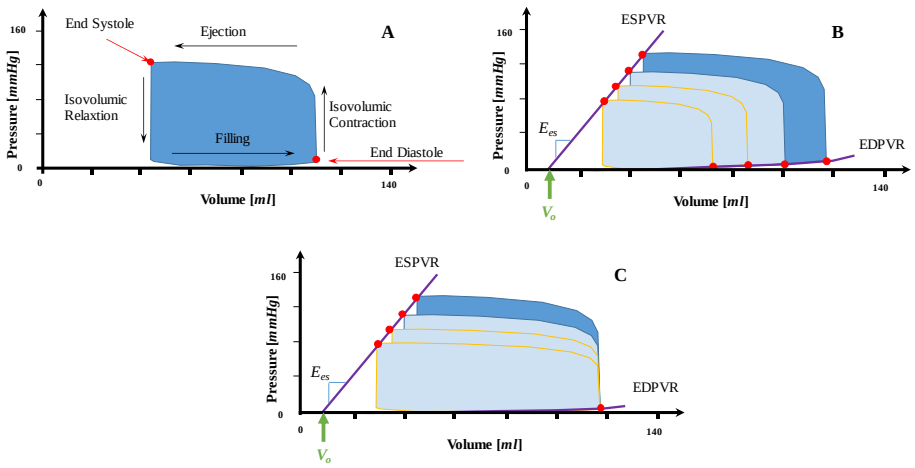

Figure 2.1 A: PV loop representing the 4 phases of the cardiac cycle obtained by plotting instantaneous pressure versus volume. **B**: a progressive reduction in ventricular filling pressure shifts the loops towards lower end-systolic and end-diastolic volumes during constant contractile state and afterload resistance. **C**: the loops become flatter and wider when afterload resistance is increased at a constant preload pressure. In ideal conditions, the end-systolic pressure-volume points fall on the same ESPVR obtained with preload reduction. All PV loops have been generated using CARDIOSIM© software simulator. From: Capoccia M, De Lazzari C. Concepts, Mathematical Modelling and Applications in Heart Failure, 2019, Nova Science Publishers.

The EDPVR is a nonlinear function and defines the passive properties of the chamber in its most relaxed state. It represents the passive filling mechanics of the chamber determined primarily by the thick-walled geometry and by

the nonlinear elasticity of the resting ventricular wall. Typical expression would be the following:

$$P_{ed}\left(V\right)=P_0+\beta\cdot V^{\alpha} \tag{2.2}$$

or

$$P_{ed}\left(V\right)=\beta\cdot\left[e^{\alpha(V\text{-}V_0)}-1\right] \tag{2.3}$$

where P_{ed} is the end-diastolic pressure, P_0 is the pressure at low volumes (generally close to 0 *mmHg*), α and β are constants determined by the mechanical properties of the muscle as well as by the structural ventricular features. The EDPVR intersects the volume axis at V_0 (Eq. (2.3)), which is the maximal volume at zero pressure; this volume is frequently referred to as the unstressed volume. The reciprocal of the derivative of the EDPVR, $(dP_{ed}(V)/dV)^{-1}$, is the compliance, which is the change in volume for a given change in pressure. Since the EDPVR is a nonlinear function, the compliance varies with volume: it is greatest at low volume and smallest at high volume. The compliance gives information about the diastolic properties of the heart in relation to whether it is working at a point on the EDPVR where the slope is high or low (Burkhoff, 2011).

The area of the PV loop is the external work (EW), which represents the energy transmitted to the blood by ventricular contraction. In more conventional terms, the loop area represents the stroke work of the ventricle on the arterial system and is mathematically approximated as follows:

$$EW=-\int_{V_{ed}}^{V_{es}}P\left(V\right)dV \tag{2.4}$$

where V_{es} and V_{ed} are the end-systolic and the end-diastolic volumes. A ventricular function curve is obtained by plotting stroke work against preload either as end-diastolic volume or end-diastolic pressure.

During isovolumic relaxation the pressure decreases from the initial value P_0 until mitral valve opening. This decay can be characterized by a single exponential function as follows:

$$P\left(t\right)=\left(P_0-P_\infty\right)e^{-\frac{t}{\tau}}+P_\infty \tag{2.5}$$

where P_∞ is the (negative) baseline pressure to which the ventricle would eventually relax if mitral valve opening did not occur and τ is the time constant characterizing the rate of fall of pressure (Yellin, 1986). Normally, τ is about 40 *ms* in dogs and humans but it is increased by various factors such as elevated afterload, asynchronous contraction associated with abnormal activation sequence or regional dysfunction, slowed cytosolic calcium reuptake to the sarcoplasmic reticulum associated with cardiac hypertrophy and failure.

The pressure and volume curves for the right ventricle are essentially the same although right ventricular and pulmonary artery pressures are a fifth of the corresponding left sided pressures. The interventricular septum separates the right and the left ventricles and can transmit forces from one to the other. An increase in right ventricular volume may increase the left ventricular pressure by septal deformation. This direct interaction is more significant during filling (Janicki, 1980). The end of diastole generally coincides with mitral valve closure while mechanical end-systole is usually considered as the end of ejection. However, since there remain considerable myofilament interactions and active tension during relaxation, it has been proposed extending systole until the onset of diastasis (Brutsaert, 1989). This distinction is important in terms of cardiac muscle mechanics because the myocardium is still active for much of diastole and may never be fully relaxed at high heart rates. The EDPVR has been approximated by an exponential function of volume and its determinants are the material properties of resting myocardium, the chamber dimensions and wall thickness (Gilbert and Glantz, 1989). Therefore, the passive chamber stiffness ($dP_{ed}(V) \,/\, dV$) is approximately proportional to the filling pressure. The extent of relaxation, ventricular interactions and pericardial constraints play also a role on the EDPVR. In fact, the EDPVR of the left ventricle may be directly affected by changes in the loading conditions of the right ventricle through septal interactions (Glantz and Parmley, 1978).

The ventricles also interact indirectly since the output of the right ventricle is returned as the input to the left ventricle via the pulmonary circulation. A transversely isotropic computational model of the canine left ventricle with bi-axial active stress gives a realistic representation with experimental agreement (Usik, 2000). During isovolumic contraction and relaxation, the model requires volumetric constraint equations to calculate the pressure boundary condition at each time step to keep left and right ventricular cavity volume constant.

To simulate the interaction between the left (right) ventricle and the aortic (pulmonary) system, the model of the left (right) ventricle can be coupled to

a two-element windkessel model (Westerhof, 2010) to simulate aortic (pulmonary) input impedances so that ventricular pressures can be calculated during ejection. The equation of this model is:

$$\frac{dV}{dt} = C \cdot \frac{dP}{dt} + \frac{P}{R} \tag{2.6}$$

The parameters C and R are chosen for the aortic and pulmonary circulations to obtain physiological systolic pressures; P and V are pressure and volume.

2.3 Time-Varying Elastance Theory

The time-varying elastance theory is based on the instantaneous relationship between ventricular pressure and volume. The pressure to volume ratio at any time in one cardiac cycle can be defined as follows (Suga and Sagawa, 1974):

$$E(t) = \frac{P(t)}{V(t) - V_d} \tag{2.7}$$

where $E(t)$ is the time-varying elastance, $P(t)$ is the instantaneous intraventricular pressure, $V(t)$ is the instantaneous intraventricular volume and V_d is the fixed correction volume.

From an experimental point of view, the instantaneous intraventricular pressure to volume ratio during systole is a unique feature of the ventricular contractile state which appears to be independent of mechanical loading conditions but varies significantly with changes in the contractile state of the ventricle. Simulations of cardiac responses to different haemodynamic conditions based on a mathematical model derived from the above findings (Suga, 1971) suggest that the pressure to volume ratio is a link between the ventricle as a hydraulic element defined in terms of input-output relationships and the ventricle as an active chamber whose contraction is described in terms of intraventricular pressure and volume. The peak value (E_{max}) of $E(t)$ and the time to E_{max} from the onset of systole (T_{max}) are the characteristic parameters of the instantaneous pressure to volume ratio curve: they are independent of wide variations in preload and afterload conditions under a given contractile state but they are sensitive to changes in the contractile state of the ventricle (Suga and Sagawa, 1974). All the

$E(t)$ curves, normalised with respect to E_{max}, ($E_N = E/E_{max}$), against t normalised with respect to T_{max}, ($t_N = t/T_{max}$), have a common shape and reduce to a single curve $E_N(t_N)$ regardless of loading conditions, contractile state or heart rate. As a result, the instantaneous pressure to volume ratio curve $E(t)$ can be described in terms of E_{max} and T_{max} where changes in these parameters reflect the variations in the contractile state of the ventricle. Figure 2.2 shows a schematic representation of the time-varying ventricular pressure-volume relationship as a three-dimensional surface in the pressure-volume-time space.

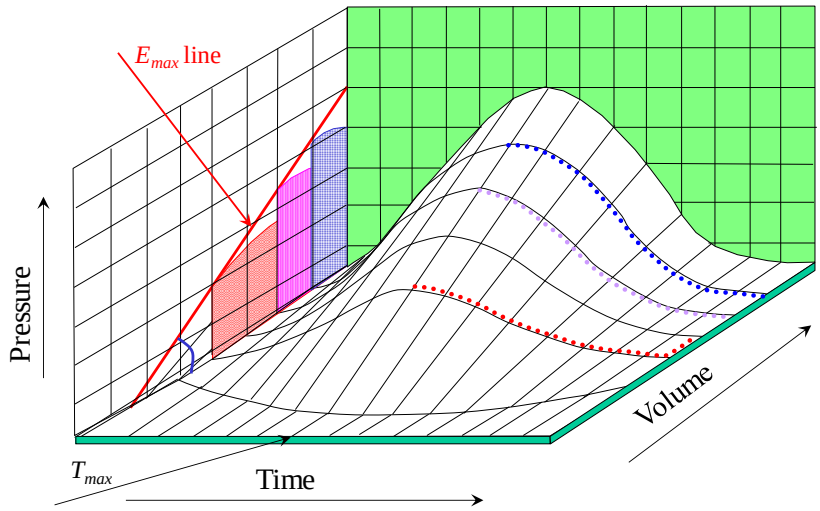

Figure 2.2 $E(t)$ surface or pressure-volume-time surface of the left ventricle. Given a constant contractile state, the instantaneous pressure-volume relationship of the ventricle travels on this surface along a path determined by preload and afterload conditions. The three dotted lines are the ejecting contractions against three values of afterload. From: Capoccia M, De Lazzari C. Concepts, Mathematical Modelling and Applications in Heart Failure, 2019, Nova Science Publishers.

If α is the ratio of E_{max} under a given contractile state over that under an arbitrarily defined control contractile state and β is the ratio of T_{max} under the control contractile state over that under a given contractile state, both parameters can be used empirically as measures of a change in contractile state from a control contractile state (Suga, 1972). In mathematical terms, the $E(t)$ curve under a given contractile state can be described as:

$$E(t) = \alpha \cdot E_0(\beta t) \tag{2.8}$$

where $E_0(t)$ represents $E(t)$ under an arbitrarily defined control contractile state and heart rate with α and β being magnitude and duration parameters of the given $E(t)$ with respect to $E_0(t)$ (Suga, 1972).

The mathematical analysis of the mechanical relationship between ventricular performance represented by $E(t)$ and myocardial contraction shows that α and β are related to myocardial force (F) and shortening velocity of the contractile element (v_{ce}) (Suga, 1972), suggesting a link between the ventricle as an active chamber and the ventricle as an assemblage of myocardial fibres whose shortening is described in terms of force-velocity relation (Sonnenblick, 1962).

Using a two element model of the myocardium and a thick-wall sphere or cylinder model of the ventricle we observe that:

$$F(t) = \alpha \cdot H \cdot E_0(\beta t) \tag{2.9}$$

and

$$v_{ce}(t) = \frac{\beta K_j}{E_0(\beta t)} \cdot \left[\frac{dE_0(\beta t)}{d(\beta t)} \right] \tag{2.10}$$

where H and K_j are functions of the ventricular volume and are specific to the geometric model used. K_j is affected by the afterload mode (j) (isobaric, isotonic and isovolumetric contraction). The mathematically derived F-v_{ce} curves and their shifts following variations of α, β, H and K_j under isotonic, isobaric and isovolumetric conditions reflect the experimentally derived F-v_{ce} curves suggesting that $E(t)$ is an expression of the dynamic characteristics of myocardial contraction and can be used as a useful index of the ventricular contractile state (Suga, 1972).

Given the small difference in ESPVR between isovolumic and ejecting contractions (Suga and Yamakoshi, 1977), the following equation is appropriate:

$$P_{es} = E_{es} \cdot (V_{es} - V_d) \tag{2.11}$$

The end-diastolic volume V_{ed} does not appear in the equation because ESPVR is insensitive to preload. According to Eq. (2.11), the greater the P_{es} the larger V_{es} is going to be with smaller stroke volume from a given V_{ed}. Stroke volume (SV) is formulated as:

$$SV = V_{ed} - V_{es} \tag{2.12}$$

E_{es} is a very versatile parameter in describing ventricular pumping performance under different loads. In fact, stroke volume changes with end-systolic pressure can be predicted by Eq. (2.11).
Rearranging Eq. (2.11), we obtain:

$$V_{es} = \frac{P_{es}}{E_{es}} + V_d \tag{2.13}$$

Substituting Eq. (2.13) in Eq. (2.12), we obtain:

$$SV = V_{ed} - \left(\frac{P_{es}}{E_{es}} + V_d \right) = V_{ed} - V_d - \frac{P_{es}}{E_{es}} \tag{2.14}$$

According to Eq. (2.14), SV from a given end-diastolic volume decreases linearly with end-systolic pressure in a ventricle with a constant contractile state (Weber, 1974; Elzinga, 1976).
An increase or decrease in end-diastolic volume should also cause a parallel shift of the P_{es}-SV line upward or downward without a significant change in its slope although this is not always the case (Weber, 1974; Elzinga, 1976).
E_{es} allows a quantitative estimation of the variation in ventricular contractility by physiological mechanisms (Suga, 1973; Suga and Sagawa, 1974; Suga, 1976). Unlike ejection fraction, E_{es} is preload independent and, like end-systolic volume, it is not affected by changes in systolic arterial pressure because it is a ratio of end-systolic pressure to end-systolic ventricular volume:

$$E_{es} = \frac{P_{es}}{V_{es} - V_d} \tag{2.15}$$

which also appears to be significantly insensitive to end-diastolic volume and to the mode of contraction as long as the ventricular contractile state remains constant (Suga and Sagawa, 1974).
Therefore, in more general terms the ratio of ventricular pressure to ventricular volume can be considered a reasonable approximation of the systolic phase as follows:

$$E(t) = \frac{P(t)}{V(t) - V_d(t)} \tag{2.16}$$

If the PV data specified at a particular time after the onset of contraction is represented by a line, the slope $E(t)$ increases with time until it reaches the highest value E_{max} at the end of systole. E_{max} is therefore exactly the same as E_{es} . The value of V_d decreases in the early systolic phase but subsequently it becomes virtually time-invariant. Therefore, the end-systolic value of V_d may be considered a constant given its little change following inotropic intervention. Although the time T_{max} to E_{max} is significantly insensitive to end-diastolic volume, the average T_{max} for isovolumic contractions is slightly shorter than that for ejecting contractions (Suga and Sagawa, 1974).

As far as clinical application is concerned, the estimation of V_d in each patient and how to normalise the calculated E_{max} value to allow comparison between patients remain key issues. If a large V_d were to be neglected, $E(t)$ would be significantly underestimated particularly in the presence of a small end-systolic volume. Besides, a significant decrease in E_{max} with or without an increase in V_d is observed in patients with low ejection fraction. Finally, E_{max} remains load-insensitive provided that the contractile state is not affected by neuro-humoral control mechanisms (Sagawa, 1978).

E_{max} and T_{max} are determined almost completely by the ventricular contractile state. Preload and afterload cause minimal difference unless they are excessively unphysiological (Sagawa, 1978).

E_{es}, or E_{max}, is a phenomenological parameter of ventricular contraction and not an entirely empirical index without physiological meaning. It gives information about ventricular wall stiffening and can be used to predict end-systolic volume and stroke volume if end-systolic pressure and end-diastolic volume are known (Sagawa, 1978).

Following its popularity, the original meaning of the end-systolic pressure-volume relationship and its parameters (E_{max} , V_d , V_o) have become ambiguous and misinterpreted. V_0 and V_d have been used interchangeably but they are fundamentally different. V_0 is the volume axis intercept of $E(t)$ and varies from end diastole (unstressed volume) to end systole (Suga and Sagawa, 1974; Maughan, 1979). Given its little variation near end systole, it can be treated as a constant if the interest is confined to E_{max} (Sagawa, 1981). Instead, V_d originally appeared to represent a functionally dead volume at which the ventricle could not generate any supra-atmospheric

pressure. Measurements of the behaviour of the end-systolic and end-diastolic pressure-volume relationship curves in the negative pressure region have shown convergence of the two curves at a point with a negative pressure coordinate of -15 to -20 *mmHg* and a volume coordinate only slightly less than V_0 (Fig. 2.3). This is the true V_d at which the ventricle cannot develop any systolic pressure (Sagawa, 1981).

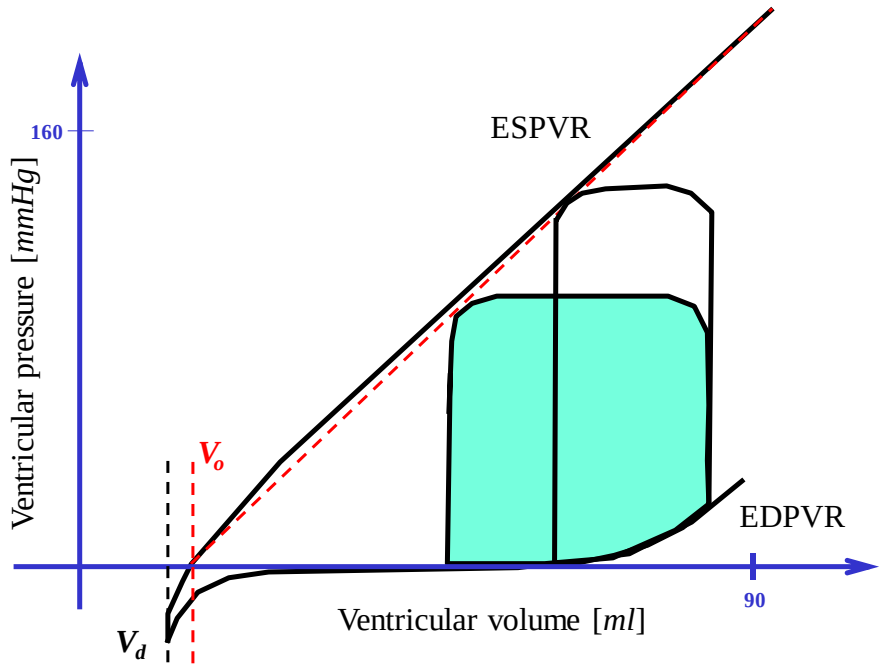

Figure 2.3 V_0 is the volume axis intercept, namely the maximal volume at zero pressure often referred to as the unstressed volume. V_d is the volume where the left ventricle cannot generate any systolic pressure. The PV loops, ESPVR and EDPVR have been generated using CARDIOSIM© software simulator. From: Capoccia M, De Lazzari C. Concepts, Mathematical Modelling and Applications in Heart Failure, 2019, Nova Science Publishers.

Therefore, the left ventricle has a time-varying elastance $E(t)$ according to the following more appropriate equation:

$$E(t) = \frac{P(t)}{V(t) - V_0} \tag{2.17}$$

where at any instance during systole the ventricular volume $V(t)$ in *ml* is simply proportional to the instantaneous pressure $P(t)$ in *mmHg* through a time-varying elastance $E(t)$ in *mmHg/ml* and V_0 is the volume axis intercept of ESPVR. Therefore, the left ventricle is considered as a chamber with its stiffness changing over time and with its intracavitary pressure determined

by instantaneous left ventricular volume. In addition, end systole is defined as an instant of time during the ejection phase where $E(t)$ reaches its maximum value E_{max}. Finally, the elastance is a system property, not a material property (Sagawa, 1988).

If the variation of V_0 is taken into account, a more accurate expression for the time-varying pressure-volume relationship is obtained as follows:

$$E(t) = \frac{P(t)}{V(t) - V_0(t)} \tag{2.18}$$

The validity of the approximated equation is subject to the time variation of V_0. When preload is varied in the presence of nearly constant afterload arterial impedance, V_0 variation is small. If the preload is kept constant in the presence of greatly altered afterload impedance, then V_0 variation is large.

From a theoretical point of view, $E(t)$ is an explicit expression of the dynamic characteristics of myocardial contraction (Suga, 1972) and supports the experimental evidence that E_{max} can be considered as a reliable index of ventricular contractility in view of its independence of preload and afterload within physiological range but sensitivity to changes in myocardial contractile state (Suga, 1973; Suga and Sagawa, 1974; Sagawa, 1977).

ESPVR and EDPVR can be considered linear functions with a common volume axis intercept, V_0, during most of the cardiac cycle (Suga, 1973; Suga and Sagawa, 1974). When different PV loops are obtained in the presence of preload and afterload changes, points of different cardiac cycles that occur at the same time can be joined to form isochrones. The slope of an isochrone is the elastance at that particular moment in time. This means that during each cardiac cycle the elastance increases from its diastolic value, E_{min}, to its systolic value, E_{es}, returning to its diastolic value again. E_{min} is the slope of EDPVR while E_{es} is the slope of ESPVR. The maximum elastance, E_{max}, becomes an index of cardiac contractility as previously mentioned. E_{max} increases following an increased inotropic state of the myocardium such as with catecholamine infusion; E_{max} decreases following a negative inotropic state of the myocardium such as a reduction in coronary artery pressure (Burkhoff, 2011).

There is a fundamental difference between E_{max} and E_{es} which must be considered to avoid conceptual errors in measurements (Kass and Maughan, 1988). E_{max} is the maximal single beat time-varying elastance while E_{es} is the slope of the end-systolic pressure-volume relationship or

end-systolic elastance relationship (Sagawa, 1981). These two terms are not interchangeable. E_{max} and E_{es} are nearly identical in isolated hearts with isovolumic or ejecting beats measured over a range of preload. When the afterload is changed significantly during the cardiac cycles used for the measurements, E_{max} and E_{es} can be very different (Kass and Maughan, 1988). In view of preload and afterload interrelation, E_{max} and E_{es} are frequently different *in vivo* because of likely resistive and inertial factors on end-systolic pressures (Hunter, 1983; Shroff, 1985; Campbell, 1986; Little and Freeman, 1987) as well as changes in the time to reach end systole as a function of load (Maughan, 1987).

Therefore, E_{max} is often significantly steeper than E_{es} and does not fall at the corners of the pressure-volume loops. E_{es} is a more useful measure of systolic properties in order to assess pump function. Estimation of E_{max} remains a useful concept for ventricular modelling but with limited clinical application for the assessment of systolic function.

The $E(t)$ surface or pressure-volume-time surface of the left ventricle is a three-dimensional representation of the concept that the time-varying elastance is independent of the loading conditions and E_{max} is derived by the contractile state of the ventricle.

Experimental evidence has shown a curvilinear ESPVR when a wide range of loading conditions is considered (Mirsky, 1987; Su, 1989; Kass, 1989; Suga, 1986; van der Velde, 1991), where the degree of nonlinearity depends on the contractile state (Burkhoff, 1987; Sato, 1998). A time-varying curvilinearity is observed during isovolumic contraction, ejection and isovolumic relaxation (Claessens, 2006).

Experimental and clinical studies *in vivo* measure ESPVR over a limited range of variable loading with few individual pressure-volume loops. The frequent observation of negative values for V_0 could be explained by ESPVR nonlinearity (Kass and Maughan, 1988). The ESPVR has never been intended to define myocardial properties directly but rather to give a useful measure of chamber systolic properties. Given the complex ventricular geometry, ESPVR nonlinearity seems a logical consequence. Quadratic (Burkhoff, 1987, Kass, 1989), logarithmic (Mirsky, 1987; Claessens, 2006) and exponential (Suga, 1986) functions have been proposed. Their expressions are in Table 2.1. α_0, α_1, β_0, β_1, β_2, γ, δ, ζ and η are suitable coefficients.

Quadratic and logarithmic functions with time-varying volume intercept seem to best describe the ESPVR while a logarithmic function seems superior in estimating the fixed volume intercept of the ESPVR. A linear approximation with fixed volume intercept gives a worse result particularly during

isovolumic relaxation and early filling (Claessens, 2006).

Table 2.1	
$P_{es} = \alpha_1 V_{es} + \alpha_0$	Linear
$P_{es} = \beta_2 V_{es}^2 + \beta_1 V_{es} + \beta_0$	Quadratic
$P_{es} = (\gamma + \delta V_{es})^{-1} \cdot \ln(V_{es}/V_0)$	Logarithmic
$P_{es} = \zeta[1 - e^{-\eta(V_{es} - V_0)}]$	Exponential

The curvilinear shape of the ESPVR may be related to the combination of a nonlinear active muscle function, the passive exponential stress-length relationship of myocardial tissue and the left ventricular geometry (Drzewiecki, 1989).

The EDPVR of isolated canine hearts shows appropriate fitting to an exponential function (Diamond, 1971; Janz, 1973; Glantz and Kernoff, 1975; Ingels, 1996). In addition, increasingly negative pressure is required to reduce volume in sub-physiological range (Sagawa, 1988; Burkhoff, 2005).

E_{es} can be normalised under controlled conditions (Suga, 1984; Belcher, 1985) but it is unlikely that large ventricles will always have lower E_{es} values in view of the wide clinical range of myocardial disease (Kass and Maughan, 1988). E_{es} is highly correlated with inotropic state in isolated hearts with homogeneous wall properties. Heterogeneity of mechanical properties or systolic timing in regionally ischaemic (Sunagawa, 1983) or locally paced ventricles (Park, 1985) can make the correlation between net chamber contractility and E_{es} much less direct (Kass and Maughan, 1988). For example, a rightward ESPVR shift is related to a reduced mechanical performance because of lower end-systolic pressure and stroke work measurements for any given starting volume but end-systolic elastance can be unchanged.

Another measure of systolic chamber function is the slope of the relationship between the highest value of the first derivative of left ventricular pressure, $(dP/dt)_{max}$, and end-diastolic volume (Little, 1985). A correlation between this slope and E_{es} can be predicted because interventions that shift ESPVR without affecting E_{es} do the same with the $(dP/dt)_{max}$-end-diastolic volume relation without affecting its slope (Little, 1987). Therefore, the preload recruitable stroke work ($PRSW$) or the slope of the stroke work-end-diastolic volume relationship (SWEDVR), is another measure of chamber contractility state (Sarnoff, 1961; Glower, 1985). The SWEDVR is quite linear over a wide range of physiological conditions where the dependent variable (stroke work) varies more with changes in end-diastolic volume than end-systolic

pressure does with end-systolic volume. $PRSW$ remains stable over a range of physiological afterloads despite the potential of afterload sensitivity: stroke work is zero at both no load and infinite load (Kass and Maughan, 1988). The SWEDVR integrates systolic and diastolic properties. In animal studies, EDPVR is usually flat and this interdependence is not significant.

In patients with chronic hypertrophy where diastolic function may be significantly impaired, the relation between systolic and diastolic properties may make $PRSW$ difficult to interpret as a pure systolic index. Finally, stroke work becomes ejection-history dependent at some stage and care must be taken when $PRSW$ is obtained from cardiac cycles under different preloads but with relatively stable ejection patterns (Kass and Maughan, 1988).

A broader view of the pressure-volume diagram has been advocated where the steepness of the ESPVR combined with the EDPVR allows the clinician to appreciate the effect of afterload changes on systolic pressure and stroke volume, or the dependence of both variables on changes in ventricular filling (Kass and Maughan, 1988). Shifting the focus from a single value, E_{es}, as a contractility index to the whole pressure-volume description with particular reference to the inter-relation between diastolic and systolic properties is much more likely to give the clinician useful information about the cardiac function and the outcome following therapeutic intervention.

2.4 Modifications to the Time-Varying Elastance Model

The load independence of the time-varying elastance theory has been challenged by further experimental evidence (Suga, 1979; Suga, 1980a; Sunagawa, 1982; Hunter, 1983; Maughan, 1984). Volume is not the only determinant of instantaneous pressure in the left ventricle. A key role is played experimentally by the measurement of the instantaneous pressure deficit, which is the difference between isovolumic pressure and ejecting pressure at a specific time in systole and at a specific volume of the isolated left ventricle. The pressure deficit is correlated with contributing factors such as the instantaneous ventricular ejection rate, the peak of the previous ejection rate within the given contraction and the amount of blood ejected up to the specified time (Suga, 1977; Sagawa, 1988). Normalized pressure (*%P*) at any specified time and volume decreases with increases in the instantaneous velocity of ejection ($-dV/dt$), the peak velocity of ejection $(-dV/dt)_{peak}$ and the volume ejected up to the specified time ($-\int dV$).

Multiple regression analysis of data (Suga, 1980a) gives the following equation:

$$\%P = A_0 - A_1\left(-\frac{dV}{dt}\right) - A_2\left(-\frac{dV}{dt}\right)_{peak} - A_3\left(-\int dV\right) \quad (2.19)$$

where A_0=100, A_1=0.14 s/m^3, A_2=0.07 s/m^3 and A_3=0.54 m^{-3}. Therefore, the original time-varying elastance (Eq. (2.17)) can be rearranged as follows (Sagawa, 1988):

$$P(t) = E_{iv}(t)\cdot\left[V(t) - V_0\right]\cdot\left[1 + k_1\frac{dV}{dt} + k_2\left(\frac{dV}{dt}\right)_{peak} + k_3\int dV\right] \quad (2.20)$$

where $E_{iv}(t)$ is the time-varying elastance measured from isovolumic beats; k_1=A_1/100; k_2=A_2/100 and k_3=A_3/100.

Considering that the instantaneous isovolumic pressure ($P_{iv}(t)$) that would be measured in the presence of a fixed ventricular volume $V(t)$ is

$$P_{iv}(t) = E_{iv}(t)\cdot\left[V(t) - V_0\right] \quad (2.21)$$

we can write the above expression in a more generic form as follows:

$$P(t) = P_{iv}(t)\cdot\left[1 + k_1\frac{dV}{dt} + k_2\left(\frac{dV}{dt}\right)_{peak} + k_3\int dV\right] \quad (2.22)$$

The ejection-dependent factors of the pressure deficit increase with isovolumic pressure $P_{iv}(t)$ and vary indirectly with time (Sagawa, 1988).

Dividing both sides of Eq. (2.22) by $[V(t) - V_0]$, we obtain:

$$E(t) = E_{iv}(t)\cdot\left[1 + k_1\frac{dV}{dt} + k_2\left(\frac{dV}{dt}\right)_{peak} + k_3\int dV\right] \quad (2.23)$$

Equation (2.23) states that the instantaneous volume elastance of ejecting beats is reduced from the isovolumic elastance in the same contractile state by three key factors of which the instantaneous ejection rate (dV/dt) gives the major contribution, the peak velocity $(-dV/dt)_{peak}$ is the next contributing factor while the ejected volume ($-\int dV$) pays the least contribution to the pressure deficit.

The time-varying elastance model gives accurate predictions of the events occurring during isovolumic contraction and at the end of systole but it

underestimates isovolumic left ventricular pressure in mid systole (Little, 1987). An initial attempt to overcome this issue is the use of an alternative formulation (Little, 1987) with the introduction of a source resistance (R) as follows:

$$P(t) = E(t) \cdot \left[V(t) - V_0(t) \right] + R \frac{dV}{dt} \tag{2.24}$$

The source resistance reduces the pressure generated at any left ventricular (LV) volume in proportion to the ejection rate. Therefore, the pressure generated by an isovolumic beat during mid-systole would be greater than the pressure generated by an ejecting beat with similar LV volume (Little, 1987). If the resistance is assumed to be proportional to the isovolumic pressure with proportionality constant K according to the following equation (Shroff, 1983; Shroff, 1985):

$$R = K \cdot E(t) \left[V(t) - V_0(t) \right] \tag{2.25}$$

Then, substituting in Eq. (2.24), we obtain:

$$P(t) = E(t) \cdot \left[V(t) - V_0(t) \right] \cdot \left[1 + K \frac{dV}{dt} \right] \tag{2.26}$$

The time-varying elastance theory describes the intact left ventricle during early systole and at end systole but not during mid-systole when LV contraction occurs. The introduction of a pressure-dependent resistance allows a consistent description of the left ventricle throughout systole despite changes in loading conditions and inotropic state. This formulation does not predict the timing of peak isovolumic pressure accurately suggesting that other factors may play a role during left ventricular contraction (Little, 1987).
The interactions between the left ventricle and the peripheral arterial circulation (SA) are described in terms of a feedback system connecting left ventricular outflow, peripheral arterial input-impedance, left ventricular pressure and pump properties (Campbell, 1984). An elastance-resistance left ventricular model (Campbell, 1982) coupled with a simple second-order peripheral arterial load model (Burattini and Gnudi, 1982) accounts for most of the observed interactions although a left ventricular pump component coupling ejection with relaxation and filling events may need to be considered for completion (Campbell, 1984). The in series LV component of

the LV-SA model relates the left ventricular pressure (P) to left ventricular volume (V) and left ventricular outflow (Q) according to the following equation:

$$P(t) = E(t) \cdot \left[V(t) - V_d(t) \right] - R \cdot Q(t) \tag{2.27}$$

where $V_d(t)$ is the time-varying dead volume and R is the internal LV resistance. Equation (2.27) can be rewritten as follows:

$$P(t) = E(t) \cdot \left[V_{ed} - V_d(t) \right] - E(t) \int_0^t Q(t) dt - R \cdot Q(t) \tag{2.28}$$

or

$$P(t) = P_{iso}(t) - E(t) \int_0^t Q(t) dt - R \cdot Q(t) \tag{2.29}$$

where P_{iso} is the LV isovolumic pressure, defined as:

$$P_{iso}(t) = E(t) \cdot \left[V_{ed} - V_d(t) \right] \tag{2.30}$$

Rearranging Eq. (2.29), we obtain:

$$P_D(t) = P_{iso}(t) - P(t) = E(t) \int_0^t Q(t) dt + R \cdot Q(t) \tag{2.31}$$

The difference between LV isovolumic pressure (P_{iso}) and the left ventricular pressure (P) generates a driving pressure (P_D) which is related to LV outflow (Q) according to the internal LV loading properties (Campbell, 1984). These properties consist of active functions, responsible for the development of P_{iso}, and loading functions, responsible for the relation between P_D and Q. Despite an apparent good predictive performance, the elastance-resistance LV model cannot explain a single-beat response to sudden or gradual changes in arterial loading resistance suggesting the existence of a LV pump element that couples ejection events with relaxation and filling events (Campbell, 1984).

2.5 Deviation from Elastance-Resistance Behaviour

Although elastance-resistance ($E(t)$-R) models of the left ventricle are attractive because they allow identification of instantaneous left ventricular pump properties from data recorded from only one or two heart beats (Campbell, 1990), they fail to predict instantaneous left ventricular pressure $P(t)$ during late ejection, which is quantitatively important for left ventricular pumping. This is most likely due to inadequate representation of end-systolic events (Campbell, 1986) without taking the deactivation component into account (Hunter, 1983).

The basic elastance-resistance model considers LV pressure as the sum of an elastance and a resistance component according to the following equation:

$$P(t) = E(t) \cdot \left[V_{ed} - V_d(t) - V_{ej}(t)\right] - R \cdot \dot{V}_{ej}(t) \qquad (2.32)$$

where the first term on the right-hand side is the elastance component, the second term is the resistance component, $E(t)$ is the time-varying elastance, $V_d(t)$ is the dead volume, $V_{ej}(t)$ is the instantaneous ejected volume, R is the internal LV resistance and $\dot{V}_{ej}(t)$ is the LV outflow (Campbell, 1986).

Competing forms of the basic model have been evaluated using two different parameterisation approaches for $E(t)$.

The first parameterisation approach is based on the assumption that under isovolumic conditions resistance plays no role in the relationship between pressure and volume, where the time course of $E(t)$ is set by the isovolumic pressure $P_{iso}(t)$ as follows:

$$E(t) = \frac{P_{iso}(t)}{V_{ed} - V_d(t)} \qquad (2.33)$$

If $V_d(t)$ remains constant, then:

$$\frac{P_{iso}(t)}{V_{ed} - V_d(t)} = \frac{P_{iso}(t)}{\alpha_1^*} \qquad (2.34)$$

If $V_d(t)$ is a function of time, then:

$$\frac{P_{iso}(t)}{V_{ed} - V_d(t)} = \frac{P_{iso}(t)}{\alpha_1 + \alpha_2 t} \qquad (2.35)$$

The parameters α_1^*, α_1 and α_2 are constants determined from the parameter estimation procedure (Campbell, 1986). They represent the stretched LV volume during an isovolumic beat.
Substituting Eq. (2.35) in Eq. (2.32), we obtain:

$$P(t) = E(t) \cdot \left[\alpha_1 + \alpha_2 t - V_{ej}(t)\right] - R \cdot \dot{V}_{ej}(t) \tag{2.36}$$

Rearranging Eq. (2.36), it yields:

$$E(t) = \frac{P(t)+R\cdot\dot{V}_{ej}}{\alpha_1+\alpha_2 t-V_d(t)} \tag{2.37}$$

The use of the above parameterisation is subject to $P_{iso}(t)$ measurements following total aortic occlusion in an experimental set up (Campbell, 1986).
The second form of parameterisation for $E(t)$ consists of a third-order polynomial with suitable coefficients α_0, α_1, α_2, α_3:

$$E(t) = \alpha_0 + \alpha_1 t + \alpha_2 t^2 + \alpha_3 t^3 \tag{2.38}$$

The first type of parameterisation has fewer parameters with physical meaning and the optimisation procedure is more likely to give better results. This approach can be used only when measurements give two sets of pressure and flow waveforms from beats with different afterload but equal preload and inotropic state. The second parameterisation has many parameters but it does not require two sets of measurements for its implementation.
The $E(t)$-R models have been tested by specifying V_d as a constant or as a function of time and R as a constant or as a linear function of P or P_{iso} as follows:

$$R = k \tag{2.39}$$

$$R(P) = b_1 + b_2 P \tag{2.40}$$

$$R(P_{iso}) = b_2' \; P_{iso} \tag{2.41}$$

where k , b_1 , b_2 and b_2' are suitable parameters, although nonlinear representations of R can be considered as well.

A descriptive validation test favours a model with V_d as a function of time and $R = k$ as the most suitable formulation to describe LV pumping. Although there is strong evidence that R depends either on $P(t)$ or $P_{iso}(t)$ (Shroff, 1983; Shroff, 1985; Hunter, 1979; Hunter, 1983), the validation test outcome suggests that other factors may be relevant and responsible for the failure of $E(t)$-R models to describe and predict LV behaviour appropriately (Campbell, 1986).

Events during late systole are not accounted for by $E(t)$-R models due to their inability to generate the biphasic $P_D(t)$ waveform, which is the instantaneous difference between $P_{iso}(t)$ and $P(t)$ of a normal ejecting beat. $E(t)$-R models also fail to predict the response to afterload increase by giving a shortened duration of $\dot{V}_{ej}(t)$ rather than a prolongation of $\dot{V}_{ej}(t)$ as a result of lack of features to maintain or terminate systole (Campbell, 1986).

The discrepancies of the $E(t)$-R models can be addressed by adding a third element. In fact, three components are observed in the LV response to a flow pulse: elastance, resistance and deactivation (Suga, 1980a; Hunter, 1983; Shroff, 1985). The deactivation component is absent during early systole, becomes evident during mid-systole and is most pronounced during late systole.

The late systole prominence of a deactivation event can partially explain the poor behaviour of $E(t)$-R models at end-systole. The missing third element should account for the active effect related to the paradoxically high $P(t)$ at the notch in the $P_D(t)$ waveform and account for the deactivation effect related to the fall in $P(t)$ at the second hump in the $P_D(t)$ waveform.

Further evaluation of $E(t)$-R models has been considered in relation to their ability to reproduce instantaneous pressure $P(t)$ and outflow $Q(t)$ (Campbell, 1990). Measurements of $P(t)$ and $Q(t)$ are obtained during steady-state ejecting beats and during a beat following partial or total aortic occlusion. The total occlusion beat is considered the isovolumic one that generates an isovolumic pressure $P_{iso}(t)$ with a characteristic time $T_{pisomax}$ to maximal $P_{iso}(t)$.

The extra-pressure $P_{ext}(t)$ and the extra-outflow $Q_{ext}(t)$ are the components of $P(t)$ and $Q(t)$ not accounted for by $E(t)$-R models (Campbell, 1990).

If we consider the pressure $\hat{P}(t)$ generated by the $E(t)$-R model, we have:

$$\hat{P}(t) = P_E(t) - P_R(t) \tag{2.42}$$

where $P_E(t)$ is the pressure component due to $E(t)$ (Sagawa, 1978):

$$P_E(t) = E(t) \cdot \left[V(t) - V_0 \right] \tag{2.43}$$

and $P_R(t)$ is the pressure component due to R (Shroff, 1985):

$$P_R(t) = \rho \cdot P_E(t) \cdot Q(t) \tag{2.44}$$

ρ is the coefficient that determines the resistance effect and

$$V(t) = V_{ed} - V_{ej}(t) \tag{2.45}$$

Substituting Eq. (2.45) in Eq. (2.43), we obtain:

$$P_E(t) = E(t) \cdot \left[V_{ed} - V_{ej}(t) - V_0 \right] = E(t) \cdot \left[V_{ed} - V_0 \right] - E(t) \cdot V_{ej}(t) \tag{2.46}$$

But

$$P_{iso}(t) = E(t) \cdot \left[V_{ed} - V_0 \right] \tag{2.47}$$

and $\alpha = V_{ed} - V_0$ is a constant volume. Then

$$P_{iso}(t) = \alpha \cdot E(t) \quad \Rightarrow \quad E(t) = \frac{1}{\alpha} \cdot P_{iso}(t) \tag{2.48}$$

Substituting Eq. (2.47) and Eq. (2.48) into Eq. (2.46), it yields:

$$P_E(t) = P_{iso}(t) - \frac{1}{\alpha} P_{iso}(t) \cdot V_{ej}(t) = P_{iso}(t) \cdot \left[1 - \frac{V_{ej}(t)}{\alpha} \right] \tag{2.49}$$

Substituting Eq. (2.49) into Eq. (2.44), it yields:

$$P_R(t) = \rho \cdot P_{iso}(t) \cdot \left[1 - \frac{V_{ej}(t)}{\alpha} \right] \cdot Q(t) \tag{2.50}$$

Then, substituting Eq. (2.50) and Eq. (2.49) in Eq. (2.42), we obtain:

$$\hat{P}(t) = P_{iso}(t)\cdot\left[1-\frac{V_{ej}(t)}{\alpha}\right] - \rho\cdot P_{iso}(t)\cdot\left[1-\frac{V_{ej}(t)}{\alpha}\right]\cdot Q(t) = \\ = P_{iso}(t)\cdot\left[1-\frac{V_{ej}(t)}{\alpha}\right]\cdot\left[1-\rho\cdot Q(t)\right] \quad (2.51)$$

$\hat{P}(t)$ is calculated by using measured values of $P_{iso}(t)$, $V_{ej}(t)$ and $Q(t)$ and given values of α and ρ. An inverse formulation of Eq. (2.51) gives the following equation:

$$\hat{Q}(t) = \frac{1}{\rho}\cdot\left\{1-\frac{P(t)}{P_{iso}(t)\cdot\left[1-\frac{\hat{V}_{ej}(t)}{\alpha}\right]}\right\} \quad (2.52)$$

where $P(t)$ is the input, while $\hat{Q}(t)$ and $\hat{V}_{ej}(t)$ are the output of the model. Considering that

$$\hat{Q}(t) = \frac{d\hat{V}_{ej}(t)}{dt} \quad (2.53)$$

substituting Eq. (2.53) in Eq. (2.52), we obtain:

$$\frac{d\hat{V}_{ej}(t)}{dt} = \frac{1}{\rho}\cdot\left\{1-\frac{P(t)}{P_{iso}(t)\cdot\left[1-\frac{\hat{V}_{ej}(t)}{\alpha}\right]}\right\} \quad (2.54)$$

The solution of Eq. (2.52) and Eq. (2.54) relies on measured values of $P(t)$ and $P_{iso}(t)$ and estimated values of α and ρ. If α and ρ correspond to a best fit to $P(t)$ or $Q(t)$ over the interval $0 < t < T_{pisomax}$, $P_{ext}(t)$ and $Q_{ext}(t)$ can be calculated as:

$$P_{ext}(t) = P(t) - \hat{P}(t) \quad (2.55)$$

$$Q_{ext}(t) = Q(t) - \hat{Q}(t) \tag{2.56}$$

over the interval $0 < t < T_{ej}$, where T_{ej} is the end ejection time. Data obtained following partial aortic occlusion are used to calculate changes in $P_{ext}(t)$ and $Q_{ext}(t)$ and check their trend (Campbell, 1990).

The addition of extra elements to the $E(t)$-R model is an attempt to account for $P_{ext}(t)$ and $Q_{ext}(t)$: an active function $A(t)$ that gives additional energy and a deactive function $D(t)$ that dissipates energy (Campbell, 1990). Then the extra function $F_{ext}(t)$ accounting for $P_{ext}(t)$ or $Q_{ext}(t)$ is as follows:

$$F_{ext}(t) = A(t) - D(t) \tag{2.57}$$

Further analysis confirms the inadequate representation of instantaneous LV pumping pressure by $E(t)$-R models during late systole (Campbell, 1986) but also throughout the whole ejection period. The addition of active and deactive components to the basic $E(t)$-R model allows a better data fitting but fails to improve their predicting ability (Campbell, 1990).

Kinetic models seem a valid alternative (Hunter, 1989) due to their intrinsic mechanism to express late-systolic flow-dependent positive functional potential and their relation to kinetic processes occurring within the myocyte.

2.6 Ventricular-Arterial Coupling

Ventricular-arterial coupling can be described by overlooking the pulsatile nature of pressure and flow (Van den Horn, 1984; Van den Horn, 1985; Van den Horn, 1986) with the introduction of a mean total resistance R_p coupled to a ventricular "source resistance" R_s derived from a mean ventricular pressure-flow function curve. Although the advantage of this approach is the use of measurable parameters such as pressure and flow, the mean pressure-flow relation is affected by preload and characteristic impedance (Elzinga, 1978; Maughan, 1984); it is nonlinear and it does not consider diastolic function and energetics into the overall coupling analysis. Alternatively, ventricular-arterial coupling is usually measured in the pressure-volume plane from the ratio of effective arterial elastance E_a to left ventricular end-systolic elastance E_{es} to obtain information on mechanical efficiency and performance of the ventricular-arterial system. The left ventricle is considered an elastic chamber that periodically increases its volume to E_{es}, which is the slope of the end-systolic pressure-volume relationship. The arterial load property is described by an effective elastance

E_a, which is the slope of the arterial end-systolic pressure-stroke volume relationship (Sunagawa, 1983; Sunagawa, 1985). The mean and the end-ejection arterial pressures are approximated by the ventricular end-systolic pressure. The use of a 3-element windkessel model predicts that the ratio of end-systolic pressure P_{es} to stroke volume SV is constant under a given steady state vascular impedance load (Kass, 1992).

An analytical quantification of ventricular-arterial interaction is obtained using the P_{es}-SV relationship of the ventricle and the arterial system. This approach can be extended to the analysis of cardiac output with a set of equations to understand the role of the different parameters and components of the circulation including coupling of ventricular diastolic behaviour with total vascular properties and total blood volume (Sunagawa, 1984). Given ESPVR linearity within physiological range and its relative insensitivity to changes in loading conditions, the relation between left ventricular end-systolic pressure P_{es} and stroke volume SV can be written as follows:

$$P_{es} = E_{es} \cdot \left(V_{ed} - SV - V_0\right) \tag{2.58}$$

P_{es} varies inversely with SV in a linear way at a given V_{ed}. If the arterial system properties are also described by a P_{es}-SV relationship, the balancing stroke volume is obtained when the ventricle is coupled with the arterial system as the intersection between the two P_{es}-SV relationship lines. The P_{es}-SV relationship of the arterial system can be derived considering a three-element windkessel model (Fig. 2.4), which consists of characteristic resistance R_c, peripheral resistance R and arterial compliance C (Sunagawa, 1983).

The average arterial flow $\overline{Q}_a$ over the duration T of one cardiac cycle is:

$$\overline{Q}_a = \frac{\overline{P}_a}{R_c + R} \tag{2.59}$$

where $\overline{P}_a$ is the average arterial pressure over one cardiac cycle. But $\overline{Q}_a$ = SV/T and $\overline{P}_a$= A_T/T, where A_T is the total area under the arterial pressure curve over one cardiac cycle.

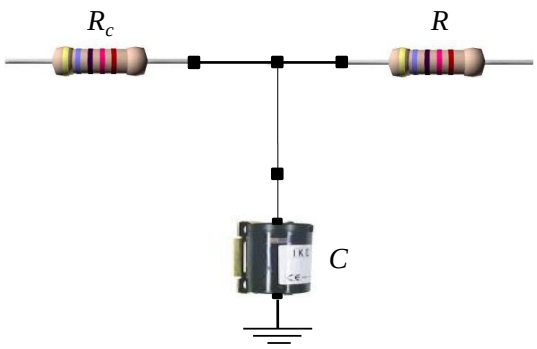

Figure 2.4 The electrical analogue circuit for the three-element windkessel model. R_c is the characteristic resistance, R is the peripheral resistance and C is the arterial compliance. From: Capoccia M, De Lazzari C. Concepts, Mathematical Modelling and Applications in Heart Failure, 2019, Nova Science Publishers.

Therefore, Eq. (2.59) can be rewritten as follows:

$$\frac{SV}{T} = \frac{A_T \cdot T^{-1}}{R_c + R} \qquad \Rightarrow \qquad SV = \frac{A_T}{R_c + R} \tag{2.60}$$

If the difference between end-systolic pressure and end-ejection pressure is neglected by approximating mean and end-ejection arterial pressure with the end-systolic ventricular pressure P_{es}, the diastolic pressure area A_d can be written as follows (Sagawa, 1981):

$$A_d = P_{es} \cdot \tau \cdot \left[1 - e^{\left(\frac{-t_d}{\tau}\right)} \right] \tag{2.61}$$

where t_d is the duration of "arterial diastole" and $\tau = RC$ is the time constant of diastolic arterial pressure decay. The systolic pressure area A_s can also be approximated as $A_s = P_{es} \cdot t_s$, where t_s is the duration of "arterial systole". Therefore, the total area A_T under the arterial pressure curve becomes:

$$A_T = A_s + A_d = P_{es} \left\{ t_s + \tau \cdot \left[1 - e^{\left(\frac{-t_d}{\tau}\right)} \right] \right\} \tag{2.62}$$

Substituting Eq. (2.62) in Eq. (2.60), we obtain the following approximated P_{es}-SV relationship of the arterial system:

$$P_{es} = \frac{R + R_c}{t_s + \tau \cdot \left[1 - e^{\left(\frac{-t_d}{\tau} \right)} \right]} \cdot SV \tag{2.63}$$

According to Eq. (2.63), P_{es} is a linear function of SV provided that all the other parameters remain constant.

Therefore, if $E_a = (R + R_c)/\{t_s + \tau[1 - e^{(-t_d/\tau)}]\}$ is the slope of the P_{es}-SV relationship, Eq. (2.63) becomes:

$$P_{es} = E_a \cdot SV \tag{2.64}$$

where E_a is the effective arterial elastance.

Coupling between ventricular and arterial systems is achieved when the balancing stroke volume is obtained by solving Eq. (2.58) and Eq. (2.64) simultaneously as follows:

$$E_a \cdot SV = E_{es} \cdot (V_{ed} - SV - V_0) \quad \Rightarrow \quad SV = \frac{V_{ed} - V_0}{1 + \frac{E_a}{E_{es}}} \tag{2.65}$$

Ventricular-arterial coupling using the P_{es}-SV relationship of both ventricular and arterial systems has been found to be an effective approach to quantify the interaction between the ventricle and the arterial circulations with further extension to the analysis of cardiac output (Sunagawa, 1983; Sunagawa, 1984).

If we consider the external work (EW) as the approximated product of stroke volume SV and end-systolic pressure P_{es} (Fig. 4.5), we have:

$$EW = P_{es} \cdot SV \tag{2.66}$$

Substituting Eq. (2.64) and Eq. (2.65) in Eq. (2.66), it yields:

$$EW = E_a \cdot SV^2 = E_{es} \cdot (V_{ed} - V_0)^2 \cdot \frac{\frac{E_a}{E_{es}}}{\left(1 + \frac{E_a}{E_{es}} \right)^2} \tag{2.67}$$

Considering that the maximal transfer of energy from one elastic chamber to another occurs when they have equal elastance, the left ventricle will do maximal external work if E_{es} = E_a (Sunagawa, 1985). This can be demonstrated by rearranging Eq. (2.67) as follows:

$$EW = \frac{E_a \cdot E_{es}^2 \cdot a^2}{\left(E_{es} + E_a\right)^2} \tag{2.68}$$

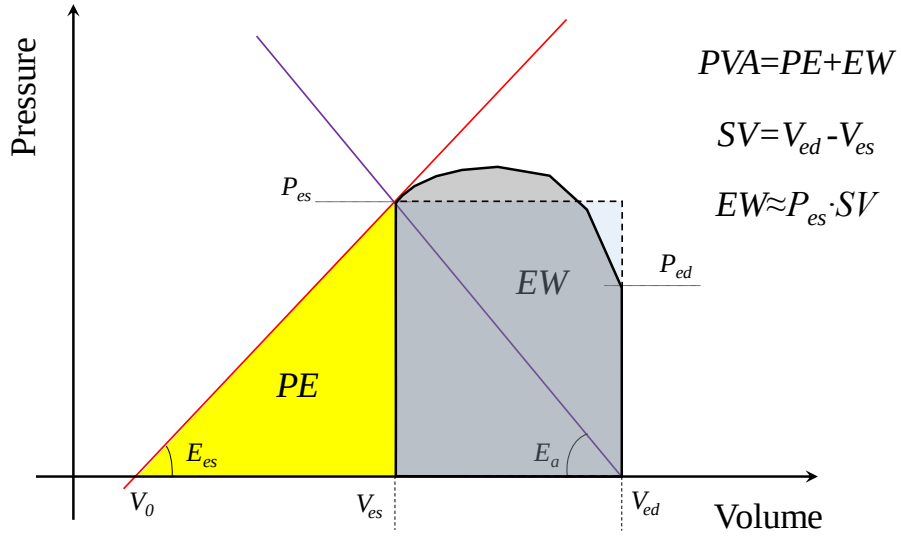

Figure 2.5 Approximated external work (EW), end-systolic potential energy (PE) and pressure-volume area (PVA). From: Capoccia M, De Lazzari C. Concepts, Mathematical Modelling and Applications in Heart Failure, 2019, Nova Science Publishers.

where $a = V_{ed} - V_0$.

Differentiating Eq. (2.68) with respect to E_a, we obtain:

$$\frac{d\left(EW\right)}{dE_a} = \frac{E_{es}^2 \cdot a^2 \cdot \left(E_{es} + E_a\right)^2 - 2 \cdot E_a \cdot E_{es}^2 \cdot a^2 \cdot \left(E_{es} + E_a\right)}{\left(E_{es} + E_a\right)^4} \tag{2.69}$$

Setting the result equal to zero and solving, we obtain the maximum and minimum of the function as follows:

$$\left(E_{es} + E_a\right) \cdot \left(E_{es}^3 \cdot a^2 + E_a \cdot E_{es}^2 \cdot a^2 - 2 \cdot E_a \cdot E_{es}^2 \cdot a^2\right) = 0 \tag{2.70}$$

$$E_{es}^2 \cdot a^2 \cdot \left(E_{es} + E_a\right) \cdot \left(E_{es} - E_a\right) = 0 \tag{2.71}$$

with the following solutions:

$$E_a = -E_{es} \qquad \text{and} \qquad E_a = E_{es} \tag{2.72}$$

where only the positive value can be accepted.
If the ESPVR is nonlinear and can be approximated by the following parabolic expression with suitable constants a and b (Burkhoff, 1987; Kass, 1989):

$$P_{es} = a \cdot \left(V_{es} - V_0\right)^2 + b \cdot \left(V_{es} - V_0\right) \tag{2.73}$$

maximal stroke work will still occur when E_a equals the instantaneous slope of the nonlinear ESPVR (Kass, 1992). In fact, if the ESPVR is defined as follows:

$$P_{es} = f\left(V_{es}\right) \tag{2.74}$$

where f is a monotonically increasing function of V_{es}, $E_{es_{V_{es}}} = f'(V_{es})$ is the local slope of the ESPVR at a given V_{es}. Considering that E_a is given by the P_{es}/SV ratio, then we obtain:

$$E_a = \frac{P_{es}}{SV} = \frac{P_{es}}{V_{ed} - V_{es}} = \frac{f\left(V_{es}\right)}{V_{ed} - V_{es}} \tag{2.75}$$

and

$$EW = P_{es} \cdot SV = f\left(V_{es}\right) \cdot \left(V_{ed} - V_{es}\right) \tag{2.76}$$

Differentiating Eq. (2.76) with respect to V_{es} at a given end-diastolic volume V_{ed}, we obtain:

$$\frac{d\left(EW\right)}{dV_{es}} = f'\left(V_{es}\right)\left(V_{ed} - V_{es}\right) - f\left(V_{es}\right) \tag{2.77}$$

Setting the result equal to zero and solving, we obtain:

$$f'(V_{es})(V_{ed}-V_{es})-f(V_{es})=0 \quad \Rightarrow \quad f'(V_{es})=\frac{f(V_{es})}{(V_{ed}-V_{es})} \tag{2.78}$$

but $f'(V_{es}) = E_{es_{V_{es}}}$ and $f(V_{es})/(V_{ed} - V_{es}) = E_a$, then optimal stroke work is obtained when $E_{es_{V_{es}}} = E_a$ (Kass, 1992).

An important clinical application of ventricular-vascular coupling analysis is the ability to predict integrated cardiovascular performance according to separate changes in ventricular or vascular properties in terms of stroke volume, stroke work, ejection fraction, mean pressure and flow. For this purpose, Eq. (2.65) can be rearranged as follows:

$$\frac{SV}{V_{ed}-V_0}=\frac{1}{1+\frac{E_a}{E_{es}}} \tag{2.79}$$

Starting values for E_{es}, E_a, V_0 and V_{ed} are entered; then, percent changes in E_{es} and E_a obtained following intervention are used to predict net ejection fraction changes. The ventricular-vascular coupling approach can be applied to analyse data obtained *in vivo* under certain operating conditions and can be used to predict the response under new operating conditions (Kass, 1992).

The ventricular-arterial elastance model predicts that optimal stroke work occurs when $E_{es} = E_a$ (Sunagawa, 1985). Considering that:

$$EF=\frac{SV}{V_{ed}} \tag{2.80}$$

substituting Eq. (2.65) in Eq. (2.80), we obtain:

$$EF=\frac{1}{V_{ed}}\cdot\frac{V_{ed}-V_0}{1+\frac{E_a}{E_{es}}} \tag{2.81}$$

Starting from Eq. (2.81) we obtain the results in Table 2.2.

Considering that V_0 has a small volume rather than zero, each of the above operating states would correspond to slightly different ejection fraction with particular reference to E_a/E_{es} = 1 whose ejection fraction would be slightly less than 50%, which is not the norm in healthy humans.

Table 2.2		
If $V_0 \rightarrow 0$ and E_{es}=E_a	EF=1/2	EF=50%
If $V_0 \rightarrow 0$ and E_{es}=2E_a	EF=2/3	EF=66%
If $V_0 \rightarrow 0$ and $E_{es} = \frac{1}{2}E_a$	EF=1/3	EF=33%

Using a linear ESPVR, E_a and the linear relationship between myocardial oxygen consumption (MVO_2) and pressure-volume area (PVA), we can generate equations that predict coupling ratios at optimal work and efficiency (Burkhoff, 1986).

Ventricular pump efficiency (Eff) is defined as the ratio between the external mechanical work done by the heart (EW) and the total energy supplied to it, which is equivalent to cardiac O_2 consumption:

$$Eff = \frac{EW}{MVO_2} \tag{2.82}$$

The amount of EW performed by the ventricle and the amount of consumed O_2 vary with the loading conditions imposed on the ventricle and with the contractile state of the heart (Burkhoff, 1986).

We already know from Eq. (2.67) that EW can be expressed by the following equation:

$$EW = E_{es} \cdot \left(V_{ed} - V_0\right)^2 \cdot \frac{\frac{E_a}{E_{es}}}{\left(1 + \frac{E_a}{E_{es}}\right)^2} \tag{2.83}$$

assuming that ventricular end-diastolic pressure is negligible compared with the pressure during ejection, which is reasonable in the normal heart but it may be invalid in a diseased status where end-diastolic compliance is often decreased. The small inertia-related work performed by the heart is also not taken into account (Burkhoff, 1986).

As far as myocardial oxygen consumption is concerned, there is a known linear relationship between left ventricular MVO_2 and PVA (Suga, 1979; Suga, 1980b; Suga, 1983):

$$MVO_2 = A \cdot PVA + B \tag{2.84}$$

with suitable constants A and B. PVA is a measure of the total mechanical energy generated by ventricular contraction and it can be considered as the sum of EW and the end-systolic potential energy (PE) (Fig. 2.5):

$$PVA = EW + PE \tag{2.85}$$

PE can be expressed as follows:

$$PE = \frac{P_{es} \cdot (V_{es} - V_0)}{2} = \frac{P_{es}^2}{2E_{es}} \tag{2.86}$$

Substituting Eq. (2.64) and exploiting Eq. (2.67), we obtain:

$$PE = \frac{E_a^2 SV^2}{2E_{es}} = \frac{E_a}{2E_{es}} EW \tag{2.87}$$

Consequently, PVA becomes:

$$PVA = EW + \frac{E_a}{2E_{es}} EW = \left(1 + \frac{E_a}{2E_{es}}\right) EW \tag{2.88}$$

From the previous equations we obtain:

$$Eff = \frac{EW}{A \cdot EW + A \cdot EW \frac{E_a}{2E_{es}} + B} = \frac{1}{A \cdot \left(1 + \frac{E_a}{2E_{es}}\right) + \frac{B \cdot \left(1 + \frac{E_a}{E_{es}}\right)^2}{E_a \cdot (V_{ed} - V_0)^2}} \tag{2.89}$$

E_a must always be smaller than E_{es} to obtain physiological conditions (Burkhoff, 1986). Further analysis of the dependence of EW and efficiency on the E_a/E_{es} ratio over a broad range of E_a values shows that EW is maximal when E_a/E_{es} = 0.8 whereas efficiency is maximal when E_a/E_{es} = 0.7 (De Tombe, 1993). The E_a/E_{es} range observed in large groups of normal humans is 0.62÷0.82 (Redfield, 2005; Chirinos, 2009). EW and efficiency are more than 90% of their optimal value over a broad E_a/E_{es} range (0.3÷1.3) corresponding to a wide ejection fraction range (40%÷80%). Therefore, optimisation of either EW or efficiency does not play a major role in the absence of abnormal E_a or E_{es} and other regulatory mechanisms such as blood pressure control, circulating volume and oxygenation are more

likely to intervene (De Tombe, 1993). Ventricular EW is relatively insensitive to afterload over a wide range of E_a values, whereas ventricular efficiency is significantly more affected by afterload. Understanding the behaviour of the performance index for optimal control of ventricular-arterial coupling under physiological conditions may well give an idea about changes of ventricular and arterial properties during stress or a diseased status (Burkhoff, 1986).

Despite its limitations and criticism, pressure-volume analysis remains an effective way to assess the influence of ventricular and vascular stiffness on net cardiovascular function from non-invasive single-beat measurements without the need for preload alterations (Takeuchi, 1991; Senzaki, 1996; Chen, 2001). The effective arterial elastance E_a and the end-systolic elastance E_{es} share the same units in the time domain and are a suitable match to study ventricular-arterial interaction (Sunagawa, 1983; Sunagawa, 1985). E_a is a lumped parameter that reflects the net impact of mean and pulsatile loading on the heart (Borlaug, 2008). The ratio of end-systolic pressure to stroke volume P_{es}/SV gives an accurate estimation of E_a in normal subjects and hypertensive patients (Kass, 1992). The E_a/E_{es} ratio is an expression of effective ventricular-arterial coupling (Asanoi, 1989; De Tombe, 1993), which can be defined as the optimal blood transfer from the heart to the periphery with limited changes in blood pressure or, in other words, as the provision of optimal cardiovascular flow reserve without compromising arterial pressure (Borlaug, 2008). The E_a/E_{es} ratio is preserved in normal subjects to maintain optimal efficiency in men but declines in women because of significant increase in E_{es} compared to E_a (Redfield, 2005).

From a theoretical and experimental point of view, a E_a/E_{es} ratio within the range 0.6÷1.2 achieves near optimal external work and efficiency (Sunagawa, 1983; De Tombe, 1993). The E_a/E_{es} ratio normally drops during exercise because the increased contractility E_{es} exceeds the increased afterload E_a but it can become significantly high when systolic heart failure occurs, where a reduced E_{es} following impaired systolic function is coupled to a high E_a as a reflection of significantly increased arterial impedance (Fig. 2.6a and Fig 2.6b) (Borlaug, 2008).

Although the E_a/E_{es} ratio remains a useful measurement of ventricular-arterial coupling in terms of operating mechanical efficiency and performance, it is argued that E_a poorly characterises pulsatile left ventricular load and does not depend exclusively on arterial properties. In addition, the systolic loading sequence which is an important aspect of ventricular-arterial coupling is neglected by pressure-volume analysis and it may significantly impact left ventricular function, remodelling and

progression to heart failure (Chirinos, 2013). Pulsatile arterial load measurement has been proposed as a more suitable approach to assess ventricular-arterial coupling in heart failure with preserved ejection fraction and other diseased states (Chirinos, 2017). Ventricular-arterial coupling in terms of pulsatile pressure-flow relationship gives incremental information about the physiological status of the cardiovascular system.

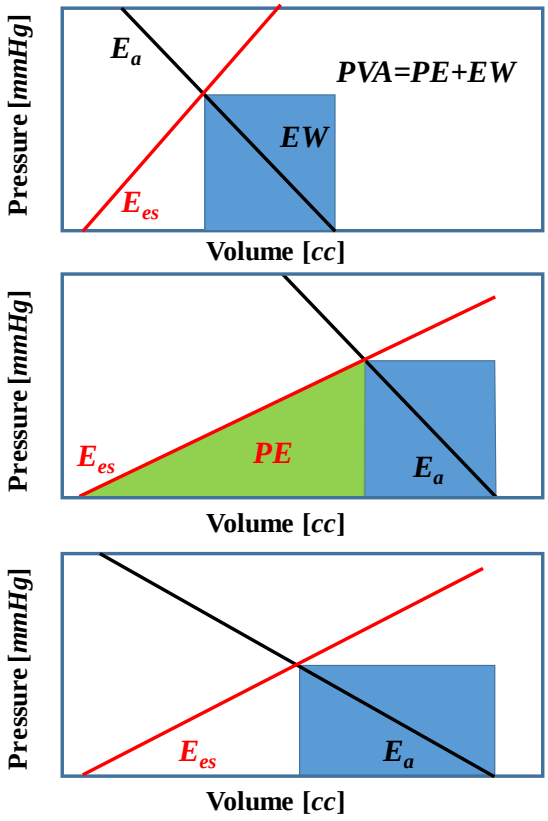

$E_{es} = 1\,AU$
$E_a = 1\,AU$
$E_a/E_{es} = 1$
$EW/PVA \approx 2/3$
$EF = 50\%$

$E_{es} = 0.5\,AU$
$E_a = 1\,AU$
$E_a/E_{es} = 2$
$EW/PVA \approx 1/2$
$EF = 33\%$

$E_{es} = 0.5\,AU$
$E_a = 0.5\,AU$
$E_a/E_{es} = 1$
$EW/PVA \approx 2/3$
$EF = 50\%$

Figure 2.6a Potential effects on ventricular-arterial coupling following E_{es} reduction.

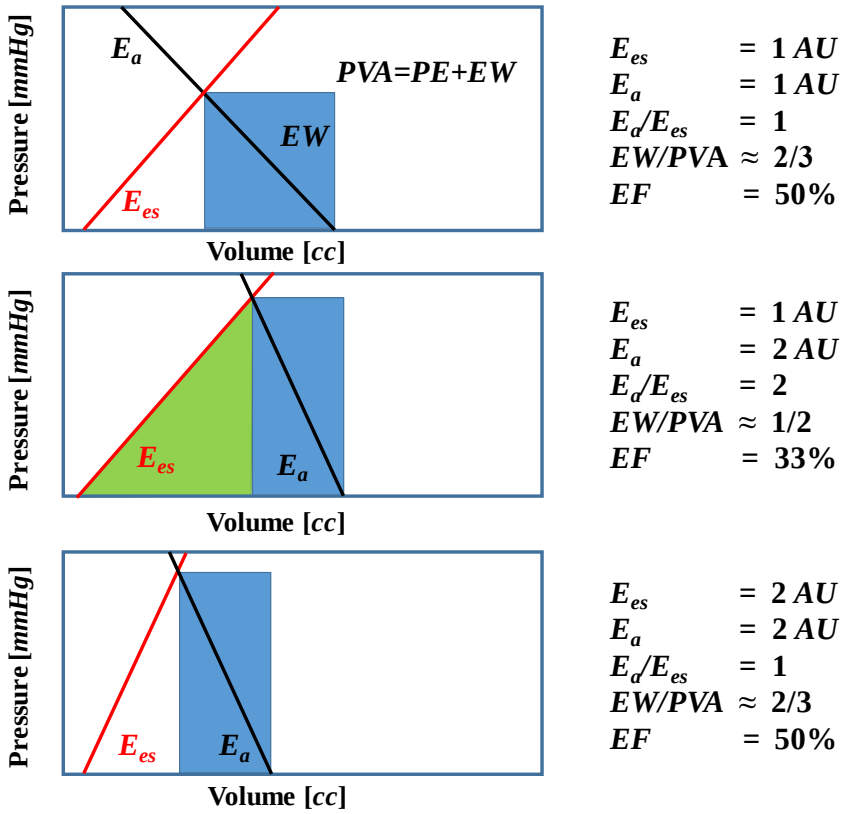

Figure 2.6b Potential effects on ventricular-arterial coupling following E_a reduction.

2.7 Pressure-Volume Loop Analysis during Mechanical Circulatory Support

The effect of different working conditions on the left ventricle or the assessment of myocardial recovery during mechanical circulatory support remains a challenging subject.

Pressure-volume loop analysis is a traditional and effective technique for the evaluation of cardiovascular dynamics.

Different methods have been proposed to assess myocardial recovery (Mancini, 1998; Slaughter, 2001; Farrar, 2002) including the attempt to address intrinsic contractility or the so-called “load-independent” cardiac function using ESPVR at the time of LVAD implantation and explantation (Ferrari, 2005). Although convenient, the assumption of ESPVR as a load-independent index of cardiac function is valid within certain limits because extremes of loading conditions can change both the maximun time-varing systolic elastance (E_{max}) and the slope of ESPVR (E_{es}) (Burkhoff, 1987; Kass, 1987; Kass, 1989). E_{es} and E_{max} give load-independent indexes of cardiac contractility based on acutely increased left ventricular afterload or decreased preload (Burkhoff, 1987; Kass, 1987; Kass, 1989). When left

ventricular preload is reduced by occlusion of the inferior vena cava, mean arterial pressure drops with an instantaneous change in left ventricular end-systolic pressure, P_{es}. Progressive left ventricular unloading with an axial flow pump is different because the device supports the systemic circulation. Therefore, mean arterial pressure should remain unchanged with only minor changes in left ventricular systolic pressure until the left ventricle is deprived of a sufficient volume of blood to allow ejection. As a result, left ventricular unloading is not related to an instantaneous drop of P_{es} that may affect E_{es} or E_{max}. Also, the ESPVR is nonlinear in extreme unloading conditions of the left ventricle, for example when left ventricular systolic pressure ($P_{s,LV}$) is lower then mean arterial pressure (MAP) during LVAD support. Although MAP is maintained during LVAD support, a significant reduction in left ventricular volume and myocardial oxygen consumption occurs before $P_{s,LV} < MAP$, which may affect left ventricular contractility. Therefore, the assumption of a linear ESPVR during this level of unloading may not be correct (McConnell, 2006).

The slope of the relationship between stroke work and end-diastolic volume (SWEDVR) is known as preload recruitable stroke work ($PRSW$). SWEDVR shows the linearity of Frank-Starling curve in the intact heart (Glower, 1985). It is sensitive to changes in contractility like E_{es} and E_{max} (Kass, 1987; Glower, 1985; Little, 1988; Krukenkamp, 1987) but remains linear over the complete physiological range because it takes into account changes in systolic and diastolic function unlike E_{es}, which only considers changes in systolic function (Kass, 1987). During unloading with an axial flow pump, SWEDVR remains linear not just after $P_{s,LV} < MAP$ but over the complete range of device support (McConnell, 2007). In contrast, E_{max} and E_{es} appear more significantly affected by the left ventricular unloading strategy.

Left ventricular volume analysis during mechanical circulatory support in an experimental setting shows a significant correlation between end-systolic volume index ($ESVI$) and end-diastolic volume index ($EDVI$) due to auto-regulatory mechanisms, which should be considered in relation to driving strategies for a ventricular assist device (Moscato, 2007).

The widespread use of rotary blood pumps has focused the attention on the remaining contractile function of the native heart, which is crucial both for myocardial recovery and long-term support.

A reliable measurement parameter for cardiac contractility should be sensitive to changes in myocardial properties but insensitive to changes in ventricular preload and afterload.

Clinically used indices such as ejection fraction (EF), maximal derivative of left ventricular pressure ($(dP_{LV}/dt)_{max}$) and maximal value of the hydraulic

power generated by the left ventricle (PWR_{max}) are sensitive to ventricular preload and afterload (Mason, 1969; Kass, 1991; Suga, 2003). Other indices derived from pressure-volume relationships such as E_{max}, PWR_{max} divided by end-diastolic volume (PWR_{max}/V_{ed}), $PRSW$ and $(dP_{LV}/dt)_{max}$ vs V_{ed} are insensitive to changes in ventricular preload and afterload (Little, 1985; Glower, 1985; Kass, 1987; Burkhoff, 2005). The applicability of these indices is limited in patients with continuous flow pumps because of the need for invasive measurements and continuous unloading of the left ventricle by the device. More recently, a method requiring only pump flow and speed has been proposed to assess cardiac contractility (Naiyanetr, 2010). The new contractility index is based on the observation that ventricular pressure pulsatility affects the pulsatility in pump flow (Q_{pump}) and on the concept that $(dP_{LV}/dt)_{max}$ is an indicator of contractility. Therefore, the maximal derivative of pump flow ($(dQ_{pump}/dt)_{max}$) must include information about ventricular contractility. The flow generated by the interaction between axial flow pump and native ventricle depends on pump speed, pressure-flow features of the pump, inertia in the cannula and pressure difference between inlet and outlet. The difference between instantaneous aortic pressure $P_{AO}(t)$ and instantaneous left ventricular pressure $P_{LV}(t)$ modulates the flow pattern according to the following equation:

$$P_{AO}(t) - P_{LV}(t) = B_P \cdot \omega^2 - R_P \cdot Q_{pump}(t) - L_P \cdot \frac{dQ_{pump}(t)}{dt} \tag{2.90}$$

where Q_{pump} is the pump flow, ω is the pump speed, R_P and L_P are the hydraulic resistance and the fluid inertance of the pump and cannulae, and B_P is a pump specific factor. R_P, L_P and B_P are considered constant.
Time differentiation of Eq. (2.90) gives:

$$\frac{dP_{AO}}{dt} - \frac{dP_{LV}}{dt} = -R_P \cdot \frac{dQ_{pump}}{dt} - L_P \cdot \frac{d^2Q_{pump}}{dt^2} \tag{2.91}$$

At constant speed and relatively low pulsatility of P_{AO}, $dP_{AO}/dt = 0$ and the term $L_P \cdot (d^2Q_{pump}/dt^2)$ can be neglected. Therefore:

$$-\frac{dP_{LV}}{dt} = -R_P \cdot \frac{dQ_{pump}}{dt} \qquad \Rightarrow \qquad \frac{dQ_{pump}}{dt} = \frac{1}{R_P} \cdot \frac{dP_{LV}}{dt} \tag{2.92}$$

Considering maximum rise of P_{LV} and Q_{pump}, we obtain:

$$\left(\frac{dQ_{pump}}{dt}\right)_{max} = \frac{1}{R_P} \cdot \left(\frac{dP_{LV}}{dt}\right)_{max} \tag{2.93}$$

When the pump flow reaches its maximum and minimum values, a relationship between the peak-to-peak value of pump flow in eah cardiac cycle ($Q_{pump_{P2P}}$) from minimum ($Q_{pump_{min}}$) to maximum ($Q_{pump_{max}}$) values and the developed pressure from minimum diastolic ($P_{d,LV}$) to maximum systolic ($P_{s,LV}$) values, can be obtained as follows:

$$Q_{pump_{max}} - Q_{pump_{min}} = Q_{pump_{P2P}} = \frac{1}{R_P} \cdot \left(P_{s,LV} - P_{d,LV}\right) \tag{2.94}$$

The conditions for Eq. (2.94) are again a constant speed and a relatively low pulsatility of P_{AO} with a difference between systolic and diastolic aortic pressure close to zero.

Considering that $Q_{pump_{P2P}}$ is highly influenced by the actual speed, it may be appropriate to normalise the maximal derivative of pump flow ($dQ_{pump}/dt)_{max}$ by $Q_{pump_{P2P}}$, which gives an index $(dP_{LV}/dt)_{max}/IP$ where IP is the instantaneous developed pressure. At different pump speeds, the slope of the regression line between the various measurements points is the normalised flow derivative, $I_{Q_{pump}}$, which is the proposed contractility index (Naiyanetr, 2010):

$$\left(\frac{dQ_{pump}}{dt}\right)_{max} = I_{Q_{pump}} \cdot Q_{pumpP_{P2P}} + \alpha_0 \tag{2.95}$$

where α_0 is the intercept of the regression line. The expression for the slope of the straight line is:

$$I_{Q_{pump}} = \frac{\left(\frac{dQ_{pump}}{dt}\right)_{max} - \alpha_0}{Q_{pump_{P2P}}} \tag{2.96}$$

There are similarities with two very well known contractility indices (Kass, 1987):

$$\left[\left(\frac{dP_{LV}}{dt}\right)_{max} \text{ vs } V_{ed}\right] = \frac{\left(\frac{dP_{LV}}{dt}\right)_{max}}{V_{ed} - \beta_0} \qquad \text{and} \qquad PRSW = \frac{SW}{V_{ed} - \delta_0} \qquad (2.97)$$

where β_0 and δ_0 are constants and SW is the ventricular stroke work.

In an experimental setting (Glower, 1985; Little, 1985), the calculation of contractility indices in a non-assisted heart requires a change in preload which is obtained by partial occlusion of venous return. The same scenario can be achieved in an assisted heart by changes in pump speed.

The contractility index $I_{Q_{pump}}$, which is obtained from pump flow data only, is sensitive to changes in cardiac contractility and insensitive to changes in ventricular preload, afterload and heart rate. Potentially, it may be a more useful and practical parameter to monitor residual cardiac function in patients on LVAD support.

2.8 Ventricular Interdependence during Mechanical Circulatory Support

VADs operate in parallel or in series with the native ventricles and affect both haemodynamic and mechanical interactions with changes in ventricular function (Farrar, 1985a; Farrar, 1994; Santamore, 1996).

The presence of long-standing pulmonary vascular disease in heart failure patients suggests that the right ventricle is not just a simple conduit for the passage of systemic venous blood to the lungs. Following LVAD insertion, potential alterations of right ventricular blood flow, compliance and anatomy can unmask an otherwise occult degree of right ventricular dysfunction accounting for up to 30% incidence of right sided heart failure (McCarthy, 1995; Dang, 2006). Right heart dysfunction has an impact on survival, length of stay in intensive care unit and hospital stay (Kavarana, 2002). Early identification of patients who are at risk for right heart dysfunction may lead to concomitant temporary or long-term biventricular support at the time of LVAD implantation as an attempt to reduce the negative impact on patients' outcome.

The significant alteration of right ventricular loading conditions induced by a well functioning LVAD in parallel with a weak left ventricle (Fig. 2.7) may have a potential beneficial but also detrimental effect on the overall right ventricular function (Farrar, 1985a).

In view of the in-series nature of the right and left side of the heart, any increase in flow to the systemic circulation from the LVAD will result in an increased venous return to and an increased cardiac output from the right

ventricle. Therefore, the right ventricle must be capable of increasing its cardiac output to at least the same amount of volume being pumped by the LVAD in order to achieve successful return of flow to the left heart and to the LVAD itself. An approximate doubling of cardiac index (CI) is observed in adavanced heart failure patients following LVAD insertion compared to their preoperative status: from 1.6 ± 0.6 to 2.8 ± 0.5 *L/min/m*^{2} (Farrar, 1997). Therefore, the right ventricle must be capable of pumping at least 2.8 *L/min* in patients with isolated LVAD. In patients undergoing insertion of a biventricular assist device (BiVAD), the average LVAD flow increases from 1.4 ± 0.8 to 3.0 ± 0.5 *L/min* (Farrar, 1997). Therefore, the sum of blood flow from the right ventricular assist device (RVAD) and the output from the native right ventricle must be at least 3.0 *L/min* in these patients (Fig. 2.8).

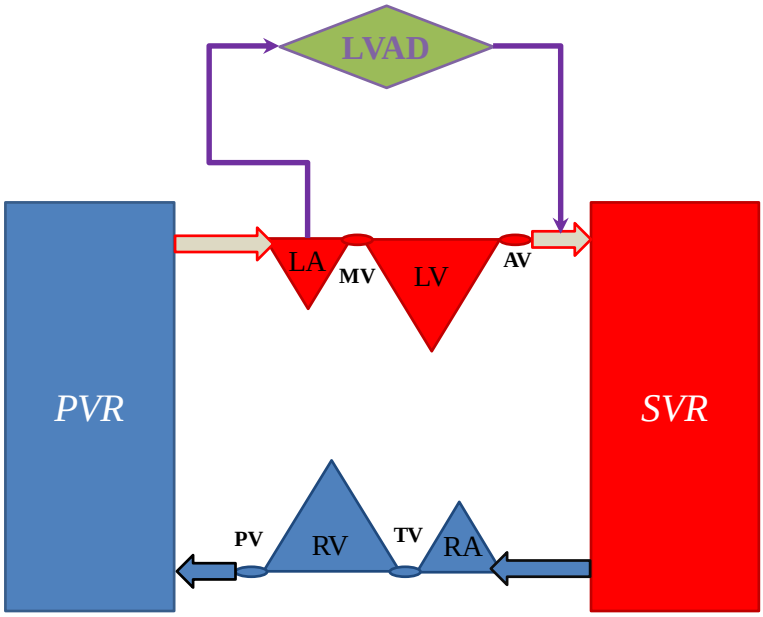

Figure 2.7 Schematic representation of the circulatory network with LVAD. LV and RV is the left and right ventricle; LA and RA is the left and right atrium; SVR and PVR is the systemic and pulmonary vascular resistance; MV and AV is the mitral and aortic valve; TV and PV is the tricuspid and pulmonary valve. LVAD is connected in parallel with the left ventricle. LVAD draws blood from the left atrium (LA) and ejects it into the ascending aorta. LVAD support modifies RV preload and afterload by shifting blood volume from the pulmonary to the systemic circulation. LV unloading results in a leftward septal shift with reduction of the trans-septal pressure gradient. If pulmonary artery and RV pressures are also reduced during LV support, both ventricles can become dimensionally unloaded. From: Capoccia M, De Lazzari C. Concepts, Mathematical Modelling and Applications in Heart Failure, 2019, Nova Science Publishers.

Right ventricular dysfunction may only become clinically evident after LVAD support. There is a consistent right ventricular response to left ventricular unloading by LVAD support in experimental settings: reduced right

ventricular afterload, increased compliance and reduced contractility. Right ventricular contractility is impaired with a leftward septal shift but output power and myocardial efficiency are maintained through a decrease in right ventricular afterload and an increase in right ventricular preload (Miyamoto, 1983; Farrar, 1984; Fukamachi, 1990; Elbeery, 1990; Moon, 1993). In normal hearts, the overall effect is either no change or an increase in cardiac output. The response of the right ventricle is qualitatively the same in the presence of regional myocardial ischemia: reduced afterload, increased compliance and reduced contractility.

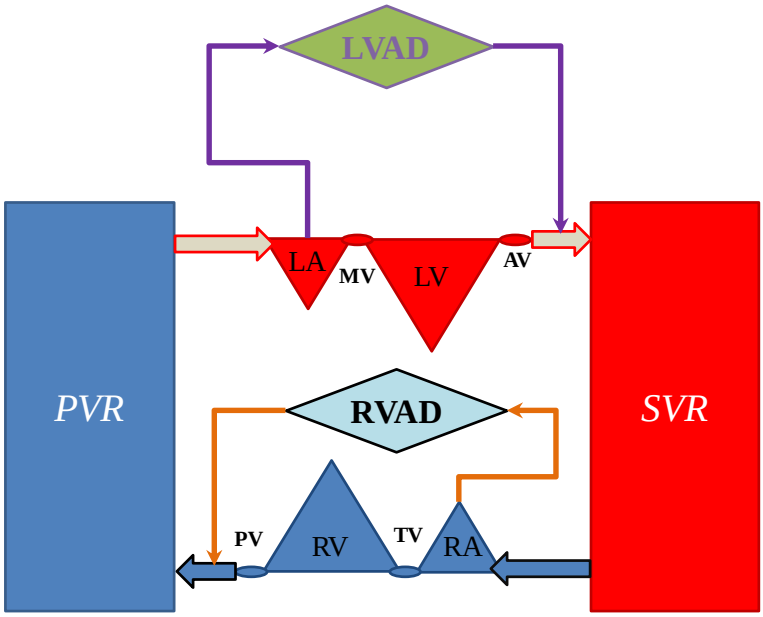

Figure 2.8 Schematic representation of the circulatory network with a biventricular assist device consisting of LVAD and RVAD. The LVAD and RVAD are connected in parallel with the left and right ventricle. The RVAD draws blood from the right atrium (RA) and ejects it into the pulmonary artery. From: Capoccia M, De Lazzari C. Concepts, Mathematical Modelling and Applications in Heart Failure, 2019, Nova Science Publishers.

Anatomical ventricular interaction is accentuated with a greater reduction in right ventricular contractility. The global effect is either no change or a reduced cardiac output, which may require inotropic or right ventricular mechanical support (Nishigaki, 1990; Farrar, 1991; Chow, 1992). The response in human hearts is similar to the experimental setting: reduced right ventricular afterload, increased right ventricular preload and increased cardiac output in the absence of regional ischemia (Farrar, 1985b).

The in series connection and ventricular interdependence (Fig. 2.9) can explain the observed right ventricular response to LVAD support (Santamore, 1996). The in series connection decreases left ventricular preload, which decreases pulmonary artery pressure. Right ventricular

preload is increased by the increased left ventricular output during LVAD support and further assisted by the reduced left ventricular diastolic volume. The reduction in left ventricular diastolic volume increases right ventricular compliance leading to the observed changes in right ventricular shape and septal position with increased right ventricular volume and reduced right ventricular filling pressure. These effects have to compensate for the reduced left ventricular systolic assistance, which leads to a reduced right ventricular systolic function. Because of ventricular interdependence, the reduced left ventricular systolic function decreases left ventricular assistance to right ventricular function leading to a positive feedback mechanism: the reduced left ventricular assistance decreases right ventricular systolic pressure and stroke volume followed by reduced left ventricular filling. The impaired right ventricular function reflects the observed changes in right ventricular septal position during systole and the reduction in right ventricular elastance and maximal rate of change of right ventricular pressure. Finally, the role played by the residual left ventricular wall stress must be taken into account despite the absence of left ventricular pressure due to decompression following LVAD support.

The possible mechanism for right ventricular failure during LVAD support can be compared to a bellows effect (Rushmer, 1953). The right ventricle ejects blood through a uniform reduction in its free wall area and a reduced septal-to-free wall distance. Because of its large surface area-to-volume ratio, small decreases in septal-to-free wall distance cause large volume displacements (Santamore, 1979). Based on ventricular interdependence, the hands holding the bellows are the right ventricular free wall and the whole left ventricle (Santamore, 1996). During normal contraction, both hands contribute to right ventricular ejection. Following LVAD support, right ventricular afterload is decreased in view of the increased motion of the right ventricular free wall while the left ventricular contribution is less because of decreased ventricular interdependence. In the presence of septal ischemia, the left ventricle moves away from the right ventricle. The right ventricular free wall cannot compensate leading to right ventricular impairment and reduced cardiac output. The key role is the change in the interventricular septum from its normal shape to a flattened or inverted shape in systole leading to a net motion of the septum away from the right ventricular cavity. Given the bellows-like contraction of the right ventricle, this septal motion significantly reduces right ventricular output and may explain the observed right ventricular impairment. The degree of right ventricular impairment is subject to the underlying right ventricular dysfunction, the degree of right

ventricular afterload reduction and the presence of regional ischemia, particularly in the septum (Santamore, 1996).

In summary, increased venous return following LVAD support affects right ventricular function by increasing preload. At the same time, LVAD support improves right ventricular filling by unloading the left ventricle with reduction of its size and septal shift to the left. Right ventricular function is highly afterload dependent. LVAD support is beneficial for right ventricular function in relation to pulmonary vascular resistance (Farrar, 1985b). LVAD support improves right ventricular function by reducing the afterload in patients with high pulmonary pressure caused by left ventricular failure in the presence of a normal pulmonary vascular bed (Farrar, 1984). Complete decompression of the left ventricle leads to a significant reduction in left atrial pressure and concomitant decrease in pulmonary artery pressure followed by a decrease in right ventricular afterload. LVAD support will be detrimental in the presence of fixed high pulmonary pressure because of increased right ventricular afterload and volume due to high blood flow through an irreversible high pulmonary vascular resistance (Farrar, 1985a).

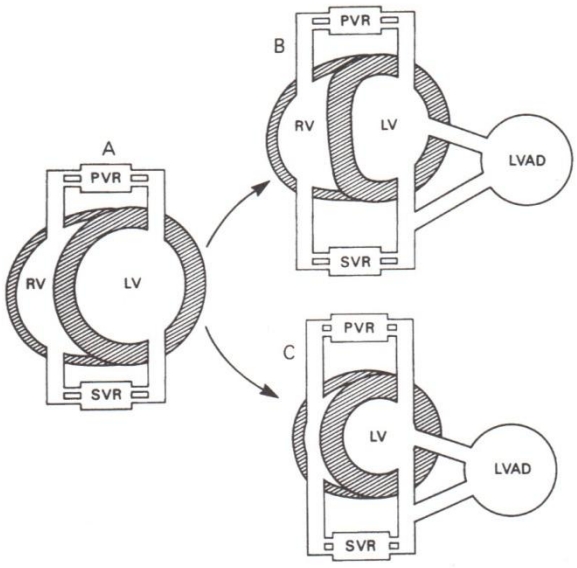

Figure 2.9 Hemodynamic and mechanical interactions between right (RV) and left (LV) ventricles. LVAD support in parallel with the LV (B and C) modifies RV preload and afterload following shift of blood volume from the pulmonary to the systemic circulation. LVAD support results in LV unloading due to a leftward septal shift with reduction of the trans-septal pressure gradient (B). From: Circulation 1985; 72: 1279-1285.

2.9 Coupling between VADs and the Cardiovascular System

A pulsatile LVAD can operate “in phase” and “out of phase” with the native heart (Maybaum, 2002; Bolno, 2003). When LVAD-heart coupling is “in-

phase", ventricular systole occurs during LVAD diastole resulting in the highest filling of the device with decreased left ventricular pressure. When LVAD-heart coupling is "out-of-phase", the two pumps are in competition resulting in decreased device filling and increased left ventricular pressure. The "in-phase" operation mode of the device achieves a more controlled ability to partially unload the native heart with potential for myocardial recovery (Emergy, 1991; Bolno, 2003; Maybaum, 1999; Lisy, 2000). In addition, coronary blood flow may be favourably influenced by "in-phase" operating mode of the device because LVAD systole occurs during left ventricular diastole (counterpulsation). Decreased coronary perfusion during LVAD support may be due to either "out-of-phase" operating mode or decreased myocardial oxygen consumption as a result of an impaired coronary circulation. Optimal loading conditions may change during LVAD support. Complete ventricular resting may be beneficial during the initial period of circulatory support but gradual reloading of the ventricle may well improve myocardial perfusion and metabolism (Maybaum, 1999). The degree of LVAD synchronisation with the native heart has important implications for myocardial recovery as well as myocardial perfusion. Also, LVAD timing can be optimised to increase the pressure difference between the left atrium and the left ventricle during diastole. As pump rate increases to match output demand, synchronisation plays a major role (Saito, 2001).

During maximal LVAD decompression there is no antegrade flow through the aortic valve, which remains closed. Patients with a mechanical prosthesis in the aortic position are at risk for thrombus development and embolism when the native ventricle is able to eject. Replacement of the mechanical prosthesis with a bioprosthesis before LVAD implantation may reduce potential complications although additional bypass time would be required for an already demanding procedure and a bioprosthesis may still undergo leaflets fusion. Patch closure of the already in situ mechanical prosthesis has been advocated as a better option (John, 2010). Aortic valve stenosis is not going to adversely impact on the haemodynamic performance of the device but the risk of thrombosis remains. In the presence of normal or stenotic native aortic valve, the aim is to maintain a 1:3 opening of the valve with continuous flow LVADs and replace the stenotic aortic valve if myocardial recovery is likely (John, 2010). The presence of mild aortic regurgitation may help wash out the cusps of the aortic valve and possibly prevent thrombus formation. Severe aortic regurgitation has a negative haemodynamic impact on the device because the retrograde flow will decrease the net forward flow from the pump. Mild to moderate aortic regurgitation may be exacerbated by the insertion of the

device; repair with a circular purse-string suture is recommended (John, 2010). Mitral regurgitation is not a limiting factor for LVAD performance because the device fully unloads the left ventricle eliminating any degree of functional regurgitation. Mitral stenosis may limit device filling with significant decrease in net output. The native valve can be replaced with either a bioprosthesis or a mechanical prosthesis because transmitral flow is in continuity with LVAD function. In the presence of tricuspid regurgitation due to reversible pulmonary hypertension, LVAD implantation leads to gradual reduction of pulmonary artery pressure with normalisation of ventricular geometry and re-establishment of tricuspid function. Tricuspid regurgitation may persist in severe right heart failure causing elevated central venous pressure and hepatic congestion with ultimately end-organ dysfunction. In case of severe tricuspid regurgitation, replacement should be considered.
Therefore, valvular pathology should be addressed before LVAD implantation (Kasirajan, 1997; John, 2010).

2.10 Aortic Valve Physiology during Mechanical Circulatory Support

The aortic valve consists of three semilunar leaflets contained within a connective tissue sleeve (Yoganathan, 2004). The valve leaflets are attached to a virtual fibrous ring enclosed partly in the fibrous skeleton and partly in the muscular outlet portion of the left ventricle. The aortic root is the portion of the left ventricular outflow tract supporting the leaflets of the aortic valve. The aortic region immediately above the fibrous ring is known as sinuses of Valsalva, which are the expanded portions of the aortic root confined proximally by the attachments of the valve leaflets and distally by the sinotubular junction. The aortic root is a dynamic structure with relations to the aorta and the left ventricle. Its configuration changes from a cone to a cylinder and then to an inverted cone when the ventricle fills and contracts (Sutton, 1995). The sinuses allow the formation of systolic vortexes, which likely aid valve closure due to the development of a transverse pressure difference (Yoganathan, 2004). Therefore, the fluid dynamics of the aortic root plays a key role for optimal valve function, which is significantly changed following LVAD insertion (John, 2010).
LVAD support diverts blood from the left ventricle directly into the aorta leading to increased cardiac output and decreased LV pressure with reduced wall stress and potential for reverse remodelling. Consequently, the pressure difference between the aortic root and the left ventricle, namely the transvalvular pressure (TVP), is increased (Fig. 2.10). The aortic valve opens when the TVP is close to zero and closes under pressure. The

magnitude and duration of the TVP is increased with a prolonged diastolic period for the aortic valve in LVAD patients (John, 2010). During periods of high LVAD support, blood flow is completely through the LVAD which operates in series with the native LV in the presence of a continuously closed aortic valve. When sufficient intrinsic contraction occurs, the aortic valve partially opens and becomes overloaded by the LVAD operating in parallel with the native LV. The loss of cyclic relaxation causes permanent overstretching of the aortic valve tissue with likely deterioration and remodelling.

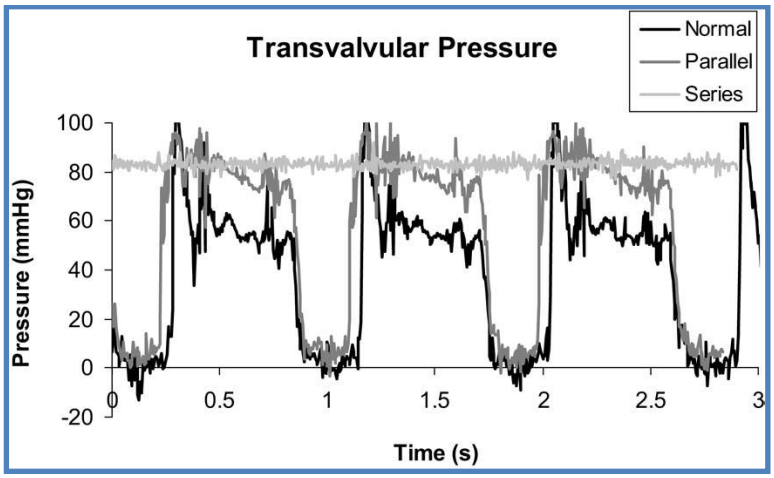

Figure 2.10 Transvalvular pressure for three different blood flow patterns: normal (without LVAD), LVAD in series and LVAD in parallel with the left ventricle. From: Capoccia M, De Lazzari C. Concepts, Mathematical Modelling and Applications in Heart Failure, 2019, Nova Science Publishers.

If we consider the LVAD as a flow generator connected in parallel with the left ventricle, then we can analyse and quantify the effects of aortic regurgitation on the pumping efficacy of continuous and pulsatile pumps (Kim, 2016; Lim, 2009; Lim, 2012). A computational approach based on an eight compartment lumped parameter model and the time-varying elastance can give a quantitative assessment according to the following baseline equations (Fig. 2.11) (Kim, 2016):

$$\begin{cases} Q_i = \dfrac{P_i(t) - P_{i-1}(t)}{R_i} \\ \dfrac{dV_i(t)}{dt} = Q_{in,i}(t) - Q_{out,i}(t) \\ P_i(t) = P_{ex,i}(t) + \dfrac{V_i(t) - V_{un,i}(t)}{C_i} \end{cases} \tag{2.98}$$

where i is the compartment index, V is the blood volume, Q_{in} is the blood inflow rate, Q_{out} is the blood outflow rate, P is the internal blood vessel

pressure, P_{ex} is the external blood vessel pressure, C is the blood vessel or cardiac wall compliance and V_{un} is the volume when the blood vessel pressure is different from the outside.

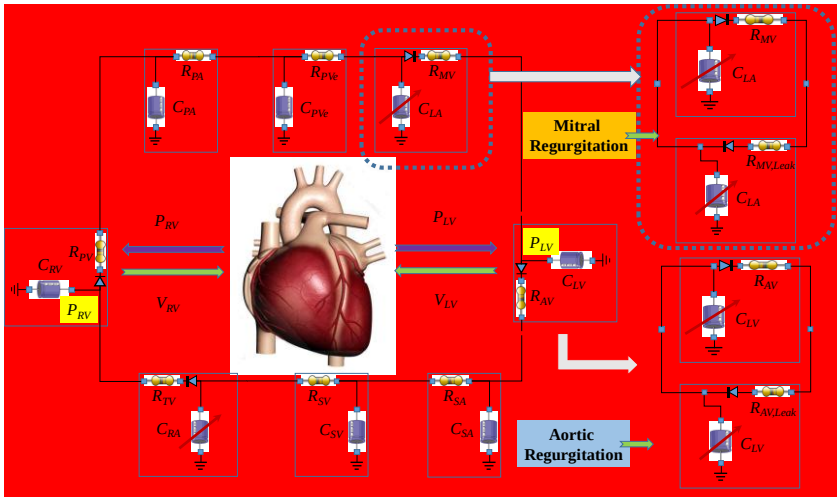

Figure 2.11 Electrical representation of aortic and mitral regurgitation. R_{PA} and C_{PA} is the pulmonary artery resistance and compliance; R_{PVe} and C_{PVe} is the pulmonary vein resistance and compliance; R_{MV} and $R_{MV,Leak}$ is the forward and leakage resistance of the mitral valve; C_{LA} and C_{RA} is the left and right atrial compliance; R_{AV} and $R_{AV,Leak}$ is the forward and leakage resistance of the aortic valve; R_{SA} and C_{SA} is the peripheral arterial resistance and compliance; R_{SV} and C_{SV} is the peripheral venous resistance and compliance; R_{TV} and R_{PV} is the tricuspid and pulmonary valve resistance. From: Capoccia M, De Lazzari C. Concepts, Mathematical Modelling and Applications in Heart Failure, 2019, Nova Science Publishers.

Aortic regurgitation is simulated as follows (Fig. 2.11) (Lim, 2015; Kim, 2016):

$$Q_{AV}(t)=\begin{cases}\dfrac{P_{LV}(t)-P_{AO}(t)}{R_{AV}} & P_{LV}>P_{AO}\\ \dfrac{P_{LV}(t)-P_{AO}(t)}{R_{AV,Leak}}=\dfrac{P_{LV}(t)-P_{AO}(t)}{R_{AV}}\cdot\dfrac{SF}{100} & P_{LV}\le P_{AO}\end{cases} \tag{2.99}$$

where Q_{AV} is the forward flow through the aortic valve, P_{LV} is the left ventricular pressure, P_{AO} is the aortic blood pressure, R_{AV} is the forward flow resistance through the aortic valve, $R_{AV,Leak}$ is the leakage flow resistance through the aortic valve and SF is a scale factor indicating the severity of aortic regurgitation.

Despite the limitations of this model, the simulations confirm the reduced ability of the LVAD to unload the left ventricle in the presence of aortic regurgitation (Fig. 2.12).

Dynamic speed support based on a control algorithm able to time the peak flow of the device at mid-diastole may yield longer opening time of the aortic valve with potential for reduced aortic regurgitation in the long term (Bozkurt, 2015).

Pump speed modulation will be further discussed in Chapter 3.

Aortic valve opening is currently monitored with echocardiographic assessment, intermittent pump speed reduction and pulse pressure measurement. Electrical current analysis as a mean to develop a physiological feedback algorithm for constant regulation and optimisation has been proposed (Bishop, 2010).

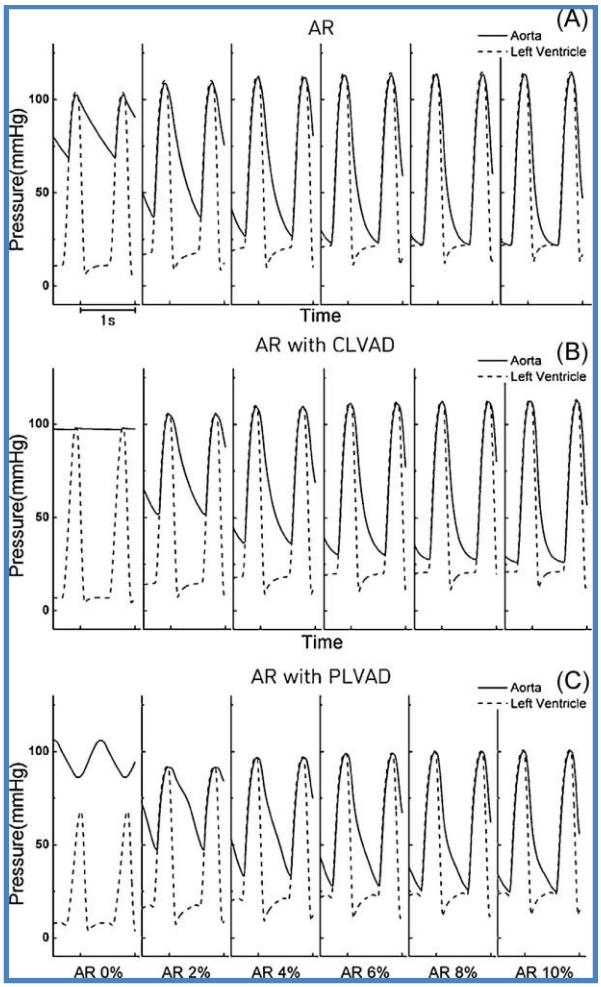

Figure 2.12 Left ventricular and aortic pressure profiles in the presence of aortic valve regurgitation. (A) Without LVAD treatment. (B) With continuous LVAD (CLVAD) treatment. (C) With pulsatile LVAD (PLVAD) treatment. AR stands for aortic regurgitation. From: Capoccia M, De Lazzari C. Concepts,

Mathematical Modelling and Applications in Heart Failure, 2019, Nova Science Publishers.

2.11 Mitral Valve Physiology during Mechanical Circulatory Support

Mitral regurgitation is simulated as (Lim, 2015; Kim, 2016):

$$Q_{MV}(t)=\begin{cases}\dfrac{P_{LA}(t)-P_{LV}(t)}{R_{MV}} & P_{LA}>P_{LV}\\ \dfrac{P_{LA}(t)-P_{LV}(t)}{R_{MV,Leak}}=\dfrac{P_{LA}(t)-P_{LV}(t)}{R_{MV}}\cdot\dfrac{SF}{100} & P_{LA}\le P_{LV}\end{cases} \quad (2.100)$$

where Q_{MV} is the mitral valve inflow rate, P_{LA} is the left atrial pressure, P_{LV} is the left ventricular pressure, R_{MV} is the forward flow resistance through the mitral valve, $R_{MV,leak}$ is the leakage flow resistance through the mitral valve and SF is a scale factor indicating the severity of mitral regurgitation.

Although the outcome of the simulations shows that LVAD performance is maintained in the presence of mitral regurgitation with better unloading for a pulsatile device (Fig. 2.13), significant residual mitral regurgitation is associated with persistent pulmonary hypertension, worse right ventricular function and death in patients supported with a continuous-flow LVAD (Kassis, 2017).

2.12 Pulse Wave Analysis during LVAD Support

Haemodynamic evaluation during LVAD support is critical to understand coupling between the device and the vascular system. The pressure waveform undergoes significant amplification with discrepancy between central aortic pressure and the peripheral circulation. Pulse wave analysis can provide helpful insights about the pattern of pump ejection and the properties of the arterial system. The pressure waveform recorded at any site in the arterial tree consists of a forward waveform generated by the pump source (LV or LVAD) and a backward waveform, which is the “echo” of the incident wave reflected at peripheral sites. Analysis of the incident wave gives information about the pump source while analysis of the reflected wave gives information about the properties of the arterial system. Peripheral tonometry has been used as a simple, non-invasive method for the evaluation of central haemodynamics in patients with heart failure and LVAD support (Vlachopoulos, 2001).

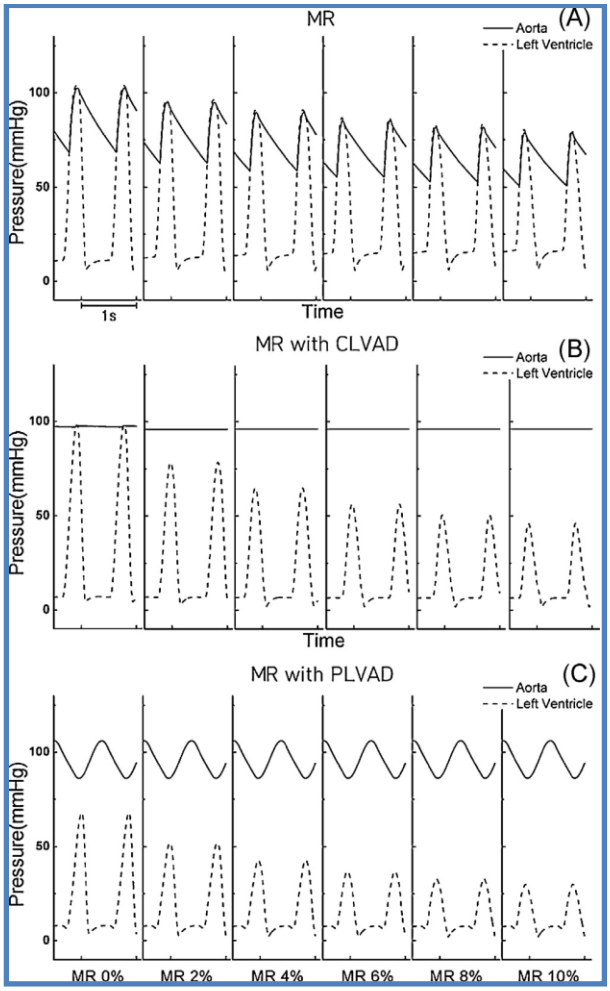

Figure 2.13 Left ventricular and aortic pressure profiles in the presence of mitral valve regurgitation. (A) Without LVAD treatment. (B) With continuous LVAD (CLVAD) treatment. (C) With pulsatile LVAD (PLVAD) treatment. MR stands for mitral regurgitation. From: Capoccia M, De Lazzari C. Concepts, Mathematical Modelling and Applications in Heart Failure, 2019, Nova Science Publishers.

Pulse pressure is inadequate for precise quantification of pulsatile and non pulsatile perfusion modes during chronic mechanical circulatory support because the generation of pulsatile flow depends on energy gradient rather than pressure gradient (Shepard, 1966; Wright, 1994; Wright, 1997; Ündar, 2002). Both arterial pressure and pump flow waveforms should be used to quantify different perfusion modes because different pulsatile pumps with the same pulse pressure have significantly different haemodynamic energy levels (Ündar, 1999; Ündar, 2001; Ündar, 2003). If both pressure and pump flow waveforms are available, then the energy equivalent pressure formula should be used (Shepard, 1966), otherwise the use of pulse power index and/or pulsatility index is advisable (Kawahito, 2000a; Kawahito, 2000b). Non-invasive arterial blood pressure waveform measurement seems a

reliable and accurate method for the assessment of patients supported by a continuous flow LVAD (Martina, 2014).

2.13 Energy Equivalent Pressure

The energy equivalent pressure (EEP [*mmHg*]) is the ratio between the area under the haemodynamic power curve and the area under the pump flow curve during each pulse cycle:

$$EEP = \frac{\int_{t_1}^{t_2} (f \cdot p)\, dt}{\int_{t_1}^{t_2} f dt} \tag{2.101}$$

where f is the pump flow rate, p is the arterial pressure, $[t_1, t_2]$ is the time interval and dt is the increment in time.

Under adequate pulsatility, EEP is always higher than mean arterial pressure (MAP). The difference between EEP and MAP is the extra energy generated by each pulsatile or non-pulsatile device. The difference between EEP and MAP in the normal human heart is approximately 10% (Wright, 1994).

In the presence of complete non-pulsatile flow, $EEP = MAP$ and the extra energy is zero.

The total haemodynamic energy (THE) is the energy equivalent pressure EEP expressed in erg/cm^2. It's obtained by multiplying EEP by the converting factor (1.332) from *mmHg* to *dyne per cm^2* that is equivalent to *erg/cm^3*:

$$THE = 1.332 \cdot \left[\frac{\int_{t_1}^{t_2} (f \cdot p)\, dt}{\int_{t_1}^{t_2} f dt} \right] \tag{2.102}$$

The surplus haemodynamic energy (SHE) is the extra energy generated by the device expressed in *erg/cm^3*:

$$SHE = 1.332 \cdot \left[\frac{\int_{t_1}^{t_2} (f \cdot p)\, dt}{\int_{t_1}^{t_2} f dt} - MAP \right] \tag{2.103}$$

SHE is the extra energy that is generated only in the presence of some degree of pulsatility in pressure or flow. It is zero under complete non-pulsatile conditions. At equal MAP and pump flow rate, adequate pulsatile flow always generates significantly more extra energy compared to non-

pulsatile flow (Ündar, 1999; Ündar, 2005a; Ündar, 2005b). This is a disadvantage when non pulsatile devices are used for either acute or chronic circulatory support.

If we consider a 70 ml Pierce-Donachy pneumatic pulsatile LVAD in a mock loop system, the EEP formula can be used to quantify the pressure-flow waveforms. At a constant pump flow rate of 5 *L/min*, aortic pressure of 80 *mmHg*, 90 *mmHg* and 100 *mmHg*, and pump rates of 65 *bpm*, 70 *bpm* and 80 *bpm*, the difference between EEP and aortic pressure is 9-11% (Ündar, 2004). The extra haemodynamic energy generated by this device achieves the physiological level of 10%, which is equivalent to a normal heart. When axial flow or centrifugal pumps are used and the native heart is not ejecting, EEP becomes MAP and no extra energy is generated by these devices. As a matter of fact, most of the time in a clinical setting there is still some residual function of the native heart leading to some difference between EEP and MAP. In the presence of some myocardial recovery, near physiological pulsatility can be achieved using a rotary blood pump (Potapov, 2000). The Jarvik 2000 is the only continuous flow device which generates complete non-pulsatile flow under any condition (Saito, 2002), the remaining rotary blood pumps show some degree of pulsatility (Potapov, 2000).

2.14 Pulse Power Index

The pulse power index (PPI) overcomes the limitations of the EEP formula, which requires both instantaneous arterial pressure and pump flow to be recorded: if one of the parameters is not available, the formula is not applicable. PPI is defined as:

$$PPI = \sum_{i=0}^{n} \frac{A_i^2 \cdot w^2 \cdot i^2}{A_0^2} \tag{2.104}$$

where n is the number of flow harmonics, A_i is the amplitude of the i-th harmonic of flow, A_0 is the amplitude of mean flow and w is the frequency of flow (*cycle/s*). The pulse power index formula is useful to determine whether a continuous flow LVAD achieves physiological support (Grossi, 1985; Kawahito, 2000a; Kawahito, 2000b).

2.15 Pulsatility Index

Continuous blood flow generated in a non-physiological manner by rotary pumps avoids the need for valves and compliance chambers. Continuous

flow VADs have a mode of operation (pulsatility index) that allows aortic valve opening during systole by adjusting the speed of the device in order to mimic physiological flow (Wilson, 2009). Therefore, the pulsatility index is a measure of the size of flow pulse generated by the pump during a cardiac cycle. Maximum flow (Q_{max}) will occur during ventricular systole when the inlet-to-outlet pressure difference is the least, and minimum flow (Q_{min}) will occur during left ventricular diastolic filling when the inlet pressures are lower and the *PI* is greater. In mathematical terms, we have:

$$PI = \frac{Q_{max} - Q_{min}}{Q_{avg}} \tag{2.105}$$

where Q_{avg} is the average flow during the cardiac cycle.

Patients with very poor left ventricles have minimal pulsatility with ($Q_{max} - Q_{min} = 0$). The same low PI would be possible for a more functional left ventricle if the pump speed were excessive and the ventricle driven to collapse (speed excessive for preload). The pulsatility index is the balance of native ventricular function and unloading by a continuous flow VAD. It is routinely monitored and adjusted to ensure safe automatic flow control and may be helpful when assessing a change in clinical status.

The PI index generally is set between 0.3 and 1.0 to ensure safe but responsive auto control (Griffith, 2001).

In the case of the HeartMate II, the PI is the amount of pulsatility seen by the pump over a fifteen-second interval. This value is related to the amount of native heart function. PI is calculated from pump power normalised by mean power (Arnold, 2013).

2.16 Chapter Summary

An overview of pressure-volume analysis of cardiac mechanics and dynamics is given. The concept of time-varying elastance with its modifications and ventricular-arterial coupling are presented in details. Pressure-volume loop analysis based on the time-varying elastance theory is an established approach to study and understand the interactions between rotary blood pumps and the cardiovascular system. Despite the successful application of the time-varying elastance, its role has been questioned in the context of LVAD support. The assumption of ESPVR as a load-independent index of cardiac function holds within certain limits because extreme loading conditions can affect both E_{max} and E_{es}. A reliable method to assess cardiac contractility on LVAD support should be sensitive

to changes in myocardial properties but not affected by preload and afterload. Alternatives have been proposed but invasive measurements are required. The normalised flow derivative , $I_{Q_{pump}}$, is an attractive contractility index based on pump flow and speed without the need of invasive measurement and is not affected by preload, afterload and heart rate. LVADs are connected either in series or parallel to the left ventricle. The interventricular septum plays a key role during LVAD support and balance must be maintained to avoid right sided failure requiring RVAD. Coupling between LVAD and native heart needs synchronisation, timing and appropriate decompression for the purposes of myocardial recovery although suction must be avoided. Aortic and mitral valve physiology is important: aortic regurgitation affects the LVAD ability to unload the left ventricle; mitral regurgitation is associated with persistent pulmonary hypertension and worse right ventricular function. Haemodynamic evaluation during LVAD support is essential to understand coupling between the device and the vascular system. The energy equivalent pressure (EEP), the total haemodynamic energy (THE) and the surplus haemodynamic energy (SHE) are useful haemodynamic parameters. The pulsatility index (PI) is a measure of the size of flow pulse generated by the pump during a cardiac cycle. In other words, it is a balance of native ventricular function and unloading by a continuous flow LVAD: a lower PI reflects higher amount of pump support; a higher PI means more native heart ejection.

Chapter 3

Mathematical Modelling of Mechanical Circulatory Support

3 Mathematical Modelling of Mechanical Circulatory Support

3.1 Introduction

Numerical modelling of the interactions between VADs and the cardiovascular system is a challenging subject. Nevertheless, this issue has been increasingly addressed over the past years. Further progress in this direction would lead to more accurate predictions of the performance of the device *in vivo* and of its effect on the human body.

Computational fluid dynamics (CFD) simulations and experimental validation with particle image velocimetry (PIV) for rotary blood pumps are usually performed under steady flow conditions. Optimisation of the device is based on these results. Although computationally and experimentally less demanding, this approach may not adequately represent the significant flow modulation and therefore the unsteady flow field caused by the native ventricular contractility during LVAD support (Shu, 2009). The flow field within the pump at a given impeller rotational speed ω is determined by the flow rate Q and its time derivative dQ/dt. Comparison between unsteady flow fields and steady conditions at the same flow rates shows significant differences where flow deceleration promotes separation within the outlet diffuser whereas acceleration stabilises the velocity field. This difference supports the role played by inertial fluid forces and the importance of dQ/dt as an independent variable for detailed evaluation and validation of rotary blood pumps (Shu, 2009).

The pressure head H for a device operating with a constant rotational speed ω can be assumed to follow a single speed line from the pressure head-flow rate (H-Q) curve, oscillating along the line as the flow rate Q changes during the cardiac cycle. Nevertheless, the inertia of the blood results in hysteresis with a closed loop in the H-Q curve (Song, 2004a; Song, 2004b; Shu, 2009). The effects of flow pulsatility are important but calculations are far more computationally expensive, with inlet and outlet boundary conditions being difficult to determine (Song, 2004a).

In steady flow calculations, the inlet boundary is set to a specific steady velocity profile while the outlet boundary is fixed at a steady pressure. The actual unsteady boundary conditions will be dependent on the flow from the heart and the aortic pressure, which are the result of the interactions between the device and the cardiovascular system (Fraser, 2011).

The study of the interaction between VADs and the whole cardiovascular system with a 3-D CFD software package is highly demanding although limited parts of the assisted circulation have been developed with this

method (Bazilevs, 2009). A more simplified approach is the use of 1-D or 0-D models where space dependence is confined to the axial coordinate (1-D) or addressed by splitting the cardiovascular system in compartments (0-D) (Peiró, 2009).

A ventricular assist device consists of a pump, an inflow cannula and an outflow cannula. Energy loss caused by the pressure drop in both cannulae as a result of viscosity is simulated by adding a resistive component to the model. An additional pressure drop is observed in a pulsatile flow device because of fluid acceleration and deceleration, requiring the inclusion of an inductance component in the model. This is also applicable to continuous-flow devices where the interaction between the heart and the varying pressure head may generate pulsatile pump flow.

A typical cannula model consists of a resistor and an inductor operating in series. A compliance component does not necessary consider that cannulae are made of synthetic material, which is very stiff compared with blood vessels. A compliance component may be useful when simulation of ventricular suction is required due to a rotary blood pump running at high speed (Vollkron, 2002).

A rotary blood pump can be modelled either considering the hydraulic component only or including the motor component too. Modelling hydraulic and motor component together is a more useful approach because of the relation between the pump model and measurable parameters following device implantation such as power consumption and rotational speed. If a correlation between measurable pump and circulatory parameters is achievable by a mathematical model, then power and speed can be used to estimate the circulatory status of the patient without invasive measurement techniques. Finally, the simulation of the motor is required for the development and validation of physiological control algorithms in order to provide higher flows when the patient becomes more active and also to reduce the risk of ventricular suction.

The flow generated by rotary blood pumps depends on the pressure head in contrast to displacement pumps where preload and afterload are independent factors. An equation for a rotary blood pump obtained fitting *in vitro* data is as follows (Zhou, 1999):

$$Q_{pump} = \pm\sqrt{\left|K_{vad,1}\cdot\omega^2 - K_{vad,2}\cdot\Delta P - K_{vad,3}\right|} \qquad (3.1)$$

where Q_{pump} is the pump flow [*L/min*], ω is the impeller rotational speed [*rpm*], ΔP is the pump pressure head [*mmHg*], $K_{vad,1}$ = 3.571×10^{-5} *L*^{2}·*min*$^-$

^{2}·*rpm*$^{-2}$, $K_{vad,2}$ = 2.838 *L*^{2}·*min*$^{-2}$·*mmHg*$^{-1}$ and $K_{vad,3}$ = 12.66 *L*^{2}·*min*$^{-2}$. When the rotary pump is connected as LVAD, we have $\Delta P = P_{AO} - P_{LV}$ where P_{AO} is the aortic pressure and P_{LV} is the left ventricular pressure. The fitting is performed for different curves presenting the generated flow as a function of the pressure head, obtained from *in vitro* data, with pump rotational speed at 2500, 3000, 3500 and 4000 *rpm*.

Preload and afterload have an inverse effect on a rotary blood pump performance, with flow sensitivity to either variable being equal for a certain rotational speed. An increase in preload causes a decrease in the pressure head; the same effect can be achieved by a decrease in afterload.

3.2 Rotary Blood Pumps Models

Mathematical modelling and computer simulation are invaluable tools to investigate the interactions between rotary blood pumps and the cardiovascular system for the development of a reliable automated control algorithm. The traditional modelling approach for rotary blood pumps is the use of static performance curves, which relate flow rate and pressure head at different constant speed under steady conditions.

A general equation used to describe the behaviour of a rotary blood pump (RBP) and effectively estimate the pump pressure head H using measured flow, the time derivative of flow dQ_{pump}/dt and pump speed ω is the following:

$$H = P_{OUT} - P_{IN} = f\left(c, Q_{pump}, Q_{pump}^{2}, \omega^{2}, \frac{dQ_{pump}}{dt}, \frac{d\omega}{dt}\right) \tag{3.2}$$

where P_{IN} is the pressure at the pump inlet, P_{OUT} is the pressure at the pump outlet, c is a constant, Q_{pump} is the pump flow, t is the time and $d\omega/dt$ is the angular acceleration.

With Euler's method, the pump pressure head can be simply estimated by a linear relationship with the flow rate and a quadratic relationship with the rotational speed as follows:

$$H(t) = a_1 \cdot Q_{pump}(t) + c_1 \cdot \omega^{2}(t) \tag{3.3}$$

where a_1 and c_1 are coefficients derived from simple curve fitting of the pressure head-flow rate relationships at different constant speeds under steady conditions.

In order to improve the accuracy of pressure head estimation, additional parameters have been added such as a quadratic function of the flow to account for viscous loss across the pump, the time derivative of flow for energy loss due to fluid inertia and the angular acceleration for pulsating operation mode (Vandenberghe, 2002; Vandenberghe, 2003; Gwak, 2005; Moscato, 2009; Shu, 2009). The outcome is consistent with improved accuracy as shown by curve fitting and statistical analysis (Pirbodaghi, 2011) although complexity is increased.

The above parameters can be combined as follows (Pirbodaghi, 2011):

$$H(t) = a_2 \cdot Q_{pump}(t) + b_2 Q_{pump}^2(t) + c_2 \cdot \omega^2(t) \tag{3.4}$$

$$H(t) = a_3 \cdot Q_{pump}(t) + b_3 Q_{pump}^2(t) + c_3 \cdot \omega^2(t) + e_3 \frac{d\omega(t)}{dt} \tag{3.5}$$

$$H(t) = a_4 \cdot Q_{pump}(t) + b_4 Q_{pump}^2(t) + c_4 \cdot \omega^2(t) + d_4 \frac{dQ_{pump}(t)}{dt} \tag{3.6}$$

$$H(t) = a_5 \cdot Q_{pump}(t) + b_5 Q_{pump}^2(t) + c_5 \cdot \omega^2(t) + d_5 \frac{dQ_{pump}(t)}{dt} + e_5 \frac{d\omega(t)}{dt} \tag{3.7}$$

where a_i, b_i, c_i, d_i, and e_i $(i = 2, 3, 4, 5)$ are coefficients derived from simple curve fitting of the H-Q relationships at different constant speeds under steady conditions. Different mathematical models of the CentriMag RBP (Levitronix GmbH, Zürich, Switzerland) can be described (Pirbodaghi, 2011) setting the coefficients a_i, b_i, c_i, d_i, and e_i as listed in Table 3.1. In order to identify the model parameters of Eqs. (3.3), (3.4), (3.5), (3.6) and (3.7), a chirp signal (Fig 3.1) is applied to the CentriMag speed command while implanted in a live animal. Subsequently the least square curve fitting method, which minimizes the sum of squared residuals between the measured and estimated pressure head, is used to obtain the model parameters.

Table 3.1

	a_i	b_i	c_i	d_i	e_i
Eq. (3.3)	-3.630	-	20.71	-	-
Eq. (3.4)	-1.377	-0642	21.50	-	-
Eq. (3.5)	-1.140	-0.681	21.41	-	0.109
Eq. (3.6)	-1.815	-0.684	22.11	-0.112	-
Eq. (3.7)	-1.384	-0.771	21.99	-0.121	0.233

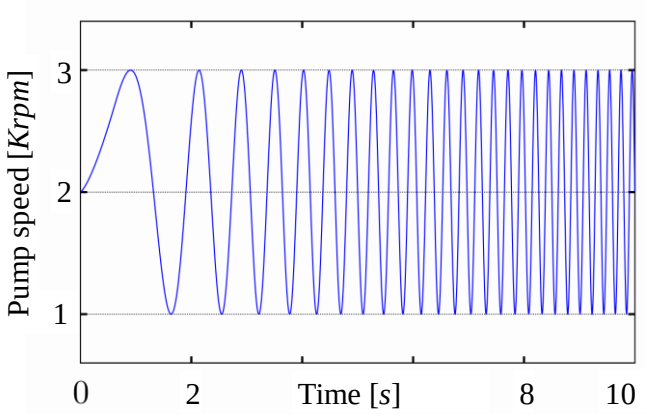

Figure 3.1 Chirp signal applied to RBPs. The frequency increases (up-chirp) with time. From: Capoccia M, De Lazzari C. Concepts, Mathematical Modelling and Applications in Heart Failure, 2019, Nova Science Publishers.

A more suitable model is required for a rotary blood pump inserted in a pulsatile environment such as the cardiovascular system where the time-derivative of pump flow and inertia effect play a significant role (Pirbodaghi, 2017).

3.2.1 Brushless DC Axial Flow LVAD

A model of a continuous-flow pump driven by a brushless DC motor is presented (Choi, 1997; Giridharan, 2002). A typical brushless DC motor can be described by the following equation:

$$J \cdot \frac{d\omega}{dt} = T_e - B \cdot \omega - T_p \tag{3.8}$$

where J represents the rotor inertia, ω is the rotor speed, T_e is the motor torque, T_p is the load torque and B is the damping coefficient. If the motor has a sinusoidal back electromotive force EmF, the phase current has a sinusoidal waveform. Therefore, the relationship between the motor torque and the amplitude of the phase current is as follows:

$$T_e = \frac{3}{2} \cdot K_b \cdot I \tag{3.9}$$

where I is the amplitude of the phase current and K_b is the constant of the back EmF. The relationship between pump rotational speed, flow and load torque is:

$$T_p = a_0 \cdot \omega^3 + a_1 \cdot Q_{pump} \cdot \omega^2 \quad (3.10)$$

where a_0 and a_1 are constants. Combining Eqs. (6.8), (6.9) and (6.10) the resulting motor model is:

$$J \cdot \frac{d\omega}{dt} = \frac{3}{2} \cdot K_b \cdot I - B \cdot \omega - (a_0 \cdot \omega^3 + a_1 \cdot Q_{pump} \cdot \omega^2) \quad (3.11)$$

The axial pump is characterized by the relation between pressure difference, flow and speed. Under steady state conditions, a linear relationship with the flow and a quadratic relationship with the pump speed are observed. In mathematical terms, we have:

$$H \equiv P_{OUT} - P_{IN} = b_0 \cdot Q_{pump} + b_1 \cdot \frac{dQ_{pump}}{dt} + b_2 \cdot \omega^2 \quad (3.12)$$

where b_0, b_1 and b_2 are coefficients. In addition, pressure difference is linearly dependent on flow derivative. Table 3.2 shows the estimated values for the motor model and for the pump model parameters (Choi, 1997). The model identifies the features of the pump and the state variables related to its operation and provides estimates of flow and pressure difference of the axial pump without the need of flow and pressure sensors, which may jeopardise long-term reliability (Schima, 1992). This is an example of LVAD controller using a sensor-less approach to regulate pump speed without causing suction in the left ventricle (Choi, 2005).

Table 3.2

Motor			
J	B	a_0	a_1
0.916×10^{-6}	0.66×10^{-6}	0.738×10^{-12}	0.198×10^{-10}
Pump			
-	b_0	b_1	b_2
-	-0.296	-0.027	0.0000933

3.2.2 Diagonal Flow Rotary Blood Pump

A mathematical model for a micro-diagonal rotary pump is discussed (Vandenberghe, 2002; Vandenberghe, 2003). The pump and the cannulae are modelled separately. Only the hydraulic component of the pump is modelled and the rotational speed of the impeller is the only pump parameter that can be set by the user. The model is based on apical to

ascending aorta cannulation where the cannulae are assumed to have a cylindrical shape. A rotary pump can be considered as a series combination of an ideal pressure source and a resistive component that models energy loss. Therefore, the pump is modelled as the sum of two terms: one as a function of the rotational speed (generated energy) and the other as a function of the flow (energy loss). The pump flow pattern is expected to be turbulent. Therefore, the pump pressure loss is related to the square of the flow.

The pump equation is as follows (Vandenberghe, 2007):

$$H \equiv \Delta P_H = A \cdot \omega^2 + R_{pump} \cdot Q_{pump}^2 \tag{3.13}$$

where A [*mmHg·rpm*$^{-2}$] is a pump constant, R_{pump} [*mmHg·s·ml*$^{-1}$] is the pump resistance and Q_{pump} [*ml/s*] is the pump flow and ω is the rotational speed [*rpm*].

Each cannula is modelled as a series combination of an inductor and a resistor (Fig. 3.3). Therefore, the additional pressure drop generated by each cannula is as follows:

$$\Delta P_C = \Delta P_L + \Delta P_R = \left(L_{IN} + L_{OUT}\right) \cdot \frac{dQ_{pump}}{dt} + \left(R_{IN} + R_{OUT}\right) \cdot Q_{pump}^2 \tag{3.14}$$

where ΔP_C is the pressure drop in the cannula, ΔP_L is the pressure drop due to inertance effect, ΔP_R is the pressure drop due to viscous effect, L_{IN} and R_{IN} is the inertance and resistance of the inlet cannula, L_{OUT} and R_{OUT} is the inertance and resistance of the outlet cannula.

Combining Eqs. (3.13) and (3.14), we obtain the total pressure drop across the pump (ΔP_{TOT}):

$$\begin{aligned} \Delta P_{TOT} &= \Delta P_H + \Delta P_L + \Delta P_R = A \cdot \omega^2 + R_{pump} \cdot Q_{pump}^2 + \\ &+ \left(L_{IN} + L_{OUT}\right) \cdot \frac{dQ_{pump}}{dt} + \left(R_{IN} + R_{OUT}\right) \cdot Q_{pump}^2 \end{aligned} \tag{3.15}$$

Rearranging we have:

$$\Delta P_{TOT} = A \cdot \omega^2 + \left(R_{pump} + R_{IN} + R_{OUT}\right) \cdot Q_{pump}^2 + \left(L_{IN} + L_{OUT}\right) \cdot \frac{dQ_{pump}}{dt} \tag{3.16}$$

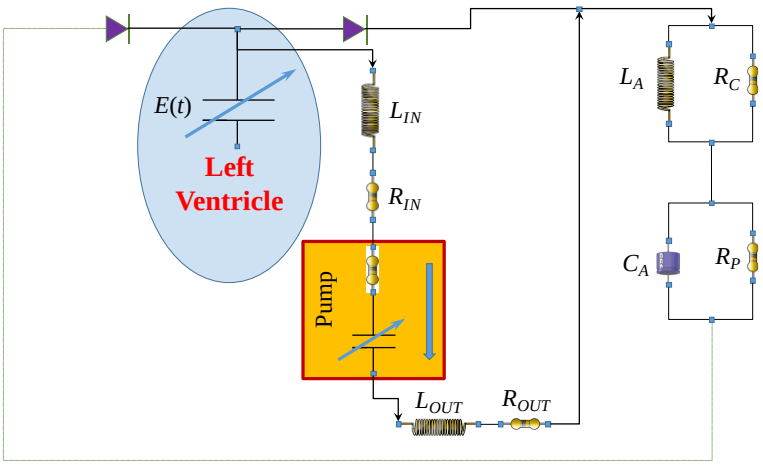

Figure 3.2 Electrical analogue of a diagonal pump coupled to the left ventricle and the arterial circulation consisting of a four-element windkessel model. $E(t)$ is the time-varying elastance, L_{IN} and R_{IN} is the inertance and resistance of the inlet cannula, L_{OUT} and R_{OUT} is the inertance and resistance of the outlet cannula. From: Capoccia M, De Lazzari C. Concepts, Mathematical Modelling and Applications in Heart Failure, 2019, Nova Science Publishers.

Considering that $\Delta P_{TOT} = P_{AO} - P_{LV}$, the final equation becomes:

$$P_{AO} - P_{LV} = A \cdot \omega^2 + R_{TOT} \cdot Q_{pump}^2 + L_{TOT} \cdot \frac{dQ_{pump}}{dt} \qquad (3.17)$$

where $L_{TOT} = L_{IN} + L_{OUT}$ is the cannula inertance [$mmHg \cdot s^2 \cdot ml^{-1}$] and $R_{TOT} = R_{pump} + R_{IN} + R_{OUT}$ is the flow-dependent resistance [$mmHg \cdot s \cdot ml^{-1}$].

In Fig. 3.2, the cardiac model includes the left ventricular function based on the time-varying elastance theory (Suga, 1974) as follows:

$$E(t) = \frac{P_{LV}(t)}{V_{LV}(t) - V_0} \qquad (3.18)$$

where $E(t)$ is the left ventricular elastance, V_{LV} represents the left ventricular volume and V_0 is the volume intercept of the end-systolic pressure-volume relationship.

The pressure drop across the mitral valve is derived from the electric analogue described in Fig. 3.3 as follows:

$$P_{LV} - P_{LA} = L_{MV} \cdot \frac{dQ_{MV}}{dt} + R_{MV} \cdot Q_{MV} \qquad (3.19)$$

where Q_{MV} is the flow through the mitral valve, L_{MV} and R_{MV} is the inertance and resistance of the valve. The pressure drop across the aortic valve is:

$$P_{AO} - P_{LV} = L_{AV} \cdot \frac{dQ_{AV}}{dt} + R_{AV} \cdot Q_{AV} \tag{3.20}$$

where Q_{AV} is the flow through the aortic valve, L_{AV} and R_{AV} is the inertance and resistance of the valve.

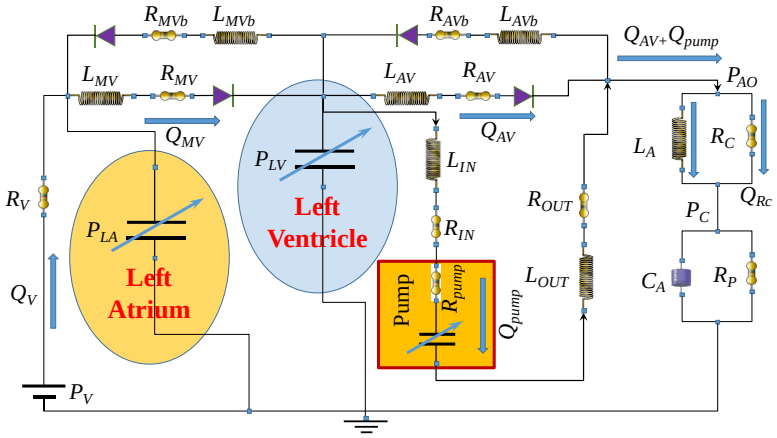

Figure 3.3 Electrical analogue of the mathematical model for a diagonal rotary blood pump and the cardiovascular network. Q_{Rc} and Q_{pump} is the flow through the characteristic resistance and the pump; Q_V is the venous flow from the lungs; Q_{MV} and Q_{AV} is the flow through the mitral and aortic valve; P_C is the pressure drop across the characteristic resistor; P_V is the venous pressure. From: Capoccia M, De Lazzari C. Concepts, Mathematical Modelling and Applications in Heart Failure, 2019, Nova Science Publishers.

According to Kirchhoff's laws, the total flow going to node P_C must equal the sum of the flows through C_A and R_P:

$$Q_{AV} + Q_{pump} = C_A \cdot \frac{dP_C}{dt} + \frac{P_C}{R_P} \tag{3.21}$$

The volume change in the left atrium is the difference between the flow into the left atrium (venous flow Q_V) and the flow out of the left atrium (mitral flow Q_{MV}):

$$\frac{dV_{LA}}{dt} = Q_V - Q_{MV} = \frac{P_V - P_{LA}}{R_V} - Q_{MV} \tag{3.22}$$

The volume change in the left ventricle is the difference between the flow into the left ventricle (mitral flow) and the flow out of the left ventricle (aortic flow Q_{AV} and pump flow):

$$\frac{dV_{LV}}{dt} = Q_{MV} - Q_{AV} - Q_{pump} \tag{3.23}$$

Finally, the pressure drop across the afterload inductor (inertance L_A) equals the pressure drop across the characteristic resistor because they are placed in parallel:

$$L_A \cdot \frac{dQ_{L_A}}{dt} = P_{AO} - P_C = R_C \cdot Q_{Rc} \tag{3.24}$$

The described model allows the implementation of continuous and pulsatile mode simulations according to the type of modulation and the phase shift between the pump and the cardiac cycles as a percentage of the total cycle (Fig 3.4).

Figure 3.5 shows the effects induced by different pump speeds on the left ventricular pressure-volume loop. LVAD support with different rotational speeds is considered in the context of a diseased state. The LVAD generates continuous blood flow. The continuous line represents a left ventricular PV loop when the speed of the pump is 2000 *rpm*; the dashed line relates to a pump speed of 10000 *rpm*. When the pump rotational speed is set at 2000 *rpm*, the PV loop keeps an isovolumetric contraction and relaxation phase. When the pump speed is set at 10000 *rpm*, the isovolumetric contraction and relaxation phases are no longer present in the PV loop (dashed line).

According to the above model, a rotary blood pump running at constant speed can unload the left ventricle completely only at high rotational speeds. A more efficient unloading is obtained when the pump runs in a pulsatile manner with a counterpulsation pattern, which decreases left ventricular external work, wall stress and oxygen consumption without affecting the flow. Therefore, it may be beneficial to run a low pump speed during systole and high pump speed during diastole.

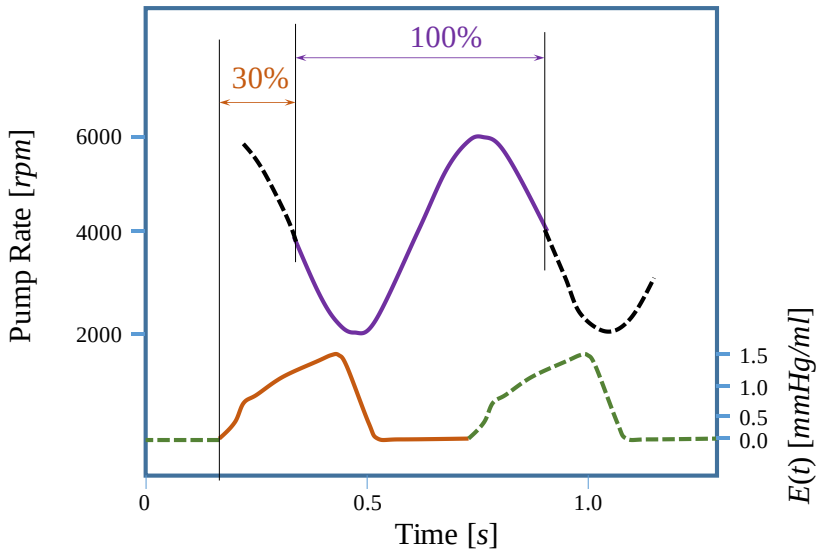

Figure 3.4 Example of pulsatile pump speed pattern with a time shift of 30% of the full cycle. The onset of systole is the landmark assessed by the time-varying elastance curve. From: Capoccia M, De Lazzari C. Concepts, Mathematical Modelling and Applications in Heart Failure, 2019, Nova Science Publishers.

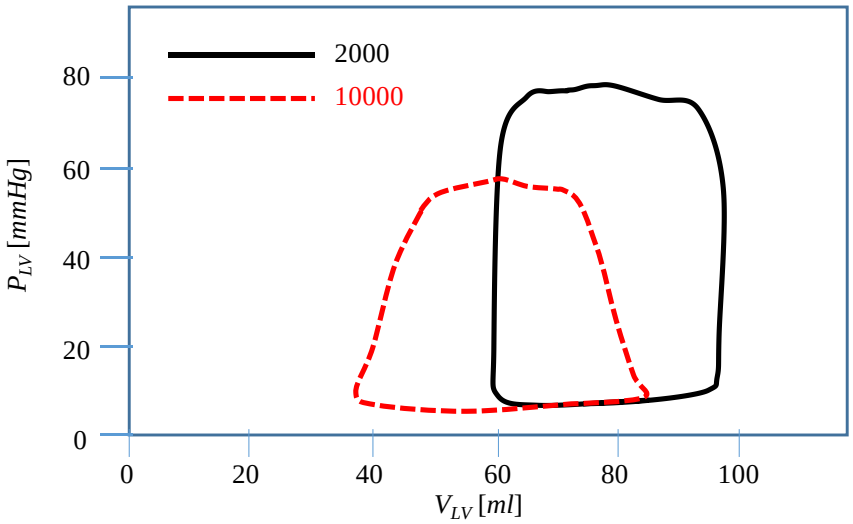

Figure 3.5 Continuous mode simulation with pump speed at 2000 *rpm* (continuous line) and 10000 *rpm* (dashed line). P_{LV} and V_{LV} is the left ventricular pressure and volume. From: Capoccia M, De Lazzari C. Concepts, Mathematical Modelling and Applications in Heart Failure, 2019, Nova Science Publishers.

3.2.3 HeartWare HVAD

Continuous-flow blood pumps operate at constant speed with a flow waveform related to the waveform of the pressure difference between the pump inlet (left ventricular pressure) and outlet (aortic pressure) (Moscato, 2009; Granegger, 2012). Therefore, a centrifugal-flow pump like the

HeartWare HVAD (HeartWare, Miami Lakes, FL, USA) is affected by the pulsatility of the left ventricular pressure and its intrinsic features.

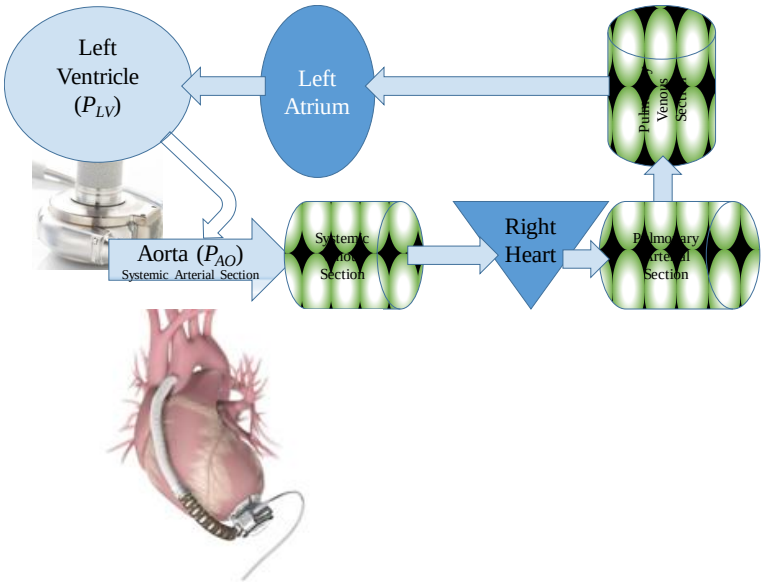

Figure 3.6 The centrifugal ventricular assist device HeartWare HVAD connected as LVAD draws blood from the left ventricle and ejects it into the ascending aorta. From: Capoccia M, De Lazzari C. Concepts, Mathematical Modelling and Applications in Heart Failure, 2019, Nova Science Publishers.

An equation for the HeartWare HVAD is as follows (Granegger, 2012):

$$H(t) = P_{AO} - P_{LV} = a \cdot \omega^2(t) - b \cdot Q_{pump}^2(t) - L \cdot \frac{dQ_{pump}}{dt} \qquad (3.25)$$

where ω is the rotational speed, a (1.29×10^{-3} $mmHg{\cdot}s^2$) is a parameter related to the impeller speed, b (3.94×10^{-3} $mmHg{\cdot}s^2{\cdot}ml^2$) is a hydraulic resistance parameter and L (0.02 $mmHg{\cdot}s^2{\cdot}ml^1$) is a fluid inertance parameter. Figure 6.6 shows a schematic cardiovascular network including left ventricular assist device support using the HeartWare HVAD.

The features of the centrifugal pump motor yield a dependence between motor current (I) and pump flow (Q_{pump}) via the load torque (T_p) (Pillay 1989):

$$J \cdot \frac{d\omega}{dt} = K \cdot I - B \cdot \omega - T_p\left(Q_{pump}, \omega\right) \qquad (3.26)$$

where the load torque T_p is a function of pump flow Q_{pump} and rotational speed ω; K is the back electromotive force constant (which is equal to the motor torque constant); B is the damping coefficient, and J is the rotor

moment of inertia, which mainly contributes to the energy losses caused by the inertial moment of the rotor under dynamic conditions.

The static features of the pump motor can be derived from Eq. (3.26) when $J \cdot d\omega/dt = 0$. Considering measured parameters, static current-flow curves can be approximated using the following nonlinear relationship (Granegger, 2012):

$$Q_{pump} = a \cdot I + b \cdot I^2 + c \cdot I^3 + d \cdot \omega + e \cdot \omega^2 + g \cdot I \cdot \omega + h \cdot I \cdot \omega^2 + k \quad (3.27)$$

The variations of the parameters a-k with fluid viscosity μ [*mPa·s*] identified in the steady-state condition are listed in Table 3.3.

Table 3.3

a	b	c	d
$-4.3\mu + 54$	11.4	$0.23\mu - 2.8$	$-1.5 \cdot 10^{-4}\mu - 1.3 \cdot 10^{-3}$
e	g	h	k
$1.4 \cdot 10^{-7}\mu + 3.3 \cdot 10^{-7}$	$8.7 \cdot 10^{-4}\mu - 0.021$	$-1.3 \cdot 10^{-7}\mu + 1.9 \cdot 10^{-6}$	$(0.49\mu - 3)\mu$

3.3 Modelling and Development of a Rotor Speed Controller

The amount of blood pumped by a LVAD is closely related to the pump rotational speed, which is controlled directly by the pump motor current: a higher pump speed allows more blood into the circulation. The development of an appropriate rotor speed controller is currently one of the challenging aspects of the increasing use of VADs. A controller must be reliable, physiologically adaptable (Schima, 1992; Olsen, 2000; Boston, 2003) and avoid excessive suction that may cause potential myocardial damage (Yuhki, 1999; Vollkron, 2006; Ferreira, 2006). The development of such a controller requires a mathematical model that takes into account the interactions between the LVAD, the left ventricle and the circulation. The model should be easy enough to understand but comprehensive enough to capture the essential haemodynamic relationships without additional unnecessary variables (Simaan, 2009). The suction phenomenon is accounted for by adding a nonlinear resistance to the inflow cannula model, which becomes active when the left ventricular pressure falls below a certain level. A basic model assumes the right ventricle and the pulmonary circulation to be normal with negligible effect on the LVAD (Fig. 3.7).

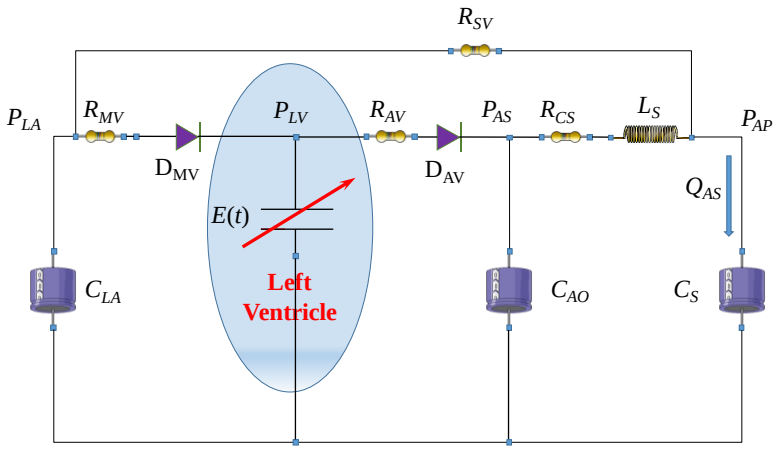

Figure 3.7 Electrical analogue of the cardiovascular system. R_{MV} and R_{AV} is the mitral and aortic valve resistance; D_{MV} and D_{AV} is the mitral and aortic valve diode; R_{CS} and R_{SV} is the characteristic and systemic vascular resistance; C_{LA} and C_{AO} is the left atrial and aortic compliance; C_S is the systemic compliance; P_{LA} and P_{LV} is the left atrial and ventricular pressure; P_{AS} and P_{AP} is the aortic and arterial pressure; L_S is the inertance of blood in the aorta; Q_{AS} is the total flow. From: Capoccia M, De Lazzari C. Concepts, Mathematical Modelling and Applications in Heart Failure, 2019, Nova Science Publishers.

The left ventricle is modelled with the ventricular elastance function $E(t)$. In mathematical terms:

$$E(t) = \frac{P_{LV}(t)}{V_{LV}(t) - V_0} \tag{3.28}$$

where V_0 is the theoretical ventricular volume at zero pressure.

The elastance function $E(t)$ can be approximated as follows:

$$E_H(t) = \left(E_{max} - E_{min}\right) \cdot E_n\left(t_n\right) + E_{min} \tag{3.29}$$

where $E_H(t)$ is the elastance of a healthy heart, $E_n(t_n)$ is the normalised elastance ("double hill" function) represented by the expression (Stergiopoulos, 1996):

$$E_n\left(t_n\right) = 1.55 \cdot \left[\frac{\left(\frac{t_n}{0.7}\right)^{1.9}}{1 + \left(\frac{t_n}{0.7}\right)^{1.9}}\right] \cdot \left[\frac{1}{1 + \left(\frac{t_n}{1.17}\right)^{1.9}}\right] \tag{3.30}$$

where $t_n = t/T_{max}$ with T_{max} = 0.2+0.15t_c, where t_c= *60/HR* [s] is the cardiac cycle; HR is the heart rate. E_{max} (E_{min}) is related to the end-systolic (end-diastolic) pressure volume relationship. Figure 3.8 shows a plot of $E_H(t)$ for a healthy heart with E_{max} = 2 *mmHg/ml*, E_{min} = 0.06 *mmHg/ml* and HR = 60 *bpm*.

The LVAD considered on this occasion is a rotary blood pump (Fig. 3.9) where the pressure difference between the left ventricle and the aorta is given by the following differential equation:

$$P_{LV}(t) - P_{AS}(t) = L_{IN} \cdot \frac{dQ_{vad}}{dt} + R_{IN} \cdot Q_{vad} + R_{SU} \cdot Q_{vad} + R_{vad} \cdot Q_{vad} + \\ + L_{vad} \cdot \frac{dQ_{vad}}{dt} + H_{vad} + R_{OUT} \cdot Q_{vad} + L_{OUT} \cdot \frac{dQ_{vad}}{dt} \tag{3.31}$$

In Eq. (3.31), R_{IN} and R_{OUT} is the flow resistance of the inlet and outlet cannula; L_{IN} and L_{OUT} is the flow inertance of the inlet and outlet cannula; R_{vad} and L_{vad} is the flow resistance and inertance of the pump; H_{vad} is the pressure (head) gain across the pump and Q_{vad} is the blood flow through the pump. The nonlinear time-varying resistance R_{SU} has the form:

$$R_{SU} = \begin{cases} 0 & P_{LV}(t) > \overline{x} \\ \alpha \cdot \left[P_{LV}(t) - \overline{x} \right] & P_{LV}(t) \le \overline{x} \end{cases} \tag{3.32}$$

R_{SU} relates to the suction phenomenon, which is zero when the pump is operating normally and is activated when $P_{LV}(t)$ becomes less than a predetermined small threshold $\overline{x}$, a condition that represents suction. The parameter α is a cannula dependent scaling factor. The values used for the suction parameters are α = -3.5 *s/ml* and $\overline{x}$ = 1 *mmHg*. In the model, H_{vad} is described as follows:

$$H_{vad} = \lambda \cdot \frac{I(t)}{Q_{vad}} = \beta \cdot \omega^2(t) \tag{3.33}$$

with suitable parameters λ and β. Assuming a voltage supply *V* = 12 *V* to the pump motor, the constant λ = 89,944 *mmHg·ml/*(*s·A*) for the LVAD. The expression for the pump speed $\omega(t)$ in terms of the pump motor current $I(t)$ is the following:

$$\omega(t) = \sqrt{\frac{\lambda \cdot I(t)}{\beta \cdot Q_{vad}}} \tag{3.34}$$

where β = 9.9025×10^{-7} *mmHg/rpm*^{2} (Stergiopoulos, 1996).

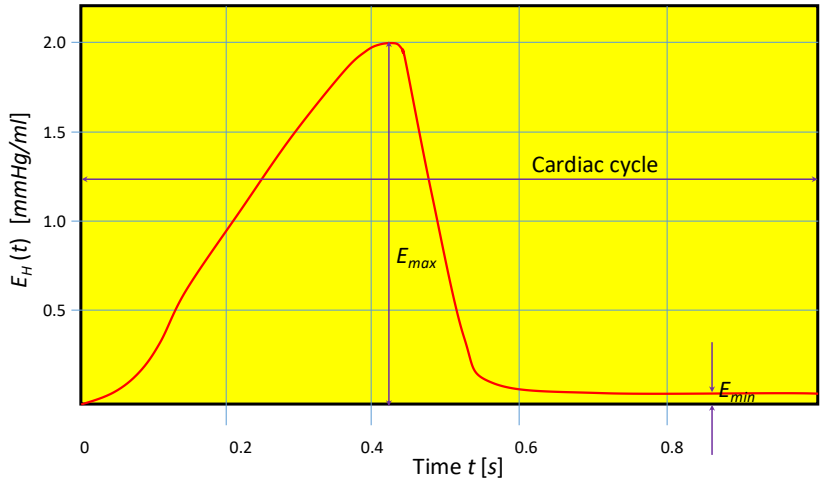

Figure 3.8 Elastance function $E_H(t)$ of a healthy heart. From: Capoccia M, De Lazzari C. Concepts, Mathematical Modelling and Applications in Heart Failure, 2019, Nova Science Publishers.

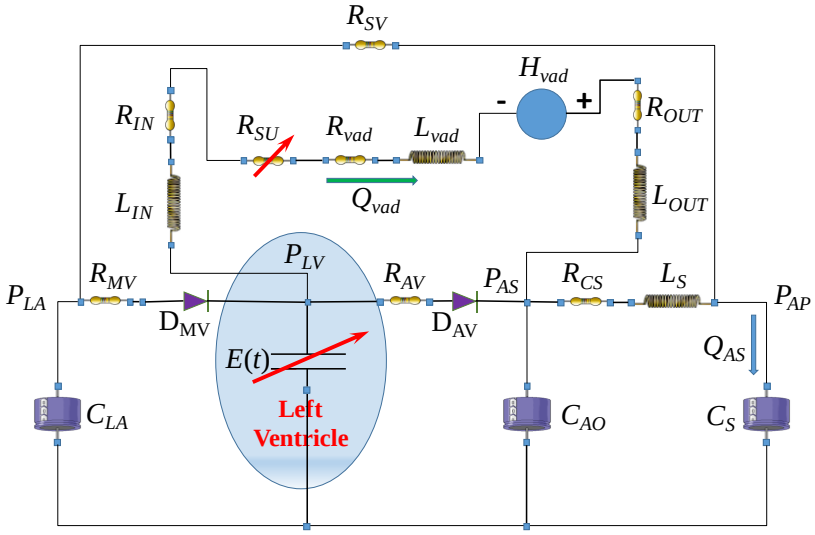

Figure 3.9 Electrical analogue of the cardiovascular system with LVAD support. The LVAD pumps blood continuously from the left ventricle into the aorta. From: Capoccia M, De Lazzari C. Concepts, Mathematical Modelling and Applications in Heart Failure, 2019, Nova Science Publishers.

3.4 Control Strategies for Rotary Blood Pumps

The feature of rotary blood pumps currently used in clinical practice is a constant speed operation mode, which reduces pulse pressure and the pulsatility index over a cardiac cycle. Although successful in unloading the heart, control on the cardiac workload is limited as shown by optimisation studies of the interaction between rotary blood pumps and the

cardiovascular system (Lim, 2010; Lim, 2012a; Lim, 2012b). There is perception that reduced arterial pulsatility may be responsible for complications including gastrointestinal bleeding, arterial-venous malformations, haemolysis, aortic regurgitation and pump thrombosis with reduced left ventricular recovery rate (Garcia, 2008; Cheng, 2014). Acquired von Willebrand disease may explain these findings (Geisen, 2008; Crow, 2010a) considering that loss of von Willebrand factor is higher in patients supported by continuous-flow LVADs (Malehsa, 2009; Crow, 2010b). Therefore, the development of control algorithms to generate pulsatility may help decrease the observed adverse events and increase the myocardial recovery rate through the delivery of a more physiological pattern.

Speed modulation has been investigated as a potential solution to optimise pulsatility control and cardiac workload (Pirbodaghi, 2012; Pirbodaghi, 2013). In addition, a preload-based Starling-like controller is being developed and proposed as an alternative to pulsatility control (Mansouri, 2015). Numerical simulations seem to show superiority of a Starling-like controller in comparison with pulsatility control and constant speed operation during transition from baseline to exercise, blood loss and reduced left ventricular function (Mansouri, 2015). The ability to estimate pump flow and differential pressure is critical for the development of an automatic, physiological control system whose aim is to adapt pump output according to the haemodynamic changes that occur in an ambulant patient. The aim of the following paragraphs is to give some insights of the mathematics behind some of the different physiological control strategies proposed for LVADs (AlOmari, 2013).

3.5 Speed Modulation for Pulsatile Control of Rotary Blood Pumps

The rotor speed controller described in the previous paragraph is based on the time-varying elastance concept, which may not be completely suitable to model the interactions between LVADs and the cardiovascular system (Vandenberghe, 2006) as discussed in Chapter 2. The one-fibre model is an alternative approach, which relates left ventricular cavity pressure and volume with systolic fibre stress and strain in the wall (Arts, 1991). The model considers global left ventricular pump function in terms of cavity pressure and volume, which are related to local wall tissue function in terms of myocardial fibre stress and strain. A fibrous shell model is introduced with rotational symmetry of the ventricular wall and homogeneous distribution of muscle fibre stress and strain. Based on these assumptions, the ratio of muscle fibre stress (σ_f) to left ventricular pressure (P_{LV}) is dependent on the ratio of cavity volume (V_{LV}) to wall volume (V_w) and is independent of other

geometric parameters. In mathematical terms, we obtain the following relationship:

$$\frac{P_{LV}}{\sigma_f} = \frac{1}{3} ln\left(1 + \frac{V_W}{V_{LV}}\right) \tag{3.35}$$

A baroreflex component can be added to the one-fibre model in order to obtain more accurate simulations of the interaction between LVADs and the cardiovascular system taking into account changes in heart rate (Cox, 2009). This integrated model describes left and right ventricular contraction according to the one-fibre model; systemic, pulmonary and coronary circulation according to a previously developed and validated lumped-parameter haemodynamic model (Bovendeerd, 2006); heart rate variability according to the baroreflex model (Van Roon, 2004). An overview of the main features of this integrated model is given.

Ventricular pressures are calculated according to Eq. (3.35). The intramyocardial pressure P_{im} is calculated in order to model the coronary circulation. P_{im} is linearly dependent on the transmural position in the wall: P_{im}= P_{LV} at the endocardial surface and P_{im} = 0 at the epicardial surface.

Cardiac valves are considered ideal diodes and vessels are modelled with constant resistance R, inertance L and compliance C. Pressure drops are as follows:

$$\Delta P_R = R \cdot Q \qquad \Delta P_L = L \cdot \frac{dQ}{dt} \qquad \Delta P_C = \frac{V - V_0}{C} \tag{3.36}$$

where Q is the flow, V the volume and V_0 is the volume at zero pressure.

The baroreflex heart rate is modulated by the cardiopulmonary reflex and controlled by the vagal and sympathetic system. The baroreceptor activity B_p is transformed into vagal (F_{vag}) and sympathetic (F_{sym}) frequencies as follows (Cox, 2009):

$$\begin{aligned} F_{vag} &= K_{vag} \cdot B_b + D_{vag} \\ F_{sym} &= -K_{sym} \cdot B_b + D_{sym} \end{aligned} \tag{3.37}$$

K_{vag} and K_{sym} convert activity values to frequency values; D_{vag} and D_{sym} are the vagal and sympathetic outputs when there is no feedback from the

baroreceptors. The baroreflex heart rate ($f_{h,b}$) is a nonlinear combination of F_{vag} and F_{sym} as follows:

$$f_{h,b} = f_{h,d}\left(1-\frac{F_{vag}}{F_{vag}+c_{F,vag}}\right)\cdot\left(1+\frac{F_{sym}}{c_{F,sym}}\right) \qquad (3.38)$$

where $f_{h,d}$ is the heart rate of a denervated heart, $c_{F,sym}$ and $c_{F,vag}$ are constants.

The purpose is to evaluate whether pulsatile operation of a rotary blood pump is more beneficial than standard fixed pump speed currently used.

Simulations of pulsatile operation of a continuous-flow LVAD have been made for the HeartMate II using the following equation (Cox, 2009):

$$Q_{pump} = a(\Delta P_H)v_{pump} + b(\Delta P_H) \qquad (3.39)$$

where Q_{pump} is the pump flow in *L/min*, v_{pump} is the pump speed in *rpm/*1000, ΔP_H is the pressure head across the pump in *mmHg*, a and b are fitting parameters dependent on ΔP_H (a = 0.0091ΔP_H + 1.4; b = −0.19ΔP_H − 1.9).

To obtain pulsatile support, a pulsatile speed component v_p is added to the constant pump speed according to the following expression:

$$v_p = A_{v_p}\cdot sin\left[\frac{2\pi\cdot(t-t_{start})}{T}\right] \qquad 0 \le t < T \qquad (3.40)$$

where A_{v_p} is the amplitude of the pulsatile speed component, t_{start} is the starting time at the end of ventricular contraction and t is the relative time within the cardiac cycle, starting at the onset of ventricular contraction. By choosing t_{start} equal to the end of ventricular contraction, the pulsatile pump speed is highest during ventricular relaxation and lowest during ventricular contraction.

Simulations results show greater increase in cardiac index and coronary blood flow during varying speed support compared with constant speed support confirming better perfusion. Stroke work and heart rate are significantly lower with varying speed support confirming better left ventricular unloading in the presence of pulsatile mode (Cox, 2009). Although numerical simulations based on the one-fibre model with baroreflex component and sinusoidal pump speed variation is a significant

improvement compared to the time-varying elastance and confirm the beneficial haemodynamic effects of a pulsatile mode, it does not necessarily show an improvement in arterial pulsatility. If the pump flow rate is the controlled variable with direct dynamic control of the pump output over a cardiac cycle, then true pulsatility improvement is observed during varying pump speed support (Bozkurt, 2014). Numerical simulations with this approach require a baroreflex heart rate control model (Ursino, 1998), dynamic modelling of a continuous-flow LVAD (Moscato, 2009) and a proportional-integral (PI) flow rate controller for the device (Bozkurt, 2014).
The baroreflex is modelled with a sigmoidal function and first order linear differential equations as follows (Bozkurt, 2014; Ursino, 1998):

$$\sigma_{T,S}(t) = \begin{cases} G_{T,S} \cdot ln\left[f_{es}\left(t - D_{T,S}\right) - f_{es,min} + 1 \right] & f_{es} \geq f_{es,min} \\ 0 & f_{es} < f_{es,min} \end{cases}$$

$$\frac{d\Delta T_S(t)}{dt} = \frac{-\Delta T_S(t) + \sigma_{T,S}(t)}{\tau_{T,S}}$$

$$\sigma_{T,V}(t) = G_{T,V} \cdot f_{ev}\left(t - D_{T,V}\right) \qquad (3.41)$$

$$\frac{d\Delta T_V(t)}{dt} = \frac{-\Delta T_V(t) + \sigma_{T,V}(t)}{\tau_{T,V}}$$

$$T = \Delta T_V + \Delta T_S + T_0$$

where $\sigma_{T,S}$ and $\sigma_{T,V}$ are the sympathetic and vagal activities with strength $G_{T,S}$ and $G_{T,V}$, time delays $D_{T,S}$ and $D_{T,V}$ and time constants $\tau_{T,S}$ and $\tau_{T,V}$; f_{es} and f_{ev} are the sympathetic and vagal efferent pathway frequencies; ΔT_S and ΔT_V are the sympathetic and vagal stimulations; T_0 is the heart period in the absence of cardiac innervations and t is the instantaneous time.
The equations for the continuous-flow LVAD (Micromed VAD) are (Bozkurt, 2014; Moscato, 2009):

$$\Delta P = K \cdot \omega^2 - R \cdot Q_{pump} - L \cdot \frac{dQ_{pump}}{dt} \qquad R = k_1 \cdot Q_{pump} + k_2 \qquad (3.42)$$

where ΔP and Q are the pump pressure difference and flow rate; L and R are the pump inertance and resistance; K, k_1 and k_2 are the estimated parameters (Moscato, 2009) and ω is the pump rotational speed.

The proportional-integral (PI) control applied to the pump flow rate is defined as (Bozkurt, 2014):

$$u(t) = K_p \cdot e(t) + K_i \cdot \int_0^t e(\theta)\, d\theta \tag{3.43}$$

where K_p is the proportional gain, K_i is the integral gain, $e(t)$ is the error and $u(t)$ is the output of the controller.

The pulsatility index I_p is defined as follows:

$$I_p = \frac{v_{systolic} - v_{diastolic}}{v_{mean}} \tag{3.44}$$

where $v_{systolic}$ ($v_{diastolic}$) is the systolic (diastolic) velocity and v_{mean} is the mean velocity.

This type of control strategy leads to increased pump flow during systole and reduced flow during diastole with increased arterial pulsatility index following adjustment of the pump operational speed without reducing the level of support. Suction is unlikely to occur because the left ventricle is unloaded in systole with reduced blood flow through the pump in diastole. Therefore, the left ventricle is filled in diastole without blood being ejected through the pump (Bozkurt, 2014).

3.6 LVAD Modelling with Korakianitis-Shi Model

The Korakianitis-Shi cardiovascular model (Korakianitis, 2006a; Korakianitis, 2006b) has been successfully applied to study the interactions between the cardiovascular system and LVAD support with displacement and rotary blood pumps (Shi, 2006; Shi, 2007; Shi, 2011). This is quite an interesting numerical model based on the concentrated parameter method where individual components are analysed according to flow resistance, vessel elasticity and blood inertial effects in each segment (Shi, 2007). Heart valve dynamics is a key feature of this model, which takes into account pressure difference, frictional force and vortex effect acting on valve leaflets resulting in a more accurate description of cardiac response. The LVAD is connected in parallel with the native left ventricle with the inlet in the left ventricular apex and the outlet to the ascending aorta. Dynamic modelling of the pump

is based on flow changes at the inlet and outlet of the device (Shi, 2007). Three LVAD support modes are considered for a rotary blood pump connected in parallel with the left ventricle: constant flow, counterpulsation and copulsation. A rotary pump has no variable chamber volume; therefore, LVAD inflow ($Q_{LVAD,i}$) and outflow ($Q_{LVAD,o}$) are the same.

A constant rotational speed generates a constant LVAD flow:

$$Q_{LVAD,i} = Q_{LVAD,o} = Q_0 \tag{3.45}$$

where Q_0 is the initial value.

A lower rotational speed in systole and a higher speed in diastole generate a counterpulsation mode as follows:

$$Q_{LVAD,i} = Q_{LVAD,o} = \begin{cases} Q_0 & 0 \le t \le T_{T2} \\ Q_0 + \frac{1}{2} \cdot Q_p \left(1 - cos \frac{\pi \left(t - T_{T2} \right)}{T_{U2} - T_{T2}} \right) & T_{T2} < t \le T_{U2} \\ Q_0 + \frac{1}{2} \cdot Q_p \left(1 - cos \frac{\pi \left(t - T_{U2} \right)}{T - T_{U2}} \right) & T_{U2} < t \le T \end{cases} \tag{3.46}$$

where Q_p is the pulse value, T is the heart cycle, T_{T2} is the end of the T wave and T_{U2} is the end of the U wave in the ECG signal.

An offset value where $Q_0 = 2Q_p$ is added to the sine curve to maintain the impeller with the same rotational direction during the cardiac cycle and avoid regurgitant pump flow, which is likely to occur in the presence of low rotational speed (Shi, 2007; Vandenberghe, 2003).

A higher rotational speed in systole and a lower rotational speed in diastole generate a copulsation mode leading to a competitive set up between the native left ventricle and the LVAD as follows:

$$Q_{LVAD,i} = Q_{LVAD,o} = \begin{cases} Q_0 + \frac{1}{2} \cdot Q_p \left(1 - cos \frac{\pi t}{T_{T1}} \right) & 0 < t \le T_{T1} \\ Q_0 + \frac{1}{2} \cdot Q_p \left(1 - cos \frac{\pi \left(t - T_{T1} \right)}{T_{T2} - T_{T1}} \right) & T_{T1} < t \le T_{T2} \\ Q_0 & T_{T2} < t < T \end{cases} \tag{3.47}$$

where T_{T1} is the onset of the T wave in the ECG signal.

Again, an offset value is added to maintain the same rotational direction and avoid regurgitant pump flow during the cardiac cycle.

Two LVAD support modes are considered for a displacement pump where inflow and outflow are different during the cardiac cycle due to a variable chamber volume. When the pump empties into the aorta during diastole and fills during systole, a counterpulsation mode is generated. Therefore, the LVAD inlet becomes:

$$Q_{LVAD,i} = \begin{cases} \frac{1}{2} \cdot Q_{p,i} \left(1 - cos\left(\frac{2\pi t}{T_{T2}} \right) \right) & 0 \le t \le T_{T2} \\ 0 & T_{T2} < t < T \end{cases} \quad (3.48)$$

and the LVAD outlet becomes:

$$Q_{LVAD,o} = \begin{cases} 0 & 0 \le t < T_{T2} \\ \frac{1}{2} \cdot Q_{p,o} \left(1 - cos \frac{2\pi \cdot (t - T_{T2})}{T - T_{T2}} \right) & T_{T2} < t < T \end{cases} \quad (3.49)$$

In copulsation mode, the LVAD inlet becomes:

$$Q_{LVAD,i} = \begin{cases} 0 & 0 \le t < T_{T2} \\ \frac{1}{2} \cdot Q_{p,i} \left(1 - cos \frac{2\pi \cdot (t - T_{T2})}{T - T_{T2}} \right) & T_{T2} < t < T \end{cases} \quad (3.50)$$

and the LVAD outlet becomes:

$$Q_{LVAD,o} = \begin{cases} \frac{1}{2} \cdot Q_{p,o} \left(1 - cos \frac{2\pi t}{T_{T2}} \right) & 0 \le t \le T_{T2} \\ 0 & T_{T2} < t < T \end{cases} \quad (3.51)$$

where $Q_{p,i}$ and $Q_{p,o}$ is the inlet and outlet flow pulse.

An alternative option is the reciprocating-valve pump, which is a pulsatile-type assist device connected in series with the native heart. The flow through the device is modelled as follows (Shi, 2007):

$$Q_{LVAD} = \begin{cases} A_{LVAD} \frac{dx}{dt} + CQ_{LVAD} + A \cdot R_{LVAD} \cdot \left(\sqrt{P_{SA} - P_{AO}} \right) & P_{SA} \ge P_{AO} \\ A_{LVAD} \frac{dx}{dt} + CQ_{LVAD} + A \cdot R_{LVAD} \cdot \left(\sqrt{P_{AO} - P_{SA}} \right) & P_{SA} < P_{AO} \end{cases} \quad (3.52)$$

The pumping motion profile $x(t)$ consists of a sinusoidal wave in a cardiac cycle as follows (Shi, 2007):

$$x(t)=\begin{cases}\dfrac{X_{LVAD}}{2}\cdot\left(1-cos\left(\dfrac{\pi t}{T_{T2}}\right)\right) & 0\le t\le T_{T2}\\ \dfrac{X_{LVAD}}{2}\cdot\left(1-cos\dfrac{\pi\left(t-T_{T2}\right)}{T-T_{T2}}\right) & T_{T2}<t\le T\end{cases} \tag{3.53}$$

A_{LVAD} is the LVAD sectional area, CQ_{LVAD} is a coefficient, R_{LVAD} is the LVAD resistance, X_{LVAD} is the LVAD displacement.

Numerical simulations show that rotary blood pumps generate some degree of pulsatility, which is significantly lower compared to volume displacement pumps although they require the least power input. Rotary and displacement pumps connected in parallel (Fig.6.10) need to unload the left ventricle completely in order to maintain arterial pressure and cardiac output within normal range with potential for aortic leaflets fusion, which can be avoided using a reciprocating pump connected in series (Shi, 2007). A feedback control can accommodate pump performance according to changes in physiological conditions (Shi, 2011b).

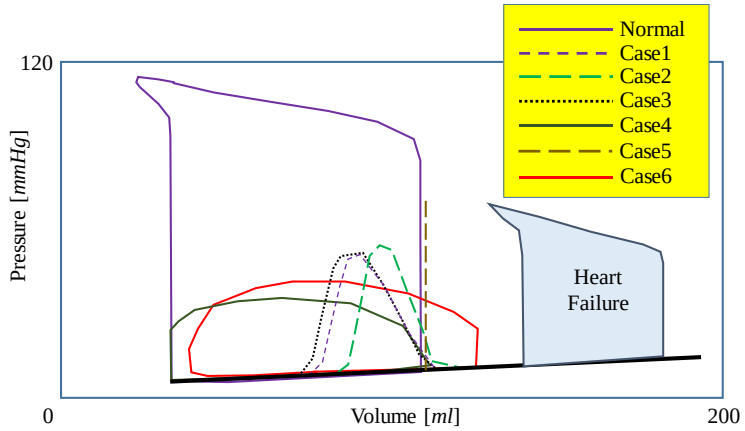

Figure 3.10 Case1 rotary pump, constant flow, in parallel connection; Case 2 rotary pump, counterpulsation, in parallel connection; Case 3 rotary pump, copulsation, in parallel connection; Case 4 displacement pump, counterpulsation, in parallel connection; Case 5 displacement pump, copulsation, in parallel connection; Case 6 reciprocating-valve pump, copulsation, in series connection. From: Capoccia M, De Lazzari C. Concepts, Mathematical Modelling and Applications in Heart Failure, 2019, Nova Science Publishers.

Although a constant pump speed is the most efficient operating mode for rotary blood pumps (Shi, 2010), the lack of adaptation to changing

physiological conditions remains a limiting factor. Speed modulation may be desirable to achieve pulsatility but optimisation is required to avoid pump regurgitant flow, which may decrease pump efficiency significantly (Shi, 2011a; Shi, 2018). Energy equivalent pressure and pulse pressure are useful parameters for the evaluation of blood flow pulsatility (Shepard, 1966; Ündar, 2003; Vandenberghe, 2005). Cardiac output and energy equivalent pressure decrease with increasing levels of pulsatility ratio leading to the development of pump regurgitant flow or inlet suction. Synchronisation between LVAD and cardiac cycle shows that a 75% phase shift and a 0.5 pulsatility ratio or a 42% phase shift and a 0.55 pulsatility ratio generate arterial pulse pressure with a magnitude up to 28 *mmHg* at the expense of reduced cardiac output and pump efficiency (Shi, 2010). Optimisation is therefore required although difficult to achieve due to vascular impedance changes in advanced heart failure (Shi, 2011a).

Numerical and in vitro simulations comparing in parallel and in series LVAD connection with the circulation show superiority of in parallel connection between LVAD and ascending aorta (Fig. 3.11) in terms of mechanical support; in parallel connection between LVAD and descending thoracic aorta (Fig. 3.12) is not optimal due to retrograde flow in the aortic arch during high level of support; in series connection between the pump and the descending thoracic aorta (Fig. 3.13) shows improved pulsatility and may be considered an alternative for long-term support (Rezaienia, 2014; Rezaienia, 2015; Rezaienia, 2016; Rezaienia, 2017).

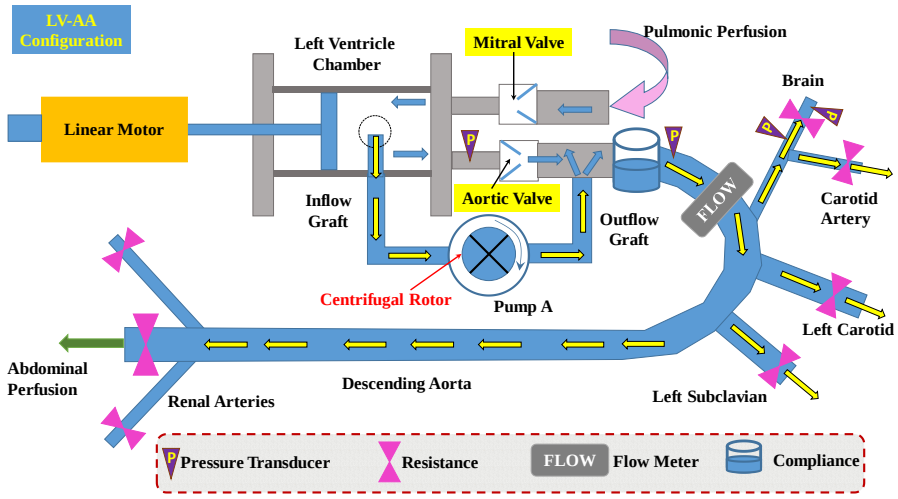

Figure 3.11 In parallel LVAD connection between left ventricle and ascending aorta (LV-AA). From: Capoccia M, De Lazzari C. Concepts, Mathematical Modelling and Applications in Heart Failure, 2019, Nova Science Publishers.

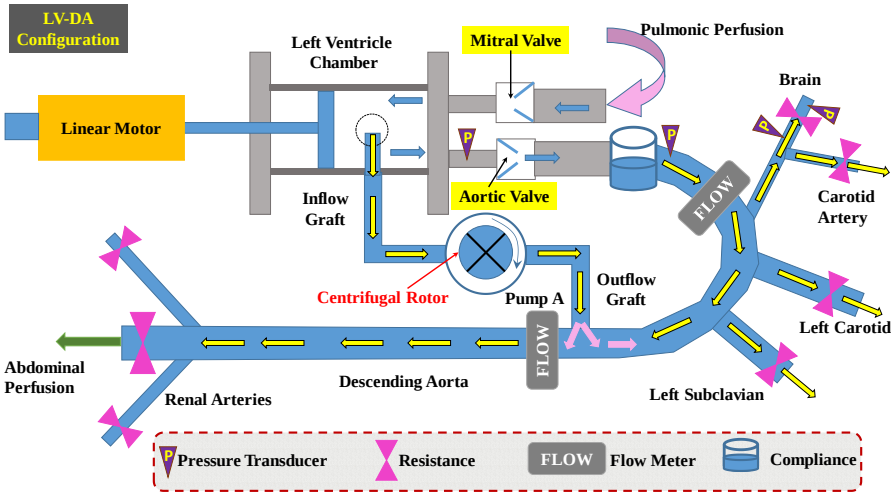

Figure 3.12 In parallel LVAD connection between left ventricle and descending thoracic aorta (LV-DA). From: Capoccia M, De Lazzari C. Concepts, Mathematical Modelling and Applications in Heart Failure, 2019, Nova Science Publishers.

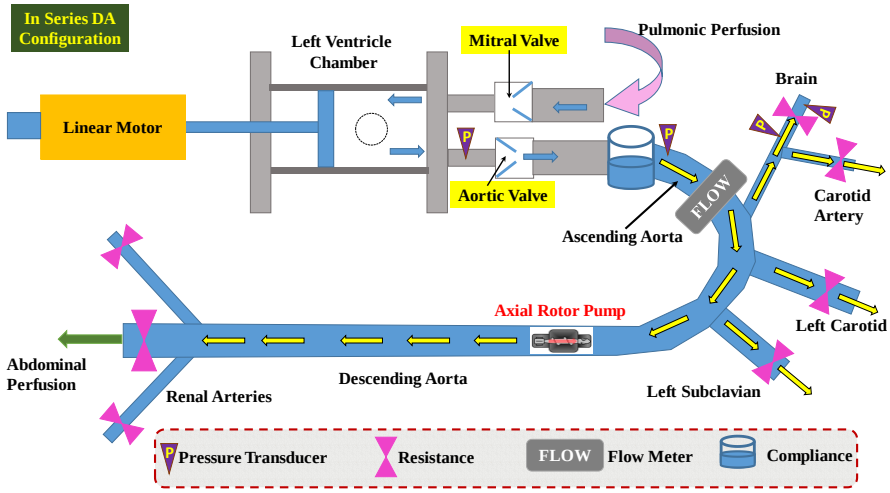

Figure 3.13 In series LVAD connection with the descending thoracic aorta. From: Capoccia M, De Lazzari C. Concepts, Mathematical Modelling and Applications in Heart Failure, 2019, Nova Science Publishers.

3.7 Starling-like Controller

The response of rotary blood pumps to preload and afterload changes at constant rotational speed is unphysiological when compared with the left ventricle. Centrifugal pumps like HeartWare and Duraheart show high preload sensitivity in the presence of high afterload whereas their high afterload sensitivity is equally distributed across a preload range. Axial flow pumps have a less uniform behaviour. The HeartMate II shows increased preload sensititvity in the presence of low afterload whereas the Incor has a more uniform preload and afterload sensitivity across the range used in clinical practice (Salamonsen, 2011).

Maximum preload sensitivity and minimum afterload sensitivity allow right and left ventricular output synchronisation without humoral or neural intervention according to the Frank-Starling mechanism. A preload sensitive control system would allow the combined LVAD and left ventricle to adapt to changes in right ventricular output according to different physiological conditions eliminating under- or over-pumping (Salamonsen, 2011; Salamonsen, 2012).

A linear Starling-like controller based on pump flow pulsatility as the feedback variable (Salamonsen, 2012) is justified by a linear relationship between pump flow pulsatility and left ventricular stroke work ($LVSW$) as long as the aortic valve remains closed (Salamonsen, 2009; Salamonsen, 2012). Diversion from linearity occurs due to preferential blood ejection through the low resistance pathway following opening of the aortic valve. The performance of other pulsatility indices such as pressure head, pump speed and pump current are significantly worse (Salamonsen, 2012). Flow pulsatility is defined as the amplitude of the flow profile through a rotary pump whose operating point is on a "control straight line" at an angle θ with the horizontal flow pulsatility axis. According to physiological demand, the operation point may divert from the control line requiring modulation of the pump rotational speed by the controller to restore the operating point back on the control line in a new position (Gaddum, 2014) along a circular path defined by the following relationship (Mansouri, 2015):

$$\overline{Q}_p = \left[\sqrt{\left(\overline{Q}_{Pm}\right)^2 + \left(PIQ_{Pm}\right)^2} \right] \cdot \sin\theta \qquad (3.54)$$

where $\bar{Q}_p$ is the desired average pump flow, $\bar{Q}_{Pm}$ is the mean pump flow provided by the model and PIQ_{Pm} is the pump flow pulsatility.

Pump pulsatility is related to left ventricular contraction. In the presence of severe left ventricular dysfunction, there are no major changes in pulsatility with small dynamic range of the pulsatility index and limited ability as a control input.

A preload-based Starling-like controller using left ventricular end diastolic pressure ($P_{ed,LV}$) as the feedback variable is safer and more effective (Fig. 6.14) (Mansouri, 2015). The control line is generated by a cubic function relating $\bar{Q}_p$ and $P_{ed,LV}$ as follows (Gaddum, 2014; Mansouri, 2015):

$$\overline{Q}_p = \left[0.0003 \cdot P^3_{ed,LV(m)} + 0.0276 \cdot P^2_{ed,LV(m)} + 0.9315 \cdot P_{ed,LV(m)} - 0.0928 \right] \cdot K \qquad (3.55)$$

where K is a scaling factor reflecting the ability of the controller to adapt to changes in $P_{ed,LV}$ and the circulation and $P_{ed,LV(m)}$ is the left ventricular end diastolic pressure provided by the model.

Mean pump flow is regulated according to the measured $P_{ed,LV}$ using a predefined control line reflecting the status of the circulation at each instant. Preload sensitivity for individual patients is modified by changing the scaling factor K as a means of altering pump sensitivity to changes in $P_{ed,LV}$. Due to its shape, a single preload control line enables a major decrease in flow at low left ventricular preload to avoid suction and limit increases at high preload to avoid overpumping (Mansouri, 2015). The *in vitro* evaluation of a preload-based Starling-like controller confirms its superiority compared to constant speed control (Mansouri, 2017; Stephens, 2017) as shown by numerical simulation (Mansouri, 2015; Salamonsen, 2012).

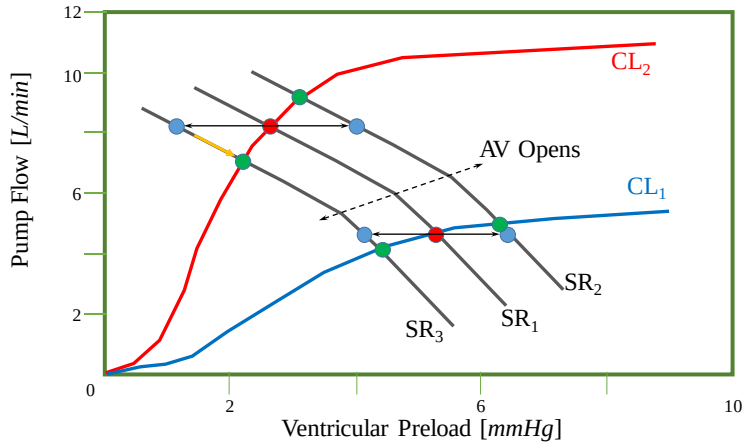

Figure 3.14 Schematic representation of the Frank-Starling controller. CL_1 and CL_2 are control lines. SR_1 is the initial system response; SR_2 and SR_3 are the diverted system responses. A circle at the intersection between the control line and the initial system line is the original position of the operating point (OP). A circle on the SR_2 or SR_3 line joined by an arrow is the diverted position of OP. A circle at the intersection between the SR_2 or SR_3 line and a control line is the position of OP when returned to the control line. From: Capoccia M, De Lazzari C. Concepts, Mathematical Modelling and Applications in Heart Failure, 2019, Nova Science Publishers.

3.8 Clinical Implications of Physiological Flow Adjustment in Rotary Blood Pumps

As discussed in previous paragraphs, there is enough evidence to suggest that fixed rotational speed remains inadequate for rotary blood pumps due to insufficient preload sensitivity to emulate the Frank-Starling mechanism observed in the native heart. Coupling with variable residual left ventricular function, limited sensitivity to preload and significant sensitivity to afterload

may lead to underpumping or overpumping (suction) with potentially harmful consequences on the long-term such as right ventricular dysfunction, arrhythmias and organ hypoperfusion (Tchantchaleishvili, 2017). There is no doubt that active control strategies would improve synchronisation between LVAD and the cardiovascular system and would allow rotary blood pumps achieve their full potential. Although still at a developing stage, significant progress is being made towards their clinical application (Kishimoto, 2013; Arakawa, 2014; Ochsner, 2017; Petrou, 2017; Grinstein, 2018).

A control strategy should be considered according to patient's need. Modulation by preload achieves superior volume unloading and it may be the ideal approach for myocardial recovery whereas asynchronous modulation achieves superior pulsatility and it may be more suitable in an acute setting such as cardiogenic shock where pulsatility and sensorless pump speed modulation would be beneficial. Direct measurement of preload with left ventricular end-diastolic pressure seems to offer greatest potential compared to estimates through surrogates such as central venous pressure, right atrial pressure, pulmonary artery pressure, pulmonary capillary wedge pressure and left atrial pressure. Therefore, the use of passive or battery-operated implantable sensors may well be the way forward (Tchantchaleishvili, 2017).

3.9 Chapter Summary

Device optimisation is usually based on CFD simulation and experimental validation under steady conditions for convenience. Nevertheless, the role played by fluid forces and the importance of the flow derivative has been acknowledged. Modelling requires assumptions to reduce complexity and computational effort. This aspect needs to be taken into account following the interpretation of results. The hydraulic component plays a significant role in the whole context. The time-varying elastance and the electric circuit theory have been applied successfully. Criticism related to the suitability of the time-varying elastance during LVAD support has seen the application of alternative approaches such as the one-fibre model and the Korakianitis-Shi model. The right heart and the pulmonary circulation are assumed to be normal with negligible effect on the LVAD. A constant rotational speed is the current setting in clinical practice with appropriate unloading achieved at high speed with potential for myocardial damage due to suction. A pulsatile mode with low pump speed in systole and high pump speed in diastole (counterpulsation pattern) would be more appropriate. Speed modulation to optimise pulsatility control and cardiac workload requires a modelling

approach that takes into account the LVAD interaction with the left ventricle and the circulation. Suction is accounted for by adding a nonlinear resistance. A preload-based Starling-like controller which emulates the natural physiological mechanism has been proposed as an alternative. Significant modelling effort is being pursued to develop active control strategies to improve synchronisation between LVAD and the cardiovascular system and allow rotary blood pumps achieve their full potential.

Chapter 4

Computational Fluid Dynamics Analysis of Rotary Blood Pumps

4 Computational Fluid Dynamics Analysis of Rotary Blood Pumps

4.1 Introduction

Computational fluid dynamics (CFD) is widely used in the design and development of ventricular assist devices. CFD is a convenient and efficient method for the analysis of pressure-flow performance of the device, hydraulic efficiency, flow profile through the pump and fluid stress levels (Wood, 2005). Significant progress in blood modelling has made CFD a powerful approach for the estimation of flow-induced blood damage. Information such as location and extent of stagnation zones, local shear stress and exposure time of red blood cells can be correlated to the degree of haemolysis and thrombus formation. Pump optimisation can be achieved according to blood-specific requirements. Although computational resources for CFD studies can be very demanding, this technique is time-saving and cost-effective because significantly reduces experiments and prototype building. In addition, it can address the exact flow features inside the device with a view to design and performance enhancement (Behbahani, 2009).

CFD is a very attractive tool in VADs development because it allows the virtual analysis of functional performance of different designs for a wide range of operating conditions. Different approaches have been used but controversy still remains (Fraser, 2011; Lopes, 2017). VADs operate in the transitional region at the boundary of laminar and turbulent flow (low Reynolds number). Blood behaviour during this transition remains not completely understood and difficult to simulate. Assuming a Newtonian behaviour for the blood and neglecting the influence of red blood cells (RBCs) is convenient for the purposes of simulations but it may lead to incorrect predictions during the transition phase. This is a key aspect for the design of blood recirculation devices with the aim to minimise blood damage and reduce potential for thrombosis enhanced by blood recirculation regions. Shear-thinning rheology may have to be taken into account to accurately model transitional blood flow in recirculation devices (Kelly, 2020). This aspect will be further discussed later in this chapter. Simulations for continuous flow VADs are usually performed under steady flow conditions where the inlet boundary is set to a specific steady velocity profile while the outlet boundary is fixed at a steady pressure. The actual unsteady boundary conditions will be dependent on the flow from the heart and the aortic pressure, which are the result of the interactions between the device and the cardiovascular system (Fraser, 2011). The study of the interactions between LVADs and the whole cardiovascular system with a 3D CFD model

is highly demanding although limited parts of the assisted circulation have been developed with this method (Bazilevs, 2009; Marsden, 2014; Morris, 2016). The flow pattern in most regions of rotary blood pumps is turbulent because of the disturbance caused by the rotating impeller. The choice of a turbulence model is important for the outcome of the simulation but remains a controversial issue when applied to rotary blood pumps (Song, 2003a). None of the available turbulence models is universally recognised as being superior for all classes of problems. The choice depends on the physics of the flow, the established practice for a specific type of problem, the level of accuracy required, the available computational resources and the amount of time required for the simulation.

4.2 Turbulence Models for CFD Analysis of Rotary Blood Pumps

The Reynolds number (Re) is the criterion used to determine whether flow is laminar (low Re), transitional (increasing Re) or turbulent (higher Re). In mathematical terms, it is defined as:

$$Re = \frac{\rho v l}{\mu} \tag{4.1}$$

where ρ is the fluid density, v is the fluid velocity, l is the length of the system and μ is the fluid viscosity.

Turbulence is the three-dimensional unsteady random motion observed in fluids at moderate to high Reynolds numbers (ANSYS Fluent User's Guide, 2016). Instantaneous fluctuations of mass, momentum and scalar quantities are unpredictable and irregular in time and space. Turbulence is a classical multi-scale problem and the most challenging area in fluid dynamics (Menter, 2011). Although it remains a limiting factor for the resolution capabilities of even the most powerful parallel computers, an approximate solution of the Navier-Stokes equations is usually sufficient for most applications. Turbulence modelling is an attempt to develop general methods to achieve this outcome. Different methods are available to make turbulence computationally more approachable.

Direct numerical simulation (DNS) of the full unsteady Navier-Stokes equations resolves the whole spectrum of scales and no modelling is required. The disadvantage of this method is related to the prohibitive high computational cost and can be applied only to very low Re numbers with simple and limited geometries (Moser, 1999; Rudman, 2006; Vreman, 2014). Therefore, an averaging procedure has to be applied to the Navier-Stokes equations to reduce complexity. Reynolds-averaged Navier-Stokes

equations (RANS) are formulated in terms of time-averaged flow field (velocity, pressure, density and temperature) and all turbulent length scales are modelled. The elimination of turbulence fluctuations makes the equations amenable to CFD analysis on a desktop computer. Nevertheless, the averaging process introduces additional unknown terms into the transport equations (Reynolds stresses and fluxes) requiring turbulence closure by a suitable model able to provide a link between the mean velocity field and Reynolds stresses. The RANS concept addresses turbulence as a whole focusing on mean flow only without attempting to resolve turbulent structures in time and space (Menter, 2011). RANS models achieve high accuracy in computation of wall-bounded flows. Increased accuracy requirements and more shape complexity need turbulence models able to predict flow separation from smooth surfaces under adverse pressure gradients and allow for integration to the wall. Low-Reynolds numbers or viscous sublayer models (VSM) are suitable for this purpose (Kalitzin, 2005; Popovac, 2007). Besides, the impact of the scale equation is also important with particular reference to wall boundary layers. More specifically, the ε-equation has been successfully applied to CFD simulations, often in combinations with wall functions, but shows a weak response to adverse pressure gradients with a strong tendency to miss or under-predict separation. Instead, the ω- equation offers a more accurate and robust modelling framework for boundary layers (Menter, 2011). This is related to the built-in elliptic relaxation of the k-ω model. Near the wall, for constant viscosity μ, the ω- equation becomes:

$$\mu \frac{\partial^2 \omega}{\partial x_j^2} = \beta \rho \omega^2 \qquad (4.2)$$

Equation (4.2), combined with the values specified for ω at the wall, efficiently communicates the wall presence to the flow in the near-wall region without the need for additional transport equations or damping functions (Menter, 2011). Despite its strength, the ω- equation has shown a disturbing sensitivity to free-stream values imposed for ω at the boundary layer edge through the inlet values (Menter, 1992; Menter, 2009). This has been overcome by combining the advantages of the ε- and ω- equation (Menter, 1994) leading to the baseline (BSL) model formulation, which is closely related to the shear stress transport (SST) model. The SST model provides the best agreement against experimental data in view of its ability to accurately predict flow separation under pressure gradients present in many technical devices (Menter, 2011). In addition, the ω- equation is

appropriate when combined with laminar-turbulent transition modelling (Menter, 2006; Menter, 2009). Reynolds stress models (RSM) solve an individual equation for each of the six independent Reynolds stresses directly and a scale equation (ε- or ω-equation). Although RANS remains the most widely used modelling approach because of steady state simulations and computationally not expensive, scale-resolving simulation (SRS) models are being increasingly considered for certain flows where all or part of the turbulence spectrum is resolved in at least a portion of the numerical domain (Menter, 2011; Menter, 2015). Their use is justified by the potential for improved accuracy when the resolution of the largest eddies is important or when unsteady data is needed. Nevertheless, they are computationally expensive and a higher grid resolution is required. In addition, unsteady simulations with small time steps generate long run times (days instead of hours or minutes). Large Eddy Simulation (LES) is the most widely used SRS model. This method resolves only the large scales of turbulence (problem-dependent and difficult to model) and models the small scales (more universal and isotropic and easier to model). LES filters the Navier-Stokes equations over a finite spatial region (the grid volume) and aims at resolving the portions of turbulence larger than the filter width. Turbulence structures smaller than the filter are then modelled according to a simple eddy viscosity approach. It is easier to resolve the largest turbulence scales for free shear flows as they are of the order of the shear layer thickness. In contrast, in wall boundary layers the turbulence length scale near the wall becomes very small relative to the boundary layer thickness. This is a severe limitation for the use of LES. Therefore, hybrid models would be an appropriate choice where large eddies are resolved only away from walls and the wall boundary layers are addressed with a RANS model. Examples are Detached Eddy Simulation (DES) (Spalart, 2000) or Scale-Adaptive Simulation (SAS) (Menter and Egorov, 2010). More recent developments consist of the Shielded Detached Eddy Simulation (SDES) and the Stress-Blended Eddy Simulation (SBES) proposed by ANSYS turbulence team (Menter, 2015).

RANS two-equation models (k-ε and k-ω) have been extensively used to model the haemodynamic behaviour in rotary blood pumps. A more detailed description of these models and their different forms is given in order to better understand their application to the study of the interaction between rotary blood pumps and the cardiovascular system.

4.3 RANS Models

The focus will be on those models with specific application to blood recirculation devices. Turbulence models give more accurate results than the laminar model. The use of k-ε and Reynolds stress models (RSM) have been considered suitable for the study of flow behaviour in circulatory assist devices (Zhang, 2013). More specifically, a k - ω model seems more appropriate for a centrifugal pump (Song, 2003a) and a k-ε model for an axial flow pump (Throckmorton, 2008).

These models are based on the Reynolds-averaged Navier-Stokes (RANS) equations as follows:

$$\frac{\partial \rho}{\partial t} + \frac{\partial}{\partial x_i}(\rho u_i) = 0 \tag{4.3}$$

$$\frac{\partial}{\partial t}(\rho u_i) + \frac{\partial}{\partial x_j}(\rho u_i u_j) = -\frac{\partial p}{\partial x_i} + \frac{\partial}{\partial x_j}\left[\mu\left(\frac{\partial u_i}{\partial x_j} + \frac{\partial u_j}{\partial x_i} - \frac{2}{3}\delta_{ij}\frac{\partial u_l}{\partial x_l}\right)\right] + \frac{\partial}{\partial x_j}(-\rho\overline{u_i' u_j'}) \tag{4.4}$$

The Reynolds stresses $-\rho\overline{u_i' u_j'}$ are additional terms representing the effects of turbulence and must be modelled to close equation (4.4). The Boussinesq hypothesis allows this step by relating the Reynolds stresses to the mean velocity gradients as follows:

$$-\rho\overline{u_i' u_j'} = \mu_t\left(\frac{\partial u_i}{\partial x_j} + \frac{\partial u_j}{\partial x_i}\right) - \frac{2}{3}(\rho k + \mu_t \frac{\partial u_k}{\partial x_k})\delta_{ij} \tag{4.5}$$

The k-ε and the k-ω models are based on the Boussinesq hypothesis. The advantage of this approach is the relatively low computational effort to address the turbulent viscosity μ_t. Two additional transport equations are solved for the k-ε and the k-ω models (for the turbulence kinetic energy, k, and either the turbulence dissipation rate, ε, or the specific dissipation rate, ω) and μ_t is computed as a function of k and ε or k and ω. The disadvantage of the Boussinesq hypothesis is the assumption that μ_t is an isotropic scalar quantity, which is not strictly true. Nevertheless, this works very well for shear flows dominated by only one of the turbulent shear stresses (ANSYS Fluent Theory Guide, 2016).

4.4 The k-ε Model

The standard k-ε model has been widely used for practical engineering flow calculations since its introduction (Launder and Spalding, 1972; Launder

and Spalding, 1974). The standard k-ε turbulence model has been widely used in CFD simulations of rotary blood pumps (Chua, 2005; Anderson, 2000a; Anderson, 2000b; Song, 2004a; Miyazoe, 1999). The k-ε model is a semi-empirical approach based on transport equations for the turbulence kinetic energy k and its dissipation rate ε. The transport equation for k is derived from the exact equation, while the transport equation for ε is obtained by physical reasoning. It is a popular turbulence model in view of its robustness, computational economy and sufficient accuracy for a wide range of flows in industrial applications. In contrast, it is based on the assumption that the flow is fully turbulent and the effects of molecular viscosity are negligible. Therefore, the standard k-ε model is valid only for high Re turbulent flows (ANSYS Fluent Theory Guide, 2016). In view of its weaknesses (Mizunuma, 2007), modifications have been introduced in order to improve its performance such as the renormalisation group (RNG) k-ε model (Yakhot, 1986; Yakhot, 1992) and the realisable k-ε model (Shih, 1995). The turbulence kinetic energy k and its rate of dissipation ε are obtained from the following transport equations (Wilcox, 1998):

$$\rho \frac{\partial k}{\partial t} + \rho u_j \frac{\partial k}{\partial x_j} = \tau_{ij} \frac{\partial u_i}{\partial x_j} - \rho \varepsilon + \frac{\partial}{\partial x_j} \left[\left(\mu + \frac{\mu_T}{\sigma_k} \right) \frac{\partial k}{\partial x_j} \right] \tag{4.6}$$

and

$$\rho \frac{\partial \varepsilon}{\partial t} + \rho u_j \frac{\partial \varepsilon}{\partial x_j} = C_{\varepsilon 1} \frac{\varepsilon}{k} \tau_{ij} \frac{\partial u_i}{\partial x_j} - C_{\varepsilon 2} \rho \frac{\varepsilon^2}{k} + \frac{\partial}{\partial x_j} \left[\left(\mu + \frac{\mu_T}{\sigma_\varepsilon} \right) \frac{\partial \varepsilon}{\partial x_j} \right] \tag{4.7}$$

where ρ is the fluid density; μ is the fluid viscosity.
The turbulent (or eddy) viscosity μ_T is obtained combining k and ε as follows:

$$\mu_T = \rho C_\mu \frac{k^2}{\varepsilon} \tag{4.8}$$

The closure coefficients have the following values (Launder and Spalding, 1972):

$$C_{\varepsilon 1} = 1.44;\ C_{\varepsilon 2} = 1.92;\ C_\mu = 0.09;\ \sigma_k = 1;\ \sigma_\varepsilon = 1.3 \tag{4.9}$$

The known limitations of the standard k-ε model are: (i) poor performance for flows with larger pressure gradient, strong separation, high swirling

component and large streamline curvature; (ii) inaccurate prediction of the spreading rate of round jets; (iii) excessive production of k in regions with large strain rate such as stagnation points, resulting in very inaccurate predictions.

To overcome these limitations, the RNG k-ε model has been developed by refining the initial renormalisation group (RNG) approach (Yakhot, 1986), based on the elimination of small scales which are assumed to be isotropic, with scale expansions for the Reynolds stress and production of dissipation terms (Yakhot, 1992). The additional expansion parameter ($\eta = S\bar{K}/\bar{\varepsilon}$) is the ratio of the turbulent to mean strain time scale. The differential relation expressing total viscosity ν in terms of the kinetic energy K and the mean dissipation rate $\bar{\varepsilon}$ is (Yakhot, 1986):

$$d\frac{K}{\bar{\varepsilon}^{1/2}} = 1.7288{\nu_0}^{1/2}\frac{\hat{\nu}}{Y}d\hat{\nu} \tag{4.10}$$

where

$$\hat{\nu} = \frac{\nu}{\nu_0} \tag{4.11}$$

$$Y = (\hat{\nu}^3 + C - 1)^{1/2} \tag{4.12}$$

When $\nu/\nu_0 \gg 1$, the solution to Equation (4.10) is:

$$\nu = c_\nu K^2/\bar{\varepsilon} \tag{4.13}$$

with c_ν = 0.0837, which is quite close to the experimentally determined coefficient c_ν = 0.09.

At high Reynolds number, the transport equation for the mean dissipation rate $\bar{\varepsilon}$ becomes (Yakhot, 1986):

$$\frac{\partial\bar{\varepsilon}}{\partial t} + u_i\frac{\partial\bar{\varepsilon}}{\partial x_i} = \bar{P} - 1.7215\frac{\bar{\varepsilon}^2}{K} + \frac{\partial}{\partial x_i}\alpha_\varepsilon\nu\frac{\partial\bar{\varepsilon}}{\partial x_i} \tag{4.14}$$

with

$$\bar{P} = -1.063\frac{\bar{\varepsilon}}{K}\bar{\tau}_{ij}\frac{\partial\bar{v}_i}{\partial x_j} \tag{4.15}$$

At low Reynolds number, the transport equation for the mean dissipation rate $\bar{\varepsilon}$ becomes (Yakhot, 1986):

$$\frac{\partial \bar{\varepsilon}}{\partial t} + u_i \frac{\partial \bar{\varepsilon}}{\partial x_i} = \bar{P} - \hat{a} + \hat{b} + \frac{\partial}{\partial x_i} \alpha_\epsilon \nu \frac{\partial \bar{\varepsilon}}{\partial x_i} \quad (4.16)$$

with

$$P = -0.08889 \frac{K}{\nu} \bar{\tau}_{ij} \frac{\partial \bar{v}_i}{\partial x_j} \quad (4.17)$$

$$d\frac{\hat{a}}{\bar{\varepsilon}^{3/2}} = -0.8267 \frac{\hat{\nu}^3 d\hat{\nu}}{{\nu_0}^{1/2} Y^3} \quad (4.18)$$

$$d\frac{\hat{b}}{\bar{\varepsilon}^{3/2}} = -0.5764 \frac{d\hat{\nu}}{{\nu_0}^{1/2} Y} \quad (4.19)$$

The main difference between the RNG and the standard k-ε model is the additional dissipation term $\mathcal{R}$ in the dissipation rate transport equation (Yakhot, 1992):

$$\mathcal{R} = \frac{C_\mu \eta^3 (1-\eta/\eta_0)}{1+\beta\eta^3} \frac{\bar{\varepsilon}^2}{\bar{K}} \quad (4.20)$$

where η_0 = 4.38, β = 0.012. (4.21)

The crucial constrain is satisfied when $\bar{\varepsilon} \to 0$ leading to $\mathcal{R} \to 0$.
In the limit of weak strains where $\eta \to 0$ (Yakhot, 1992):

$$\mathcal{R} \simeq C_\mu \eta^3 (\frac{\bar{\epsilon}^2}{\bar{K}}) \to 0 \quad (4.22)$$

In the limit of strong strains where $\eta \to \infty$ (Yakhot, 1992):

$\mathcal{R} \simeq -\frac{C_\mu}{\beta} \frac{\eta}{\eta_0} \frac{\bar{\varepsilon}^2}{\bar{K}}$, which becomes singular (4.23)

The increased responsiveness to the effects of rapid strain and streamline curvature explains the superior performance of the RNG model compared to the standard k-ε model.
The realisable k - ε model is an additional variant, which contains an alternative formulation for the turbulent viscosity and a modified equation for the dissipation rate ε derived from an exact equation for the transport of the mean square vorticity fluctuation (Shih, 1995). Combining the Boussinesq

relationship (equation 7.5) and the eddy viscosity definition (equation 7.8), the following expression for the normal Reynolds stress in an incompressible strained mean flow is obtained:

$$\overline{u^2} = \frac{2}{3}k - 2\nu_t \frac{\partial U}{\partial x} \tag{4.24}$$

The realisable k-ε model adopts a new formulation for the eddy viscosity involving the original variable C_μ (Reynolds, 1987) and a new model equation for the dissipation, ε, based on the dynamic equation of the mean-square vorticity fluctuation. One limitation of the realisable k-ε model is the generation of non physical turbulent viscosities in settings when the computational domain contains both rotating and stationary fluid zones (multiple reference frames and rotating sliding meshes). This is related to the inclusion of the effects of mean rotation in the definition of the turbulent viscosity.

The realisable k-ε model has been extensively validated for a wide range of flows including rotating homogeneous shear flows, free flows and separated flows (Shih, 1995; Kim, 1997). Bearing in mind equation (7.8) for the eddy viscosity, the key difference between the realisable k-ε model and the other two models is that C_μ is not a constant and its expression is (Shih, 1995):

$$C_\mu = \frac{1}{A_0 + A_s \frac{kU^{(*)}}{\varepsilon}} \tag{4.25}$$

where

$$U^{(*)} \equiv \sqrt{S_{ij}S_{ij} + \tilde{\Omega}_{ij}\tilde{\Omega}_{ij}} \tag{4.26}$$

with

$$\tilde{\Omega}_{ij} = \Omega_{ij} - 2\varepsilon_{ijk}\omega_k \tag{4.27}$$

$$\Omega_{ij} = \bar{\Omega}_{ij} - \varepsilon_{ijk}\omega_k \tag{4.28}$$

where $\bar{\Omega}_{ij}$ is the mean rate-of-rotation tensor viewed in a moving reference frame with angular velocity ω_k. The value for the model constants is:

$$A_0 = 4 \qquad A_s = \sqrt{6}\cos\phi \tag{4.29}$$

where

$$\phi = \frac{1}{3}\cos^{-1}(\sqrt{6}W) \tag{4.30}$$

$$W = \frac{S_{ij}S_{jk}S_{ki}}{\tilde{S}^3} \tag{4.31}$$

$$\tilde{S} = \sqrt{S_{ij}S_{ij}} \tag{4.32}$$

C_μ is a function of the mean strain and rotation rates, the angular velocity of the system rotation, and the turbulence fields k and ε.

4.5 The k-ω Model

The standard k-ω model is an empirical model (Wilcox, 1998), subsequently modified (Wilcox, 2008), which takes into account the effects of a low Reynolds number, compressibility and shear flow spreading. The disadvantage is its strong sensitivity to free-stream conditions (Menter, 2009). The model is based on transport equations for the turbulence kinetic energy, k, and the specific dissipation rate, ω, which can be considered as the ratio of ε to k.

The mathematical formulation of the model equations is as follows (Wilcox, 1998):

$$\rho\frac{\partial k}{\partial t} + \rho u_j\frac{\partial k}{\partial x_j} = \tau_{ij}\frac{\partial u_i}{\partial x_j} - \beta^*\rho k\omega + \frac{\partial}{\partial x_j}\left[(\mu + \sigma^*\mu_T)\frac{\partial k}{\partial x_j}\right] \tag{4.33}$$

and

$$\rho\frac{\partial \omega}{\partial t} + \rho u_j\frac{\partial \omega}{\partial x_j} = \alpha\frac{\omega}{k}\tau_{ij}\frac{\partial u_i}{\partial x_j} - \beta\rho\omega^2 + \frac{\partial}{\partial x_j}\left[(\mu + \sigma\mu_T)\frac{\partial \omega}{\partial x_j}\right] \tag{4.34}$$

The turbulent viscosity, μ_T, is derived by combining k and ω as follows:

$$\mu_T = \frac{\rho k}{\omega} \tag{4.35}$$

The values for the closure coefficients are:

α = 5/9; β = 3/40; β^* = 9/100; σ = 1/2; σ^* = 1/2 (4.36)

The baseline (BSL) k-ω model (Menter, 1994) is another variant, which combines the robust and accurate formulation of the k-ω model in the near-wall region with the free-stream independence of the k-ε model in the outer part of the boundary layer. Therefore, the k-ε model is converted into a k-ω formulation. Then, the standard k-ω model and the transformed k-ε model are multiplied by a blending function and added together. The blending function equals one in the near-wall region, which activates the standard k-ω model, and zero away from the surface, which activates the transformed k-ε model. The BSL model also includes an additional cross-diffusion term in the ω- equation. Finally, the modelling constants are different (Menter, 1994). The equations are as follows (Menter, 1994; Menter, 2009):

$$\rho\frac{\partial k}{\partial t}+\rho u_i\frac{\partial k}{\partial x_i}=\tau_{ij}\frac{\partial u_i}{\partial x_j}-\beta^*\rho\omega k+\frac{\partial}{\partial x_j}\left[(\mu+\sigma_k\mu_T)\frac{\partial k}{\partial x_j}\right] \quad (4.37)$$

$$\rho\frac{\partial \omega}{\partial t}+\rho u_i\frac{\partial \omega}{\partial x_i}=\frac{\gamma}{\nu_t}\tau_{ij}\frac{\partial u_i}{\partial x_j}-\beta\rho\omega^2+\frac{\partial}{\partial x_j}\left[(\mu+\sigma_\omega\mu_T)\frac{\partial \omega}{\partial x_j}\right]+$$
$$2(1-F_1)\rho\sigma_{\omega 2}\frac{1}{\omega}\frac{\partial k}{\partial x_j}\frac{\partial \omega}{\partial x_j} \quad (4.38)$$

The shear-stress transport (SST) k-ω model (Menter, 1994; Menter, 2009) accounts for the transport of the turbulence shear stress and therefore it is more accurate and reliable for a wider class of flows compared to the standard and baseline models. . A production limiter is used in the SST model to prevent the development of turbulence in stagnation regions (Menter, 2009).

The (SST) k-ω model is based on the same equations but different constant coefficients. Additional modifications include the use of the strain rate S in the definition of eddy viscosity ν and the use of a factor 10 in the production limiter as follows (Menter, 2009):

$$\nu_t=\frac{a_1 k}{\max(a_1\omega, SF_2)} \quad (4.39)$$

$$S=\sqrt{2S_{ij}S_{ij}} \quad (4.40)$$

$$F_1=\tanh\{\{\min\left[\max\left(\frac{\sqrt{k}}{\beta^*\omega y},\frac{500\nu}{y^2\omega}\right),\frac{4\rho\sigma_{\omega 2}k}{CD_{k\omega}y^2}\right]\}^4\} \quad (4.41)$$

$$F_2 = \tanh[[\max\left(\frac{2\sqrt{k}}{\beta^*\omega y}, \frac{500\nu}{y^2\omega}\right)]^2] \quad (4.42)$$

$$CD_{kw} = \max\left(2\rho\sigma_{\omega 2}\frac{1}{\omega}\frac{\partial k}{\partial x_i}\frac{\partial \omega}{\partial x_i}, 10^{-10}\right) \quad (4.43)$$

where k is the turbulence kinetic energy, ω is the turbulence frequency, y is the distance to the nearest wall, S is the invariant measure of the strain rate, ρ is the density and u_i is the flow velocity. F_1 and F_2 are blending functions, which equal zero away from the surface and one inside the boundary layer. Another model enhancement is the inclusion of the effects of streamline curvature and system rotation (Smirnov and Menter, 2009).

4.6 The Reynolds Stress (RSM) Model

The RSM model is based on the transport equations for the individual Reynolds stress anisotropies in contrast to the Boussinesq hypothesis. It is also named as second-order closure model where the second order correlations for the fluctuating velocity components are computed whilst the higher correlations are modelled. Six additional partial differential equations are solved to describe Reynolds stresses and the flow properties. The extra transport equations include terms for production, dissipation, diffusion, turbulent pressure-strain interactions and rotations (Chipongo, 2020; Wallin and Johansson, 2000; Bosco, 2009). The transport equation for the Reynolds stresses R_{ij} can be written as follows (Bosco, 2009):

$$\frac{\partial}{\partial t}\left(\bar{\rho}\tilde{R}_{ij}\right) + \frac{\partial}{\partial x_k}(\bar{\rho}\tilde{U}_k\tilde{R}_{ij} = \bar{\rho}P_{ij} + \bar{\rho}\prod_{ij} - \bar{\rho}\epsilon_{ij} + \bar{\rho}D_{ij} + \bar{\rho}M_{ij} \quad (4.44)$$

where

$$\bar{\rho}P_{ij} = -\bar{\rho}\tilde{R}_{ik}\frac{\partial \tilde{U}_j}{\partial x_k} - \bar{\rho}\tilde{R}_{jk}\frac{\partial \tilde{U}_i}{\partial x_k} \quad (4.45)$$

is the production term, which does not need modelling because it depends on quantities requiring an equation to be solved. The other terms require modelling and they are identified as follows:

$\bar{\rho}\prod_{ij} = \overline{p'(\frac{\partial u_i^{"}}{\partial x_j} + \frac{\partial u_j^{"}}{\partial x_i})}$ is the redistribution term; (4.46)

$\bar{\rho}\epsilon_{ij} = \overline{\tau'_{\iota k}\frac{\partial u_J^{"}}{\partial x_k} + \tau'_{Jk}\frac{\partial u_\iota^{"}}{\partial x_k}}$ is the destruction term (4.47)

$\bar{\rho}D_{ij} = -\frac{\partial}{\partial x_k}[\overline{\rho u_\iota^{"} u_J^{"} u_k^{"}} + (\overline{p' u_\iota^{"}}\delta_{jk} + \overline{p' u_J^{"}}\delta_{ik}) - (\overline{\tau'_{\iota k} u_J^{"} + t'_{Jk} u_\iota^{"}})]$ is the diffusion term (4.48)

$\bar{\rho}M_{ij} = \overline{u_\iota^{"}}\left(\frac{\partial \bar{\tau}_{Jk}}{\partial x_k} - \frac{\partial \bar{p}}{\partial x_j}\right) + \overline{u_J^{"}}(\frac{\partial \bar{\tau}_{\iota k}}{\partial x_k} - \frac{\partial \bar{p}}{\partial x_\iota})$ is the contribution of the turbulent mass flux due to the compressibility effects. (4.49)

Despite the additional complexity and increased computational power requirements, the RSM model does not show significant improvement or advantage in comparison to other RANS models (Chipongo, 2019).

4.7 Laminar-Turbulent Transition Model

The Transition SST model (also known as γ - Re_θ model) solves two additional transport equations and includes experimental correlations to trigger the onset of transition. This model has been validated against a wide range of experimental data and used successfully in many industrial CFD simulations (Menter, 2011). The transition SST model is only applicable to wall-bounded flows.

4.8 Scale-Resolving Simulation (SRS) Models

SRS models enable a portion of the turbulence spectrum to be resolved in at least a portion of the numerical domain. Some of these models are described below.

4.8.1 Large Eddy Simulation (LES)

LES resolve large turbulent structures in space and time down to the grid limit everywhere in the flow. LES modelling requires excessive high resolution for wall boundary layers. The largest scales in the turbulent spectrum are geometrically very small near the wall and require a very fine grid and a small time step. Unlike RANS, the grid cannot be refined only in the wall normal direction but must also resolve turbulence in the wall parallel plane. This can be achieved only for flows at very low Reynolds number and on very small geometric scales. Therefore, LES modelling is recommended for flows where boundary layers are not relevant without the need to be resolved or for flows where the boundary layers are laminar due to a low Reynolds number. LES falls between DNS and RANS in terms of the

fraction of the resolved scales. Resolving only the large eddies allows the use of much coarser mesh and larger time-step sizes in LES than in DNS. Nevertheless, LES still requires significantly finer meshes than those used for RANS calculations. Therefore, LES modelling is computationally far more expensive than steady RANS calculations and requires high-performance parallel computing (ANSYS Fluent Theory Guide, 2016).

LES filters the Navier-Stokes equations over a finite spatial region (the grid volume) and aims at resolving the portions of turbulence larger than the filter width. Turbulence structures smaller than the filter are then modelled according to a simple eddy viscosity approach (Menter, 2015).

The filtering operation is defined as:

$$\bar{\Phi} = \int_{-\infty}^{\infty} \Phi(\vec{x}')G(\vec{x} - \vec{x}')d\vec{x} \qquad \int_{-\infty}^{\infty} G(\vec{x} - \vec{x}')d\vec{x} = 1 \quad (4.50)$$

where G is the spatial filter. If density fluctuations are neglected, filtering the Navier-Stokes equations gives the following form:

$$\frac{\partial \rho \bar{U}_i}{\partial t} + \frac{\partial \rho \bar{U}_j \bar{U}_i}{\partial x_j} = -\frac{\partial P}{\partial x_i} + \frac{\partial}{\partial x_j}(\bar{\tau}_{ij} + \tau_{ij}^{LES}) \quad (4.51)$$

The equations have an additional stress term due to the filtering operation:

$$\tau_{ij}^{LES} = \rho \bar{U}_i \bar{U}_j - \rho \overline{U_i U_j} \quad (4.52)$$

Although derived in a different way, the additional sub-grid stress tensor is modelled as in RANS using an eddy viscosity model:

$$\tau_{ij}^{LES} = \mu_t \left(\frac{\partial \bar{U}_i}{\partial x_j} + \frac{\partial \bar{U}_j}{\partial x_i}\right) \quad (4.53)$$

The practical implication of this approach is that the modelled momentum equations for RANS and LES are identical if an eddy viscosity model is used in both cases. The only information obtained from the turbulence model is the level of the eddy viscosity (Menter, 2015). The aim of LES modelling is to provide sufficient damping for the smallest (unresolved) scales based on a simple algebraic formulation. The most widely used LES model is the following (Smagorinsky, 1963):

$$\mu_t = \rho(C_s \Delta)^2 S \quad (4.54)$$

where Δ is a measure of the grid spacing the numerical mesh, S is the strain rate scalar and C_s is a constant. The disadvantage of the Smagorinsky model is that its eddy-viscosity is not zero for laminar shear flows ($\partial U/\partial y \neq 0$). Therefore, a near-wall damping function is required in the viscous sublayer. A LES formulation which gives zero eddy-viscosity for simple laminar shear flows is more appropriate, particularly in the context of flows with laminar turbulent transition where the Smagorinsky model negatively affects the laminar flow (Menter, 2015). The WALE (Wall-Adapting Local Eddy-viscosity) model and dynamic LES give this option. The simplicity of equation (7.54) suggests that LES models may not provide a highly accurate representation of the smallest scales. Modelling the dissipation of the smallest resolved scales is a more appropriate target for LES. If $E(\kappa)$ is the turbulence energy as a function of wave number κ, small κ values represent large eddies and large κ values represent small eddies. Turbulence is dissipated into heat at the smallest scales by viscosity in in a fully resolved simulation (DNS) as follows:

$$\varepsilon_{DNS} = \nu \frac{\partial U_i}{\partial x_j} \frac{\partial U_i}{\partial x_j} \tag{4.55}$$

where ν is a very small kinematic molecular viscosity. The dissipation ε_{DNS} maintains a finite value as the velocity gradients of the smallest scales are very large.

LES computations are usually performed on numerical grids that are too coarse to resolve the smallest scales. Therefore, the velocity gradients of the smallest resolved scales in LES are much smaller than those at the DNS limit. The molecular viscosity is not enough to provide the correct level of dissipation, which is achieved by increasing the viscosity using an eddy-viscosity as follows:

$$\varepsilon_{LES} = \nu_t \frac{\partial \bar{U}_i}{\partial x_j} \frac{\partial \bar{U}_i}{\partial x_j} \tag{4.56}$$

LES does not model the influence of unresolved small scale turbulence on the larger resolved scale but the dissipation of turbulence into heat (Menter, 2015).

LES modelling may be suitable for low Reynolds numbers where wall boundary layers are likely laminar and turbulence occurs only in separated shear layers and detached flow regions. If the turbulence to molecular

viscosity ratio R (μ_t/μ) is low inside the boundary layers, then laminar flow is a reasonable assumption and no resolution of near-wall turbulence is required (Menter, 2015).

4.8.2 Scale-Adaptive Simulation (SAS)

SAS models behave like standard RANS models in steady flows but they allow formation of a broadband turbulence spectrum for certain types of unstable flows (Rotta, 1972; Menter and Egorov, 2010; Egorov, 2010). This method is based on the von Karman length scale L_{vK}, which allows adjustment to resolved structures in the simulation and reduction of the eddy viscosity. The SAS model relies on instability of the flow to generate resolved turbulence; in the absence of instability, the model remains in RANS mode (Menter, 2011; Menter, 2015). The original SAS model (Menter and Egorov, 2010) is based on a two-equation approach with the variable Φ = $\sqrt{k}L_t$ for the scale equation (Menter, 2015):

$$\frac{\partial(\rho k)}{\partial t}+\frac{\partial(\rho \bar{U}_j)}{\partial x_j}=P_k-c_\mu^{3/4}\rho\frac{k}{\Phi^2}+\frac{\partial}{\partial x_j}\left(\frac{\mu_t}{\sigma_k}\frac{\partial k}{\partial x_j}\right) \quad (4.57)$$

$$\frac{\partial(\rho\Phi}{\partial t}+\frac{\partial(\rho \bar{U}_j\Phi)}{\partial x_j}=\frac{\Phi}{k}P_k\left(\zeta_1-\zeta_2\left(\frac{L_t}{L_{vK}}\right)^2\right)-\zeta_3\rho k+\frac{\partial}{\partial x_j}\left(\frac{\mu_t}{\sigma_\Phi}\frac{\partial\Phi}{\partial x_j}\right) \quad (4.58)$$

$$L_{vK}=\kappa\left|\frac{\bar{U}'}{\bar{U}''}\right|;\quad \bar{U}'=S=\sqrt{2S_{ij}S_{ij}};\quad \bar{U}''=\sqrt{\frac{\partial^2\bar{U}_i}{\partial x_j\partial x_j}\frac{\partial^2\bar{U}_i}{\partial x_k\partial x_k}};\quad S_{ij}=\frac{1}{2}\left(\frac{\partial\bar{U}_i}{\partial x_j}+\frac{\partial\bar{U}_j}{\partial x_i}\right);$$
$$L_t=\frac{\Phi}{\sqrt{k}} \quad (4.59)$$

The L_{vK} term can be transformed and implemented into any other scale-defining equation resulting in SAS capabilities. The SAS model remains in steady RANS mode for wall bounded flows but switches to SRS mode in flows with large and unstable separation zones (Menter, 2015).

4.8.3 Detached Eddy Simulations (DES)

DES is a hybrid formulation that switches between RANS and LES based on the grid resolution provided. The wall boundary layers are completely addressed by the RANS model while the free shear flows away from the wall are computed in LES mode.
The two-equation formulation is:

$$\frac{\partial(\rho k)}{\partial t}+\frac{\partial(\rho \bar{U}_j k)}{\partial x_j}=P_k-\rho\frac{k^{3/2}}{\min\left(L_t,C_{DES}\Delta_{max}\right)}+\frac{\partial}{\partial x_j}\left(\left(\mu+\frac{\mu_t}{\sigma_k}\right)\frac{\partial k}{\partial x_j}\right) \quad (4.60)$$

$$L_t = \frac{k^{3/2}}{\varepsilon} = \frac{\sqrt{k}}{\beta^* \omega} \quad (4.61)$$

The model runs in RANS mode for attached flow regions but it switches to LES mode in detached regions away from the wall (Menter, 2015).

4.8.4 Wall-Modelled LES (WMLES)

WMLES addresses the limitations of LES for high Reynolds number boundary layers. A simple and promising approach is based on a reformulation of the length scale used in LES zone and by blending it with the mixing length (RANS) model in the inner part of the boundary layer. The log-layer mismatch can be reduced to a relatively small shift at the RANS-LES interface leading to a high quality solution even at very high Reynolds numbers (Menter, 2011).

4.8.5 Zonal RANS-LES Models

When flow instabilities to generate turbulent structures in large separated regions are absent or not reliable, RANS and LES models are applied to predefined zones providing clearly defined interfaces between them. At the interface, the turbulent kinetic energy from the upstream RANS model is converted to resolved scales at an internal boundary to the LES zone. The LES zone will be limited to the region of interest for which unsteady results are required (Menter, 2011).

4.9 Design Optimisation

There is a clear difference between design improvement and optimisation. Design improvement is a manual process requiring heuristic knowledge and human interaction (Behbahani, 2009). This is often done using a sophisticated trial and error approach where CFD analysis is used over a range of designs to select the most appropriate for further development (Fraser, 2011). The impeller is an essential element but its optimum design is not necessarily intuitive because multiple parameters affect the overall pump performance such as pressure rise, efficiency, washout and leakage flow rates, torque and haemolysis. In magnetically levitated pumps, the impeller and the pump housing are separated by a clearance gap which is a secondary flow channel where high shear rates and potentially long residence time may occur (Fraser, 2011). Reducing the clearance gap is beneficial for pump efficiency although at the expense of increased shear rates (Miyazoe, 1999; Anderson, 2000a; Anderson, 2000b). Design

optimisation is an iterative and systematic approach where numerical simulation is coupled with parameter optimisation techniques. The flow field is solved for the initial design and subsequently the pump parameters are automatically adjusted according to values for efficiency, shear stress, recirculation and additional parameters considered important for the desired outcome (Antaki, 1995; Burgreen, 2001; Wu, 2005). This is a fully automated process where only limited human interaction is required. The aim is an optimal compromise between competing design criteria by defining objective functions and a corresponding performance index. The main challenges consist in finding enhanced models to describe blood flow and adequate automated algorithms for shape changes in response to computed flow features. Design optimisation can also be used successfully for the analysis of steady and unsteady blood flow in synthetic arterial grafts (Abraham, 2005a; Abraham, 2005b) with particular reference to the outflow graft of a left ventricular assist device (Bonnemain, 2013).

4.10 VADs Performance Predictions

CFD simulations are usually performed considering typical operating conditions: 5-6 *L/min* at 100 *mmHg* aortic pressure for a LVAD; 4 *L/min* at 40 *mmHg* pulmonary artery pressure for a RVAD (Wood, 2005; Behbahani, 2009). CFD analysis of steady state flow conditions is a convenient and widely used approach to assess pump performance although transient flow simulations allow more realistic calculations of the velocity and pressure fluctuations within the pump and may enhance the ability to predict device performance in a clinical setting (Wood, 2005). Two primary transient flow conditions can be used: time-varying boundary conditions, where the inlet boundary condition is specified as pulsed ventricular pressure to simulate varying pressure due to ventricular contraction, and transient rotational sliding interfaces, where the impeller interfaces rotate and slide to simulate virtual blade rotation and capture the blade frequency components (Song, 2003b; Song, 2004b; Wood, 2005; Throckmorton, 2013). Simulations combining time-varying boundary conditions and transient rotational sliding interfaces give the most realistic transient conditions in VADs although significantly more computational power is required. The analysis of flow and velocity profile at different rotational speed gives information about potential areas of irregular flow patterns (Wood, 2005). Design parameters such as clearance gap size, blades number and shroud design have an impact on shear stress exposure and flow stagnation in terms of blood damage and thrombosis potential (Wiegmann, 2018; Kumar, 2016).

4.11 Results Validation

Appropriate input for CFD calculations and analysis is of paramount importance to avoid unreliable and misleading results (Stewart, 2009). Validation is required to ascertain the accuracy of the model used and reduce uncertainty. A simulation is validated when a small difference is observed between its results and experimental data with low uncertainty (Versteeg, 2007).

The significant amount of validation studies available for industrial type pumps are not necessarily suitable for CFD analysis used in blood pumps given the difference in size, speed, flow rates and working fluid conditions (Fraser, 2011).

Validation is usually performed *in vitro* and based on non-invasive optical techniques of flow visualization for qualitative information and particle image velocimetry (Bearnson, 2006; Burgreen, 2004; Wu, 2001; Konig, 1999) or laser Doppler anemometry for quantitative measurements (Day, 2001; Day, 2002; Nishida, 2002; Triep, 2006; Medvitz, 2007; Chua, 2008). Magnetic resonance imaging (MRI) has the potential to investigate VADs flow field *in vivo* (Markl, 2007; Lorenz, 2012) although the majority of current devices are not MRI compatible.

A collaborative effort is currently in place to evaluate two benchmark models for the development of standardised methods aimed at validation of CFD simulations and damage predictions in blood recirculating devices. Models of blood flow through typical device components have been tested in multiple laboratories to provide robust experimental data on blood flow velocities, pressures and haemolysis. The results have shown some differences between simulated and measured blood flow values; specific regions of the device models where discrepancies tended to occur have been identified (Malinauskas, 2017; Hariharan, 2017).

4.12 Chapter Summary

VADs operate in the transitional region at the boundary of laminar and turbulent flow (low Reynolds number). Blood behaviour during this transition remains not completely understood and difficult to simulate. Assuming a Newtonian behaviour for the blood and neglecting the influence of red blood cells (RBCs) is convenient for the purposes of simulations but it may lead to incorrect predictions during the transition phase. CFD has played a key role in the advancement of our understanding of VADs rheology and haemodynamics. RANS models have been widely used for this purpose. More specifically, the k-ω SST model has attracted attention in view of its

low Reynolds number correction. LES modelling has shown potential for VADs application although more computational demanding than RANS approach. Validation of CFD simulations remains of paramount importance to avoid unreliable and misleading results. Benchmark models are under investigation for the development of standardised methods aimed at validation of CFD simulations and damage predictions in blood recirculating devices.

Chapter 5

Haemodynamics and Rheology in Blood Recirculating Devices

5 Haemodynamics and Rheology in Blood Recirculating Devices

5.1 Introduction

Theoretical models of the coagulation system are usually based on systems of equations describing specific dynamic processes. Models based on ordinary differential equations (ODE) assume well-mixed quantities where changes occur as a function of time without spatial variations. Models based on partial differential equations (PDE) consider both time and space variations. Significant progress has been made in the identification of the players; less progress has been made in the understanding of how flow-mediated transport and platelet deposition may affect thrombus formation. Theoretical models accounting for biochemical, biophysical and biomechanical factors give a more comprehensive view of thrombus formation. Theoretical predictions in the context of in vitro and in vivo experimental evaluation may well lead to a better understanding of the interactions involved in the coagulation system and their mechanism (Leiderman and Fogelson, 2014). An overview of key theoretical models is given as a prelude to thrombus formation in rotary blood pumps and its potential solution.

5.2 Blood Rheology

The complexity of blood rheology can usually be ignored during CFD simulations because VADs shear rates are considered high enough to fall in the shear independent range. Blood is usually considered a Newtonian fluid in VADs calculations because of the high shear rates, as its viscosity remains constant for shear rates above 100 s^{-1}. The shear thinning property of blood becomes important at low rotational speeds and low flow rates where the pressure rise generated with a shear thinning fluid is lower than the one generated with a Newtonian fluid (Fraser, 2011). The use of generalised Newtonian models of blood rheology may lead to better predictions of the continuum properties of flow in VADs.

The equations describing the isothermal flow of an incompressible viscous fluid in a domain $\Omega \subset \mathbb{R}^3$ are derived from the law of conservation of mass and linear momentum (Sequeira, 2007a; Sequeira, 2007b):

$$\begin{cases} \rho \dfrac{\partial \boldsymbol{u}}{\partial t} + \rho(\boldsymbol{u}\cdot\nabla)\boldsymbol{u} = \nabla\cdot\boldsymbol{T}_f + f \\ \nabla\cdot\boldsymbol{u} = 0 \end{cases} \tag{5.1}$$

where $\boldsymbol{u}$ is the flow velocity vector, ρ is the constant fluid density and f are the external body forces per unit volume. The fluid Cauchy stress tensor $\boldsymbol{T}_f$ is a combination of an isotropic pressure p and the viscous contribution as follows:

$$\boldsymbol{T}_f = -p\boldsymbol{I} + 2\mu\boldsymbol{D} \tag{5.2}$$

where μ is the constant dynamic viscosity and $\boldsymbol{D}$ is the rate of deformation tensor:

$$\boldsymbol{D} = \frac{1}{2}\left(\nabla\boldsymbol{u} + \left(\nabla\boldsymbol{u}\right)^T\right) \tag{5.3}$$

Assuming that the Cauchy stress tensor depends only on the fluid mass density and the velocity gradient with invariance under a superimposed rigid motion (Sequeira, 2007a), the most general form is given by the following expression:

$$\boldsymbol{T}_f = \phi_0\boldsymbol{I} + \phi_1\boldsymbol{D} + \phi_2\boldsymbol{D}^2 \tag{5.4}$$

where $\boldsymbol{D}$ is the symmetric part of the velocity gradient and ϕ_0, ϕ_1, ϕ_2 depend on the density ρ and on the three principal invariants of $\boldsymbol{D}$: $I_D = tr(\boldsymbol{D})$, $II_D = ((tr\boldsymbol{D})^2 - tr(\boldsymbol{D}^2))/2$ and $III_D = \det(\boldsymbol{D})$.
For an incompressible fluid where the stress tensor depends only on the velocity gradient, the generalised form becomes (Sequeira, 2007a):

$$\boldsymbol{T}_f = \alpha\boldsymbol{I} + \phi_1\boldsymbol{D} + \phi_2\boldsymbol{D}^2 \tag{5.5}$$

where α is a Lagrange multiplier related to the incompressibility constraint with ϕ_1 and ϕ_2 only dependent on II_D and III_D. This is typical of Reiner-Rivlin fluids. Instead, $\phi_2 = 0$ and ϕ_1 constant is typical of Newtonian fluids, while a negligible dependence of ϕ_1 on III_D is typical of generalised Newtonian fluids. Their behaviour analysis under simple shear and thermodynamic considerations gives the following expression for $\boldsymbol{T}_f$:

$$\boldsymbol{T}_f = -p\boldsymbol{I} + 2\mu\cdot\dot{\gamma}\boldsymbol{D} \tag{5.6}$$

where $\dot{\gamma} = \sqrt{2\boldsymbol{D}:\boldsymbol{D}}$ is the shear rate and $\mu(\cdot)$ is the prescribed viscosity law, intended to fit experimental data.

The power-law model is a simple example of a generalised Newtonian fluid model based on the following expression:

$$\mu\dot{\gamma} = k\dot{\gamma}^{(n-1)} \tag{5.7}$$

where k is the consistency coefficient or flow consistency index and n is the flow behaviour index. When n = 1 and $\mu = k$, the fluid has a Newtonian behaviour. When $n < 1$, the fluid has a shear thinning behaviour. When $n >$ 1, the fluid has a shear thickening behaviour. The power-law model allows different solutions of the governing equations. The disadvantage is that the zero shear rate viscosity is unbounded for the shear thinning behaviour and the asymptotic limit is zero when $\dot{\gamma} \to \infty$. This behaviour is unphysical and limits the application of the power-law model to blood flow (Robertson, 2009). The parameters values obtained by fitting experimental data of the human blood are (Cho, 1991): n = 0.61, k = 0.42.

The Carreau model is an alternative option based on the following expression:

$$\frac{\mu\dot{\gamma}-\mu_\infty}{\mu_0-\mu_\infty} = \left[1 + (\lambda\dot{\gamma})^2\right]^{\frac{(n-1)}{2}} \tag{5.8}$$

where λ is the relaxation time and the constants μ_0 and μ_∞ are the asymptotic viscosities at zero and infinity shear rates (Sequeira, 2007a):

$$\mu_0 = \lim_{\dot{\gamma}\to 0} \mu\dot{\gamma} \quad \mu_\infty = \lim_{\dot{\gamma}\to\infty} \mu\dot{\gamma} \tag{5.9}$$

When $\dot{\gamma} \ll \frac{1}{\lambda}$ (low shear rate), Carreau fluid behaves as a Newtonian fluid; when $\dot{\gamma} \gg \frac{1}{\lambda}$ (high shear rate), Carreau fluid behaves as a power-law fluid. The parameters for human blood are (Cho, 1991): λ = 3.313 *s*, μ_0 = 0.056 *Pa·s*, μ_∞ = 0.0035 *Pa·s,* n = 0.3568.

The Carreau-Yasuda model is a more realistic approach for a generalised Newtonian fluid where viscosity depends on the shear rate according to the following equation:

$$\frac{\mu\dot{\gamma}-\mu_\infty}{\mu_0-\mu_\infty} = \left[1 + (\lambda\dot{\gamma})^a\right]^{\frac{(n-1)}{a}} \tag{5.10}$$

The parameter a determines the transition between Newtonian and power-law fluid. For human blood, the parameters are (Cho, 1991): λ = 1.902 *s*, μ_0 = 0.056 *Pa·s*, μ_∞ = 0.00345 *Pa·s*, n = 0.22, a = 1.25.

The Casson model is another option described by the following equation:

$$\boldsymbol{\tau}^{\frac{1}{2}} = \boldsymbol{\tau}_y{}^{\frac{1}{2}} + s \cdot (\dot{\gamma})^{\frac{1}{2}} \tag{5.11}$$

where τ is the shear stress magnitude, τ_y is the yield stress (0.04 *dyn·cm*$^{-2}$ for normal blood at 37 *ºC*) and s is a constant. The yield stress is the minimum force that must be applied to stagnant blood before it will flow. Its effect on blood flow is small.

None of the above models can describe the viscoelastic response of blood. The elastic effects in non-Newtonian fluids can be accounted for by considering the constitutive equation for Maxwell fluid (Sequeira, 2007a):

$$\boldsymbol{S} + \lambda_1 \overset{\nabla}{\boldsymbol{S}} = 2\mu_0 \boldsymbol{D} \qquad\qquad \boldsymbol{T}_f = -p\boldsymbol{I} + \boldsymbol{S} \tag{5.12}$$

where $\boldsymbol{S}$ is the extra-stress tensor and ∇ is the upper convected derivative of a tensor field defined as follows:

$$\overset{\nabla}{\boldsymbol{S}} = \frac{\partial \boldsymbol{S}}{\partial t} + (\boldsymbol{u}\cdot\nabla)\boldsymbol{S} - (\boldsymbol{S}\cdot\nabla\boldsymbol{u}) - (\nabla\boldsymbol{u})^T \cdot \boldsymbol{S} \tag{5.13}$$

The constant $\lambda_1 > 0$ is the stress relaxation time: the larger λ_1 is, the slower is the relaxation; the material constant μ_0 is the zero shear rate viscosity coefficient.

The Oldroyd-type models are frequently used with particular reference to Oldroyd-B type; their general formulation is as follows:

$$\boldsymbol{S} + \lambda_1 \overset{\nabla}{\boldsymbol{S}} = 2\mu_0 \left(\boldsymbol{D} + \lambda_2 \overset{\nabla}{\boldsymbol{D}} \right) \tag{5.14}$$

where λ_2 is the relaxation time, with $0 \le \lambda_2 < \lambda_1$.

The total extra-stress tensor $\boldsymbol{S}$ is decomposed into a non-Newtonian (polymeric) ($\boldsymbol{S}_1$) and a Newtonian (solvent) ($\boldsymbol{S}_2$) component:

$$\boldsymbol{S} = \boldsymbol{S}_1 + \boldsymbol{S}_1 \qquad \boldsymbol{S}_1 + \lambda_1 \overset{\nabla}{\boldsymbol{S}} = 2\mu_1 \boldsymbol{D} \qquad \boldsymbol{S}_2 = 2\mu_2 \boldsymbol{D} \tag{5.15}$$

where μ_1 is the elastic viscosity and μ_2 is the Newtonian viscosity, related as follows:

$$\mu_0 = \mu_1 + \mu_2 \qquad \lambda_2 = \frac{\mu_2 \lambda_1}{\mu_0} \tag{5.16}$$

If $\lambda_2 = 0$ the model reduces to a Maxwell fluid, while if $\lambda_1 = \lambda_2 = 0$ we obtain a Newtonian fluid with viscosity μ_0.

Substituting Eq. (5.15) into the constitutive Eq. (5.14) and taking into account the conservation of linear momentum and mass, the equations of motion of an Oldroyd-B fluid can be written as:

$$\begin{cases} \rho \dfrac{\partial \boldsymbol{u}}{\partial t} + \rho (\boldsymbol{u} \cdot \nabla) \boldsymbol{u} - \mu_2 \nabla \boldsymbol{u} + \nabla p = \nabla \cdot \boldsymbol{S}_1 \\ \nabla \cdot \boldsymbol{u} = 0 \\ \boldsymbol{S}_1 + \lambda_1 \left(\dfrac{\partial \boldsymbol{S}_1}{\partial t} + \boldsymbol{u} \cdot \nabla \boldsymbol{S}_1 - \boldsymbol{S}_1 \cdot \nabla \boldsymbol{u} - \nabla \boldsymbol{u}^T \cdot \boldsymbol{S}_1 \right) = 2 \mu_1 \boldsymbol{D} \end{cases} \tag{5.17}$$

in $\Omega_t \subset \mathbb{R}^3$, with $t \in (t_0, T)$.

The governing equations of an Oldroyd-B type model have a mixed parabolic-hyperbolic nature. Usually, the constitutive equations of non-Newtonian viscoelastic fluids lead to highly nonlinear systems of partial differential equations requiring specific solution techniques for their analysis in different geometries (Arada, 2003; Anand, 2013).

5.3 Haemolysis

Haemolysis occurs when a cell is exposed to an amount of shear stress above a critical threshold (Leverett, 1972). Flow-induced haemolysis is an important aspect in the design of blood recirculating devices. Different models are available, which are suitable for CFD analysis. If the local instantaneous haemolysis is a direct function of the local instantaneous shear stress, then the model is "stress-based" and relies on empirical relations. If local instantaneous haemolysis involves a combination of intermediate variables and parameters, then the model is "strain-based". These models rely either on a Lagrangian particle-tracking approach or on the Eulerian transport equations (Yu, 2017).

The power-law equation model directly relates haemolysis, magnitude of shear stress τ and exposure time t to the shear stress according to the following original formulation (Giersiepen, 1990):

$$H(\tau,t) = C \cdot \tau^{\alpha} \cdot t^{\beta} \tag{5.18}$$

where H is the ratio $\Delta Hb/Hb$ of released haemoglobin (ΔHb) to total haemoglobin (Hb) within the red blood cell. C, α and β are constants to be determined from fitting of measurement data. A shear-stress threshold τ_s below which haemolysis does not occur has been subsequently introduced to take into account experimental evidence as follows (Yu, 2017):

$$H(\tau,t) = \begin{cases} C \cdot \tau^{\alpha} t^{\beta} & \tau > \tau_s \\ 0 & \tau \leq \tau_s \end{cases} \tag{5.19}$$

Considering that shear stress and exposure time t are not independent quantities, the shear stress threshold is treated as a function of the exposure time. Possible relationships between τ_s and t are (Nerem, 1981):

$$\tau_s = 88.905 \cdot t^{-0.3372} \tag{5.20}$$

or (Sharp, 1998):

$$t\left(\frac{\tau_s}{1500} - 1\right)^2 = 0.01 \tag{5.21}$$

All models assume that haemolysis starts with healthy red blood cells. Therefore, the relative haemolysis potential of red blood cells decreases with time when exposed to a constant shear stress above the threshold because of their highly interactive nature. A numerical haemolysis model should take this effect into account to obtain correct predictions (Yu, 2017).
An Eulerian power-law model can be implemented into a CFD solver by rewriting the original Eq. (8.18) as follows (Yu, 2017):

$$H(\tau,t) = \left[C^{\frac{1}{\beta}} \tau^{\frac{\alpha}{\beta}} t \right]^{\beta} \tag{5.22}$$

The term in brackets can be expressed in differential form as:

$$\frac{dH_L}{dt} = C^{\frac{1}{\beta}} \tau^{\frac{\alpha}{\beta}} \tag{5.23}$$

where $H_L = H^{\frac{1}{\beta}}$. Finally, the above equation can be rewritten as a standard transport equation for the CFD solver as follows:

$$\frac{\partial H_L}{\partial t} + \boldsymbol{v} \cdot \nabla H_L = \delta C^{\frac{1}{\beta}} \tau^{\frac{\alpha}{\beta}} \left(1 - H_L\right) \qquad \delta = \begin{cases} 0 & \tau < \tau_s \\ 1 & \tau \geq \tau_s \end{cases} \tag{5.24}$$

A Lagrangian formulation of the power-law model can be used based on a mechanical dose D_b as follows (Yu, 2017):

$$D_b = \tau^{\frac{\alpha}{\beta}} t \tag{5.25}$$

Assuming a constant shear stress during an infinitesimal time step, we have:

$$dD_b = \tau^{\frac{\alpha}{\beta}} dt \tag{5.26}$$

Integrating both sides:

$$D_b(t) - D_b\left(t_0\right) = \int_{t_0}^{t} \tau^{\frac{\alpha}{\beta}} dt \tag{5.27}$$

Substituting Eq. (5.25) in Eq. (5.18), we have:

$$H = C \cdot D_b^{\beta} \tag{5.28}$$

Differentiating, we obtain:

$$dH = C\beta \cdot D_b^{\beta-1} dD_b \tag{5.29}$$

Substituting Eq. (5.26) and Eq. (5.27) in Eq. (5.29), we have:

$$dH = C\beta \left[\int_{t_0}^{t} \tau^{\frac{\alpha}{\beta}} d\bar{t} + D_b\left(t_0\right) \right]^{\beta-1} \tau^{\frac{\alpha}{\beta}} dt \tag{5.30}$$

Finally, Eq. (5.30) can be reformulated as a transport equation:

$$\frac{\partial H}{\partial t} + \boldsymbol{v} \cdot \nabla H - D_b \Delta H = C\beta \left[dt + \left(\frac{H}{C\tau^{\alpha}} \right)^{\frac{1}{\beta}} \right]^{\beta-1} \tau^{\alpha} \quad (5.31)$$

Equation (5.31) takes into account the damage accumulated in previous steps in order to compute further evolution in later steps. Although more realistic, it is difficult to code into a CFD solver (Yu, 2017).

An alternative formulation similar to the power-law model is an empirical equation based on regression analysis from experimental data and originally developed for blood pumps (Arvand, 2005):

$$H(\tau, t) = 3.8 \cdot \tau^{-1.9} t^{1.5} V^{0.25} (\Delta p)^{1.4} \quad (5.32)$$

where V is the ratio of a pump's inner volume to the whole circulation volume of the experiment and Δp is the pressure head of the pump.

5.4 Mechanisms of Thrombus Formation

The endothelium of the vessel wall contains nitric oxide, prostacycline and CD39, which act against thrombus formation and maintain lumen patency. Collagen in the sub-endothelial matrix and tissue factor in the media and adventitia layers of the vessel wall provide a haemostatic barrier to maintain the integrity of a closed, high-pressure circulatory system. When the vessel-wall is injured, collagen and tissue factor become exposed to blood flow and initiate thrombus formation through two independent pathways although the outcome remains the same. In the first pathway, disruption of the endothelium facilitates collagen exposure which triggers the accumulation and activation of platelets. Platelet glycoprotein VI interacts with collagen and glycoprotein Ib-V-IX complex interacts with von Willebrand factor leading to platelet capture. Activation of the platelet integrin $\alpha_{IIb}\beta_3$ mediates recruitment of platelets to the thrombus and platelet-platelet interaction. A conformational transition in $\alpha_{IIb}\beta_3$ increases the affinity for its ligands, fibrinogen and von Willebrand factor. Fibrinogen is the main ligand at low shear rates whereas von Willebrand factor plays a key role at higher shear rates (Furie, 2008). Platelet activation releases the content of its alpha and dense granules, which are critical for thrombus formation. The release of ADP from the dense granules further stimulates platelet activation through two ADP receptors, P2Y1 and P2Y12. Glycoprotein VI is the major agonist for initial platelet activation and granule release. The platelet integrin $\alpha_2\beta_1$ plays a supportive but non essential role in the interaction between platelets and collagen. Platelet activation is independent of thrombin in this collagen-

initiated pathway (Furie, 2008). Tissue factor initiates platelet activation through a second pathway, which does not require endothelium disruption and is independent of von Willebrand factor and glycoprotein VI. Tissue factor is a cytokine receptor analogue on the surface of cells or associated with micro-particles in the blood flow. It is found in a latent or “encrypted” form without coagulant activity and in an active form. Activated endothelial cells and platelets at the site of injury release the protein disulfide isomerase (PDI), which converts inactive tissue factor on cells or micro-particles to its active form. In case of direct tissue damage, tissue factor in the vessel wall or on cell surfaces may already exist in its active form. During the initiation phase of the coagulation, tissue factor forms a complex with circulating factor VIIa. This complex plays a key role and consists of three substrates: factor VII, factor IX and factor X. Factor IXa binds to factor VIII and inefficiently activates factor X to Xa, which binds factor V on membrane surfaces. This complex converts prothrombin to thrombin. During the amplification phase, thrombin activates factor VIII and factor V leading to a burst of thrombin-generating potential. Thrombin cleavage of protease-activated receptor 1 (Par1) leads to platelet activation with the release of ADP, serotonin and thromboxane A_2 which stimulate platelet-platelet interaction and amplify the signals for thrombus formation. This second pathway does not completely explain how platelets are recruited to a site of vessel injury in the absence of collagen exposure to blood flow although adhesive molecules may be displayed by the endothelial cells to attract platelets. The exact contribution of the two pathways to platelet activation is unknown although their involvement may vary according to the underlying disease. Finally, platelet activation is monitored by calcium mobilisation in the common pathway. Platelets play a major role in thrombin generation (Monroe, 2002) with heterogeneity of response in thrombus formation (Munnix, 2009). The ability of activated platelets to support thrombin generation is defined by a subpopulation with increased adhesive receptor density (Fager, 2010). Thrombus formation is a dynamic process in which shear, flow, turbulence and the number of platelets in the circulation significantly affect the architecture of the clot (Furie, 2008). There is also increasing evidence of a more active role of red blood cells (RBCs) in thrombus formation (Du, 2014). Platelet adhesion in shear flow is significantly modulated by red blood cells. A quantitative description based on modelling and simulation of previous experiments in perfusion chambers suggest that the rate of platelet adhesion from the blood flow is mainly limited by the frequency of their near-wall rebounding collisions with RBCs under a wide range of shear rates and haematocrit values. These findings

explain the mechanism by which RBCs physically control platelet adhesion (Tokarev, 2011a). Further modelling aimed at prediction of platelet distribution profile across the flow in the presence of RBCs agrees with available experimental data for near-wall layer margination effect of platelets. The strong expulsion of platelets from the core to the periphery of the blood vessel may be related mainly to the finite platelet size, which prevents their mixing with the densely packed RBCs in the core (Tokarev, 2011b). The degree of reduction of the advection and diffusion of the coagulation proteins in regions of the clot with high platelet density may have a significant impact. Hindered transport lead to smaller and denser clot formation compared to no protein hindrance. The limitation on protein transport confines the activating complexes to small regions inside the thrombus with significant reduction of their substrates supply. This decreases the rate and amount of thrombin production leading to slow growth with small thrombus size (Leiderman and Fogelson, 2013). Multiscale modelling is a necessary step for further progress in our understanding of the key aspects of thrombus formation (Flamm, 2012; Xu, 2012).

5.5 Thrombogenesis in Ventricular Assist Devices

Although pump thrombosis remains multi-factorial in origin, an analogy with Virchow's triad may be used to explain its development. Virchow's triad describes the three key factors involved in the development of thrombosis: hypercoagulable status; haemodynamic changes (stasis, turbulence); vessel wall endothelial injury/dysfunction (Kumar, 2010). Similarly, three fundamental elements may be identified during LVAD support leading to pump thrombosis: bio-reactive material, activated platelets, aberrant flow (de Biasi, 2015).

5.6 Computational Modelling of Thrombus Formation

Blood coagulation is a complex and challenging phenomenon from a modelling point of view. The coagulation cascade involves multiple sequences of chemical reactions and feedback loops (Ataullakhanov and Panteleev, 2005; Spronk, 2003). This cascade consists of two major pathways: the extrinsic pathway (Ataullakhanov and Panteleev, 2005), related to vessel wall damage, and the intrinsic pathway (Jesty, 2003; Grigioni, 2004; Grigioni, 2005; Nobili, 2008), related to haemodynamically induced coagulation (Ataullakhanov and Panteleev, 2005; Alemu and Bluestein, 2007). Haemodynamically induced coagulation consists of three stages: initiation with platelet activation (Alemu and Bluestein, 2007),

aggregation with fibrinogen polymerisation into fibrin fibres (Longest and Kleinstreuer, 2003; Storm, 2005) and phase change of the coagulated material (Weisel, 2010; Noailly, 2008; Soares, 2010; Karšaj and Humphrey, 2009). The intrinsic pathway is more suitable for the study of how a device design can affect blood flow and induce thrombosis, while the extrinsic pathway is more suitable for the modelling of thrombosis induced by vessel wall damage (Moiseyev and Bar-Yoseph, 2013).

The computational approach plays a key role for the modelling of the coagulation cascade. Continuum (top-down) and multiscale (bottom-up) methods have been proposed, each with advantages and disadvantages. An integrated, computationally efficient, robust and simple enough coagulation model may well benefit from a combination of both methods and complemented with a mesoscopic-like approach for the modelling of particle interactions such as fibrin polymerisation and platelet activation (Moiseyev and Bar-Yoseph, 2013).

System level methods are based on the Convection Diffusion Reaction (CDR) equations with empirical estimation of the relevant constants. They show a low level of complexity and good experimental agreement but they do not take into account the spatial-temporal information (Weisel, 1992; Marx, 2006).

Continuum models can overcome this limitation by combining system level reaction kinetics with spatial information where the CDR equations are coupled to the Navier-Stokes (NS) equations to account for blood flow and achieve more realistic simulations (Anand, 2005; Anand, 2008).

Continuum models are more suitable when blood coagulation is addressed in the context of complex geometries. Simulations are easy to set up and require less computational power. The level of complexity is related to the details required and the blood constituents considered. A basic continuum model consists of the NS equations for blood flow dynamics and CDR equations for the spatial-temporal evolution of the particles concentration. Most of the available continuum models assume a rigid blood vessel wall and blood constituents as mass-less particles (Fogelson, 1984; Sorensen, 1999a; Sorensen, 1999b; Goodman, 2005; Leiderman, 2011; Fogelson, 2012; Leiderman, 2013; Govindarajan, 2016).

5.7 Models of the Coagulation System

Although a qualitative description of the coagulation system is valuable for an initial understanding of the different events, a computational modelling approach may well provide more specific quantitative information about thrombus development. The integration of the different events leading to

thrombus formation and the ability to predict its occurrence are complex and challenging tasks in view of the different spatial and temporal scales involved. Nevertheless, a modelling and simulation approach for the prediction of a quantitative response of the coagulation system to physiological and adverse events may have an impact on clinical decision-making and optimisation of therapeutic intervention (Xu, 2011).

5.7.1 Coagulation Pathway Models

First comprehensive system of ordinary differential equations (ODEs) to model the reactions of the TF pathway based on the assumption of a uniformly mixed and static blood environment with unlimited supply of phospholipids (Lawson, 1994; Jones and Mann, 1994). The ability of the model to simulate the whole procoagulant pathway using specific rate constants provides a quantitative description of the proteolytic and catalytic events leading to α -thrombin generation in good agreement with experimental data.

Further improvement of the TF-initiated coagulation model of the extrinsic coagulation system includes the TF pathway inhibitor and the antithrombin-III (AT-III). The model accurately predicts the nonlinear dependence of thrombin generation on TF, AT-III and TF pathway inhibitor based on a TF concentration threshold: when the TF concentration is below the threshold, thrombin production is suppressed by the TF pathway inhibitor and AT-III (Hockin, 2002). The use of kinetic Monte Carlo simulations takes into account the stochastic effects of coagulation factors at low concentrations ignored by deterministic models (Lo, 2005).

The integration of blood coagulation reactions with hydrodynamic factors and platelet interactions takes into account the role of surface binding sites (Kuharsky and Fogelson, 2001; Fogelson and Tania, 2005).

The dynamics of thrombin formation in vascular and non vascular compartments has been addressed with a distinction between reactions on cell membranes and in the blood flow assuming a uniformly mixed and static fluid environment without taking into account the competing role of surface and fluid diffusion (Bungay, 2003). Sensitivity analysis of the coagulation system has identified those reactions where small changes in parameter values have significant effect on thrombin generation and platelet activation (Luan, 2007).

5.7.2 Fibrin Network Models

A kinetic model of fibrin polymerisation (Weisel and Nagaswami, 1992) and a fibrinogen assembly model (Yang, 2000) may have some potential

application. A fibrin thrombus formation model (Fogelson and Keener, 2010) with generalisation of the kinetic gelation equations (Ziff, 1980; Ziff and Stell, 1980) may also have a role. Complexity may well be a limiting factor.

5.7.3 Platelet Activation Models

ADP-mediated activation (Purvis, 2008; Purvis, 2009) with steady-state kinetic modelling is another attempt to explain platelet activation. Platelets response to multiple activators (Chatterjee, 2010) has the potential for a patient-specific approach.

5.7.4 Platelet-Platelet Adhesion and Platelet-Vessel Wall Interaction Models

The Dependence of some receptor ligand interactions on shear rate (GPIb-von Willebrand factor [vWF]) and modification of GPIIbIIIa integrin receptor during platelet activation lead to changes in affinity to fibrin, fibrinogen, vWF and vitronectin. Platelet receptor – ligand interactions mediate platelet adhesion and initiate intracellular signalling pathways leading to changes in platelet shape and surface composition that affect adhesion (Gibbins, 2004; Nesbitt, 2009).

Computational modelling of platelet-platelet binding mediated by vWF and fibrinogen interaction with platelet receptors has confirmed observational findings that thrombus development requires both vWF and fibrinogen (Mori, 2008).

Further modelling approaches have shown that platelets exhibit different dynamic characteristics related to their geometry and their relative position with the surface (Modi, 2005a; Modi, 2005b; Modi, 2008a; Modi, 2008b).

5.7.5 Integrated Thrombogenesis Models

Comprehensive computational modelling aiming at the integration of spatial and temporal events involved in thrombus growth (Laurenzi, 1999; Lobanov, 2005; Anand, 2005; Wang, 2006).

Modelling including single-platelet dynamics (Pivkin, 2006) shows dependence of thrombus growth rate on blood velocity as per experimental observation (Begent and Born, 1970).

Microscale platelet aggregation modelling and continuum macroscale modelling seems another appropriate approach to the problem where platelets are considered as a single fluid-filled, closed elastic membrane immersed in a viscous fluid (Fogelson and Guy, 2008).

5.7.6 Multiscale Models of Thrombus Formation

Multiscale modelling of thrombus formation consists of the integration of coagulation reaction, platelet behaviour and blood flow. The model tracks the behaviour of individual platelets and cells in space and time. Integration of events occurring at different scales such as the flow filed around the whole thrombus and the coagulation reactions on a platelet surface (Xu, 2008; Xu, 2009; Xu, 2010).

Spatial-temporal model based on coupled partial differential equations describing coagulation biochemistry, activation and aggregate formation of platelets, interaction between blood flow and growing thrombus have been proposed. Wall shear rate and near-wall enhanced platelet concentration affect the development of growing thrombi (Leiderman and Fogelson, 2011). Multiscale modelling has the potential to identify conditions where small changes in specific parameters have significant impact on thrombus formation compared to an experimental approach. The need of high computational power can be partly overcome by large computer clusters and parallel algorithms.

Coupling between blood flow, transport of inert solutes and internal structure of the porous thrombus is obtained by implementing a combination of in vivo experiments, biomedical imaging and computer simulations to quantify the intrathrombotic microenvironment. An image-based modelling approach relies on the experiment and only two components are addressed: hydrodynamics and transport of platelet agonists. A mathematically generated thrombus structure relies on assumptions due to lack of experimental data. Therefore, multiscale computational modelling methods for the study of platelet adhesion and thrombus formation are based on the combination of four main components: fluid mechanics, coagulation cascade, cell mechanics and receptor-ligand binding (Wang, 2012).

The intrathrombus fluid dynamics simulation results show that the shell experiences higher flows and stresses compared to the core and it is significantly more permeable. Brownian transport results suggest that in normal physiological conditions molecules from the damaged endothelium would not reach the shell before exiting the thrombus (Wu, 2011; Voronov, 2013; Taylor, 2014; Bodnár, 2014; Topper, 2014; Babushkina, 2015).

5.8 Some Mathematical Considerations

Modelling of transport, activation and adhesion of platelets is critical for the prediction of thrombus formation. A shear-dependent platelet adhesive model calibrated according to *in vivo* and *in vitro* experimental data seems a suitable approach over a wide range of flow shear rates ($100 < \dot{y} < 28000\ s^{-}$

[1]). A Lagrangian description is used to model platelets as rigid spherical particles in the context of a Force Coupling Method (FCM) to address bidirectional platelets motion interaction with blood flow whereas the haemodynamics and chemical transport are obtained from the solution of NS and advection-diffusion-reaction (ADR) equations on a fixed Eulerian grid (Yazdani, 2017). To reduce computational time, blood is considered as a continuous medium where the effect of red blood cells on platelet margination is acknowledged assuming a fully developed blood flow at the inlet of the simulated vessel with platelets already marginated towards the vessel wall. Assuming blood as an incompressible Newtonian fluid, the governing equations are:

$$\begin{cases} \rho\left(\dfrac{\partial \boldsymbol{u}}{\partial t}+(\boldsymbol{u}\cdot\nabla)\boldsymbol{u}\right)=-\nabla p-\mu\nabla^2\boldsymbol{u}+\boldsymbol{f}\left(\boldsymbol{x},t\right) \\ \nabla\cdot\boldsymbol{u}=0 \\ \boldsymbol{f}\left(\boldsymbol{x},t\right)=\sum_{n=1}^{N}\boldsymbol{F}^n\Delta\left(\boldsymbol{x}-\boldsymbol{Y}^n\left(t\right)\right) \end{cases} \tag{5.33}$$

where $\boldsymbol{u}$, p, ρ and μ are the blood velocity, pressure, density and viscosity. $\boldsymbol{F}^n$ is the force due to particle n. The effect of platelets on the flow field is due to $\boldsymbol{f}(\boldsymbol{x},t)$. The contribution of each platelet with centre of mass located at $\boldsymbol{Y}^n$ to the flow at position $\mathbf{x}$ is smoothed by a Gaussian distribution kernel $\Delta(\mathbf{X}\equiv(\mathbf{x}-\mathbf{Y}^n))$ with:

$$\Delta\left(\boldsymbol{X}\right)=\left(2\pi\sigma^2\right)^{-\frac{3}{2}}e^{\left(-X\mathrm{g}\frac{X}{2\sigma^2}\right)} \tag{5.34}$$

where $\sigma = a/\sqrt{\pi}$ is the standard deviation of the kernel with a being the particle radius.

The velocity of each platelet $\mathbf{V}^n$ is calculated by interpolation of the local flow velocity at the location of a platelet using the same Gaussian kernel:

$$\boldsymbol{V}^n=\frac{d\boldsymbol{Y}^n}{dt}=\int\boldsymbol{u}\Delta\left(\boldsymbol{x}-\boldsymbol{Y}^n\left(t\right)\right)d\boldsymbol{x} \tag{5.35}$$

where the platelets position vectors are updated at each time step using a second-order Euler forward scheme (Yazdani, 2017).

The net force $\boldsymbol{F}^n$ acting on each platelet is:

$$\boldsymbol{F}^{n} = -\frac{4}{3}\pi r^{3}\left(\rho_{plat} - \rho\right)\frac{d\boldsymbol{V}^{n}}{dt} + \boldsymbol{F}_{inter} \tag{5.36}$$

where the first term is the inertial force due to the density difference between platelets (ρ_{plat}) and blood (ρ). The second term ($\boldsymbol{F}_{inter}$) accounts for platelet-platelet and platelet-wall interaction forces.

The attractive and repulsive platelets interactions are based on the Morse potential (U_{Morse}):

$$U_{Morse} = D_e\left[1 - e^{-\beta d\cdot\left(\frac{r}{d-1}\right)}\right]^2 \tag{5.37}$$

where D_e is the energy depth, β controls the width of the energy well, r is the distance between the platelets centroids and d is the equilibrium distance between two platelets.

The magnitude of the interaction forces derived from the Morse potential is:

$$\boldsymbol{F}_{inter} = -\frac{\partial U_{Morse}}{\partial r} = 2\beta D_e\cdot\left[e^{-2\beta d\cdot\left(\frac{r}{d-1}\right)} - e^{-\beta d\cdot\left(\frac{r}{d-1}\right)}\right] \tag{5.38}$$

The parameter D_e mainly controls the magnitude of the platelets interaction forces and is obtained from experimentally measured thrombus formation under different haemodynamic conditions. Three different states are considered for platelets: passive, triggered and activated. Platelets are non-adhesive in a passive or triggered state and only repulsive forces are applied to prevent cellular overlap. A passive platelet becomes triggered after a time delay τ_{act} from the interaction with an activated platelet. The interaction between two activated platelets generates a repulsive force when $r < d$ and an attractive force when $r > d$.

To take into account the correlation between adhesion force and local shear rate according to flow conditions, D_e can be defined as follows (Yazdani, 2017):

$$D_e\left(\lambda_2\right) = D_e^{h}\left[tanh\left(\frac{\lambda_2 - \lambda_2^{l}}{1000}\right) + \frac{D_e^{l}}{D_e^{h}} + 1\right] \tag{5.39}$$

where $\lambda_2 = \sqrt{(2\boldsymbol{D}:\boldsymbol{D})}$ is the square root of the second invariant of the fluid strain-rate tensor $\boldsymbol{D}$, D_e^l and D_e^h relate to the adhesive forces at low and high shear rates and λ_2^l is the shear rate threshold in transition from low to high shear rate.

The coagulation cascade model consists of 20 ADR equations in the following form (Yazdani, 2017):

$$\frac{\partial c_i}{\partial t} + \boldsymbol{u}\cdot\nabla c_i = D_i\nabla^2 c_i + S_i \qquad i = 1,\ 2,\ ...,\ 20 \tag{5.40}$$

where c_i and D_i are the concentration and diffusion coefficient for each reactant (plasma-phase enzymes, zymogens or complexes) and S_i is the rate of production or destruction of the considered reactant. Initial concentrations are set to normal plasma values for zymogens and to very small non-zero values for enzymes and complexes. A zero-flux boundary condition is imposed, except for a few reactants to initiate the coagulation. The significant agreement between simulation and experimental results confirms the validity of this approach to model venous and arterial thrombus formation (Yazdani, 2017).

A recently improved mathematical model has been successfully applied to the analysis of thrombus formation in the HeartMate II axial flow blood pump (Wu, 2016; Wu, 2017). Blood is considered as a multi-constituent mixture consisting of a linear fluid phase and a solid (thrombus) phase. The fluid phase consists of red blood cells (RBC) suspended in plasma and is governed by the equations of conservation of mass and linear momentum as follows (Wu, 2017):

$$\begin{cases} \dfrac{\partial \rho_f}{\partial t} + div\left(\rho_f \boldsymbol{v}_f\right) = 0 \\ \rho_f \dfrac{D\boldsymbol{v}_f}{\partial t} = div\left(\boldsymbol{T}_f\right) + \rho_f \boldsymbol{b}_f - C_2 f\left(\phi\right)\left(\boldsymbol{v}_f - \boldsymbol{v}_T\right) \end{cases} \tag{5.41}$$

where $\boldsymbol{v}_f$ is the velocity of the fluid phase, $\boldsymbol{v}_T$ is the velocity of the thrombus phase, $\boldsymbol{b}_f$ is the body force. $\boldsymbol{T}_f$ is the fluid stress tensor:

$$\boldsymbol{T}_f = \left[-p\left(1-\phi\right)\right]\boldsymbol{I} + 2\mu_f\left(1-\phi\right)\boldsymbol{D}_f \tag{5.42}$$

where p is the pressure, μ_f is the dynamic viscosity and the scalar field ϕ is the volume fraction of deposited platelets leading to thrombus formation. The density of the fluid phase is a function of the volume fraction as follows:

$$\rho_f = (1-\phi)\rho_{f0} \tag{5.43}$$

where ρ_{f0} is the density of the pure fluid phase. The term $C_2 f(\phi)(\boldsymbol{v}_f - \boldsymbol{v}_T)$ is the resistance force on the fluid phase from the thrombus; C_2 is a constant and $f(\phi)$ is the hindrance force.

The model includes ten chemical and biological entities among which platelets are considered in five different states: resting platelets in the flow field; activated platelets in the flow field; deposited resting platelets; deposited active platelets; deposited and stabilised platelets. The transport of these entities is described by a set of CDR equations of the form:

$$\frac{\partial[C_i]}{\partial t} + div\left([C_i]\boldsymbol{v}_f\right) = div\left(D_i \nabla[C_i]\right) + S_i \tag{5.44}$$

where $[C_i]$ is the concentration of entity i; D_i is the diffusivity of entity i in the blood; S_i is a reaction source term for entity i. Deposited platelets are governed by rate equations as follows:

$$\frac{\partial[C_i]}{\partial t} = S_i \tag{5.45}$$

Platelets adhesion to surfaces and the other entities reactions are modelled by surface-flux boundary conditions (Sorensen, 1999a; Sorensen, 1999b).

Simulations performed under unsteady (transient) conditions with a k-ω model to account for turbulence and rotational speed of 9000 *rpm* have shown interesting results. Regions of thrombus formation and accumulation included the majority of the upstream flow straightener hub, the rear of the straightener vanes and the upstream bearing region in agreement with clinical findings (Meyer, 2008; Mokadam, 2011; Capoccia, 2013). The simulations have also predicted regions free of thrombus such as the leading edge of the blades of the inlet straightener vane where higher shear stress enhances the erosion rate of deposited platelets (Wu, 2016). Currently, this is a comprehensive attempt to replicate patterns of platelet deposition and thrombus growth in a rotary blood pump. One unsolved challenge is the ability to assess the influence of flow pulsatility caused by

the cyclical contribution of the heart where the flow may be well behaved and attached or it may become chaotic during part of the diastolic phase (Yang, 2015). A key point is to determine how tolerable the degree of chaotic flow is and how long for. This model may contribute to address this challenge considering that the time-course of thrombus growth in the upstream region indicates that once a critical amount of deposition occurs, a positive-feedback effect causes platelet deposition at a greater rate (Wu, 2016). Although the high computational power requirement remains the main limiting factor, this modelling approach has the potential to become a powerful design tool and personalise clinical treatment given its more recent experimental validation (Wu, 2017).

Dissipative Particle Dynamics (DPD) has been recently gaining popularity for the simulation of the dynamics and rheological properties of simple and complex fluids (Groot, 1997; Moeendarbary, 2009) with particular reference to blood flow modelling and thrombus formation (Filipovic, 2008; Tosenberger, 2012; Tosenberger, 2013; Tosenberger, 2015; Tosenberger, 2016). The DPD method is very attractive for blood flow modelling because it can handle the non-Newtonian properties although computationally expensive (Yamaguchi, 2010).

DPD is a mesoscale particle method, which fills the gap between microscopic and macroscopic simulations. More specifically, it is a coarse-grained molecular dynamics approach where particles are considered as clusters of molecules interacting through conservative (non-dissipative), dissipative and fluctuating forces (Liu, 2015). A fluid system is simulated using a set of interacting particles with equal mass. Applying Newton's second law, the equation of motion for particle i becomes:

$$\begin{cases} \dfrac{d\boldsymbol{r}_i}{dt} = \boldsymbol{v}_i \\ \dfrac{d\boldsymbol{v}_i}{dt} = \boldsymbol{f}_i^{\,int} + \boldsymbol{f}_i^{\,ext} \end{cases} \tag{5.46}$$

where $\boldsymbol{r}_i$ and $\boldsymbol{v}_i$ are the position and velocity vectors and $\boldsymbol{f}_i^{ext}$ is the external force including gravity. The inter-particle force $\boldsymbol{f}_i^{int}$ is the resultant of conservative ($\boldsymbol{F}_{i,j}^{C}$), dissipative ($\boldsymbol{F}_{i,j}^{D}$) and random ($\boldsymbol{F}_{i,j}^{R}$) forces as follows:

$$\boldsymbol{f}_i^{\,int} = \sum_{j \neq i} \boldsymbol{F}_{i,j} = \sum_{j \neq i} \boldsymbol{F}_{i,j}^{\,C} + \boldsymbol{F}_{i,j}^{\,D} + \boldsymbol{F}_{i,j}^{\,R} \tag{5.47}$$

$\boldsymbol{F}_{i,j} = -\boldsymbol{F}_{j,i}$ is the interactive force between particle i and j where the symmetry of interaction maintaines momentum conservation (Liu, 2015).

The conservative force $\boldsymbol{F}_{i,j}^{C}$ is a soft interaction of the form:

$$\boldsymbol{F}_{i,j}^{C} = a_{i,j} w^{C}\left(r_{i,j}\right)\hat{\boldsymbol{r}}_{i,j} \qquad w^{C}\left(r_{i,j}\right) = \begin{cases} 1 - r_{i,j} & r_{i,j} < 1 \\ 0 & r_{i,j} \geq 1 \end{cases} \tag{5.48}$$

where a_{ij} is the maximum repulsion between particles i and j; $\boldsymbol{r}_{i,j} = \boldsymbol{r}_i - \boldsymbol{r}_j$; $r_{i,j} = \left|\boldsymbol{r}_{i,j}\right|$; $\hat{\boldsymbol{r}}_{i,j} = \boldsymbol{r}_{i,j}/r_{i,j}$. The weight function $w^{C}(r_{i,j})$ allows larger length and time scales in DPD.

The dissipative force $\boldsymbol{F}_{i,j}^{D}$ is related to viscosity and depends on the relative position and velocity of the particle. Its usual form is:

$$\boldsymbol{F}_{i,j}^{D} = -\gamma w^{D}\left(r_{i,j}\right)\left(\hat{\boldsymbol{r}}_{i,j} \cdot v_{i,j}\right)\hat{\boldsymbol{r}}_{i,j} \tag{5.49}$$

where γ is a coefficient, $\boldsymbol{v}_{i,j} = \boldsymbol{v}_i - \boldsymbol{v}_j$ and $w^{D}\left(r_{i,j}\right)$ is a distance-dependent weight function.

The random force $\boldsymbol{F}_{i,j}^{R}$ is related to thermal fluctuations and depends on the relative position of the particles. Its form is as follows:

$$\boldsymbol{F}_{i,j}^{R} = \sigma w^{R}\left(r_{i,j}\right)\xi_{i,j}\hat{\boldsymbol{r}}_{i,j} \tag{5.50}$$

where σ is a coefficient, $w^{R}(r_{i,j})$ is a distance-dependent weight function and $\xi_{i,j}$ is a random variable with Gaussian distribution (Liu, 2015).

The DPD method has the ability to model problems with larger time and length scale in view of its association with bigger particle size and soft conservative interaction potential. It is arguably considered the most suitable mesoscale simulation technique to model complex fluid systems (Liu, 2015). The inclusion of the dissipative and random force maintains essentially a constant system temperature with small fluctuations. The DPD method is implemented in a non-dimensional form requiring appropriate coefficients selection to match the modelling parameters with the physical properties of the real fluid/material and maintain numerical accuracy. The calculation of interaction forces between particles requires significant computational power, which can be largely reduced using a special neighbour-list algorithm and parallel techniques (Liu, 2015).

Multiscale modelling is also being considered more frequently where two or more computational methods are coupled at different length and time scale. This approach gives detailed and reliable information although

computationally expensive. Multiscale modelling of the coagulation system can give accurate simulations of its dynamics, biochemical reactions, diffusivity, viscosity, mechanical properties of thrombus formation under shear flow and red blood cells behaviour.

A multiscale approach combines the simplicity and efficiency of macroscopic models with the accuracy of a microscopic approach such as cell-based discrete models. An example is the discrete Cellular Potts Model (CPM) of platelets and blood cells aggregation combined with continuous partial differential equations (PDE) describing the hydrodynamics of blood flow and the kinetics of coagulation reactions (Xu, 2008; Xu, 2009; Xu, 2010; Xu, 2012). The CPM is a cell-level, energy-minimisation-based lattice model, which uses effective energy coupling to external fields such as local flow rate to describe cell motion, cell-cell interactions, cell adhesion and the dynamics of the inhomogeneous internal structure of thrombus formation. The effective energy (E) of the system consists of true energies, like cell-cell adhesion, and terms that mimic energy, like the response of a cell to blood flow and area constraint (Xu, 2008; Xu, 2009):

$$E = E_{adhesion} + E_{flow} + E_{area} \tag{5.51}$$

A computer simulation of the clotting system requires a multiscale and integrated description of platelet signalling and adhesion, coagulation kinetics and haemodynamics (Diamond, 2016). The wall shear rate and the wall shear stress play a key role in the events leading to thrombus formation. Phenomenological equations relating agonists and platelet activation have been used to simulate combined platelet deposition and autocrine activation by solving a pseudohomogeneous, single-phase continuum model of blood clotting over a reactive surface (Sorensen, 1999a; Sorensen, 1999b). Detailed continuum-based descriptions of clotting under flow conditions have been proposed (Kuharsky and Fogelson, 2001). An integrated, computationally efficient, robust and simple enough coagulation model may well benefit from a combination of continuum and multiscale methods complemented with a mesoscopic-like approach for the modelling of particle interactions such as fibrin polymerisation and platelet activation (Moiseyev and Bar-Yoseph, 2013). Dissipative particle dynamics is currently being used where the fluid flow is modelled as the motion of mesoscale particles subject to repulsive, dissipative and random forces (Filipovic, 2008; Li, 2015; Tosenberger, 2016). Significant efforts based on multiscale modelling and dissipative particle dynamics are addressing the coagulation cascade (Wu, 2014; Moreno, 2013; Fedosov, 2010; Fedosov, 2011;

Fedosov, 2014; Rukhlenko, 2015; Sequeira, 2011). Correlation with *in vitro* and *in vivo* results shows promising grounds for further progress (Zhang, 2017).

5.9 Thrombus Formation in Blood Recirculating Devices

The development of high shear stress in the non-physiological geometries of blood-recirculating devices is closely related to thrombus formation by chronic platelets activation. This, rather than haemolysis, seems the key aspect of blood trauma in medical devices. Platelets exposed to constant shear stress for a period of time become activated. Their behaviour following activation is critical in order to understand the increased thrombotic risk in blood recirculating devices.

Platelets exposed to an initial shear stress of 60 $dyne/cm^2$ for 40 *s* show minimal activation but their post-exposure activation rate is significantly higher compared to platelets that have not experienced an initial high shear stress. This is a so called sensitisation response, which is observed for platelets exposed to 1000 $dyne/cm^2$ for 25 *ms* as observed in blood recirculating devices (Sheriff, 2010). The activation and sensitisation response of platelets in blood recirculating devices is dependent on shear loading rate, shear stress magnitude and exposure time (Sheriff, 2013). The interaction between flow-induced stresses and blood components is related to the hypothesis that thromboembolism in blood recirculating devices is initiated and maintained by the non-physiological flow patterns and stresses, which activate and enhance platelet aggregation (Bluestein, 2010).

5.10 Thromboresistance Optimisation

Device thrombogenicity emulation (DTE) methodology is a recently developed optimisation strategy aimed at the reduction of the thrombogenic potential in blood recirculating devices with particular reference to ventricular assist devices (Girdhar, 2012). DTE combines *in silico* advanced numerical simulations with *in vitro* techniques by correlating device haemodynamics with coagulation markers. The optimisation process begins with *in silico* modelling first followed by experimental emulation of the device-specific stress loading waveforms in a haemodynamic shearing device (Nobili, 2008), where device specific effects on platelet activation are measured with a modified prothrombinase assay (Jesty, 1999). Flow through a ventricular assist device is modelled with a high fidelity two-phase fluid-structure interaction (FSI) simulation resolving all components of the stress tensor relevant to flow-induced thrombogenicity. The cumulative stress loading history that may drive platelets beyond their activation threshold is

calculated along multiple flow trajectories with the combined effect of shear stress and exposure time (Alemu, 2007; Hellums, 1994; Apel, 2001b). The stress tensor is extracted from the simulations along the corresponding platelet trajectories and rendered into a scalar stress value (Alemu, 2010; Xenos, 2010) so that both viscous and turbulent stresses (τ_{ij}) are considered in the formulation of stress accumulation:

$$\sigma = \frac{1}{\sqrt{3}} \sqrt{\tau_{11}^2 + \tau_{22}^2 + \tau_{33}^2 - \tau_{11} \cdot \tau_{22} - \tau_{11} \cdot \tau_{33} - \tau_{22} \cdot \tau_{33} + 3\left(\tau_{12}^2 + \tau_{23}^2 + \tau_{13}^2\right)} \quad (5.52)$$

A linear product of instantaneous values of the stress (σ) and exposure time (t_{exp}) is assumed for the stress accumulation (SA) and a summation is obtained as follows:

$$SA = \sigma \cdot t_{exp} = \int_{t_0}^{t_{exp}} \sigma(t)\, dt \approx \sum_{i=1}^{N} \sigma_i \cdot \Delta t \quad (5.53)$$

where σ_i is the nodal scalar value extracted from the total stress tensor described above, Δt is the corresponding time step between successive nodal points and SA is given in *Pa·s*.

The probability density function of stress accumulation along multiple trajectories is used as a surrogate for the evaluation of the overall thrombogenic potential of different ventricular assist devices; in other words, a sort of thrombogenic “footprint” of VAD design including specific regions of interest such as inlet flow straightener (vanes), inlet hub and bearing taper, impeller, impeller-shroud near wall region and tip-shroud gap clearance.

DTE methodology is based on platelets shear-loading history (Girdhar, 2012; Bluestein, 2010), which is a Lagrangian approach computing the cumulative platelet activation level for a large population of platelets flowing through the device. This method combines haemodynamics and kinetic aspects of platelet activation but it cannot predict the location within the pump where platelets are likely to accumulate because it does not consider a mechanism for platelet deposition. In addition, this approach is unable to distinguish between shear stress enhancing platelet activation and shear stress needed to remove platelets from the region of stagnation (Wu, 2016).

The study of flow patterns reveals regions of flow recirculation and stagnation with thrombogenic potential. This can be obtained either experimentally through flow visualisation (Yang, 2015) or numerically with computational fluid dynamics analysis (Chiu, 2014). Experimental and

numerical analyses are very helpful in giving information about the increased risk of thrombosis but they cannot give definitive details in relation to haemodynamics, surface chemistry and blood elements (Wu, 2016).

Analysis of the haemodynamic shear stress waveforms has shown that high frequency oscillations are significantly related to the prothrombotic behaviour of stimulated platelets in blood recirculating devices (Consolo, 2017).

A time-accumulated model has been recently suggested as the most promising approach towards computational prediction of blood damage induced by complex flow profiles in blood recirculating devices (Gharaie, 2017).

5.11 Pump Thrombosis in Long-Term Mechanical Circulatory Support Devices

The wide spread use of continuous flow LVADs has been associated with an increase in pump thrombosis, which remains the main limitation for the long-term use of these devices (Starling, 2014; Najjar, 2014; Kirklin, 2015a). Acquired von Willebrand factor deficiency and platelet dysfunction related to the high shear stress created by the pump further enhance the risk of bleeding during anticoagulant treatment making the management of these patients more challenging (Eckman, 2012; Baghai, 2015). Pump thrombosis is highly suspicious in the presence of haemolysis (elevated LDH), development of unexplained heart failure symptoms with echocardiographic findings of poor left ventricular unloading at the patient's maintenance speed and pump power elevation greater than baseline (> 2 W) or persistent for more than 24 hours (> 10 W). Nevertheless, clinically evident pump thrombosis does not develop in all patients with increased LDH. Therefore, clinical assessment and echocardiographic evaluation play a key role in the diagnosis (Kapur, 2015). Echocardiographic ramp testing is a useful diagnostic tool based on the principle that any change in pump speed should modulate the degree of left ventricular unloading if the device is functioning appropriately (Jung, 2015). Nevertheless, its diagnostic accuracy has been validated for the HeartMate II only (Uriel, 2012) and may not be extrapolated to the HVAD for which a different approach may be required (Jorde, 2015). Loading conditions may affect the relationship between speed and left ventricular unloading (Adatya, 2015). Acoustic spectral analysis has also been proposed (Kaufmann, 2014). Invasive haemodynamic assessment may be required in selected cases when non invasive evaluation remains inconclusive. Occasionally, pump thrombosis may be addressed with review of the anticoagulation treatment or with a less

invasive approach (Schlendorf, 2014; Stulak, 2015) although pump exchange will be required in most patients (Mehra, 2014; Kapur, 2015).
Accumulation of shear-mediated platelet injury due to the cyclic exposure to the hypershear environment of the pump remains the main mechanism leading to thrombus formation. Significantly high rotating speed with very narrow gap clearance between the impeller and the pump housing expose platelets to supraphysiologic shear stresses (Selmi, 2019). Although optimisation of pump geometry has led to significant reduction of in-pump thrombosis with the HeartMate III (Mehra, 2019), thrombo-embolic events have been observed. Therefore, an increased clearance gap between the housing and the blades of the device may not be enough to address the problem suggesting the involvement of other factors beyond pump hypershear. Additional haemodynamic conditions may further contribute to the thrombogenic potential of the whole LVAD system consisting of the native left ventricle, the inflow cannula, the impeller, the outflow graft and the anastomosis site on the ascending aorta. Prothrombotic haemodynamic conditions may occur at different locations within the LVAD system including recirculation zones and stagnant platelet trajectories in the pump. Specific LVAD configurations and management strategy based on partial aortic valve opening may help the system haemocompatibility and further reduce thrombotic risk (Selmi, 2019). In view of these considerations, it may be more appropriate to approach the problem in terms of LVAD system thrombosis based on a combination of engineering design of the pump, implantation configuration and angle of the outflow graft anastomosis, residual left ventricular contractility and intermittent opening of the aortic valve as contributors to the thrombogenic potential of the device used. Needless to say, a patient-specific modelling approach may help with treatment optimisation and possibly outcome prediction (Argueta-Morales, 2014; Gray, 2018).

5.12 Chapter Summary

Blood is usually considered a Newtonian fluid in VADs calculations because of the high shear rates, as its viscosity remains constant for shear rates above 100 s^{-1}. The use of generalised Newtonian models of blood rheology may lead to better predictions of the continuum properties of flow in VADs. Theoretical models accounting for biochemical, biophysical and biomechanical factors give a more comprehensive view of thrombus formation. Theoretical predictions in the context of in vitro and in vivo experimental evaluation would be desirable. Virchow's triad describes the

three key factors involved in the development of thrombosis: hypercoagulable status; haemodynamic changes (stasis, turbulence); vessel wall endothelial injury/dysfunction. Similarly, three key elements may be identified during LVAD support leading to pump thrombosis: bio-reactive material, activated platelets, aberrant flow. The development of high shear stress in the non-physiological geometries of blood-recirculating devices is closely related to thrombus formation by chronic platelets activation. Multiscale modelling of the coagulation system can give accurate simulations of its dynamics, biochemical reactions, diffusivity, viscosity, mechanical properties of thrombus formation under shear flow and red blood cells behaviour. Device thrombogenicity emulation (DTE) methodology is a recently developed optimisation strategy aimed at the reduction of the thrombogenic potential in blood recirculating devices with particular reference to ventricular assist devices. DTE combines *in silico* advanced numerical simulations with *in vitro* techniques by correlating device haemodynamics with coagulation markers. Approaching the problem in terms of LVAD system thrombosis based on patient-specific modelling may play an important role in treatment optimisation and outcome prediction.

Chapter 6

Thesis Objectives

6 Thesis Objectives

6.1 Introduction

Rotary blood pumps are increasingly used for the treatment of end-stage heart failure either as a bridge to transplant or for a more permanent solution. Since the REMATCH Trial, the technological development from pulsatile to continuous flow ventricular assist devices has led to an increased survival of patients on prolonged circulatory support. Continuous-flow left ventricular assist devices (LVADs) have proven their reliability in relation to outcome following elective surgery in chronic heart failure patients before the onset of cardiogenic shock. In patients up to 70 years of age without cardiogenic shock, diabetes and renal failure, circulatory support with a continuous-flow LVAD showed 1- and 2-year survival of 80% and 70%, which was comparable with heart transplantation. An analysis of the Interagency Registry for Mechanically Assisted Circulatory Support (INTERMACS) has showed greater durability for continuous flow LVADs in comparison with pulsatile flow devices. Durability issues are closely related to driveline infection and failure, thrombosis and haemolysis, pump drive unit failure and ultimately death following driveline or pump drive unit failure. Despite the sophisticated level of technology currently available, pump thrombosis remains the most feared complication with potentially disastrous consequences and impact on clinical outcome. Elevated flow stresses in the non physiologic geometries of blood re-circulating devices are closely related to thrombus formation by chronic platelet activation. This, rather than haemolysis, seems the key aspect of blood trauma in blood recirculating devices. VADs operate in a flow regime which has been difficult to simulate: the transitional region at the boundary of laminar and turbulent flow. Different approaches have been used but controversial issues still remain. Computational Fluid Dynamics (CFD) is an investigational tool that has played a significant role in the design and development of VADs, modelling of blood damage (thrombus formation and haemolysis) and patient-specific fluid-structure interaction analysis.

The aim of this thesis is three-fold:

a) to investigate the use of pressure-volume analysis in a clinical setting through the review of six heart failure patients previously discussed at a MDT meeting with a view to predict or guide further management;
b) to review the theory behind modelling approaches to VADs and their interactions with the cardiovascular system for better understanding of their clinical use. Then, an overview of computational fluid

dynamics (CFD) is considered as a prelude to its application to the analysis of VADs performance. Additionally, the development of a simplified model of centrifugal pump will be used in initial simulations as preliminary analysis;

c) to examine an example of a proof-of-concept pilot patient-specific model of an axial flow pump (HeartMate II) as pre-operative planning strategy in a patient-specific model with a view to identify potential critical areas that may affect pump function and outcome in a clinical setting.

It is an ambitious vision although not impossible as long as there is willingness to co-operate and pursue a different approach to treatment.

6.2 Thesis Hypothesis

It is possible to develop a mathematical approach based on patient-specific modelling with a view to tailoring treatment for each individual patient undergoing VADs support.

Device implantation is quite often based on a compromise between current available technology and patient features. The aim is to add a more informative process based on patient-specific treatment. Computational modelling of the cardiovascular system and its interactions with circulatory support devices is possible. Latest imaging technologies and their integration with computational methods allow *in vivo* visualisation and quantification of cardiac and device fluid mechanics. The aim of this work is to show its feasibility and its potential in daily clinical practice with the selection of a suitable model and boundary conditions for the planned simulations. The development of a common language between clinicians and engineering scientists is an important aspect for a successful outcome. Then, the development of simulations based on a method that is easy understandable and within the time constraints of clinical practice leading to results that are ready available to be interpreted for clinical-decision making is another achievable target with great potential for patient's management.

A more personalised approach based on patient-specific modelling is a vision in a non distant future with a view to offer predictive tools, fill gaps in imaging capabilities and contribute to further understanding of disease progression. Finally, the development of specific haemodynamic patterns to be used during patients' follow up for comparison purposes would be an invaluable tool for continuity of care.

PART B:

Results, Discussion and Concluding Remarks

Chapter 7

Pressure-Volume Analysis as a Preoperative Planning Strategy for Treatment Optimisation and Outcome Prediction

7 Pressure-Volume Analysis as a Preoperative Planning Strategy for Treatment Optimisation and Outcome Prediction

7.1 Introduction

Although still far from clinical application on a daily basis (Pedrizzetti, 2015; Bluestein, 2017), patient-specific modelling has consistently shown significant potential (Morris, 2016; Doshi and Burkhoff, 2016; Duanmu, 2018). To overcome scepticism and gain wide acceptance, a model should be robust, realistic enough and easy to understand, with the ability to deliver reliable results within the time and constraints of clinical practice.

This chapter shows how a simulation approach for the optimisation of device-based treatment may help and guide therapeutic intervention in advanced heart failure (Capoccia, 2018a; Capoccia, 2018b). The clinician remains the ultimate decision-maker.

The management of advanced heart failure is demanding in view of the complex and challenging nature of these patients with often critical clinical presentation. A simulation-based approach with patient-specific modelling as a preoperative strategy may be used as an additional tool to guide therapeutic intervention in a clinical setting, aimed at treatment optimisation of these patients. Models based on pressure–volume relationship and lumped-parameter representation of the cardiovascular system may be a suitable choice given their simplicity and versatility (Ferrari, 2015; De Lazzari, 2014; De Lazzari and Pirckhalava, 2017; Ferrari, 1992; De Lazzari, 2005; De Lazzari and Quatember, 2016; De Lazzari, 2012). Although they provide less detailed predictions of pressure and flow waveforms, these models have shown great flexibility in simulating the haemodynamics of different cardiovascular conditions and therapeutic interventions with the potential to be run in real time on desktop, laptop or mobile devices (Doshi and Burkhoff, 2016). The successful clinical application of this approach requires further haemodynamics teaching to the medical community although its importance is still far from being fully appreciated (De Lazzari, 2012; Kozarski, 2008; Fresiello, 2015).

This approach has great potential for application in heart failure where the impact of left ventricular assist devices (LVADs) has played a significant role as a bridge to transplant and more recently as a long-term solution for non eligible candidates. Continuous flow rotary blood pumps are currently the most popular devices because of their smaller size, increased reliability and higher durability compared to pulsatile-flow devices. The trend towards their use is increasing.

The native ventricular behaviour can be modelled according to the time-varying elastance theory (Suga and Sagawa, 1972; Suga, 1973; Suga and Sagawa, 1974), which remains a landmark despite its limitations (Claessens, 2006) and previous criticism when applied to a mechanically supported left ventricle (Vandenberghe, 2006). Significant elastance changes are observed during circulatory support with a blood displacement pump because of extreme and fast changing loading conditions. Therefore, the relationship between elastance and contractility may be no longer applicable when a second pump is connected to the systemic circulation (Vandenberghe, 2006). Elastance changes are also observed with continuous flow pumps where an increasing pump flow is related to a constant end-systolic volume, a decrease in end-diastolic volume and a maximum left ventricular pressure increase with a gradual increase in the slope (*Ees*) of the end-systolic pressure–volume relationship (ESPVR) to justify dissociation between contractility and elastance (Vandenberghe, 2006). Although a linear model has been proven sufficiently accurate (Stergiopulos, 1996; Segers, 2000; Segers, 2001) and adequate for realistic simulations of the instantaneous pressure–volume relation (Lankhaar, 2009), recent multi-scale modelling of the cardiovascular system (Pironet, 2013) based on previously developed approaches (Negroni and Lascano, 1999; Smith, 2003; Smith, 2004) has successfully addressed the limitations of the time-varying elastance theory with particular reference to load-dependence of ESPVR. Further modelling techniques can describe a failing cardiovascular system (Luo, 2011) and ventricular interactions (Luo, 2008; Olansen, 2000; Chung, 1997). To address the shortcomings of the original time-varying elastance theory, a nonlinear time-varying lumped parameter model of the cardiovascular system (Ursino, 1998) can be modified to include the inter-ventricular septum and a rotor-dynamic, continuous flow LVAD (Wang, 2014). This is a more accurate heart failure model where the ESPVR is a unimodal function that takes into account the descending limb of the Frank–Starling curve, making it particularly suitable to study ventricular interactions and the leftward septal shift secondary to left ventricular decompression following LVAD insertion.

7.2 Pressure-Volume Analysis in a Clinical Setting

The value of a simulation approach was investigated in the context of six heart failure patients previously discussed at a multidisciplinary meeting with a view to predict or guide further management (Capoccia, 2018a; Capoccia, 2018b; De Lazzari, 2019; De Lazzari, 2019a). The preoperative haemodynamic status of these patients was reproduced. Then, simulations

were carried out in the presence of a ventricular assist device in order to evaluate their suitability for prolonged mechanical circulatory support or other intervention.

The aim was to compare the outcome of the simulations with the previously made clinical decision in order to investigate any relationship that may be applicable on a routine basis in future patient assessment.

The key elements would be:

- A more targeted approach for different groups of patients;
- More quantitative evaluation in the clinical decision process;
- The predictive value of simulation;
- Preoperative planning and treatment optimisation.

7.3 Material and Methods

The study was carried out using CARDIOSIM©, which is a software package developed by the Cardiovascular Numerical Modelling LAB linked to the Institute of Clinical Physiology, CNR, Rome, Italy (http://cardiosim.dsb.cnr.it/). This is a numerical simulator of the cardiovascular system based on lumped parameter models, modified time-varying elastance and pressure–volume analysis of ventricular function. The software is interactive and capable of reproducing physiological and pathological conditions for clinical decision-making in a controlled environment (De Lazzari, 2014; De Lazzari and Pirckhalava, 2017). The main feature is a modular approach with an updatable library of numerical models of different sections of the cardiovascular system, which can be assembled according to the need of the simulation. The software is particularly suitable to study the interactions with pulsatile or continuous flow ventricular assist devices (De Lazzari and Pirckhalava, 2017; De Lazzari, 2006a; De Lazzari, 2006b; De Lazzari, 1998), intra-aortic balloon pump, artificial lung, biventricular assist device and biventricular pacing (De Lazzari and Pirckhalava, 2017; De Lazzari and Quatember, 2016; Darowski, 1999; De Lazzari, 2001; De Lazzari, 2010).

The following equations describe the behaviour of the instantaneous left and right ventricular pressures $P_{LV}(t)$ and $P_{RV}(t)$:

$$\begin{cases} P_{LV}(t) = \dfrac{e_{ventrSPT}(t)\cdot e_{LV}(t)}{e_{ventrSPT}(t)+e_{LV}(t)}\cdot\left(V_{LV}(t)-V_{LV,0}\right)+\dfrac{e_{LV}(t)}{e_{ventrSPT}(t)+e_{LV}(t)}\cdot P_{RV}(t) \\ P_{RV}(t) = \dfrac{e_{ventrSPT}(t)\cdot e_{RV}(t)}{e_{ventrSPT}(t)+e_{RV}(t)}\cdot\left(V_{RV}(t)-V_{RV,0}\right)-\dfrac{e_{RV}(t)}{e_{ventrSPT}(t)+e_{RV}(t)}\cdot P_{LV}(t) \end{cases} \tag{7.1}$$

with:

$$e_{LV}(t) = E_{d,LV} + \frac{E_{s,LV} - E_{d,LV}}{2} a_{LV}(t)$$
$$e_{RV}(t) = E_{d,RV} + \frac{E_{s,RV} - E_{d,RV}}{2} a_{RV}(t) \quad (7.2)$$

where $e_{LV}(t)$ and $e_{RV}(t)$ are the left and right ventricular time-varying elastances, $e_{ventrSPT}(t)$ is the inter-ventricular septum systolic elastance, $V_{LV}(t)$ and $V_{RV}(t)$ are the instantaneous left and right ventricular volumes, $V_{LV,0}$ and $V_{RV,0}$ are the left and right rest volumes, $E_{s,LV}$ and $E_{s,RV}$ are the left and right ventricular systolic elastances, $E_{d,LV}$ and $E_{d,RV}$ are the left and right ventricular diastolic elastances. $a_{LV}(t)$ and $a_{RV}(t)$ are the left and right activation functions for ventricular contraction and relaxation phases defined as:

$$a_{LV}(t) = a_{RV}(t) = \begin{cases} 1 - \cos\left(\frac{t}{T_T}\pi\right) & 0 \le t \le T_T \\ 1 + \cos\left(\frac{t - T_T}{T_{TE} - T_T}\pi\right) & T_T < t \le T_{TE} \\ 0 & T_{TE} < t \le T \end{cases} \quad (7.3)$$

where T_{TE} is the end of ventricular systole, T_T is the peak time of the T wave in the ECG signal and T is the cardiac cycle duration. The inter-ventricular septum elastance ($e_{ventrSPT}(t)$) is derived as:

$$e_{ventrSPT}(t) = E_{d,ventrSPT} + \frac{E_{s,ventrSPT} - E_{d,ventrSPT}}{2} a_{ventrSPT}(t) \quad (7.4)$$

where $E_{s,ventrSPT}$ and $E_{d,ventrSPT}$ are the inter-ventricular septum systolic and diastolic elastances. The activation function $a_{ventrSPT}(t)$ is described as follows:

$$a_{ventrSPT}(t) = \begin{cases} 1 - \cos\left(\frac{t}{T_R}\pi\right) & 0 \le t \le T_R \\ 1 + \cos\left(\frac{t - T_R}{T_{TE} - T_R}\pi\right) & T_R < t \le T_{TE} \\ 0 & T_{TE} < t \le T \end{cases} \quad (7.5)$$

where T_R is the peak time of the R wave in the ECG signal.

The following equations describe the behaviour of the instantaneous left and right atrial pressures ($P_{LA}(t)$ and $P_{RA}(t)$):

$$\begin{cases} P_{LA}(t) = \dfrac{e_{atriaSPT}(t)\cdot e_{LA}(t)}{e_{atriaSPT}(t)+e_{LA}(t)}\cdot(V_{LA}(t)-V_{LA,0}) + \dfrac{e_{LA}(t)}{e_{atriaSPT}(t)+e_{LA}(t)}\cdot P_{RA}(t) + \dfrac{e_{atriaSPT}(t)}{e_{atriaSPT}(t)+e_{LA}(t)}\cdot P_{LA,0} \\ P_{RA}(t) = \dfrac{e_{atriaSPT}(t)\cdot e_{RA}(t)}{e_{atriaSPT}(t)+e_{RA}(t)}\cdot(V_{RA}(t)-V_{RA,0}) + \dfrac{e_{RA}(t)}{e_{atriaSPT}(t)+e_{RA}(t)}\cdot P_{LA}(t) + \dfrac{e_{atriaSPT}(t)}{e_{atriaSPT}(t)+e_{RA}(t)}\cdot P_{RA,0} \end{cases} \quad (7.6)$$

where $V_{LA}(t)$ ($V_{RA}(t)$) is the instantaneous left (right) atrial volume, $V_{LA,0}$ ($V_{RA,0}$) is the resting left (right) atrial volume, $P_{LA,0}$ ($P_{RA,0}$) is the resting left (right) atrial pressure. $e_{LA}(t)$ and $e_{RA}(t)$ are the left and right atrial time-varying elastances:

$$\begin{aligned} e_{LA}(t) &= E_{d,LA} + \frac{E_{s,LA}-E_{d,LA}}{2}a_{LA}(t) \\ e_{RA}(t) &= E_{d,RA} + \frac{E_{s,RA}-E_{d,RA}}{2}a_{RA}(t) \end{aligned} \quad (7.7)$$

where $E_{s,LA}$ and $E_{s,RA}$ are the left and right atrial systolic elastances, $E_{d,LA}$ and $E_{d,RA}$ are the left and right atrial diastolic elastances. The left and right atrial activation functions $a_{LA}(t)$ and $a_{RA}(t)$ are described as follows:

$$a_{LA}(t) = a_{RA}(t) = \begin{cases} 0 & 0 \le t \le T_{PB} \\ 1+\cos\left(\dfrac{t-T_{PB}}{T_{PE}-T_{PB}}2\pi\right) & T_{PB} < t \le T_{PE} \\ 0 & T_{PE} < t \le T \end{cases} \quad (7.8)$$

where T_{PB} (T_{PE}) is the beginning (end) of atrial depolarization (P wave in the ECG signal). The inter-atrial septum elastance ($e_{atriaSPT}(t)$) is derived as:

$$e_{atriaSPT}(t) = E_{d,atriaSPT} + \frac{E_{s,atriaSPT}-E_{d,atriaSPT}}{2}a_{atriaSPT}(t) \quad (7.9)$$

where $E_{s,atriaSPT}$ and $E_{d,atriaSPT}$ are the inter-atrial septum systolic and diastolic elastances. The activation function $a_{atriaSPT}(t)$ is defined as follows:

$$a_{atriaSPT}(t)=\begin{cases}0 & 0\le t\le T_{PB}\\ 1+\cos\left(\dfrac{t-T_{PB}}{T_{PE}-T_{PB}}2\pi\right) & T_{PB}<t\le T_{PE}\\ 0 & T_{PE}<t\le T\end{cases} \tag{7.10}$$

The Berlin Heart INCOR® Pump (Fig. 7.1) is the LVAD integrated in the software and used for the simulations. The INCOR® System is a unique pump specifically designed for long-term support (destination therapy) although it can be implanted as bridge to transplant and bridge to recovery.

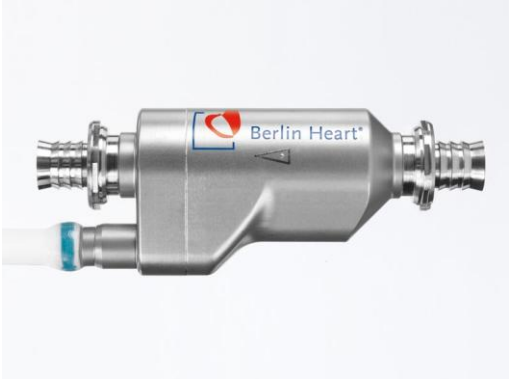

Figure 7.1 Berlin Heart INCOR® Pump. From: Capoccia M, De Lazzari C. Concepts, Mathematical Modelling and Applications in Heart Failure, 2019, Nova Science Publishers.

The blood flows from the left ventricle into the device through the inlet guide vane, which ensures laminar flow to the rotor. An active magnetic bearing enables the rotor to float contact-free and produce the required pumping work at 5000 to 10000 *rpm*. The outlet guide vane behind the rotor generates additional pressure with a specially aligned blade and directs the blood in the outlet cannula to the aorta. The INCOR® pump creates a constant blood flow which, in combination with the native left ventricle, leads to pulsatility in the patient.

An electric analogue of the device model is shown in Fig. 7.2.

P_{LV} is the left ventricular pressure and P_{AS} is the systemic arterial pressure in the circulatory network. The input and output pump cannulae are modelled with the resistances R_{vpi} and R_{vpo}, the compliances C_{vpi} and C_{vpo} and the inertances L_{vpi} and L_{vpo}. Q_{VAD} is the pump flow; Q_{vpi} and Q_{vpo} are the flows of the input and output cannulae. Q_{vpi} and Q_{vpo} can be calculated as follows:

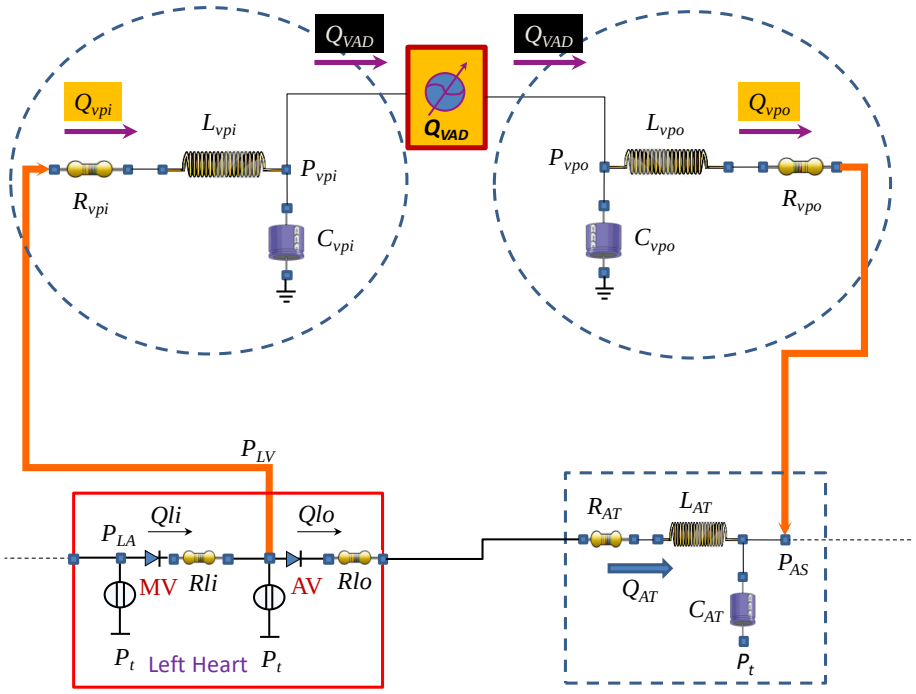

Figure 7.2 Electric analogue of the Berlin Heart INCOR® Pump. From: Capoccia M, De Lazzari C. Concepts, Mathematical Modelling and Applications in Heart Failure, 2019, Nova Science Publishers.

$$\begin{cases} \left(P_{LV}+P_t\right)-P_{vpi}=R_{vpi}\cdot Q_{vpi}+L_{vpi}\dfrac{dQ_{vpi}}{dt} \\ Q_{vpi}=Q_{VAD}+C_{vpi}\cdot\dfrac{dP_{vpi}}{dt} \end{cases} \tag{7.11}$$

$$\begin{cases} P_{vpo}-\left(P_{AS}+P_t\right)=R_{vpo}\cdot Q_{vpo}+L_{vpo}\dfrac{dQ_{vpo}}{dt} \\ Q_{vpo}=Q_{VAD}-C_{vpo}\cdot\dfrac{dP_{vpo}}{dt} \end{cases}$$

where P_{vpi} and P_{vpo} are the pressures at the inlet and outlet cannulae. P_t is the mean intrathoracic pressure.

The LVAD flow is derived as follows:

$$\begin{aligned} Q_{VAD} &= K_{vad,0}+\omega\cdot K_{vad,1}+K_{vad,2}\cdot\left(P_{vpo}-P_{vpi}\right)+K_{vad,3}\cdot\omega\cdot\left(P_{vpo}-P_{vpi}\right)+ \\ &+K_{vad,4}\cdot\omega^2\cdot\left(P_{vpo}-P_{vpi}\right)+K_{vad,5}\cdot\omega\cdot\left(P_{vpo}-P_{vpi}\right)^2+K_{vad,6}\cdot\omega^2\cdot\left(P_{vpo}-P_{vpi}\right)^2 \end{aligned} \tag{7.12}$$

where $K_{vad,i}$, i=1, 2, 3, 4, 5, 6, are constants and:

$$\omega(t)=A_0+A_p\cdot sin\left(\frac{2\pi t}{T}+\varepsilon_0\right) \tag{7.13}$$

A_0 is the component of the LVAD rotational speed, A_p is the amplitude of the pulsation component, ε_0 is the phase difference between the LVAD pulsation component and the native cardiac timing.

Table 7.1 shows the values of the parameters in Eqs. (7.11), (7.12) and (7.13) and the pump rotational speeds used in the simulations (Saltarocchi, 2018).

Table 7.1

	Inlet and Outlet Cannulae	
Parameter	**Value**	**Unit**
$\boldsymbol{C_{vpi}}$ **[**$\boldsymbol{C_{vpo}}$**]**	0.1 [0.1]	$mmHg^{-1} \cdot ml$
$\boldsymbol{R_{vpi}}$ **[**$\boldsymbol{R_{vpo}}$**]**	0.01 [0.01]	$mmHg \cdot s \cdot ml^{-1}$
$\boldsymbol{L_{vpi}}$ **[**$\boldsymbol{L_{vpo}}$**]**	$1.2 \cdot 10^{-4}$ [1.2×10^{-4}]	$mmHg \cdot s^2 \cdot ml^{-1}$
	LVAD	
Pump rotational speed	6000; 8900; 10000	*rpm*
$\boldsymbol{K_{vad,0}}$	19.51840	$L \cdot min^{-1}$
$\boldsymbol{K_{vad,1}}$	-3.0361×10^{-3}	$L \cdot min^{-1} \cdot rpm^{-1}$
$\boldsymbol{K_{vad,2}}$	-1.23045	$L \cdot min^{-1} \cdot mmHg^{-1}$
$\boldsymbol{K_{vad,3}}$	5.78974×10^{-4}	$L \cdot min^{-1} \cdot rpm^{-1} \cdot mmHg^{-1}$
$\boldsymbol{K_{vad,4}}$	-5.8777×10^{-8}	$L \cdot min^{-1} \cdot rpm^{-2} \cdot mmHg^{-1}$
$\boldsymbol{K_{vad,5}}$	-1.27359×10^{-6}	$L \cdot min^{-1} \cdot rpm^{-1} \cdot mmHg^{-2}$
$\boldsymbol{K_{vad,6}}$	2.04834×10^{-10}	$L \cdot min^{-1} \cdot rpm^{-2} \cdot mmHg^{-2}$

The cardiovascular network shown in Figure 7.3 has been assembled in the software to carry out the simulations discussed in this chapter (Saltarocchi, 2018). As shown in Fig. 7.3, the systemic arterial section consists of three RLC elements representing the aortic (R_{AT}, L_{AT} and C_{AT}), thoracic (R_{TT}, L_{TT} and C_{TT}) and abdominal (R_{ABT}, L_{ABT} and C_{ABT}) compartment. Ras is the variable systemic peripheral resistance. The main (small) pulmonary section is reproduced by a RLC element: $Rpam$, $Lpam$ and $Cpam$ ($Rpas$, $Lpas$ and $Cpas$). The arteriole (capillary) bed behaviour is reproduced by a single resistance $Rpar$ (Rpc). The pulmonary venous section consists of a compliance (Cvp) and a resistance (Rvp). P_t is the mean intrathoracic pressure. The systemic venous section is modelled with the compliance Cvs

and the two resistances $Rvs1$ and $Rvs2$. Each valve is modelled as a diode with a resistance, assuming a unidirectional blood flow. Rli and Rlo represent the resistances of the mitral and aortic valves (MV and AV); Rri and Rro are the resistances of the pulmonary and tricuspid valves (PV and TV).

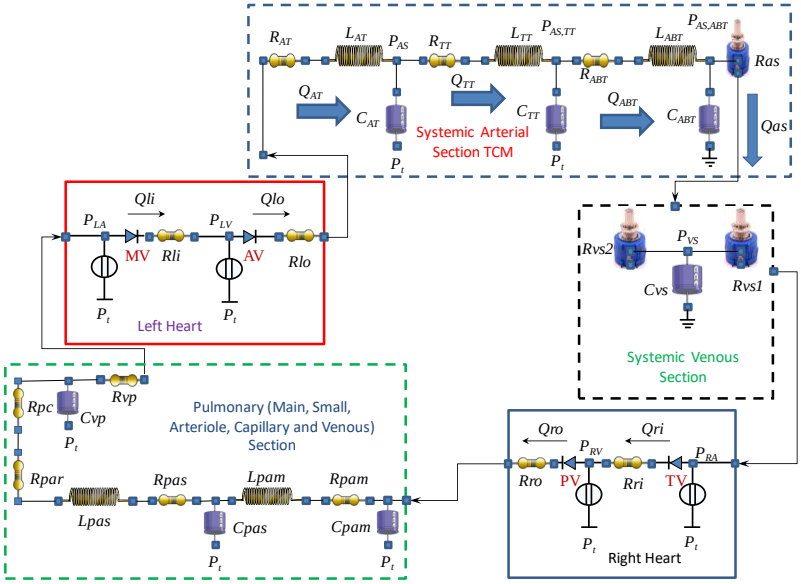

Figure 7.3 Electric analogue of the cardiovascular system used to carry out the simulations. From: Capoccia M, De Lazzari C. Concepts, Mathematical Modelling and Applications in Heart Failure, 2019, Nova Science Publishers.

7.4 Results

Patient #1

A 34-year-old female patient with severe left ventricular systolic dysfunction (LVEF 27%) secondary to extensive anterior wall myocardial infarction, which was treated with percutaneous coronary intervention and stent insertion to the left anterior descending coronary artery with only partial benefit. Co-morbidities, including high body mass index (BMI), were considered prohibitive for heart transplantation; LVAD insertion considered unlikely to be beneficial; likely need for temporary RVAD support in view of reduced right ventricular stroke work index ($RVSWI$). The outcome of the multidisciplinary team (MDT) meeting was to maintain this patient on medical treatment without any further intervention.

Table 7.2 shows baseline haemodynamic parameters measured from right heart catheterisation (RHC) and echocardiogram on admission with the results obtained after simulation of baseline parameters and LVAD support (Capoccia, 2018a). The E_a/E_{es} ratio is a reliable index of ventricular-arterial coupling as previously discussed. Cardiac output (CO) after the simulation

consists of three values: the total Cardiac Output (TOT), the left ventricular output flow (CO_{ventr}) and the LVAD output flow (Q_{VAD}). The pulmonary vascular resistance (PVR) consists of two different values: the first one is calculated as the ratio between the trans-pulmonary gradient (TPG) and CO_{ventr}; the second one is calculated as the ratio between TPG and Q_{VAD}.

Table 7.2									
Patient #1	**Measured [RHC 1]**			**Simulation [RHC 1]**			**LVAD (Simulation)**		
	Max	**Min**	**Mean**	**Max**	**Min**	**Mean**	**Max**	**Min**	**Mean**
BP **[mmHg]**	85-90	59	69.3	87.2	60.7	69.3	75.2	62.9	68.2
P_{RA} **[mmHg]**	35	17	29	10.5	3.5	6.5	10.3	3.5	6.5
P_{RV} **[mmHg]**	61	14	38	44.2	8.0	20.4	43.5	8.0	20.1
PA **[mmHg]**	62.0	30.0	42.0	44.0	39.7	42.0	43.3	38.7	40.9
$PCWP$ **[mmHg]**	36.0	21.0	32.0	31	18.7	25.0	29.6	16.8	23.1
HR **[bpm]**	100			100			100		
EF_{LV}	27%			26.9%			31.4%		
BSA **[m^2]**	1.98			1.98			1.98		
CO **[L/min]**	2.7			2.7			CO_{VENTR} 0.67 Q_{VAD} 2.15 TOT 2.82		
CI **[L/min/m^2]**	1.36			1.36			0.34		
TPG **[mmHg]**	10			17			18		
PVR **[wood unit]**	3.7			6.3			26.87 (18.0/0.67) 6.38 (18.0/2.15)		
$RVSWI$ **[g/m^2/beat]**	2.4			6.53			6.86		
	Estimated			Simulated			Simulated		
V_{ed} **[ml]**	**~100**			**100.4**			**89.76**		
V_{es} **[ml]**	**~73**			**73.4**			**61.57**		
E_a **[mmHg/ml]**	**~3.0**			**3.2**			**2.6**		
E_{es} **[mmHg/ml]**	-			**0.88**			**0.88**		
E_a/E_{es}	-			**3.64**			**2.95**		

Simulation of LVAD support at 6000 *rpm* shows a reduction in V_{ed} (10%) and in V_{es} (16%) leading to a leftward shift of the left PV loop. Left ventricular unloading is also related to the pulmonary arterial pressure (PA), which shows a 2.5% reduction from its baseline simulated value. The arterial elastance (E_a) decreases to 2.6 *mmHg/ml* and the E_a/E_{es} ratio decreases to 2.95. These effects are induced by the presence of the pump with changes in total peripheral resistance. The (total) CO improves slightly reaching a value of 2.82 *L/min* with only 0.67 *L/min* provided by the native ventricle and the remaining 2.15 *L/min* provided by the LVAD. Further increase in total

cardiac output is not observed despite changes in the LVAD rotational speed. The left ventricular ejection fraction (LVEF) shows only a slight increase of 4.4%. Patient 1 is a typical example of difficult clinical decision-making. Co-morbidities do play a role and must be taken into account during the MDT meeting. The simulation outcome for patient 1 does show a leftward shift of the pressure–volume loops for the left and right ventricles with adequate ventricular volumes (Fig. 7.4), although the gain in ejection fraction may be initially limited. Nevertheless, it is true that further improvement is observed over a period of time (Capoccia, 2015) making LVAD insertion a suitable option for this patient.

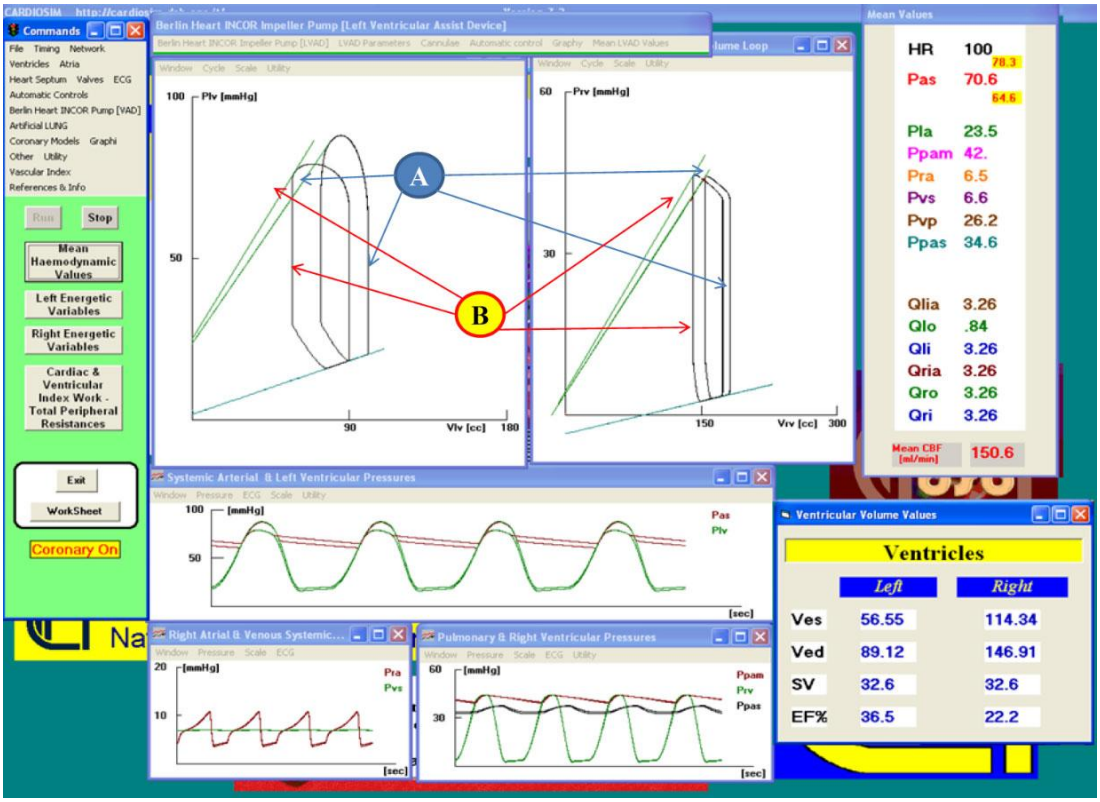

Figure 7.4 Simulation outcome for patient #1. Circle A (B) marks the left (left upper panel) and right (right upper panel) ventricular PV loop representing the diseased (assisted) status. The effects of drug administration were also simulated during LVAD support by increasing the ESPVR slope and decreasing the systemic and pulmonary resistance. From: Capoccia, 2018a J Biomed Eng Informatics.

Because of the potential complications related to the associated co-morbidities, the unanimous clinical decision to decline any further intervention but continue with medical treatment and eventually palliation may have been the way forward. Further argument in favour of LVAD insertion would be the recent evidence supporting the “obesity paradox” in cardiac surgery (Mariscalco, 2017), which is currently the subject of a hot

debate. The value of simulation on this occasion is the provision of haemodynamic data confirming the limited gain from LVAD insertion, which was only assumed during the MDT meeting.

Patient #2

Table 7.3												
Patient #2	**Measured [RHC 1]**			**Simulation [RHC 1]**			**LVAD (Simulation)**			**LVAD + Milrinone (10%) (Simulation)**		
	Max	**Min**	**Mean**	**Max**	**Min**	**Mean**	**Max**	**Min**	**Mean**	**Max**	**Min**	**Mean**
BP **[mmHg]**	95-100	58	72	97.2	60.5	72	81.7	63.3	70.6	82.2	62.6	70.5
P_{RA} **[mmHg]**	14.0	2.0	9.0	14.9	5.4	10.0	14.9	5.5	10.0	15.2	5.3	10.1
P_{RV} **[mmHg]**	39.0	2.0	17.0	33.5	5.0	14.8	33.6	5.4	15.9	33.4	3.7	14.9
PA **[mmHg]**	40.0	17.0	27.0	33.0	14.4	23.2	32.2	13.3	22.5	32.9	12.7	22.6
$PCWP$ **[mmHg]**	28.0	7.0	18.0	26.6	8.9	14.3	25.9	7.9	13.4	27.3	7.6	13.6
HR **[bpm]**	65			65			65			65		
EF_{LV}	45%			45.1%			49.8%			55.9%		
BSA **[m^2]**	2.35			2.35			2.35			2.35		
CO **[L/min]**	5.3			5.3			CO_{VENTR} 1.72 Q_{VAD} 3.67 TOT 5.39			CO_{VENTR} 2.04 Q_{VAD} 3.92 TOT 5.96		
CI **[L/min/m^2]**	2.26			2.26			0.73			0.82		
TPG **[mmHg]**	9			8.9			9.1			9.0		
PVR **[wood unit]**	1.7			1.68			5.3 (9.1/1.72) 2.48 (9.1/3.67)			4.41 (9.0/2.04) 2.30 (9.0/3.92)		
$RVSWI$ **[g/m^2/beat]**	8.5			6.23			6.0			6.63		
	Estimated			Simulated			Simulated			Simulated		
V_{ed} **[ml]**	**~181**			**180.74**			**166.4**			**163.83**		
V_{es} **[ml]**	**~99.6**			**99.2**			**83.5**			**72.2**		
E_a **[mmHg/ml]**	**~1.1**			**1.1**			**0.9**			**0.9**		
E_{es} **[mmHg/ml]**	-			**0.68**			**0.68**			**0.748**		
E_a/E_{es}	-			**1.62**			**1.32**			**1.2**		

A 55-year-old male patient with hypertrophic cardiomyopathy in previous aortic valve replacement with mechanical prosthesis and subsequent development of critical stenosis of the left anterior descending coronary artery treated with percutaneous coronary intervention. LVEF 45% in the context of chronic atrial fibrillation, history of ventricular arrhythmias and renal impairment. Symptoms deterioration had required multiple hospital admissions and significant increase of the anti-failure treatment. Finally,

commenced on milrinone infusion. Considered unsuitable for LVAD insertion; listed for heart transplant.

Table 7.3 shows the baseline haemodynamic parameters measured from right heart catheterisation and echocardiogram on admission with the results obtained after simulation of baseline parameters and LVAD support. The effect of Milrinone administration was also considered.

Simulation of the haemodynamic status on admission shows comparable mean values with those measured during right heart catheterization. LVAD support at 6000 *rpm* shows significantly improved EF_{LV}, particularly after Milrinone administration (49.8% vs 55.9%) with a reduction in V_{ed} (9%) and in V_{es} (8%) and a subsequent leftward shift of the PV loop. Global cardiac performance also improves as demonstrated by the slight decrease in the E_a/E_{es} ratio to 1.32 (1.2 with Milrinone) and in E_a (0.9 *mmHg/ml*). The total CO is 5.39 (5.96 with Milrinone) *L/min*, with 1.72 (2.04 with Milrinone) *L/min* provided by the native left ventricle and 3.67 (3.92) *L/min* provided by the LVAD. Simulation of the baseline haemodynamic status for patient 2 shows comparable mean values with those measured during right heart catheter. LVAD support shows improved left ventricular ejection fraction with some reduction in pulmonary artery pressures. Figure 7.5 shows the simulation outcome for patient #2 (Capoccia, 2018b).

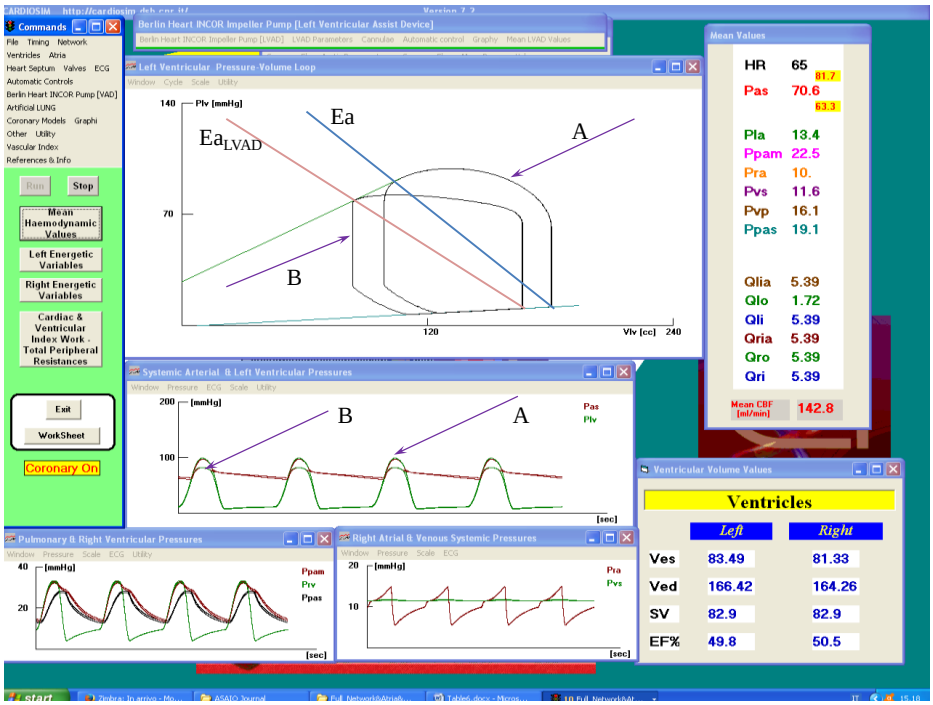

Figure 7.5 Screen output obtained from CARDIOSIM© showing baseline (PV loop A) and assisted status (PV loop B) for patient #2. From: Capoccia M, De Lazzari C. Concepts, Mathematical Modelling and Applications in Heart Failure, 2019, Nova Science Publishers.

Patient #3

A 52-year-old male patient with severe left ventricular systolic and diastolic dysfunction with dilated left ventricle and LVEF 15% in previous myocardial infarction requiring coronary artery bypass grafting and subsequent insertion of internal cardioverter defibrillator. Pulmonary hypertension and deterioration of symptoms required Milrinone and diuretics infusion with the insertion of intra-aortic balloon pump. Placed on the transplant list with a view to LVAD insertion if further deterioration. Table 7.4 shows baseline haemodynamic parameters measured from right heart catheterisation and echocardiogram on admission with the results obtained after simulation of baseline parameters and LVAD support at 6000 *rpm*.

Table 7.4

Patient #3	**Measured [RHC 1]**			**Simulation [RHC 1]**			**LVAD (Simulation)**			**LVAD + Milrinone (10%) (Simulation)**		
	Max	**Min**	**Mean**	**Max**	**Min**	**Mean**	**Max**	**Min**	**Mean**	**Max**	**Min**	**Mean**
BP [$mmHg$]	100	60	73.3	106.7	60	73.4	82.8	66.6	74.1	85.2	67.4	74.6
P_{RA} [$mmHg$]	14	12	9.0	8.8	1.7	4.4	9.0	1.7	4.6	9.2	0.5	4.6
P_{RV} [$mmHg$]	53	5.0	-	33.0	1.0	11.6	31.5	1.0	11.3	32.4	0.5	11.6
PA [$mmHg$]	58.0	27.0	37.0	32.8	22.6	28.0	31.3	20.4	26.2	32.2	19.9	26.5
$PCWP$ [$mmHg$]	39.0	29.0	31.0	28.4	12.3	18.0	26.8	9.5	15.4	28.0	8.9	15.5
HR [bpm]	75			75			75			75		
EF_{LV}	15%			15%			18.9%			21.9%		
BSA [m^2]	2.16			2.16			2.16			2.16		
CO [L/min]	4.2			4.2			CO_{VENTR} 0.74 Q_{VAD} 3.8 TOT 4.54			CO_{VENTR} 0.93 Q_{VAD} 4.22 TOT 5.15		
CI [$L/min/m^2$]	1.94			1.94			0.34			0.43		
TPG [$mmHg$]	6			10.0			10.8			11		
PVR [$wood\ unit$]	1.43			2.38			14.6 (10.8/0.74) 2.84 (10.8/3.8)			11.83 (11/0.93) 2.61 (11/4.22)		
$RVSWI$ [$g/m^2/beat$]	9.87			8.32			8.23			9.47		
	Estimated			Simulated			Simulated			Simulated		
V_{ed} [ml]	**~373**			**372.53**			**320.16**			**313.74**		
V_{es} [ml]	**~317**			**316.55**			**259.6**			**245.0**		
E_a [$mmHg/ml$]	**~1.6**			**1.9**			**1.3**			**1.2**		
E_{es} [$mmHg/ml$]	-			**0.4**			**0.4**			**0.44**		
E_a/E_{es}	-			**4.75**			**3.25**			**2.73**		

Despite some variability between measured and simulated parameters on admission, the outcome after the simulations is mostly favourable. EF_{LV} increases after LVAD support to 19% (22% with Milrinone administration) with 14% reduction in V_{ed} (16% with Milrinone), 18% reduction in V_{es} (22.5% with Milrinone) and a leftward shift of the PV loop. The lower E_a, which decreases to 1.3 (1.2 with Milrinone) *mmHg/ml*, gives a better ventricular-arterial coupling; the E_a/E_{es} ratio decreases to 3.25 (2.73) from its simulated starting value of 4.75. The total CO is 4.54 (5.15 with Milrinone) *L/min*, with 3.8 (4.22) *L/min* provided by the LVAD and 0.74 (0.93) *L/min* provided by the native left ventricle.

The outcome for patient 3 is most beneficial with significant reduction of pulmonary artery pressures confirming the primary indication for LVAD support to achieve pulmonary haemodynamics compatible with transplantation.

Patient #4

A 29-year-old male patient with dilated cardiomyopathy and severe left ventricular systolic dysfunction (LVEF 21%). Deterioration of symptoms with multiple hospital admissions despite the highest medical treatment required LVAD support followed by heart transplant 12 months later.

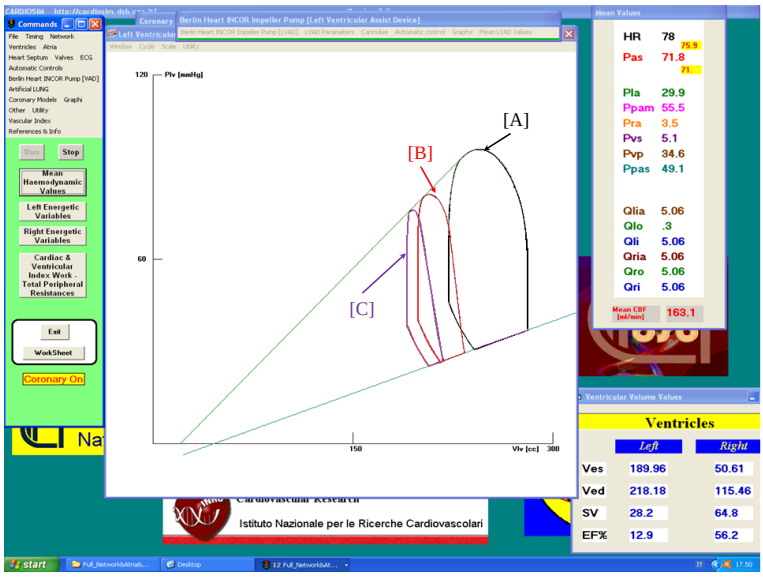

Figure 7.6 Screen output from CARDIOSIM© for patient #4. Left ventricular pressure-volume loops on admission (PV loop [A]), with LVAD at 8900 *rpm* (PV loop [B]) and 6000 *rpm* (PV loop [C]) are shown in the middle window. The simulations were performed without considering the effects induced by Milrinone. From: Capoccia M, De Lazzari C. Concepts, Mathematical Modelling and Applications in Heart Failure, 2019, Nova Science Publishers.

Table 7.5 and 7.6 show baseline haemodynamic parameters measured from right heart catheterisation and echocardiogram on admission with the results obtained after simulation of baseline parameters and LVAD support at 8900 *rpm* and 6000 *rpm*. The effect of Milrinone administration is also considered (Saltarocchi, 2018).

Table 7.5									
Patient #4	**Measured [RHC 1]**			**Simulation [RHC 1]**			**LVAD [8900 *rpm*] (Simulation)**		
	Max	**Min**	**Mean**	**Max**	**Min**	**Mean**	**Max**	**Min**	**Mean**
BP [*mmHg*]	85	69.6	59	94.0	69.6	60.0	80.6	68.0	71.0
P_{RA} [*mmHg*]	-	-	8.0	-	-	3.6	-	-	3.5
P_{RV} [*mmHg*]	60	9.0	30	65	1.0	19	61.4	1.0	18.0
PA [*mmHg*]	64	34.0	49.0	-	-	55.4	-	-	50
$PCWP$ [*mmHg*]	-	-	39.0	-	-	37.3	-	-	31.6
HR [*bpm*]	78			78			78		
EF_{LV}	21%			21%			15.1%		
BSA [m^2]	1.83			1.83			1.83		
CO [*L/min*]	4.6			4.6			CO_{VENTR} 1.13		
							Q_{VAD} 3.82		
							TOT 4.95		
CI [*L/min/m*^{2}]	2.51			2.51			0.62		
TPG [*mmHg*]	10			18.4			18.4		
PVR [*wood unit*]	2.17			4.0			16.28 (18.4/1.13)		
							4.82 (18.4/3.82)		
$RVSWI$ [*g/m*^{2}*/beat*]	17.97			22.7			21.93		
	Estimated			Simulated			Simulated		
V_{ed} [*ml*]	**~280.8**			**280.7**			**233.7**		
V_{es} [*ml*]	**~221.8**			**221.7**			**198.4**		
E_a [*mmHg/ml*]	**~1.3**			**1.6**			**2.3**		
E_{es} [*mmHg/ml*]	-			**0.468**			**0.468**		
E_a/E_{es}	-			**3.42**			**4.91**		

Simulated admission parameters show comparable mean values with those measured during right heart catheterisation. LVEF decreases to 15% after LVAD support at 8900 rpm (18.3% with Milrinone administration; 18.3% at 6000 rpm with Milrinone administration), with 18% reduction in V_{ed} (19.5%; 24%), 10% reduction in V_{es} (17%; 19.5%) and a leftward shift of the PV loop. E_a increases to 2.3 mmHg/ml at 8900 rpm (2.0 mmHg/ml with Milrinone; 2.3 mmHg/ml at 6000 rpm with Milrinone) with an increase in E_a/E_{es} ratio to 4.91 (3.88; 4.47). The total CO is 4.95 L/min at 8900 rpm (5.42 with Milrinone;

5.42 at 6000 rpm with Milrinone) with 1.13 (1.6; 0.77) L/min provided by the native left ventricle and 3.82 (3.82; 4.74) L/min provided by the LVAD.

Figure 7.6 shows the screen output obtained using CARDIOSIM© software for patient #4 (Saltarocchi 2018). The main window in the figure compares the cardiac cycle in different situations in terms of PV loops. The [A] loop shows the baseline setting on admission; the [B] loop shows simulated conditions with LVAD at 8900 rpm; the [C] loop shows simulated conditions with LVAD at 6000 rpm. The right upper box shows the simulated mean hemodynamic parameters during LVAD support at 6000 rpm. The right lower box shows V_{ed}, V_{es}, stroke volume SV and $EF\%$.

Table 7.6

Patient #4	**LVAD [8900 *rpm*] + Milrinone (10%) (Simulation)**			**LVAD [6000 *rpm*] + Milrinone (10%) (Simulation)**		
	Max	**Min**	**Mean**	**Max**	**Min**	**Mean**
BP [*mmHg*]	82	67	71	78	69	71
P_{RA} [*mmHg*]	-	-	3.6	-	-	3.6
P_{RV} [*mmHg*]	60.0	1.0	18.0	59.0	1.0	17.0
PA [*mmHg*]	-	-	49	-	-	48
$PCWP$ [*mmHg*]	-	-	30.4	-	-	29
HR [*bpm*]	78			78		
EF_{LV}	18.3			18.3		
BSA [m^2]	1.83			1.83		
CO [*L/min*]	CO_{VENTR} 1.6			CO_{VENTR} 0.77		
	Q_{VAD} 3.82			Q_{VAD} 4.74		
	TOT 5.42			TOT 5.51		
CI [*L/min/m*^{2}]	0.87			0.42		
TPG [*mmHg*]	18.6			19.0		
PVR [*wood unit*]	11.6 (18.6/1.6)			24.68 (19/0.77)		
	4.87 (18.6/3.82)			4.01 (18/4.74)		
$RVSWI$ [*g/m*^{2}*/beat*]	23.44			23.31		
	Simulated			Simulated		
V_{ed} [*ml*]	**225.5**			**212.4**		
V_{es} [*ml*]	**184.2**			**178.4**		
E_a [*mmHg/ml*]	**2.0**			**2.3**		
E_{es} [*mmHg/ml*]	**0.515**			**0.515**		
E_a/E_{es}	**3.88**			**4.47**		

Patient #5

A 58-year-old male patient with ischaemic cardiomyopathy and left ventricular systolic dysfunction (LVEF 36%). Multiple hospital admissions because of significant deterioration of the clinical picture requiring LVAD insertion.

Table 7.7									
Patient #5	**Measured [RHC 1]**			**Simulation [RHC 1]**			**LVAD [8900 *rpm*] (Simulation)**		
	Max	**Min**	**Mean**	**Max**	**Min**	**Mean**	**Max**	**Min**	**Mean**
BP [*mmHg*]	112	68	82	114	69	82	96.7	68.0	82
P_{RA} [*mmHg*]	-	-	12.0	-	-	6.4	-	-	6.6
P_{RV} [*mmHg*]	71	23	39	59	8.0	21	55	8	20
PA [*mmHg*]	67	27	43	55	45	50	51	42	47
$PCWP$ [*mmHg*]	41	20	32	42	14	30	38	10	25.5
HR [*bpm*]	80			80			80		
EF_{LV}	36%			35.9%			28.8%		
BSA [m^2]	1.88			1.88			1.88		
CO [*L/min*]	5.4			5.4			CO_{VENTR} 1.86		
							Q_{VAD} 3.78		
							TOT 5.64		
CI [*L/min/m*^{2}]	2.87			2.87			0.99		
TPG [*mmHg*]	11			20			18.4		
PVR [*wood unit*]	2.04			3.7			16.28 (18.4/1.13)		
							4.82 (18.4/3.82)		
$RVSWI$ [*g/m*^{2}*/beat*]	15.14			21.24			21.93		
	Estimated			Simulated			Simulated		
V_{ed} [*ml*]	**~187.5**			**188**			**154.3**		
V_{es} [*ml*]	**~120**			**120**			**109.9**		
E_a [*mmHg/ml*]	**~1.49**			**1.6**			**2.1**		
E_{es} [*mmHg/ml*]	-			**1.0**			**1.0**		
E_a/E_{es}	-			**1.6**			**2.1**		

Table 7.7 and 7.8 show baseline haemodynamic parameters measured from right heart catheterisation and echocardiogram on admission with the results obtained after simulation of baseline parameters and LVAD support at 8900 *rpm* and 6000 *rpm*. The effect of Milrinone administration is also considered. Some variability between measured and simulated admission parameters is observed with particular reference to the right heart haemodynamic parameters. LVEF drops to 28.8% during LVAD support at 8900 *rpm* (33.2% with Milrinone; 29.5% at 6000 *rpm* with Milrinone) with 18% reduction in V_{ed}

(22%; 28%), 8.5% reduction in V_{es} (18.5%, 20.5%) and a leftward shift of the PV loop. E_a increases to 2.1 *mmHg/ml* at 8900 *rpm* (1.9 *mmHg/ml* with Milrinone; 2.2 *mmHg/ml* at 6000 *rpm* with Milrinone) with concomitant increase in the E_a/E_{es} ratio to 2.1 (1.73; 2.0). The Total CO is 5.64 *L/min* at 8900 *rpm* (5.42 *L/min* with Milrinone; 6.03 *L/min* at 6000 *rpm* with Milrinone) with 1.86 (1.6; 1.25) *L/min* provided by the left ventricle and 3.78 (3.82; 4.78) *L/min* provided by the LVAD.

Table 7.8

Patient #5	**LVAD [8900 *rpm*] + Milrinone (10%) (Simulation)**			**LVAD [6000 *rpm*] + Milrinone (10%) (Simulation)**		
	Max	**Min**	**Mean**	**Max**	**Min**	**Mean**
BP [*mmHg*]	94.5	73.3	79	90	76,2	79.2
P_{RA} [*mmHg*]	-	-	6.8	-	-	6.8
P_{RV} [*mmHg*]	53	2	19.9	5	1	20
PA [*mmHg*]	49	39	44	48	38	43.6
$PCWP$ [*mmHg*]	37.4	10	24	36	9	23
HR [*bpm*]	80			80		
EF_{LV}	33.2			29.5		
BSA [m^2]	1.88			1.88		
CO [*L/min*]	CO_{VENTR} 1.6			CO_{VENTR} 1.25		
	Q_{VAD} 3.82			Q_{VAD} 4.78		
	TOT 5.42			TOT 6.03		
CI [*L/min/m^2*]	1.17			0.67		
TPG [*mmHg*]	20.4			20.6		
PVR [*wood unit*]	5.37 (20.4/3.8)			24.68 (19/0.77)		
	9.32 (20.4/2.19)			4.01 (18/4.74)		
$RVSWI$ [*g/m^2/beat*]	20.37			20		
	Simulated			Simulated		
V_{ed} [*ml*]	**146.3**			**135.7**		
V_{es} [*ml*]	**97.7**			**95.6**		
E_a [*mmHg/ml*]	**1.9**			**2.2**		
E_{es} [*mmHg/ml*]	**1.1**			**1.1**		
E_a/E_{es}	**1.73**			**2.0**		

The data plotted in Fig. 7.7 were obtained from the left ventricular instantaneous pressure and volume stored in an Excel file during the simulation. The PV loops represent the cardiac cycle in three specific situations: conditions on admission (continuous line); simulation conditions with LVAD at 8900 *rpm* and Milrinone (dashed line); simulation conditions with LVAD at 6000 *rpm* and Milrinone (dotted line).

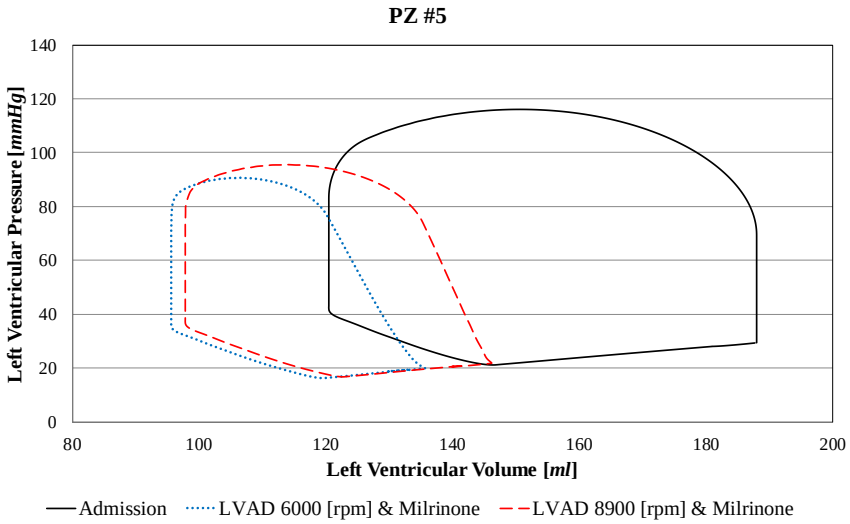

Figure 7.7 Left ventricular PV loop in patient #5. Admission (continuous line), LVAD assistance at 8900 *rpm* (dashed line) and at 6000 *rpm* (dotted line). Milrinone administration effects were also simulated during the assistance. From: Capoccia M, De Lazzari C. Concepts, Mathematical Modelling and Applications in Heart Failure, 2019, Nova Science Publishers.

Patient #6

A 51-year-old male with ischaemic cardiomyopathy and severe left ventricular systolic dysfunction (LVEF 21%). Significant deterioration of symptoms required LVAD insertion.

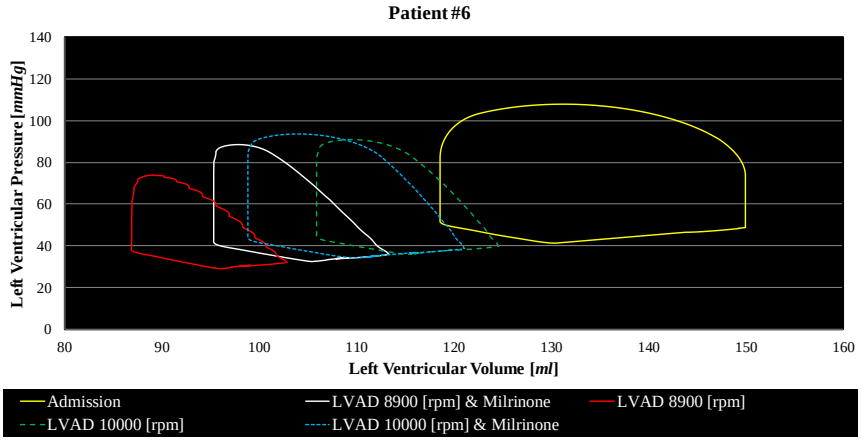

Figure 7.8 PV loops in patient #6. From right to left: status on admission; simulated conditions with: LVAD support at 10000 rpm; LVAD support at 10000 rpm and Milrinone administration; LVAD support at 8900 rpm and Milrinone administration; LVAD support at 8900 rpm. From: Capoccia M, De Lazzari C. Concepts, Mathematical Modelling and Applications in Heart Failure, 2019, Nova Science Publishers.

Table 7.9 and 7.10 show baseline haemodynamic parameters measured from right heart catheterisation and echocardiogram on admission with the

results obtained after simulation of baseline parameters and LVAD support at 8900 *rpm* and 10000 *rpm*.

Table 7.9									
Patient #6	**Measured [RHC 1]**			**Simulation [RHC 1]**			**LVAD [8900 *rpm*] (Simulation)**		
	Max	**Min**	**Mean**	**Max**	**Min**	**Mean**	**Max**	**Min**	**Mean**
BP **[*mmHg*]**	106	70	82	107	73	82	91.2	89.6	90.6
P_{RA} **[*mmHg*]**	-	-	14.0	-	-	5	-	-	4.7
P_{RV} **[*mmHg*]**	57	10	23	64	2	20	54	1	18
PA **[*mmHg*]**	68	41	53	55	45	58	49	44	46.7
$PCWP$ **[*mmHg*]**	-	-	49	-	-	47	-	-	32.4
HR **[*bpm*]**	102			102			102		
EF_{LV}	21%			21%			15.5%		
BSA **[m^2]**	2.02			2.02			2.02		
CO **[*L/min*]**	3.2			3.2			CO_{VENTR}	0	
							Q_{VAD}	3.79	
							TOT	3.79	
CI **[*L/min/*m^2]**	1.6			1.57			-		
TPG **[*mmHg*]**	4			11			14.3		
PVR **[*wood unit*]**	1.25			3.44			-		
							3.77 (14.3/3.79)		
$RVSWI$ **[*g/*m^2*/beat*]**	8.16			11.1			10.4		
	Estimated			Simulated			Simulated		
V_{ed} **[*ml*]**	**~149.4**			**149.9**			**103**		
V_{es} **[*ml*]**	**~118**			**118**			**87**		
E_a **[*mmHg/ml*]**	**~3.04**			**3.3**			**4.6**		
E_{es} **[*mmHg/ml*]**	-			**0.961**			**0.961**		
E_a/E_{es}	-			**3.43**			**4.79**		

A difference is observed between some simulated and admission parameters (such as P_{RA}, PA, PVR). LVEF decreases to 15.5% during simulated LVAD support at 8900 *rpm* (16% with Milrinone; 18.3 at 10000 *rpm* with Milrinone) with 31% reduction in V_{ed} (24,5%; 19%), 26% reduction in V_{es} (19%; 16%) and subsequent leftward shift of the PV loop. $PCWP$ drops to 32.4 (36; 38) *mmHg*; PA pressure also drops to 46.7 *mmHg* during LVAD support at 8900 *rpm*. E_a increases to 4.6 *mmHg/ml* at 8900 *rpm* (4.9 *mmHg/ml* with Milrinone; 4.2 *mmHg/ml* at 10000 *rpm* with Milrinone) leading to an increase in E_a/E_{es} ratio to 4.79 (4.64; 3.97). The total CO increases to 3.79 *L/min* during LVAD support at 8900 *rpm* (3.94 with Milrinone; 3.85 at 10000 *rpm* with Milrinone), but with no flow (0.14; 0.73 *L/min*) provided by the native left ventricle and 3.79 (3.8; 3.12) *L/min* provided completely by the LVAD.

Data plotted in Fig. 7.8 were obtained from the left ventricular instantaneous pressure and volume stored in an Excel file during the simulation. The PV loops represent the cardiac cycle in five specific situations: From right to left: "Admission" conditions; simulated conditions with LVAD support at 10000 rpm; simulated conditions with LVAD support at 10000 rpm and Milrinone administration; simulated conditions with LVAD support at 8900 rpm and Milrinone administration; simulated conditions with LVAD support at 8900 rpm.

Table 7.10

Patient #6	**LVAD [8900 *rpm*] + Milrinone (10%) (Simulation)**			**LVAD [10000 *rpm*] + Milrinone (10%) (Simulation)**		
	Max	**Min**	**Mean**	**Max**	**Min**	**Mean**
BP **[*mmHg*]**	88	84	85	93	82	85
P_{RA} **[*mmHg*]**	-	-	4.7	-	-	4.7
P_{RV} **[*mmHg*]**	56	1	18	57	2	19
PA **[*mmHg*]**	51	46	49	53	48	51
$PCWP$ **[*mmHg*]**	-	-	36	-	-	38
HR **[*bpm*]**	102			102		
EF_{LV}	16			18.3		
BSA **[m^2]**	2.04			2.04		
CO **[*L/min*]**	CO_{VENTR} 0.14			CO_{VENTR} 0.73		
	Q_{VAD} 3.8			Q_{VAD} 3.12		
	TOT 3.94			TOT 3.85		
CI **[*L/min/m^2*]**	0.07			0.36		
TPG **[*mmHg*]**	13			13		
PVR **[*wood unit*]**	3.42 (13/3.8)			4.17 (13/3.12)		
	92.86 (13/0.14)			17.81 (13/0.73)		
$RVSWI$ **[*g/m^2/beat*]**	11.41			11.65		
	Simulated			Simulated		
V_{ed} **[*ml*]**	**113.4**			**121**		
V_{es} **[*ml*]**	**95.3**			**98.8**		
E_a **[*mmHg/ml*]**	**4.9**			**4.2**		
E_{es} **[*mmHg/ml*]**	**1.057**			**1.057**		
E_a/E_{es}	**4.64**			**3.97**		

7.5 Discussion

The accuracy and reliability of CARDIOSIM© software has been confirmed by statistical analysis with Student t-test and K Cohen index with no difference between measured and simulated parameters (Saltarocchi, 2018). Despite the preliminary nature of this study and the limited number of

patients considered, CARDIOSIM© has the potential to deliver reliable simulations for a more quantitative and critical evaluation of patients in advanced heart failure. The clinician remains the ultimate decision-maker but relies on an additional tool that may reduce unnecessary guess work and perhaps give reassurance and possibly reduce uncertainty.

A simulation-based approach as a potential preoperative strategy in the context of patient-specific modelling in advanced heart failure may be an additional tool to obtain accurate predictions of device performance in a clinical setting aimed at treatment optimisation of this complex and challenging group of patients. Patients in advanced heart failure are critical and their management can be very demanding with emotion running high when dealing with younger patients. The clinical cases considered are typical heart failure patients referred for assessment for transplant or LVAD insertion. The same approach is applicable to optimise the use of the intra-aortic balloon pump (IABP) and extracorporeal membrane oxygenation (ECMO) in its different configurations (De Lazzari, 2020; De Lazzari, 2021; De Lazzari, 2022). Figure 4.15 to Figure 4.22 give additional details.

Cardiovascular modelling has been very successful in increasing our knowledge of physiological mechanisms based on simplified representations of complex biological systems that can be used to study their behaviour at different levels (Lumens, 2012).

The Cardiac Physiome project is currently the most ambitious and successful application of mathematical and computational modelling aimed at the advancement of our understanding of physiology using a quantitative multi-scale approach. Cardiovascular modelling has now reached the stage at which clinical application in the form of patient-specific modelling may become a daily routine in a non distant future. For this approach to become reality, a model must be reliable, reproducible and reduce uncertainty (Bassingthwaighte, 2009; Lumens, 2012). While effective in the laboratory, almost all the decision support tools have failed when applied to clinical practice (Yang, 2016). Therefore, it is essential to overcome skepticism by developing a strong and realistic model that can fulfil the expectations. The focus must be on modelling and simulation not as a substitute for clinical experience but as an additional tool to guide therapeutic intervention or predict clinical outcome: the clinician will be the ultimate decision-maker. The development of a comprehensive, integrated model of the cardiovascular system based on lumped-parameter models, modified time-varying elastance and pressure–volume analysis of ventricular function is an attractive prospect with a view to clinical application. The differential equations describing such a model can be solved relatively easy and yield

answers in terms of pressure–volume loops and time-dependent tracings of pressure, flow and volume that may well help the decision process and management in the clinical setting. CARDIOSIM© fulfils these requirements compared to other software such as CircAdapt Simulator, HemoLab and Harvi. The CircAdapt Simulator is based on the CircAdapt model (Arts, 2005; Lumens and Delhaas, 2012; Lumens, 2014), which has been designed to simulate the dynamics of the heart and the circulation with the inclusion of a realistic relationship between pressure–volume load and tissue mechanics where the geometry of the components is obtained by adaptation to mechanical load. The implementation of the TriSeg model (Lumens, 2009) enables realistic simulation of ventricular mechanics including interactions between left and right ventricle, dynamics of septal geometry and myofibre mechanics in the three ventricular walls. The interesting feature of the CircAdapt model is its combined adaptation of heart and vessels over a relatively long period of time resulting in self-structuring of the circulation as a system in which a steady-state solution is obtained (Arts, 2011; Arts, 2012). This feature makes the model a potential tool for clinical application with the aim of predicting the evolution of a diseased status and the effects of an interventional procedure (Lumens, 2012; Lumens and Delhaas, 2012; Lumens, 2014; Lumens, 2012b; Lumens, 2013) although there is a lack of suitable models for VADs support. Despite its limitations, the CircAdapt model is considered easy to use, requires relatively low computational time and allows realistic simulations of the circulation with boundary conditions suitable for more complicated models based on finite element analysis. HeMoLab (Haemodynamics Modelling Laboratory) is an integrated computational environment for the modelling of the cardiovascular system. It is an effective research tool and a virtual simulation laboratory (Larrabide, 2012; Blanco, 2017; HeMoLab http://hemolab.lncc.br/). HeMoLab consists of a combination of models, which can be coupled locally and globally in order to obtain the systemic response of the cardiovascular system: the so called 3-D, 1-D and 0-D models. The propagation of the arterial pulse is represented with a 1-D and 0-D model, which describes the behaviour of the flow rate, mean pressure and cross-sectional area as a function of time. HeMoLab is a suitable environment for the simulation of the effects of aging, vasodilatation, vasoconstriction, rest and exercise and calculation of characteristic impedance of the arterial network. Although attractive, the software remains confined to a research environment at present. Harvi is an interactive simulation textbook of cardiovascular physiology and haemodynamics based on a previously described electric circuit (Harvi http://www.pvloo ps.com/; Santamore, 1991;

Burkhoff, 1993) in which ventricular and atrial contraction are represented by a modified time-varying elastance approach (Doshi and Burkhoff, 2016). In view of its features, CARDIOSIM© may be a more suitable choice with particular reference to the effects of mechanical circulatory support on the cardiovascular system.

Lumped-parameter models assume a uniform distribution of pressure, volume and flow within any specific compartment at any instant in time while higher dimensional models recognise the variation in space of these parameters. Lumped-parameter models consist of simultaneous ordinary differential equations complemented by an algebraic balance equation and are suitable for examination of global distribution of pressure, flow and volume over a range of physiological conditions with inclusion of the interaction between modelled components. Higher dimensional models consist of partial differential equations complemented by balance equations. 1-D models represent wave transmission effects within the vascular system but 3-D numerical solutions are required for complex flow patterns with analytical solutions obtained only for the simplest geometry (Shi, 2011). A single-branch multiple compartment model of the vascular system is suitable for the evaluation of short-term VAD support compared to an overly detailed vessel branch model where parameter setting becomes quite difficult. Higher level lumped-parameter modelling is required to address the interaction between the circulation and other systems but a compromise between complexity and ability to set the required parameters is needed to personalise an integrated lumped model for a patient-specific approach. CARDIOSIM© does address the systems interaction with its modular approach and assembly of models with varying degree of complexity although 0-D and 1-D coupling may be required for the evaluation of long-term VAD support.

The effect on ventricular–arterial coupling following LVAD support has also been considered during the simulations. Age-related vascular stiffening and the concomitant changes in left ventricular diastolic compliance are frequently observed in heart failure with preserved ejection fraction and in aortic valve stenosis (Antonini-Canterin, 2009). Ventricular–arterial coupling is strictly related to cardiovascular performance and can be accurately quantified in terms of pressure and volume. The left ventricle and the arterial system are considered elastic chambers with known volume elastance where left ventricular performance is measured by *Ees*, which is the slope of the ESPVR while the arterial system is measured by its elastance *Ea*, which is the slope of the arterial end-systolic pressure–stroke volume– effective arterial elastance relationship (Kelly, 1992; Antonini-Canterin, 2009). The

Ea/Ees ratio may be considered as a reliable performance index for ventricular–arterial coupling. An *Ea/Ees* ratio close to 1 relates to appropriate coupling between the left ventricle and the arterial system. Impaired coupling occurs in heart failure where *Ees* decreases following left ventricular systolic dysfunction and *Ea* is increased because of elevated impedance and reduced compliance (Antonini-Canterin, 2009).
The simulations discussed in this context show that LVAD assistance can achieve appropriate ventricular–arterial coupling with an Ea/Ees ratio close to 1. The potential of this parameter may well justify further study for its routine clinical application in heart failure patients.

7.6 Conclusion

A simulation approach in a clinical setting may well add a more quantitative approach to help the whole process, generate more critical thinking and perhaps give reassurance. The clinical scenarios discussed in this article are only an example of how the subject can be further developed and used as part of a preoperative planning strategy. The development of an integrated model of the cardiovascular system based on lumped-parameter representation, modified time-varying elastance and pressure–volume analysis of ventricular function seems a feasible and suitable approach yielding a sufficiently accurate quantitative analysis in real time. The challenge remains the ability to predict outcome over a longer period of time. Patient-specific modelling may become a daily approach for clinical management and optimisation of device treatment. Willingness to adopt such an integrated approach may be the key to further progress.

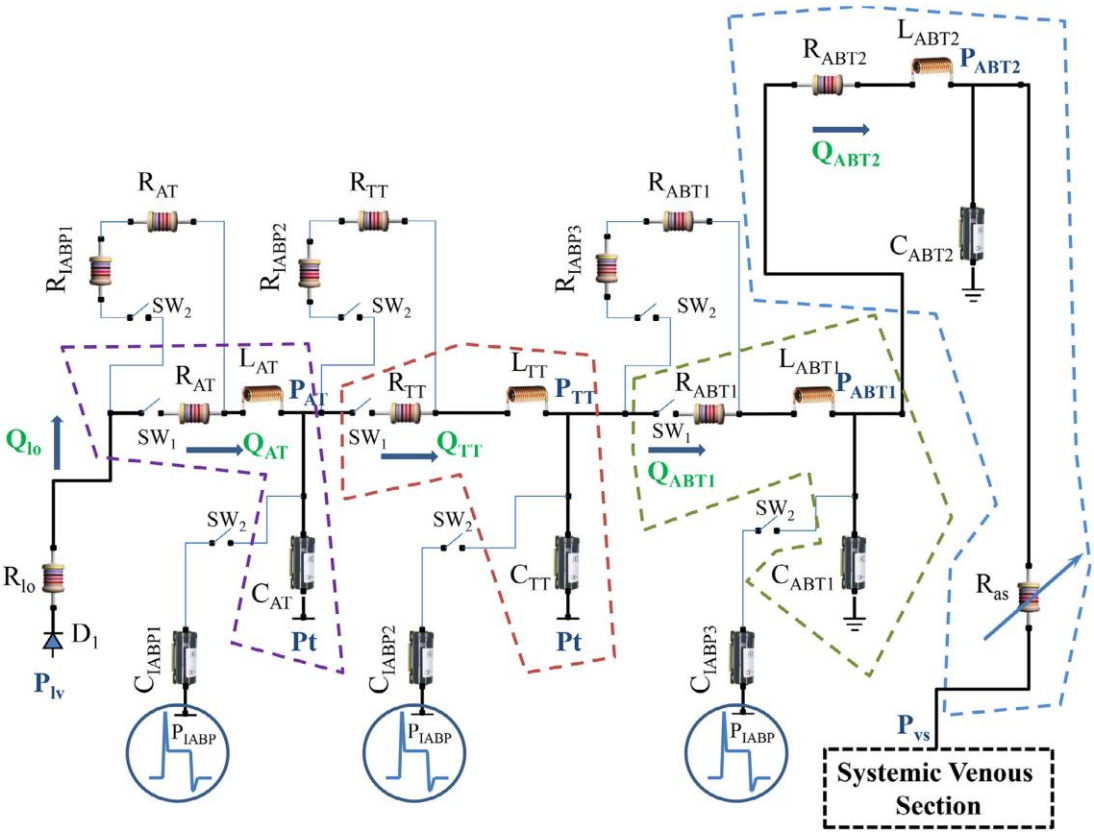

Figure 7.9 Electrical analogue of the systemic arterial section and the intra-aortic balloon pump (IABP). The systemic compartment consists of aortic (AT), thoracic (TT) and abdominal tract (ABT). The abdominal bed is divided in two parts modelled with R_{ABD1}, L_{ABD1}, C_{ABD1} and R_{ABD2}, L_{ABD2}, C_{ABD2} and R_{as} elements. The aortic, thoracic and first abdominal tract is directly influenced by IABP activation. Qi (i = AT, TT, ABT1 and ABT2) represents the flow inside each compartment. R_{AT}, L_{AT}, and C_{AT} (R_{TT}, L_{TT}, and C_{TT}) reproduce the aortic (thoracic) bed. The compliances C_{IABP1}, C_{IABP2} and C_{IABP3} and the resistances R_{IABP1}, R_{IABP2} and R_{IABP3} with the generator P_{IABP} allow simulating the effects of IABP. Pt = intrathoracic pressure. From: De Lazzari Comput Methods Progr Biomed 2020.

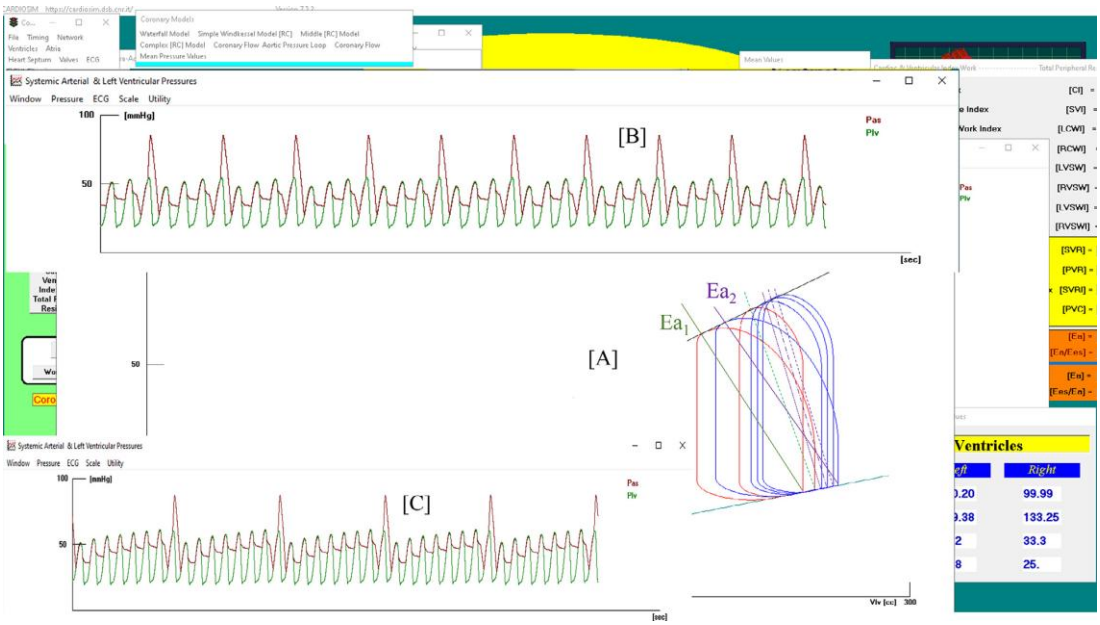

Figure 7.10 Screen output from CARDIOSIM© software simulator with instantaneous values obtained during IABP assistance. **[A]** left ventricular loops obtained when IABP ratio is set to 1:2 (red lines) and to 1:4 (blue lines). E_{a1}, green lines (E_{a2}, lilac lines) is the systemic arterial elastance when IABP ratio is set to 1:2 (1:4). **[B] ([C])** aortic (red lines) and ventricular pressures when IABP ratio is set to 1:4 (1:8). From: De Lazzari Comput Methods Progr Biomed 2020.

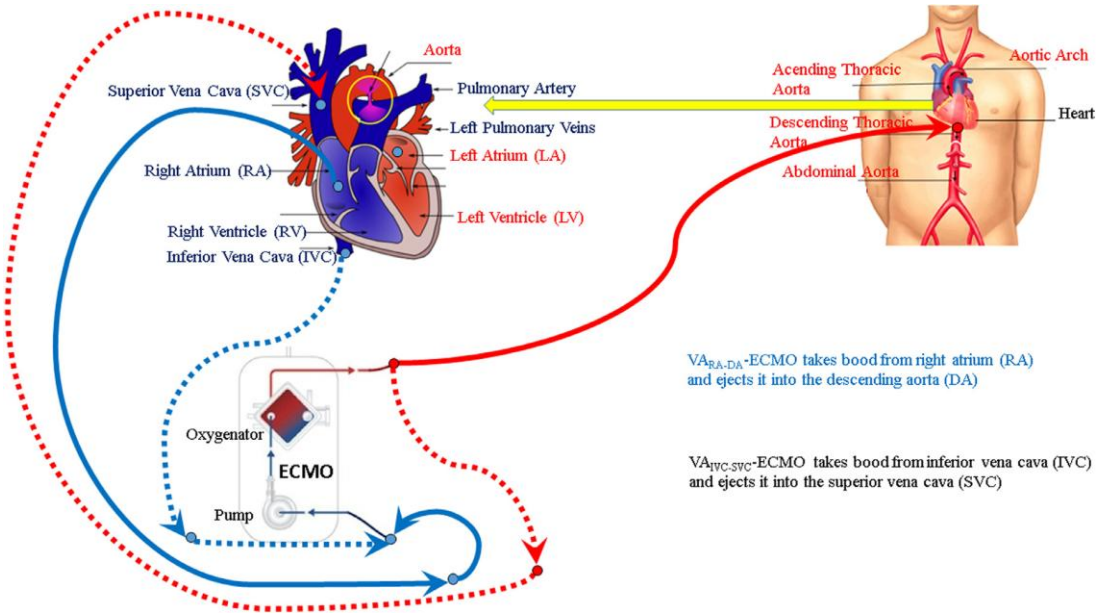

Figure 7.11 Schematic representation of $VA_{RA\text{-}DA}$ –ECMO (veno-arterial central ECMO) and VV $_{IVC\text{-}SVC}$ –ECMO (veno-venous peripheral ECMO) configurations. In $VA_{RA\text{-}DA}$ -ECMO mode, the centrifugal pump takes blood from the right atrium (continuous blue line) and ejects it into the descending aorta (continuous red line). In $VV_{IVC\text{-}SVC}$ -ECMO mode, the centrifugal pump takes blood from the inferior vena cava (dashed blue line) and ejects it into superior vena cava (dashed red line). From: De Lazzari Comput Methods Progr Biomed 2021.

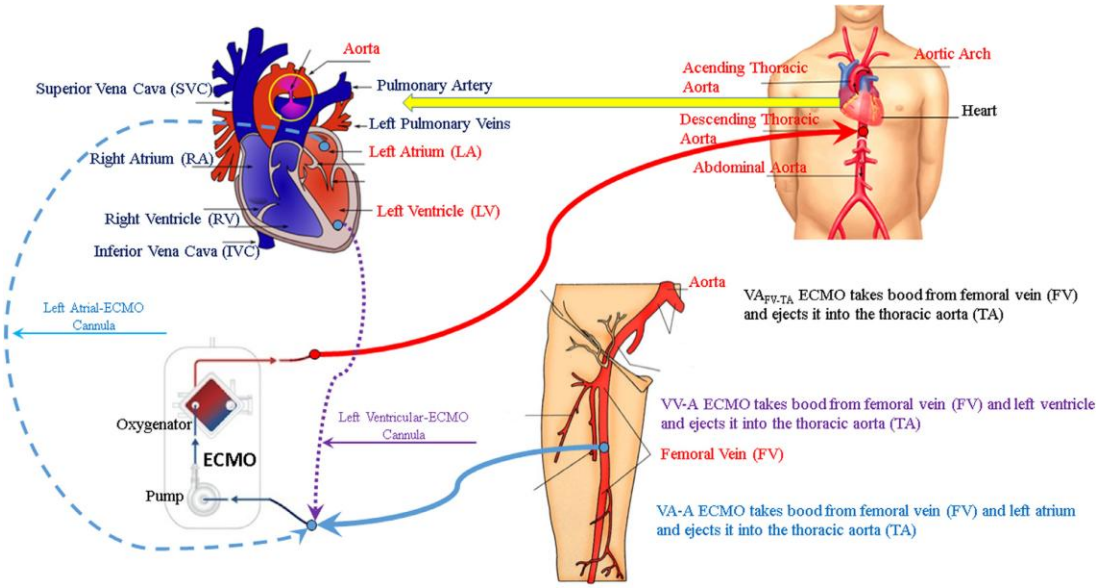

Figure 7.12 Schematic representation of $VA_{FV\text{-}TA}$ -ECMO configuration (veno-arterial peripheral ECMO). The centrifugal pump draws blood from the femoral vein (continuous blue line) and ejects it into the thoracic aorta (TA) (continuous red line). In the triple cannulation VV-A ECMO, the pump draws blood from FA (continuous blue line) and LV (dashed lilac line), and ejects it into the TA (continuous red line). In the triple cannulation VA-A ECMO, the pump draws blood from FA (continuous blue line) and LA (dashed blue line), respectively and ejects it into the TA (continuous red line). From: De Lazzari Comput Methods Progr Biomed 2021.

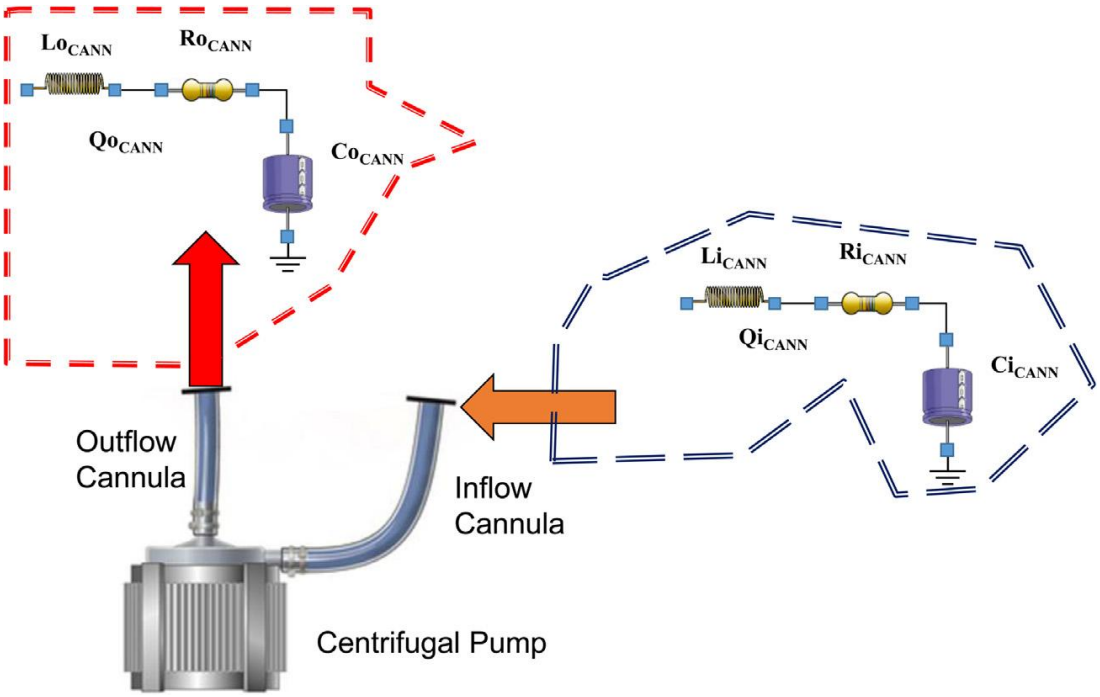

Figure 7.13 Electric analogue of the inlet and outlet cannula connected to the centrifugal pump. Q_{oCANN} (Q_{iCANN}) is the flow through the output (input) cannula. R_{oCANN}, C_{oCANN} and L_{oCANN} (R_{iCANN}, C_{iCANN} and L_{iCANN}) are the resistance, compliance and inertance of the outlet (inlet) cannula. From: De Lazzari Comput Methods Progr Biomed 2021.

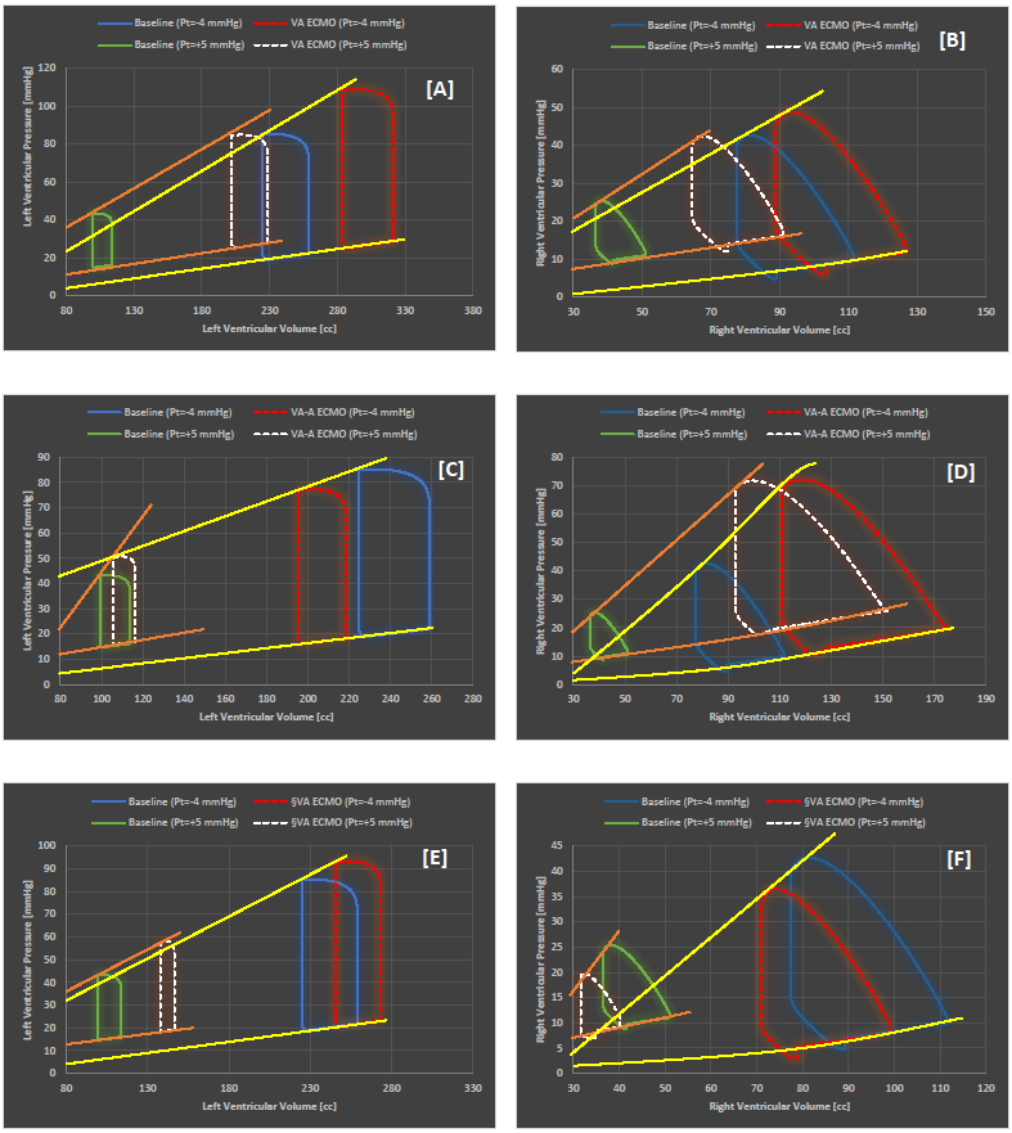

Figure 7.14 A (B): left (right) ventricular loops during baseline and $VA_{FV\text{-}TA}$ -ECMO assistance. Blue (green) loops: baseline conditions and mechanical ventilation (MV) with Pt = -4 mmHg (Pt = + 5 mmHg); dashed red (white) loops: $VA_{FV\text{-}TA}$ -ECMO assistance and MV with Pt = -4 mmHg (Pt = + 5 mmHg). **C (D)**: left (right) ventricular loops during baseline and VA-A ECMO assistance. Blue (green) loops: baseline conditions and MV with Pt = -4 mmHg (Pt = + 5 mmHg); dashed red (white) loops: VA-A ECMO assistance and MV with Pt = -4 mmHg (Pt = + 5 mmHg). **E (F)**: left (right) ventricular loops during baseline and $VA_{RA\text{-}DA}$ -ECMO assistance. Blue (green) loops: baseline conditions and MV with Pt = -4 mmHg (Pt = + 5 mmHg); dashed red (white) loops: $VA_{RA\text{-}DA}$ -ECMO assistance and MV with Pt = -4 mmHg (Pt = + 5 mmHg). $VA_{FV\text{-}TA}$ -ECMO = peripheral veno-arterial ECMO. $VA_{RA\text{-}DA}$ – ECMO = central veno-arterial ECMO. VA-A ECMO = veno-atrial-arterial ECMO. From: De Lazzari *Comput Methods Progr Biomed* 2021.

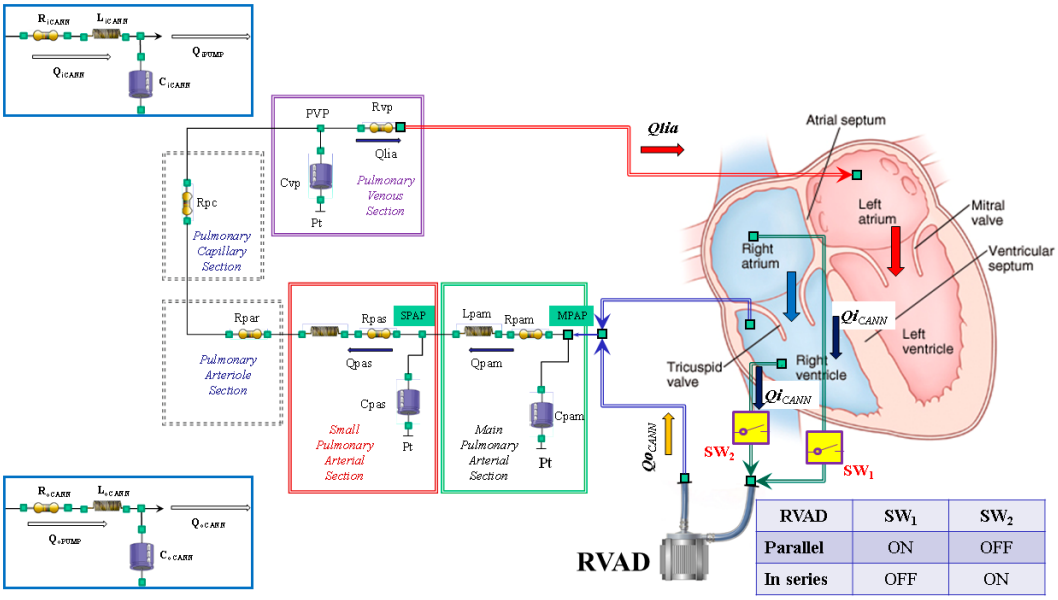

RVAD	SW_1	SW_2
Parallel	ON	OFF
In series	OFF	ON

Figure 7.15 Schematic representation of right ventricular assist device (RVAD) connection to the right circulation. When RVAD is connected in parallel, blood is removed from the right atrium (SW_1 = ON and SW_2 = OFF) and ejected into the pulmonary artery. When RVAD is connected in series, blood is removed from the right ventricle (SW_1 = OFF and SW_2 = ON) and ejected into the pulmonary artery. The input (output) RVAD cannula is modelled with RLC elements. Q_{oPUMP} (Q_{iPUMP}) = output (inlet) flow rate from the pump. Q_{oCANN} (Q_{iCANN}) = output (inlet) flow rate from the cannula. R_{oCANN} (R_{iCANN}) = RVAD output (input) cannula resistance. L_{oCANN} (L_{iCANN}) = RVAD output (input) cannula inertance. C_{oCANN} (C_{iCANN}) = RVAD output (input) cannula compliance. MPAP (SPAP) = Main (small) pulmonary arterial pressure. Rpam (Rpas) = Main (small) pulmonary arterial resistance. Lpam (Lpas) = Main (small) pulmonary arterial inertance. Cpam (Cpas) = Main (small) pulmonary arterial compliance. Q_{pam} (Q_{pas}) = Main (small) pulmonary arterial flow. Pt = mean intrathoracic pressure. R_{par} (R_{pc}) = Pulmonary arteriolar (capillary) resistance. C_{vp} = Pulmonary venous compliance. R_{vp} = Pulmonary venous resistance. PVP = Pulmonary venous pressure. Qlia = Left atrial input flow. From: De Lazzari *Comput Methods Progr Biomed* 2022.

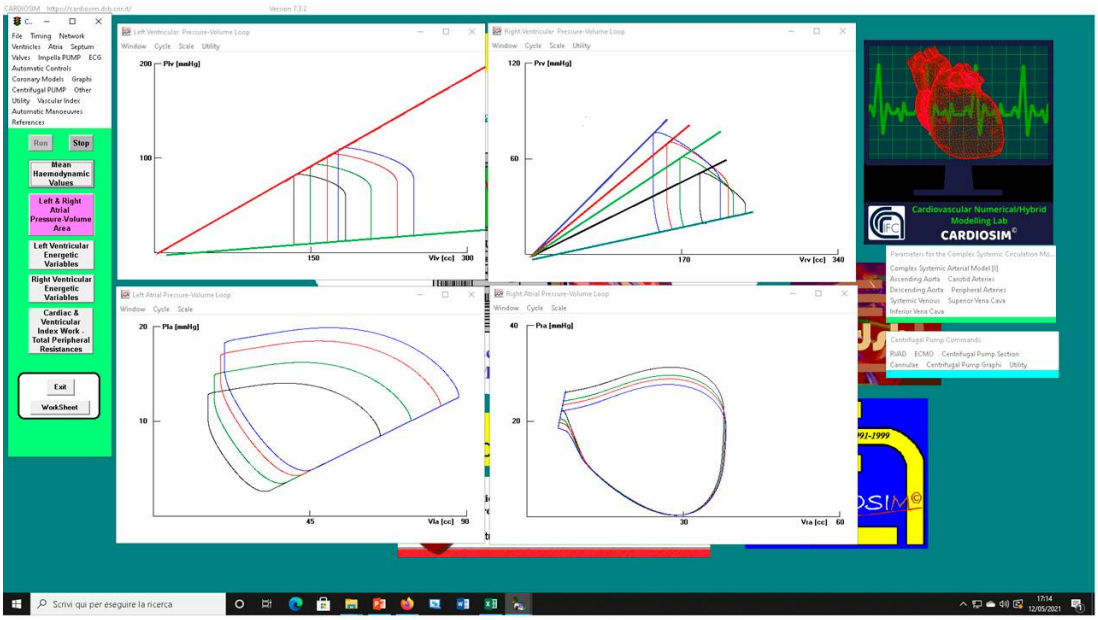

Figure 7.16 Effects on atrial and ventricular PV loops following RVAD support with different values of right ventricular end-systolic elastance $E_{esRIGHT}$. The left (right) upper panel shows four left (right) ventricular pressure-volume loops obtained by setting $E_{esRIGHT}$ = 0.3 mmHg/mL (black line); $E_{esRIGHT}$ = 0.4 mmHg/mL (green line); $E_{esRIGHT}$ = 0.5 mmHg/mL (red line); $E_{esRIGHT}$ = 0.6 mmHg/mL (blue line). The left (right) lower panel shows four left (right) atrial pressure-volume loops obtained by changing the slope of the right ventricular elastance. From: De Lazzari *Comput Methods Progr Biomed* 2022.

Chapter 8

Simulations with a simplified model of Heart Ware HVAD

8 Simulations with a simplified model of Heart Ware HVAD

8.1 Introduction

The insertion of a long-term LVAD is an elective procedure requiring discussion at a multidisciplinary team meeting (MDT) and extensive preoperative planning based on invasive and non invasive imaging investigation. The development of a simulation approach based on the ability to predict postoperative outcome and discuss different management strategies is the aim of the following chapters. A modelling approach which can be used within the time constraint of the clinical environment and in the context of a MDT meeting may become an additional tool for the management of advanced heart failure patients.

8.2 Material and Methods

An initial 3D reconstruction from CT-scan imaging of a patient who had undergone the insertion of the HeartWare HVAD was obtained. A separate reconstruction was considered for the impeller of the device, which had been previously explanted from the patient. The significant amount of artefacts precluded the original plan to combine the device and the impeller in Ansys SpaceClaim. Therefore, the geometry of the HeartWare HVAD was developed with ANSYS Design Modeller. A mesh independence analysis was considered for the purposes of quality, accuracy and convergence. Six meshes were generated ranging from 3985 to 193386 elements (Table 8.1). A mesh of 150185 elements was considered appropriate for the purposes of the simulations based on the fact that further refinement was not giving additional benefit to the simulations (Figure 8.1). The mesh consisted mainly of tetrahedral elements for the pump regions. Prism elements were used for the boundary layers of the inflow and outflow wall area (Figure 8.2).

Table 8.1 Data for mesh independence analysis

Elements	**Maximum Velocity Value (m/s)**
3985	0.332634
8981	0.264131
21595	0.275178
100458	0.31349
149843	0.323523
193386	0.327337

Blood was modelled as an incompressible, Newtonian fluid with density ρ = 1060 kg/m^3 and viscosity μ = 0.0035 *kg/m – s*. This is an appropriate

assumption considering that the shear-thinning behaviour of blood becomes negligible at high shear rate (> 100 s^{-1}).

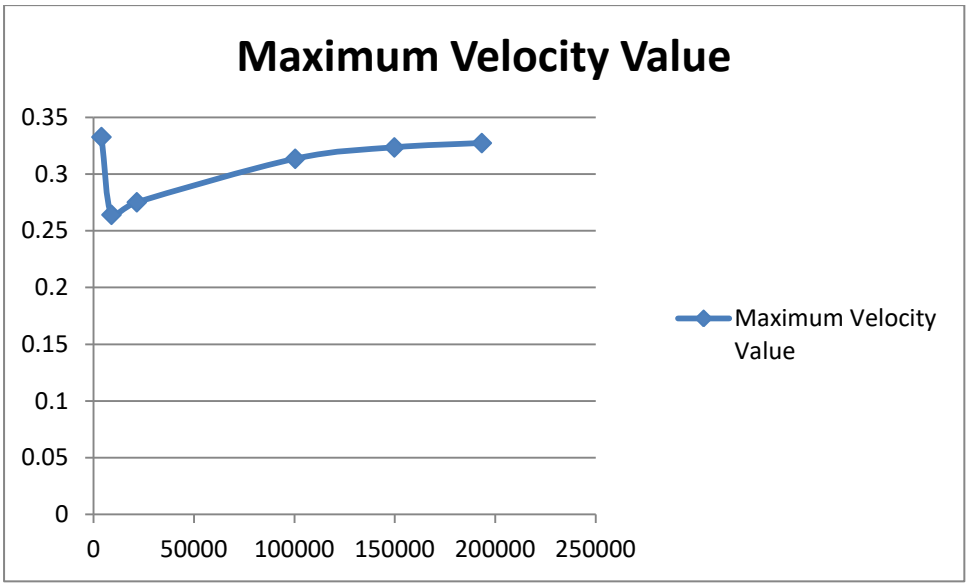

Figure 8.1 The maximum velocity value (y axis) is plotted as a function of the number of mesh elements (x axis).

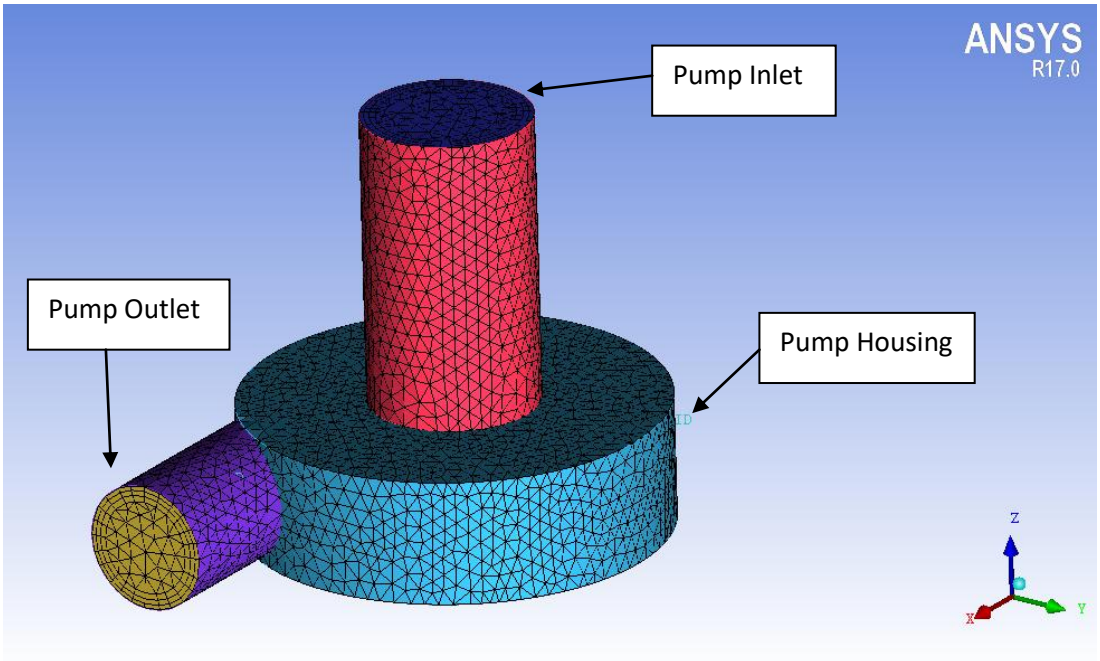

Figure 8.2 Mesh used for all the simulations. The HeartWare consists of the inflow tract (pink), pump housing (light blue) and the outflow tract (lilac).

Ansys Fluent was used for the CFD simulations based on the fundamental governing equations of motion (Truskey, 2010):

$$\frac{\partial \rho}{\partial t} + \nabla \cdot (\rho \boldsymbol{v}) = 0 \qquad \text{(continuity equation)}$$

$$\rho \frac{\partial \boldsymbol{v}}{\partial t} + \rho \boldsymbol{v} \nabla \cdot \boldsymbol{v} = -\nabla p + \nabla \cdot \boldsymbol{\tau} + \rho \mathrm{g} \qquad \text{(momentum equation)}$$

$$\rho \frac{\partial \boldsymbol{v}}{\partial t} + \rho \boldsymbol{v} \cdot \nabla \boldsymbol{v} = -\nabla p + \mu \nabla^2 \boldsymbol{v} + \rho \mathrm{g} \qquad \text{(Navier-Stokes equation)}$$

The simulations were initially developed with the laminar model as ideal baseline conditions. Subsequently, the shear stress transport (SST) k-ω model was considered for comparison purposes. The k-ω SST model was a key choice in view of its correction factor for low Reynolds number considering that rotary blood pumps run at the transition point between laminar and turbulent flow. Simulations were run in 3D, double precision, serial mode in Ansys Workbench. The solver was pressure-based with absolute velocity formulation either in steady state or transient conditions. Boundary conditions were set at a specific mass flow rate (inlet) and at a fixed steady pressure (outlet). A flow of 6 L/min corresponding to 0.105 kg/s was considered at the inlet. The total pressure was set to zero at the inlet and the static pressure was set to 100 mmHg (13332.2 Pa) at the outlet to achieve an average pressure increase of 100 mmHg. A fixed rotational speed of 3000 rpm for the impeller was considered in line with the range used in clinical practice for the HeartWare HVAD. Pressure-velocity coupling was based on the coupled scheme. Spatial discretisation consisted of least squares cell based for the gradient; second order or PRESTO! for the pressure; second order upwind for the momentum, turbulent kinetic energy and turbulent dissipation rate. The PRESTO! scheme is well suited for steep pressure gradients involved in rotating flows. It provides improved pressure interpolation in situations where large body forces or strong pressure variations are present as in swirling flows. The pseudo transient algorithm and the warped-face gradient correction were also used to add an unsteady term to the solution equations with the aim to improve stability and enhance convergence. Walls were assumed rigid with no-slip boundary condition. The rotation of the impeller was simulated according to the moving reference frame (MRF) approach, which is a steady-state method available in Ansys Fluent for the flow analysis of rotating parts. The equations of motion are modified with additional acceleration terms to account for the non-inertial motion of the moving frame. Boundary conditions are also defined in relation to the moving zone. Solutions become steady with respect to the moving reference frame and can be coupled with stationary

domains through interfaces. The advantage of using a moving reference frame is that a flow field which is unsteady when viewed from the stationary frame becomes steady in the moving reference frame. Adjacent zones can be coupled to the moving zones through grid interfaces to create a simplified model of a complex moving zone system. A steady-state problem is desirable because it is easier and less computationally expensive to solve; boundary conditions are simpler; it is more straightforward to post-process and analyse. A “stationary wall” condition implies that the wall is stationary with respect to the adjacent cell zone. Therefore, in the case of a rotating reference frame, a stationary wall is actually rotating with respect to the absolute reference frame. To specify a non-rotating wall, selection of “moving wall” is needed during the set up procedure specifying an absolute rotational speed of 0 rpm (i.e., moving with respect to the rotating reference frame). Therefore, the wall of the HeartWare body was set to “moving wall” with a rotational speed of 0 rpm; the impeller zone was set to “moving wall” with a rotational speed of 3000 rpm. The rotational movement of the impeller would cause displacement of the fluid zone. For this reason, a rotational speed of 0 rpm for the fluid zone was required.

The use of the sliding mesh method was subsequently considered to take into account the unsteady interaction between the stationary and rotating part. Nevertheless, the MRF approach was preferred in view of its features as previously mentioned. Finally, a time scale factors of 1 s was considered. Both steady state and transient simulations were considered according to the approach used. In addition, simulations with a variable (unsteady) pressure or velocity at the inlet using UDFs specifically developed for this purpose were considered.

Streamlines and contours of velocity, pressure distribution, and wall shear stress were considered for the analysis of flow in the pump. The discrete phase model (DPM) was used to estimate the particle residence time in the pump. An injection of mass-less particles from the inlet surface was considered for this purpose. The discrete random walk model was enabled during the DPM setting to take into account the lateral diffusion effect of the particles due to turbulence.

8.3 Results

8.3.1 Laminar model with MRF approach and DPM model

Laminar flow conditions in the pump were initially assumed as an ideal case. The simulation setting consisted of the laminar model in steady state conditions. The MRF approach was considered for the rotating impeller. The DPM model was used for the analysis of the particles residence time. A

pump rotational speed of 3000 rpm was considered. Boundary conditions included mass flow inlet of 6 L/min equivalent to 0.105 Kg/s and pressure outlet of 13332.2 Pa corresponding to 100 mmHg. A time scale factor of 1 s was considered with an input of 1000 iterations.

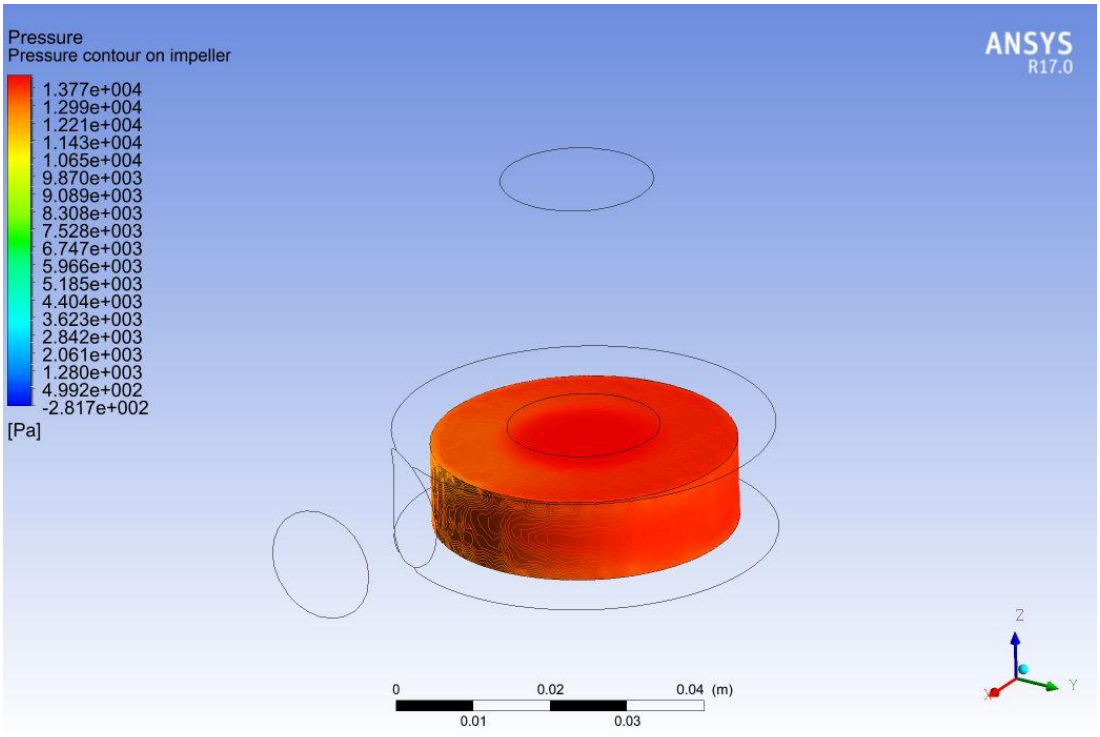

Figure 8.3 Pressure distribution in the rotating zone with values in the high spectrum.

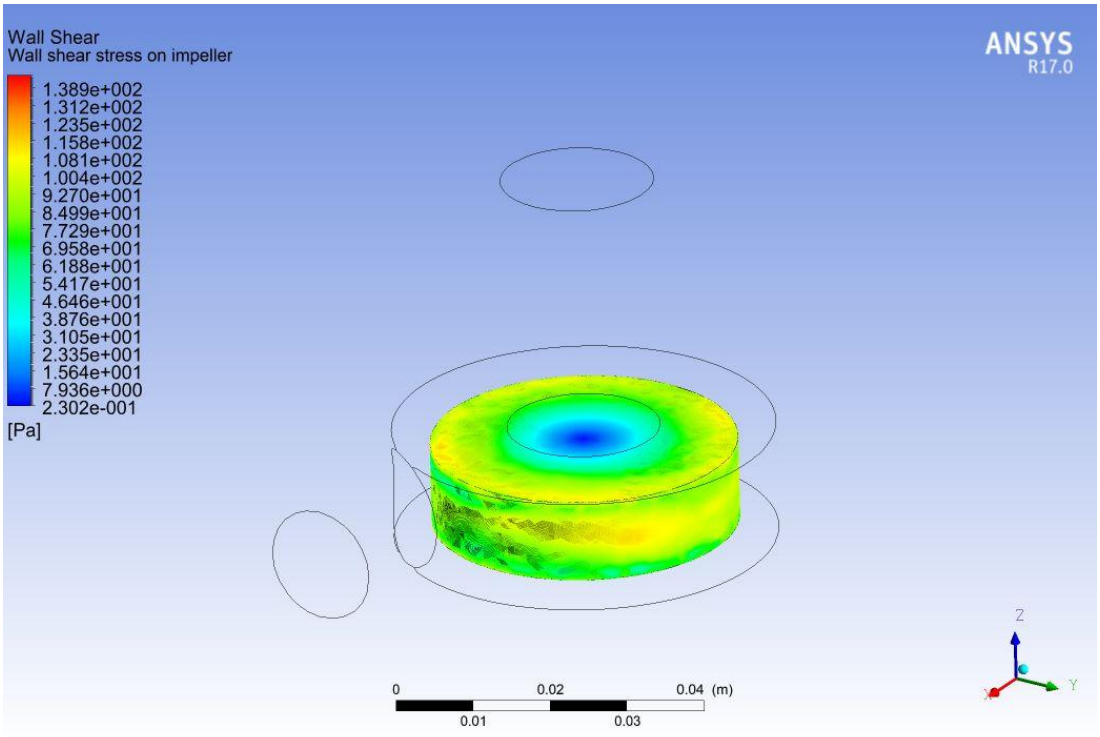

Figure 8.4 Wall shear stress distribution in the rotating zone. Higher values are observed towards the contact region with the wall of the pump case compared to the centre of the rotating zone.

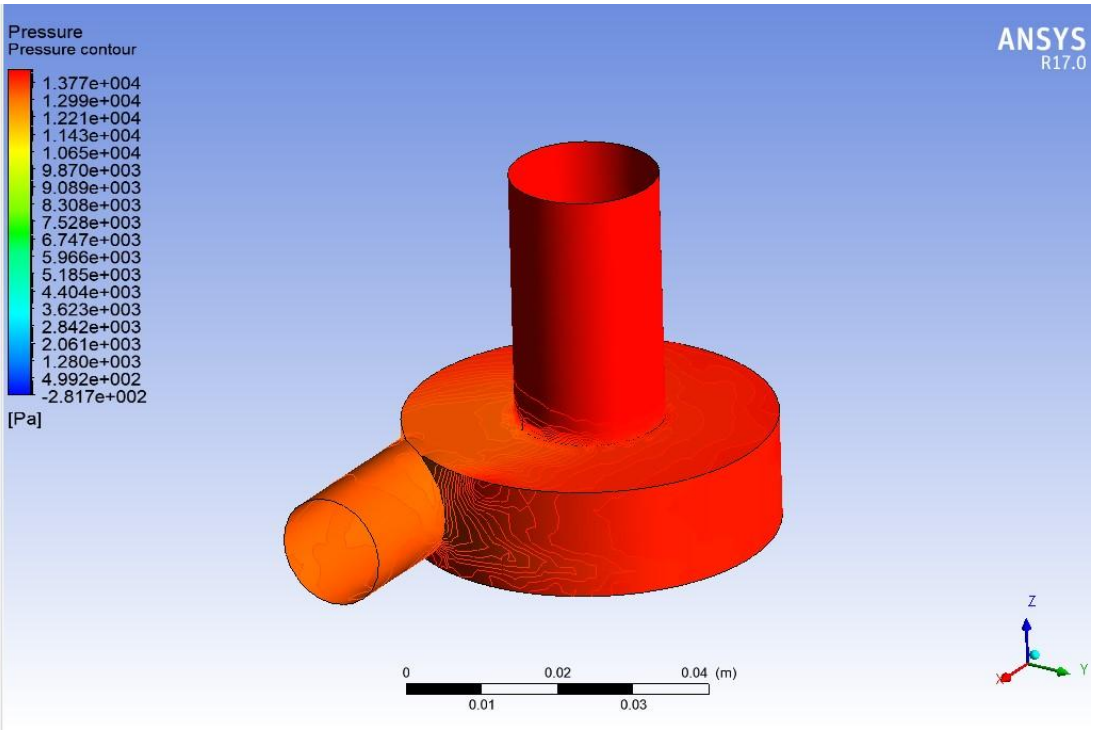

Figure 8.5 Pressure distribution in the pump with values in the high spectrum although slightly lower in the outflow tract.

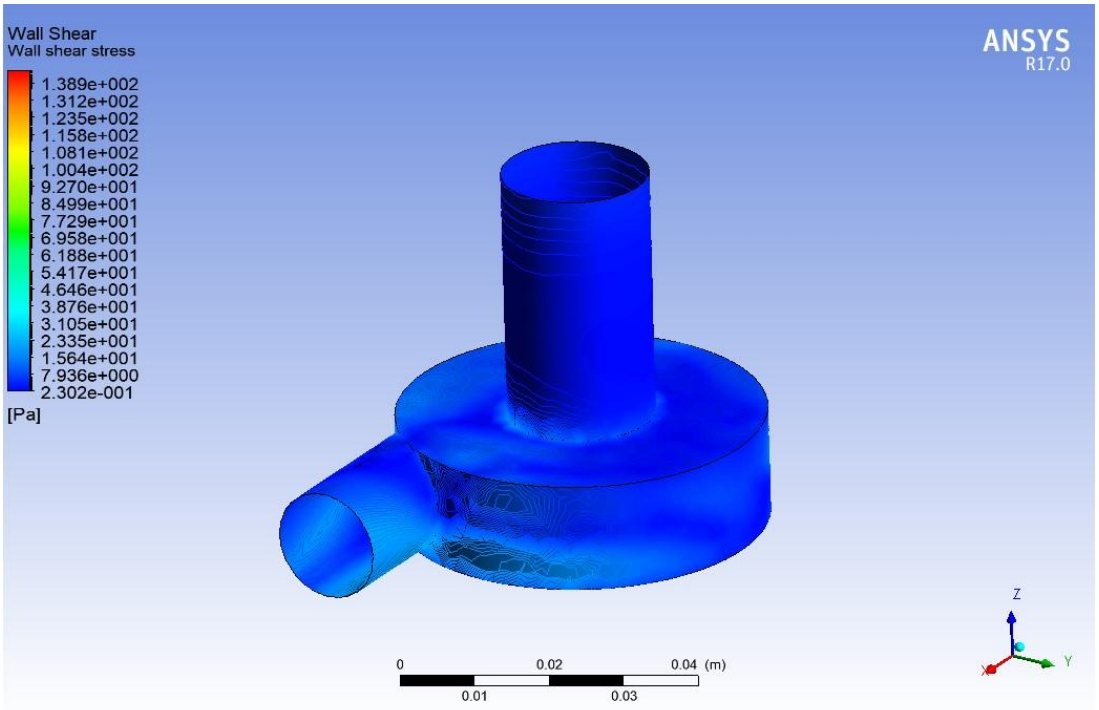

Figure 8.6 Wall shear stress distribution in the pump with values in the lower spectrum and slightly higher in the outflow tract.

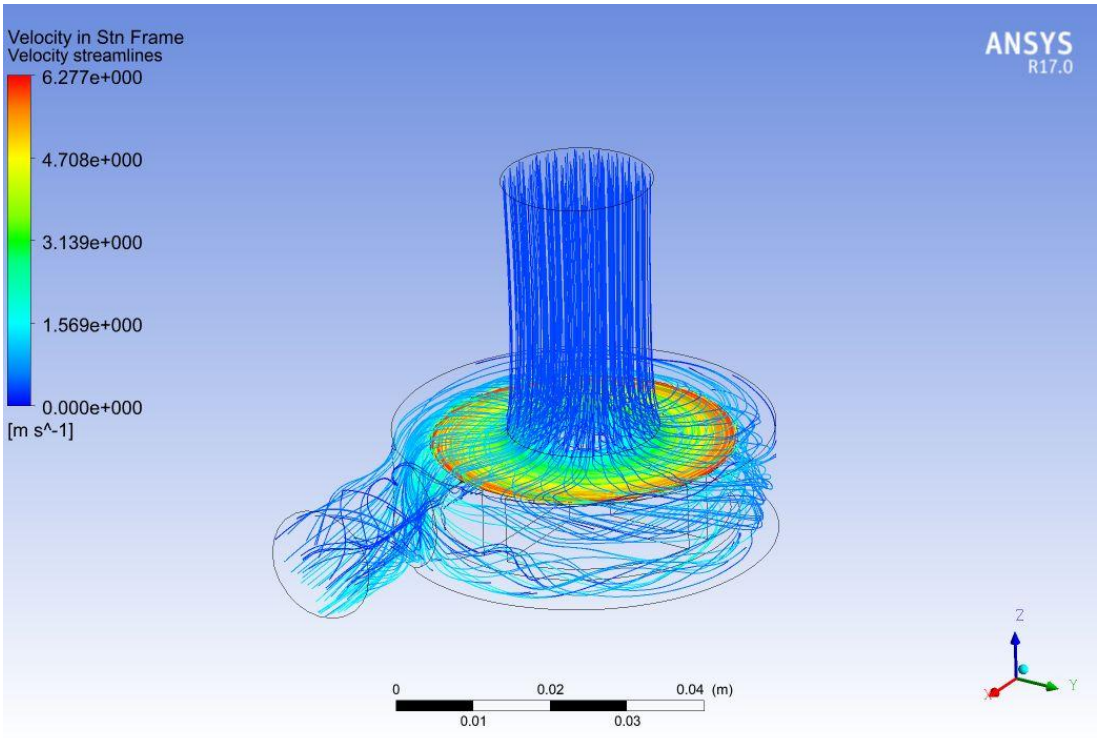

Figure 8.7 Velocity streamlines distribution with initial low values in the inflow area of the pump, than rising to high values in the rotating zone and finally returning to low values towards the outflow area of the pump.

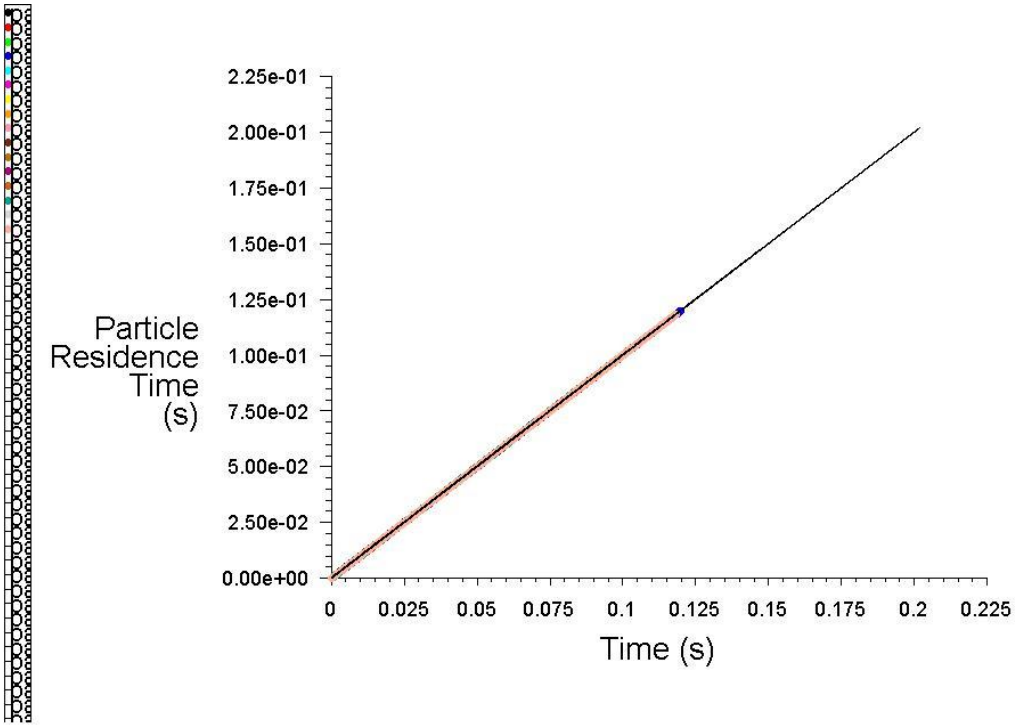

Figure 8.8 Laminar flow conditions in the pump show a particle residence time up to 0.225 s according to the DPM model.

8.3.2 k-ω SST model with MRF approach and DPM model

Subsequently, the k-ω SST model was used to account for the development of turbulence in the pump. Steady state conditions were considered and the MRF approach was implemented for the rotating impeller. The DPM model was used for the analysis of the particles residence time. A pump rotational speed of 3000 rpm was considered. Boundary conditions included mass flow inlet of 6 L/min equivalent to 0.105 Kg/s and pressure outlet of 13332.2 Pa corresponding to 100 mmHg. A time scale factor of 1 s was considered with an input of 1000 iterations.

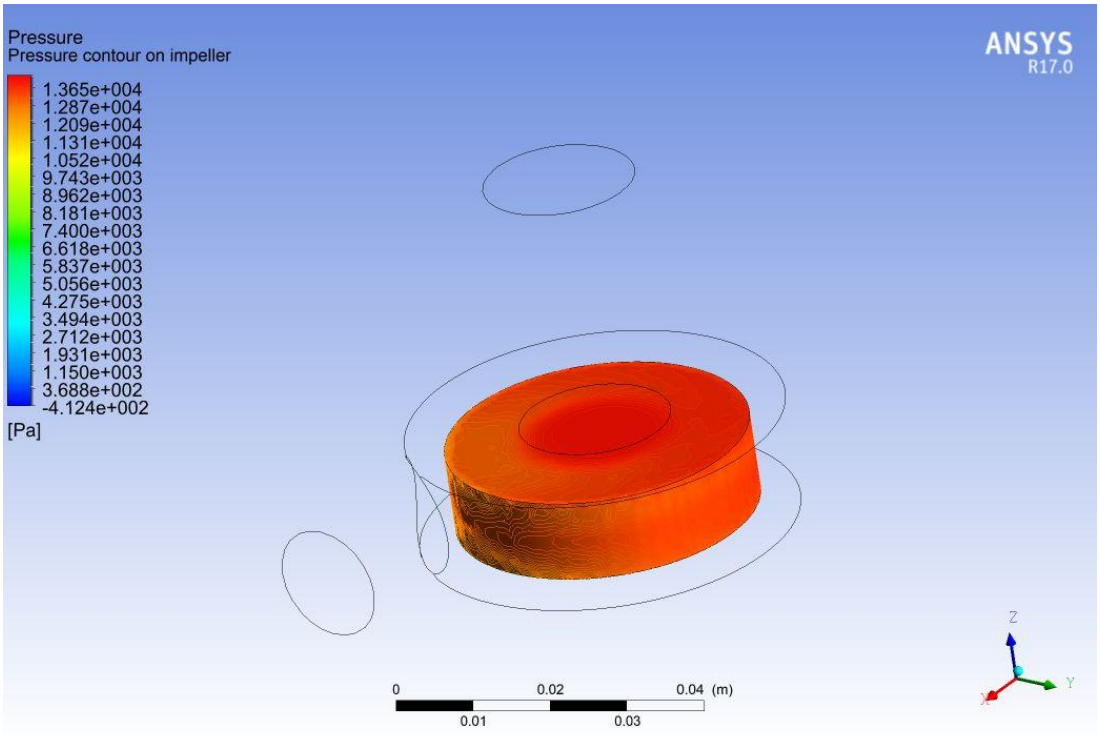

Figure 8.9 Pressure distribution in the rotating zone with values in the higher spectrum, particularly in the central area.

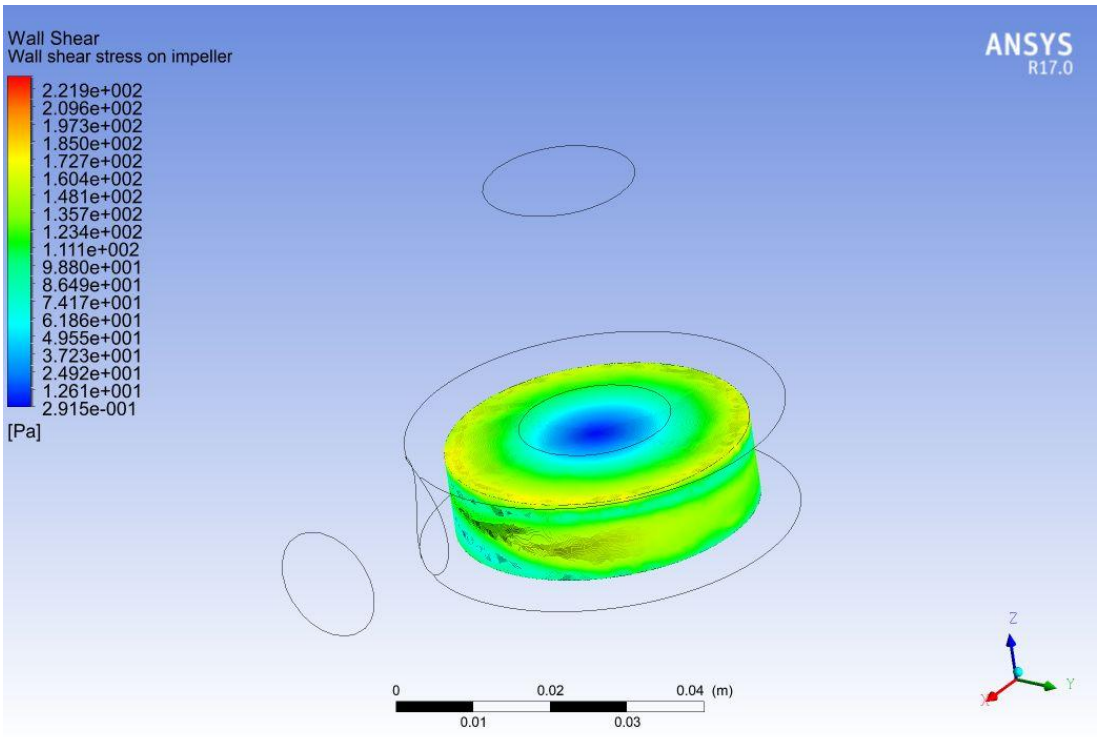

Figure 8.10 Wall shear stress distribution in the rotating zone with high values towards the contact region with the pump case and lower values in the centre.

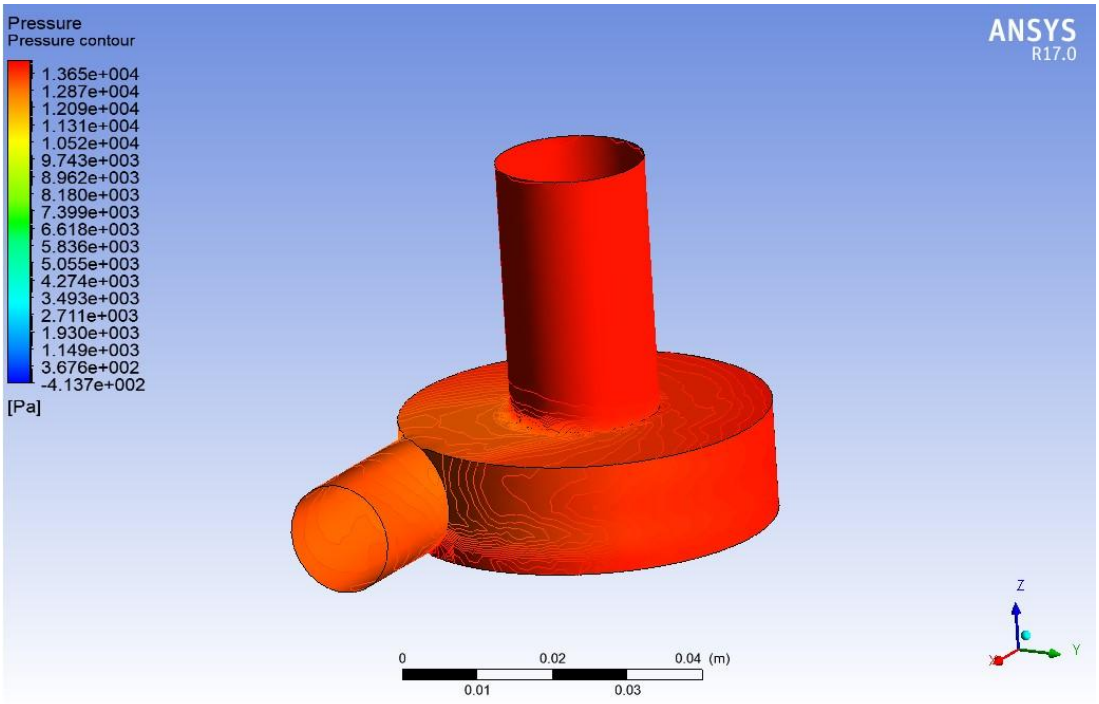

Figure 8.11 Pressure distribution in the pump with values in the higher spectrum although slightly lower in the outflow tract.

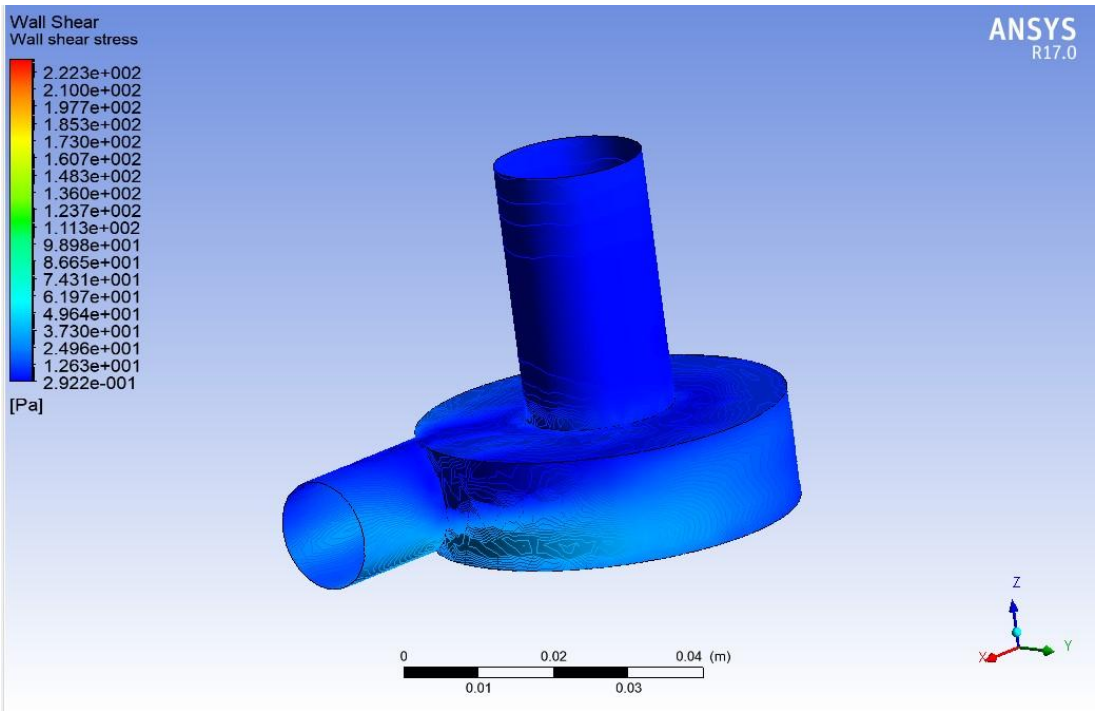

Figure 8.12 Wall shear stress distribution in the pump with values in the lower spectrum although slightly higher in the outflow tract.

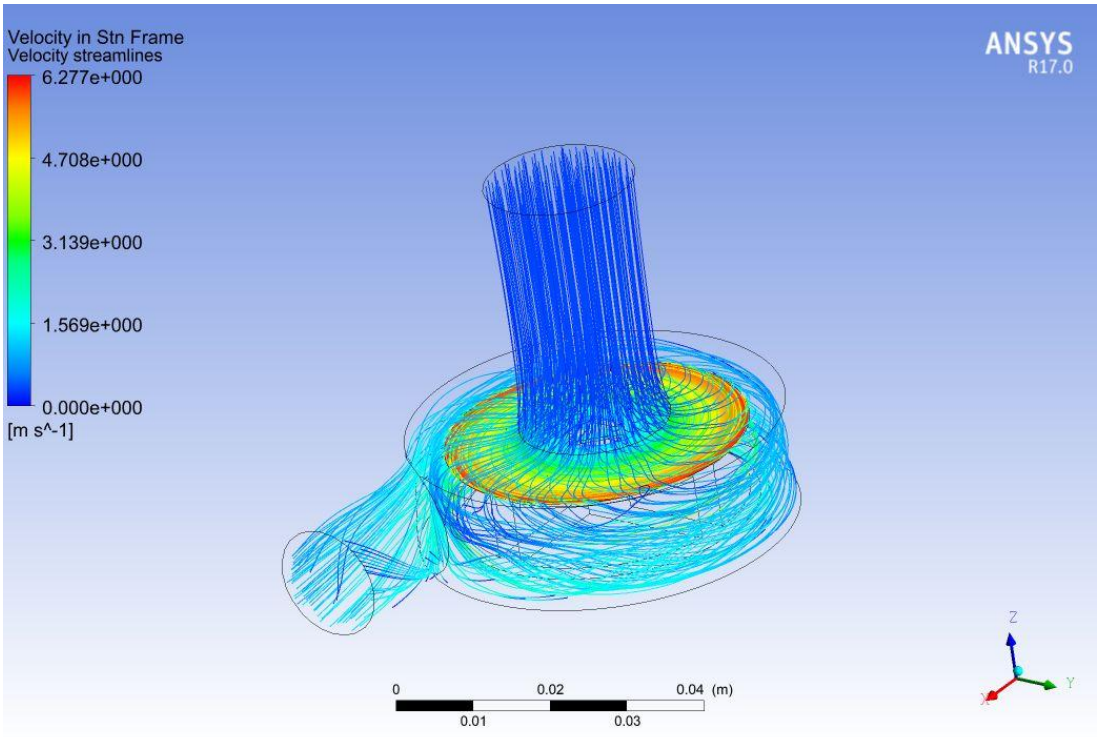

Figure 8.13 Velocity streamlines distribution with low values in the inflow tract of the pump, rising towards the centre of the rotating zone and finally returning to lower values in the outflow tract of the pump.

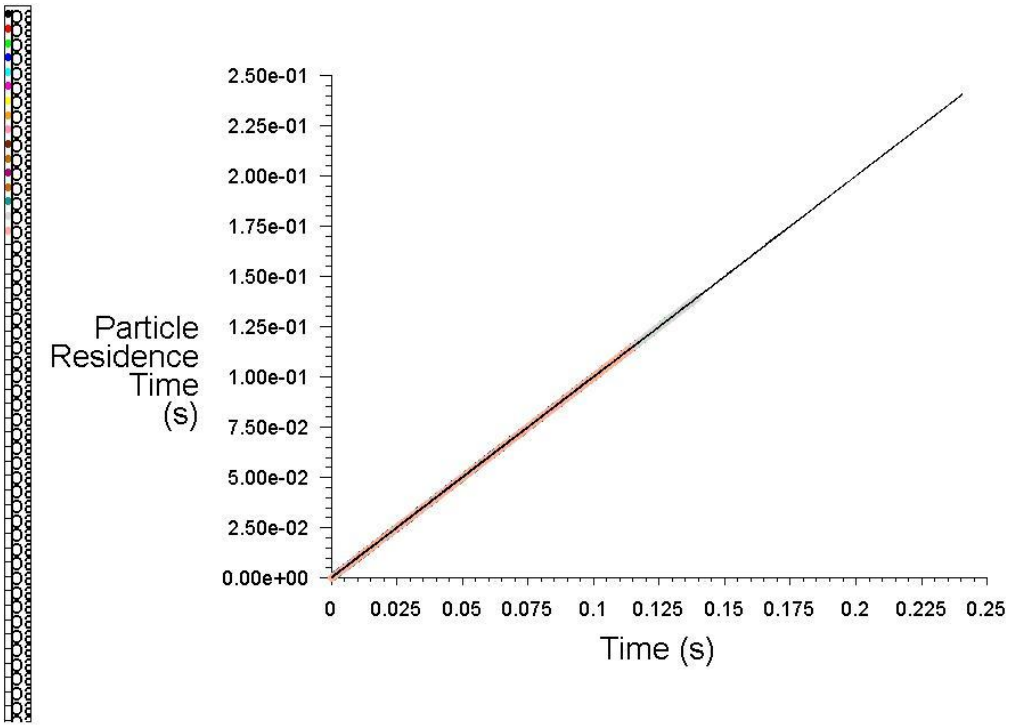

Figure 8.14 Onset of turbulent flow conditions in the pump show a particle residence time up to 0.25 s according to the DPM model.

8.3.3 k-ω SST model with sliding mesh method and DPM model

Finally, the sliding mesh method was considered for comparison purposes in relation to accuracy of results. The k-ω SST model was used to account for the development of turbulence in the pump. A transient simulation was required. The DPM model was used for the analysis of the particles residence time. A pump rotational speed of 3000 rpm was considered. Boundary conditions included mass flow inlet of 6 L/min equivalent to 0.105 Kg/s and pressure outlet of 13332.2 Pa corresponding to 100 mmHg. A time scale factor of 1 s was considered with an input of 1000 iterations.

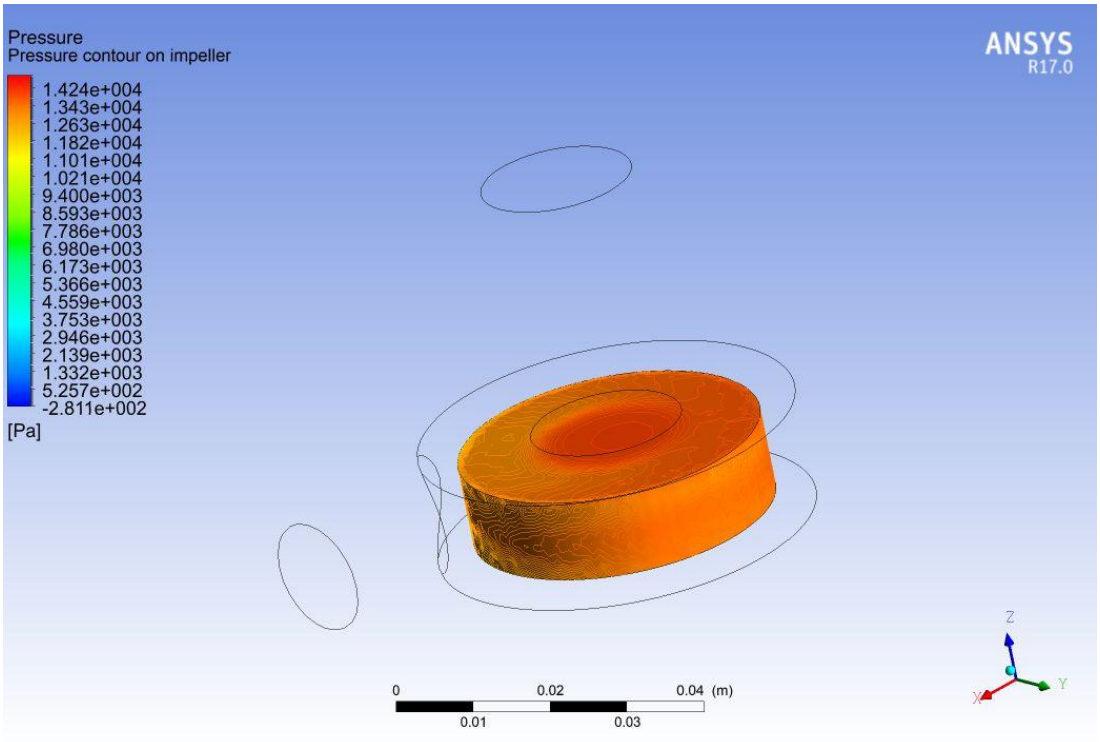

Figure 8.15 Pressure distribution in the rotating zone with high spectrum values in the centre although reduced in the peripheral areas, particularly towards the outflow tract of the pump.

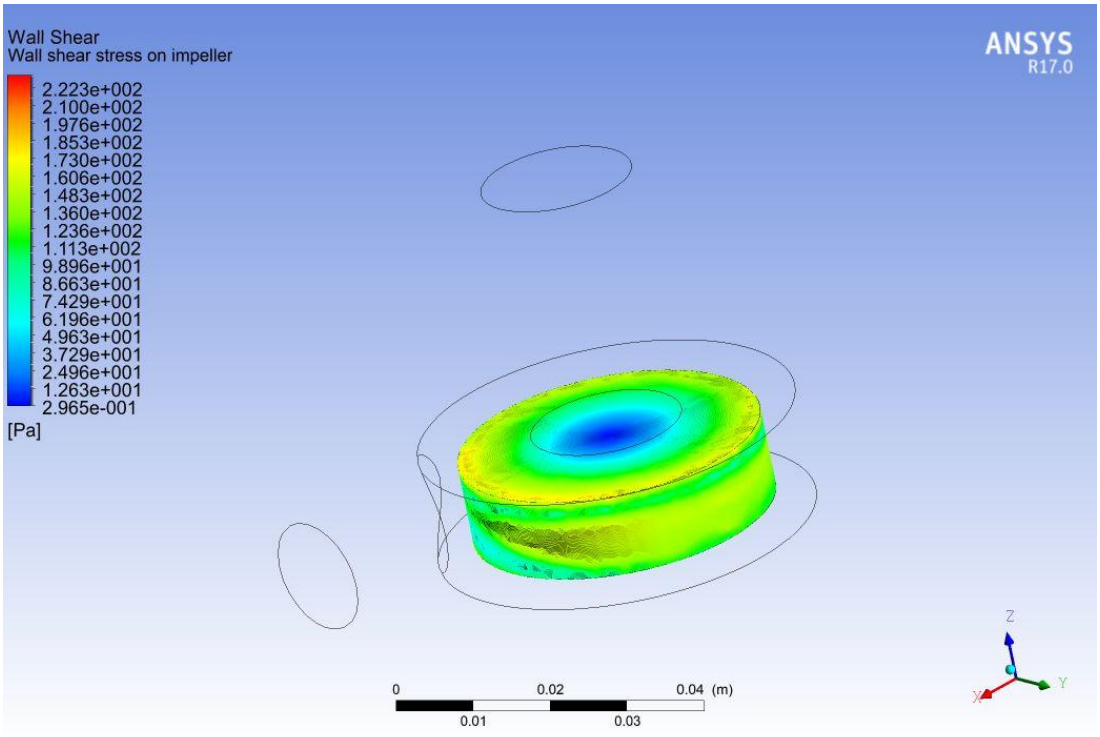

Figure 8.16 Wall shear stress distribution in the rotating zone with low values in the centre and higher values towards the peripheral contact region.

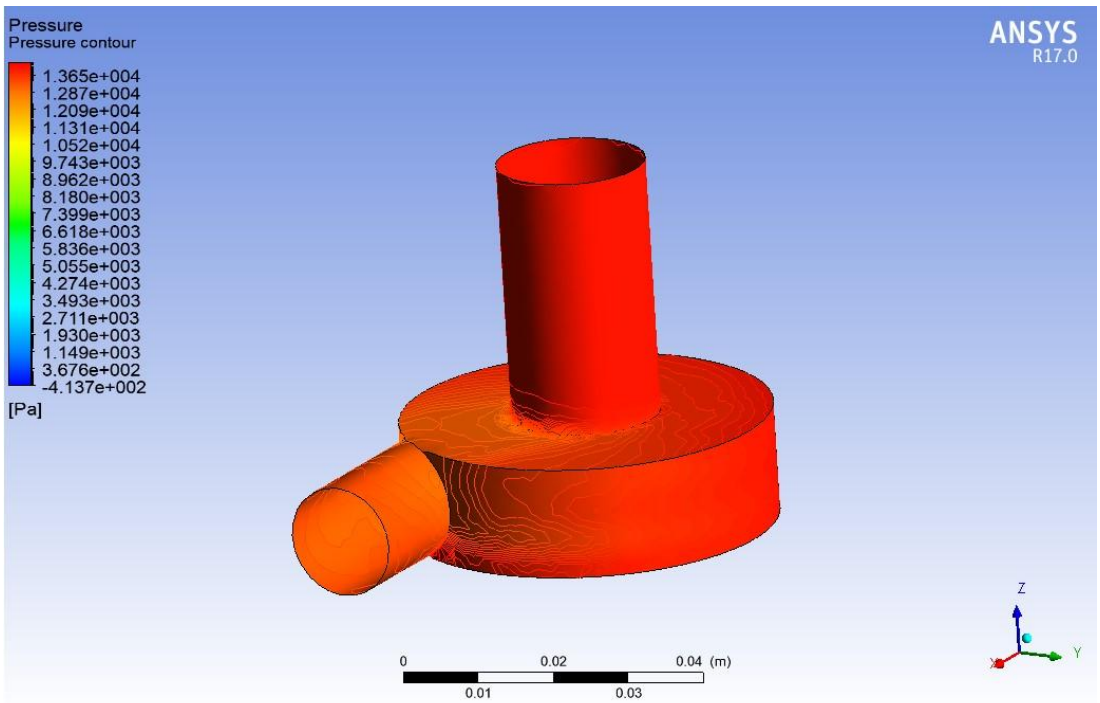

Figure 8.17 Pressure distribution in the pump with values in the higher spectrum although slightly lower in the outflow tract.

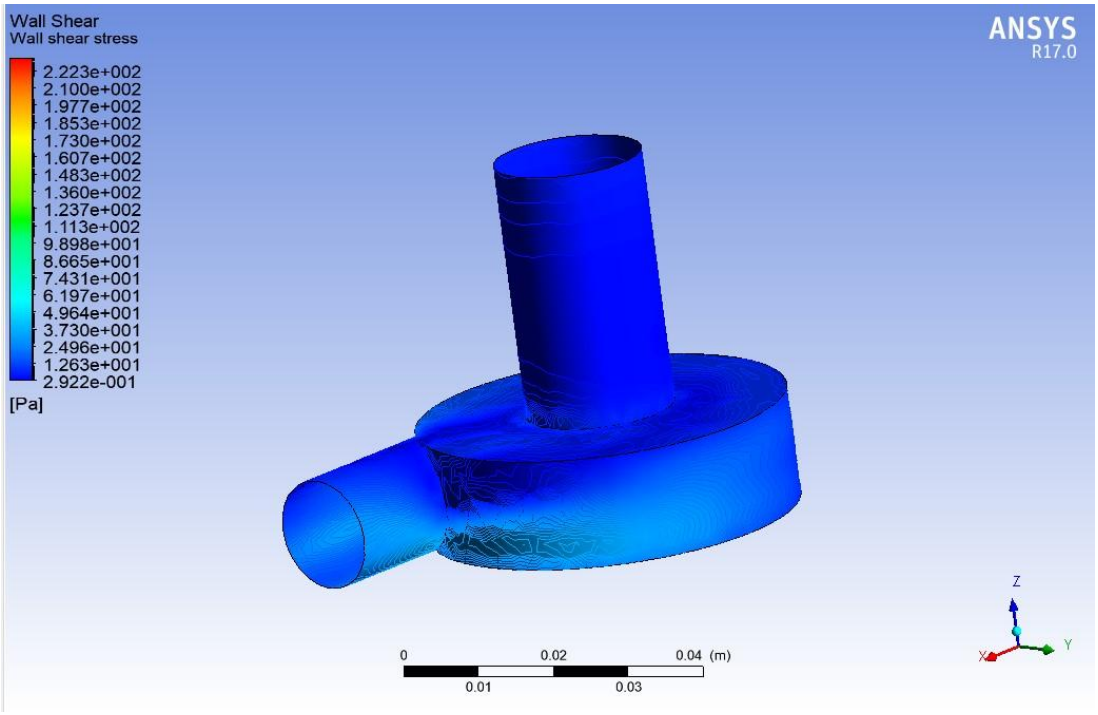

Figure 8.18 Wall shear stress distribution in the pump with values in the lower spectrum although slightly higher in the outflow tract.

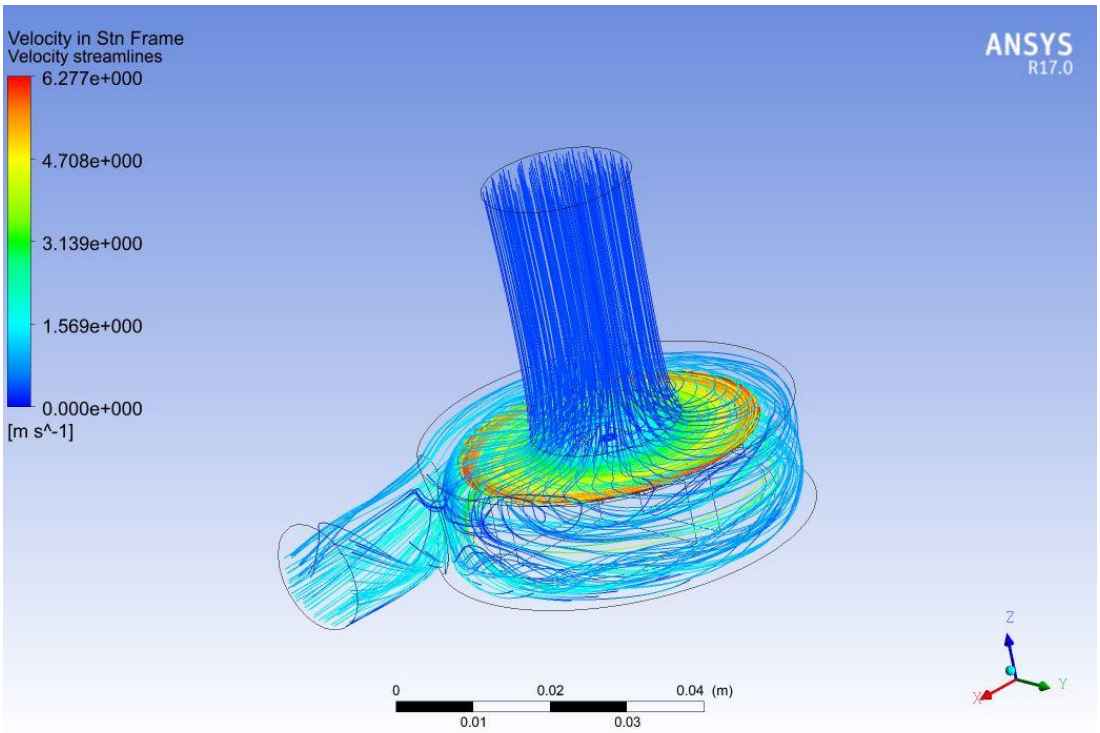

Figure 8.19 Velocity streamlines distribution with low values in the inflow area of the pump, rising towards the centre of the rotating zone and finally returning to lower values in the outflow tract of the pump.

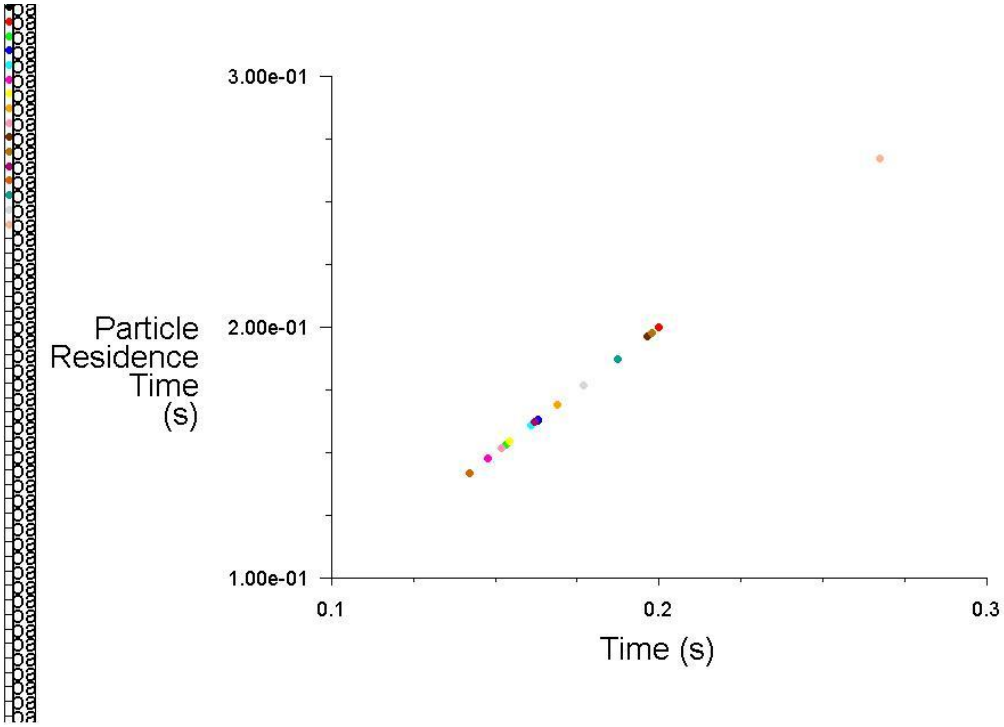

Figure 8.20 Onset of turbulent flow conditions in the pump show a particle residence time up to 0.3 s according to the DPM model in the context of the sliding mesh method.

8.3.4 k-ω SST model with pulsatile velocity inlet, MRF approach and DPM model

A pulsatile velocity profile at the inlet was considerd to take into account the effect of speed modulation on the physiological environment. The k-ω SST model was used to account for the development of turbulence in the pump. Steady state conditions were considered and the MRF approach was implemented for the rotating impeller. The DPM model was used for the analysis of the particles residence time. A pump rotational speed of 3000 rpm was considered. Boundary conditions included pulsatile velocity inlet according to a specific prof.file and pressure outlet of 13332.2 Pa corresponding to 100 mmHg. A time scale factor of 1 s was considered with an input of 1000 iterations.

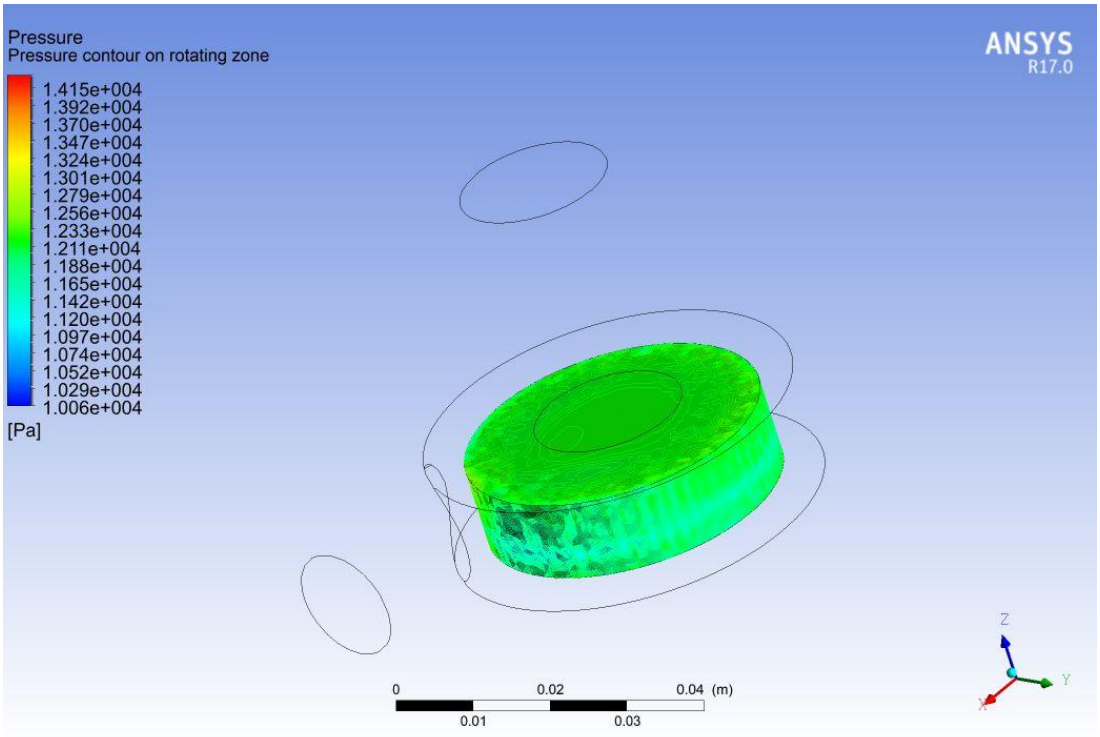

Figure 8.21 Pressure distribution in the rotating zone with values in the medium spectrum. Higher values are observed in the centre of the rotating zone.

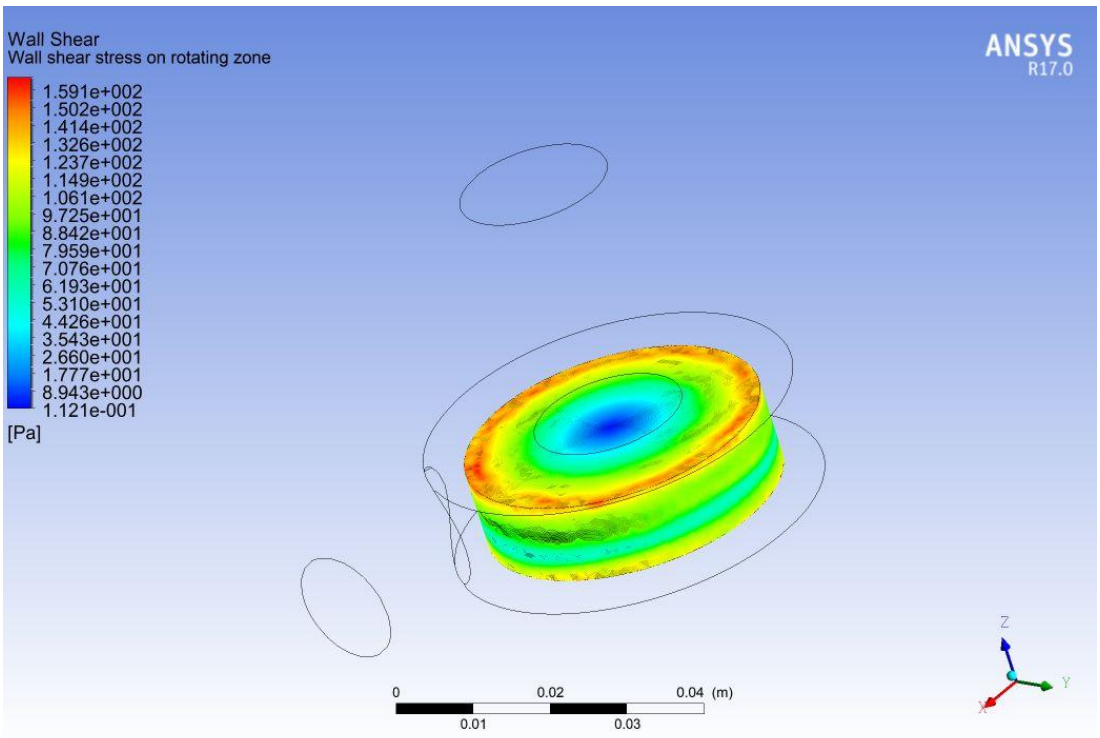

Figure 8.22 Wall shear stress in the rotating zone with high values at the edges and much lower values in the centre.

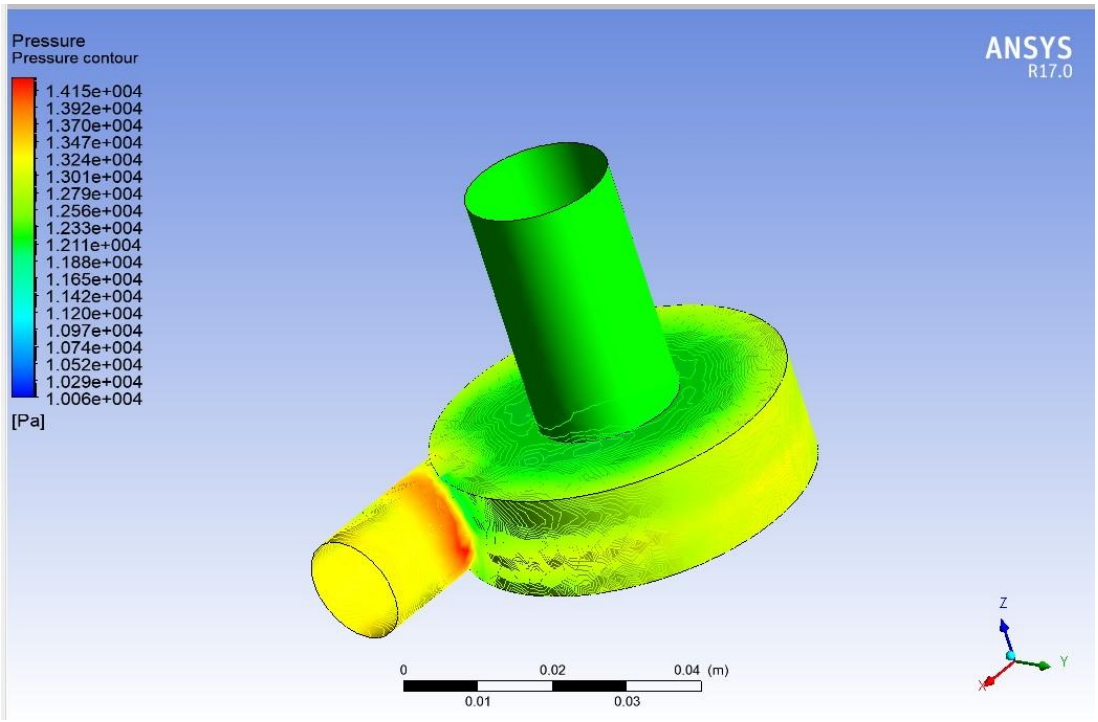

Figure 8.23 Pressure distribution in the pump with values in the medium spectrum although higher in the outflow tract.

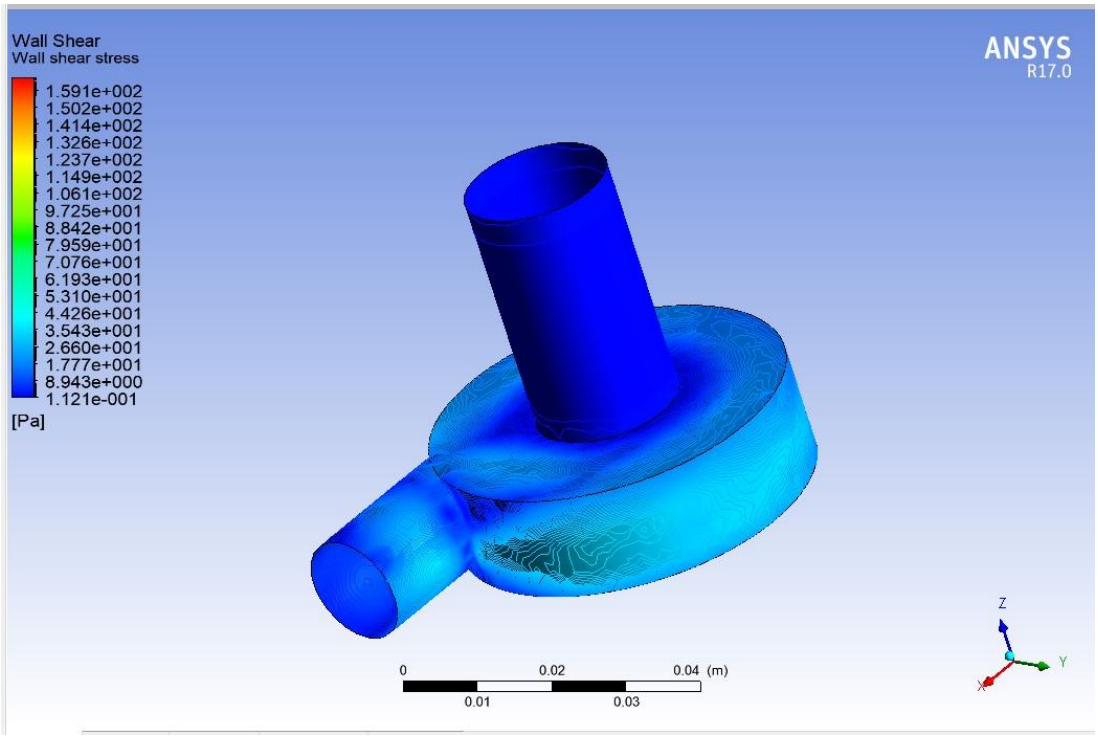

Figure 8.24 Wall shear stress distribution in the pump with values in the lower spectrum although slightly higher towards the edge of the pump case and in the outflow tract.

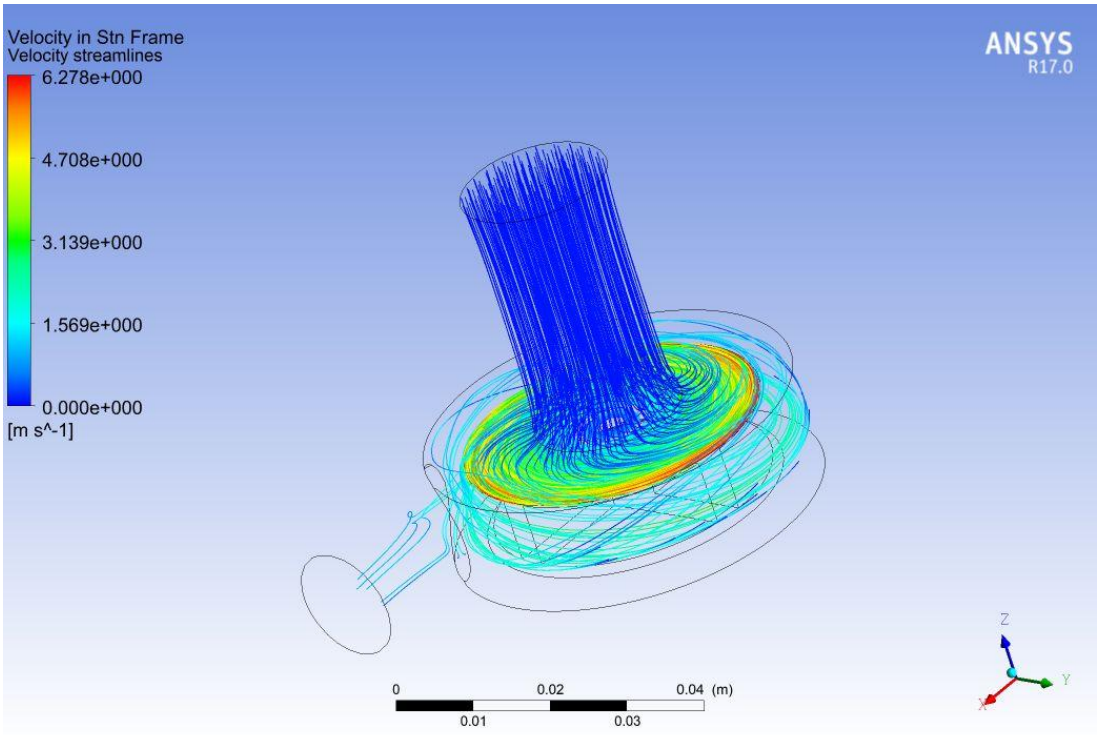

Figure 8.25 Velocity streamlines with low values in the inflow tract, high values in the rotating zone and again lower values towards the outflow tract.

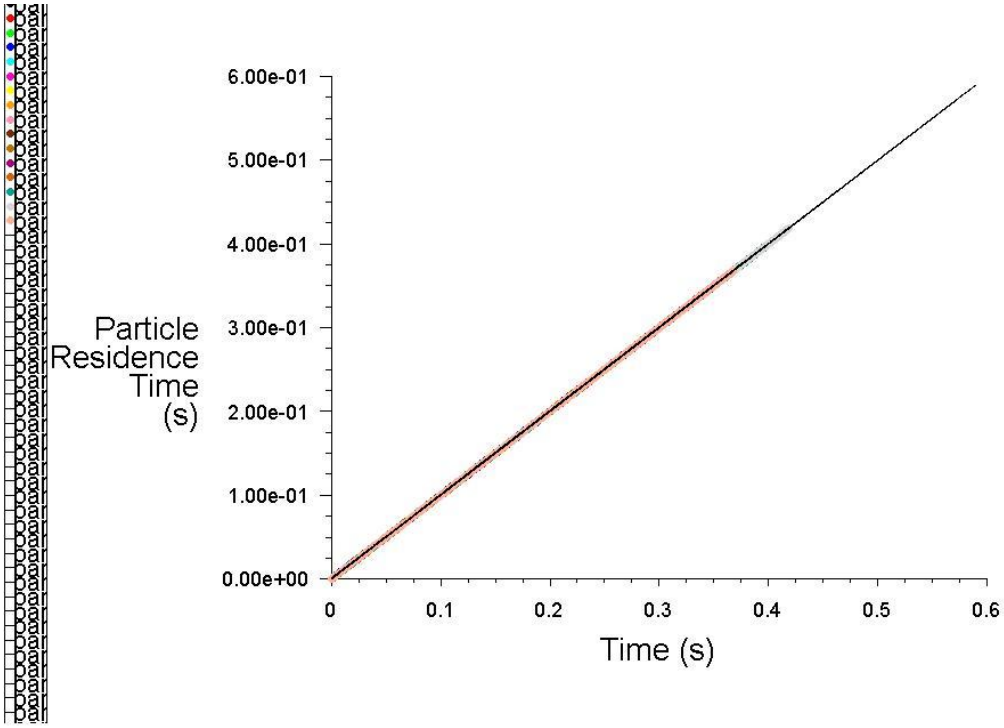

Figure 8.26 Onset of turbulent flow in the pump during pulsatile conditions show a particle residence time up to 0.6 s according to the DPM model in the context of the MRF approach.

8.3.5 k-ω SST model with pulsatile velocity inlet, sliding mesh method and DPM model

A pulsatile velocity profile at the inlet was considerd to take into account the effect of speed modulation on the physiological environment. The k-ω SST model was used to account for the development of turbulence in the pump. Transient conditions were considered and the sliding mesh method was implemented for the rotating impeller. The DPM model was used for the analysis of the particles residence time. A pump rotational speed of 3000 rpm was considered. Boundary conditions included pulsatile velocity inlet according to a specific prof.file and pressure outlet of 13332.2 Pa corresponding to 100 mmHg. A time scale factor of 1 s was considered with an input of 1000 iterations.

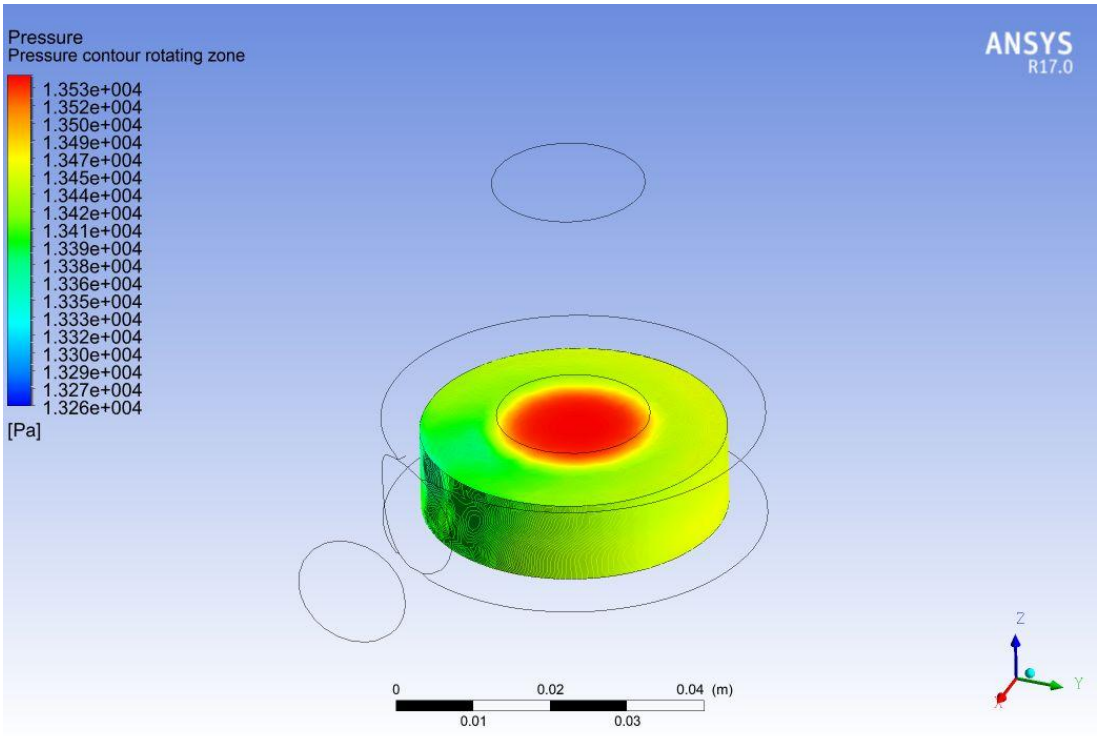

Figure 8.27 Pressure distribution in the rotating zone with progressive high values towards the centre of the impeller.

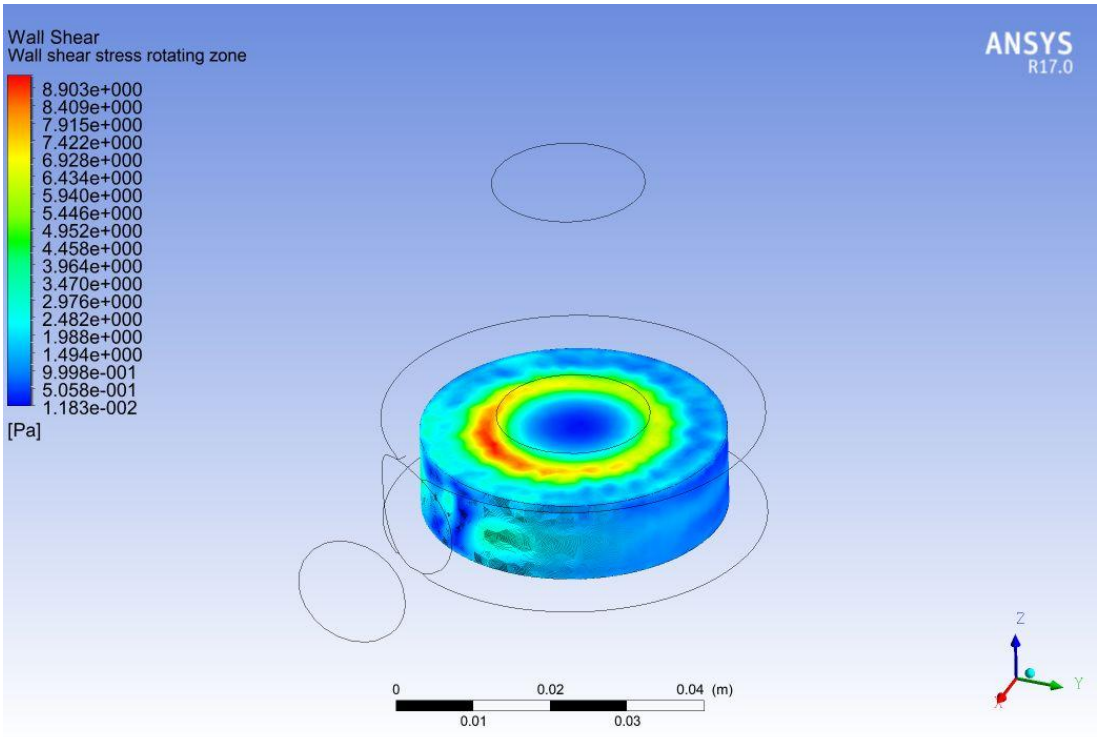

Figure 8.28 Wall shear stress distribution in the rotating zone with low values peripherally and in the centre but higher in the mid portion.

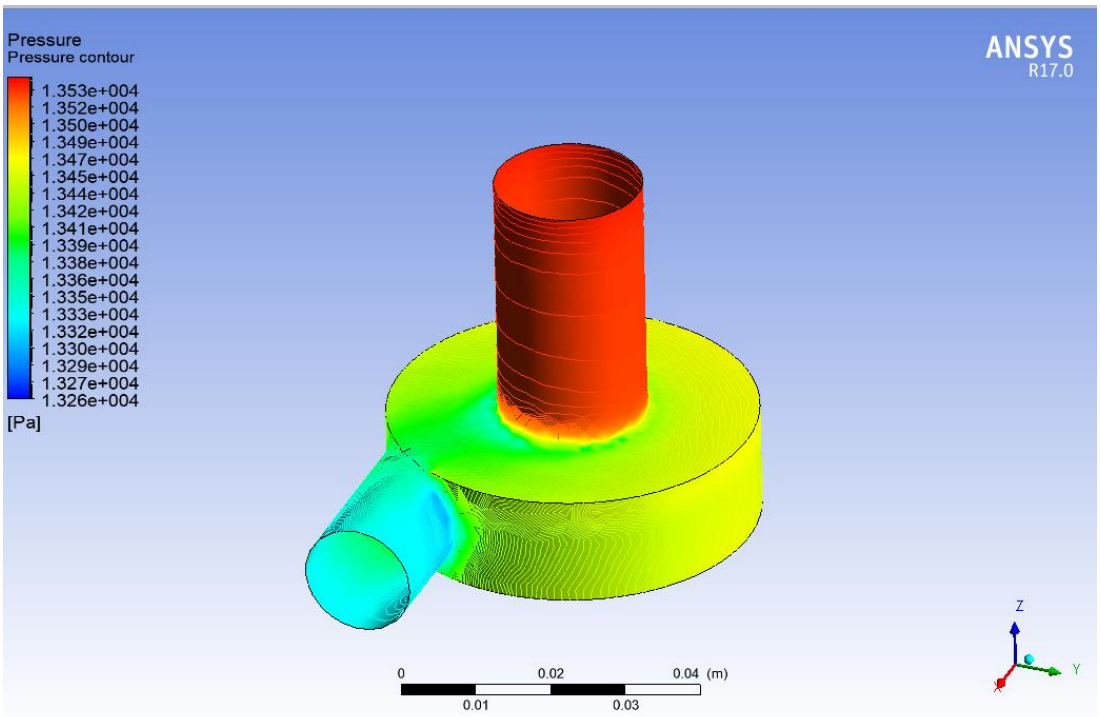

Figure 8.29 Pressure distribution in the pump with high values at the inflow tract, reducing in the pump case and even lower in the outflow tract.

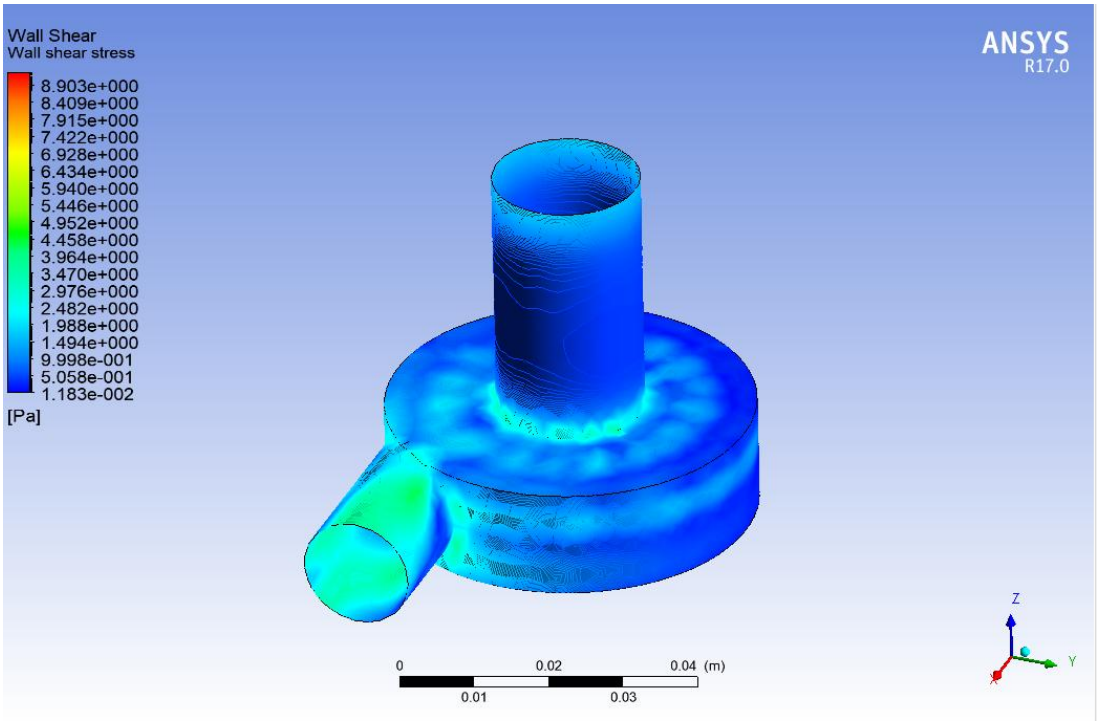

Figure 8.30 Wall shear stress distribution in the pump with values in the lower spectrum although higher towards the outflow tract.

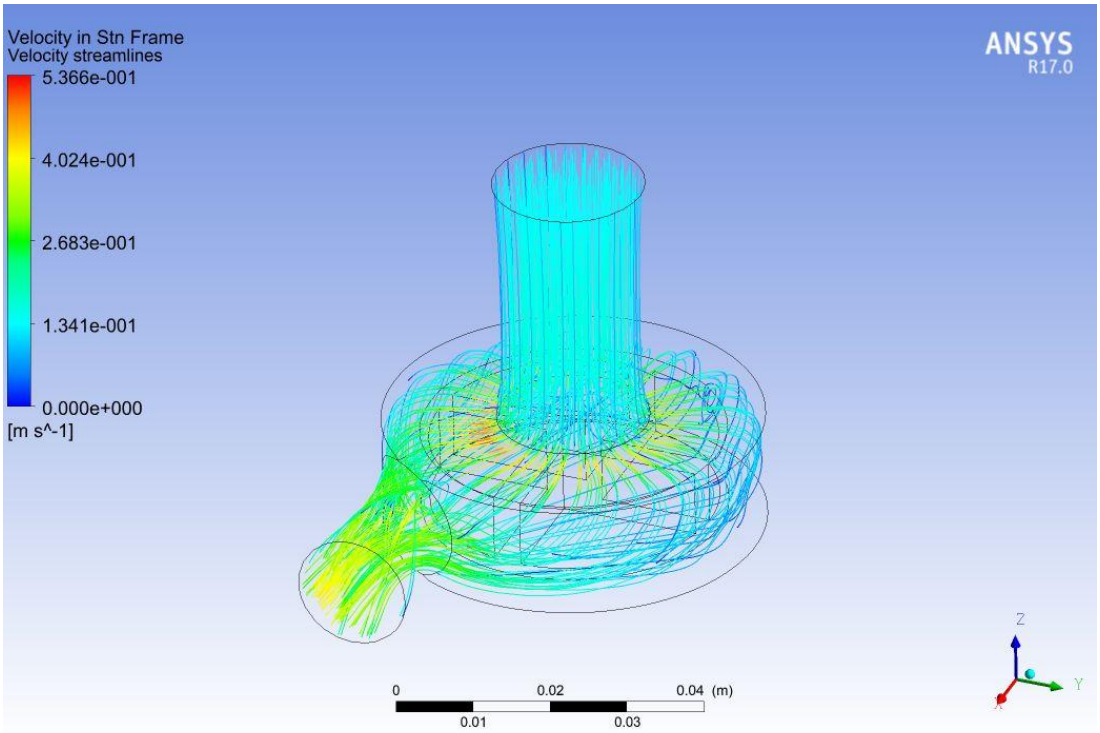

Figure 8.31 Velocity streamlines with low values at the inflow tract, rising towards the centre of the rotating zone and finally slightly reduced in the outflow graft.

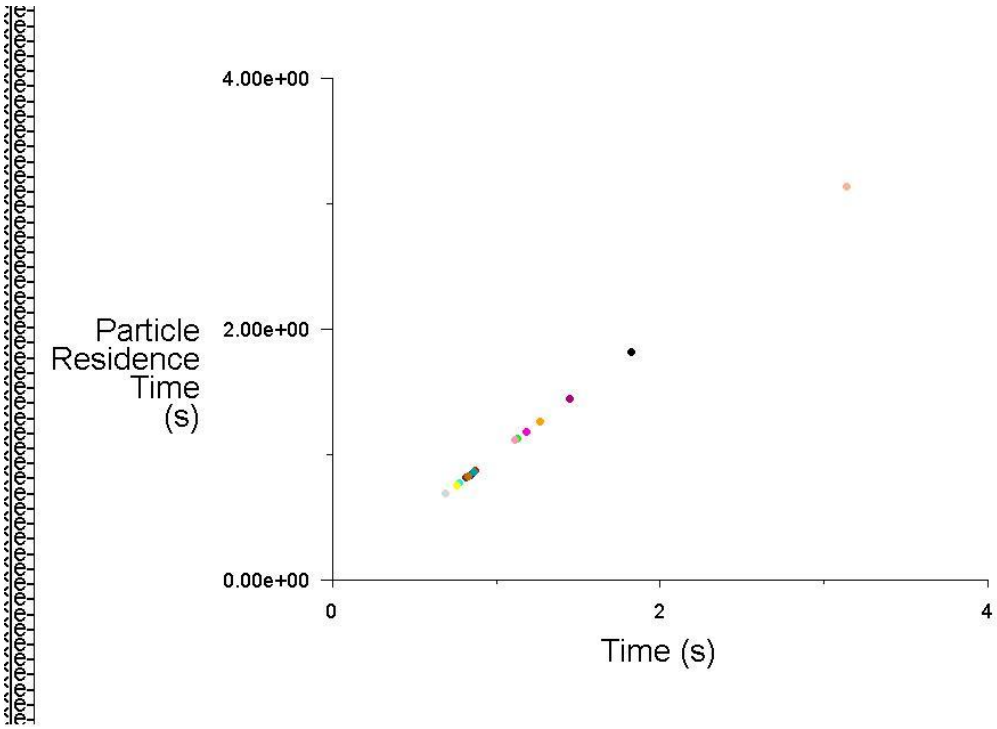

Figure 8.32 Onset of turbulent flow in the pump during pulsatile conditions show a particle residence time up to 2 s according to the DPM model in the context of the sliding mesh method.

8.4 Discussion

The overall wall shear stress distribution on the pump housing wall of the HeartWare HVAD showed low scale values, although slightly higher in proximity of the outlet (Fig. 8.6; Fig. 8.12; Fig. 8.18; Fig. 8.24; Fig. 8.30). The use of the sliding mesh method may have given slightly more accurate results at the expense of increased computational time. Nevertheless, this is only an assumption considering that there is no validation to substantiate it. Pressure distribution on the pump housing wall of the HVAD showed high scale values (Fig. 8.5; Fig 8.11; Fig. 8.17). Nevertheless, pulsatile velocity inlet in the context of k-ω SST model with MRF approach gave lower values although still in the high scale range (Fig. 8.23). Pulsatile velocity inlet in the context of k-ω SST model and sliding mesh method gave high scale values at the pump inlet as per Fig. 8.5 to Fig. 8.17 but low values in pump housing wall and even lower at the pump outlet (Fig. 8.29). Again, the sliding mesh method may have generated more accurate values at the expense of more computational time. Pressure distribution in the rotating zone gave high scale values particularly in the centre (Fig. 8.3; Fig. 8.9; Fig. 8.15). Once

again, pulsatile velocity inlet in the context of k-ω SST model and MRF approach generated lower values although still in the high spectrum range (Fig.8.21). Pulsatile velocity inlet in the context of k-ω SST model and sliding mesh method gave high scale values in the centre as per Fig. 8.3 to Fig. 8.15 and lower values peripherally (Fig. 8.27). They seem arguably more accurate values although at the expense of increased computational time. The wall shear stress distribution in the rotating zone was fairly consistent with low scale values in the centre but higher peripherally (Fig. 8.4; Fig. 8.10; Fig. 8.16; Fig. 8.22). Pulsatile velocity inlet in the context of k-ω SST model and sliding mesh method generated low scale values in the centre, rising significantly in the mid portion of the rotating zone but returning to lower scale values peripherally (Fig. 8.28). The behaviour of the velocity streamlines is quite consistent with low scale values at the pump inlet, rising significantly in the rotating zone and then reducing towards the pump outlet (Fig. 8.7; Fig. 8.13; Fig. 8.19; Fig. 8.25). A different behaviour was observed with pulsatile velocity inlet in the context of k-ω SST model and sliding mesh method: slightly higher values at the pump inlet, rising in the rotating zone but less compared to Fig. 8.7 to Fig. 8.25 and finally settling at medium values at the pump outlet (Fig. 8.31). A different behaviour has always been observed during pulsatile velocity inlet using k-ω SST model and sliding mesh method. These findings are suggestive of potential beneficial effect from a pulsatile pattern and may be related to higher accuracy generated by the sliding mesh method although at the expense of increased computational time. The particle residence time was between 0.2 and 2 s (Fig. 8.8; Fig. 8.14; Fig. 8.20; Fig. 8.26; Fig. 8.32).

Simulations based on the laminar model give initial information that could be discussed at a MDT meeting. The duration of the simulations remains within hours, which allows appropriate advanced planning in order to discuss an elective surgical procedure. Simulations based on the k-ω SST model take into account the transitional status from laminar to turbulent flow that is typical of rotary blood pumps. There are similar findings when using the laminar model and the k-omega SST in the context of the MRF approach and DPM model. Nevertheless, the use of the sliding mesh method seems to give slightly more accurate results although this is only an assumption in the absence of validation. Despite this limitation, it is reasonable to assume that an initial simulation based on the laminar model may be suitable for initial information that can be further refined according to the needs.

The use of a pulsatile profile considered the potential effects of speed modulation on the physiological environment.

Chapter 9

Simulations based on a patient-specific approach with model reconstruction of the Heart Mate II from CT-scan imaging

9 Simulations based on a patient-specific approach with model reconstruction of the Heart Mate II from CT-scan imaging

9.1 Material and Methods

A patient who underwent the insertion of the HeartMate II axial-flow pump was considered for the purposes of more realistic simulations. A 3D reconstruction of the pump from CT-scan imaging of the chest and upper abdomen (Figure 9.0) was obtained using Mimics Materialise. The aim was to analyse the fluid dynamics of the device as it was originally implanted in relation to the orientation of the inlet cannula in the left ventricle and the anastomosis of the outlet graft to the ascending aorta. Then, the impeller was scanned separately to highlight its features, which were not completely clear following the previous reconstruction of the device. The pump and its impeller were now available in two separate STL files which were assembled using Ansys SpaceClaim. This would enable to study the interactions between the impeller, the fluid and the wall of the pump. The combined STL file was meshed using Ansys ICEM CFD and imported into Ansys Fluent to set up and run the simulations accordingly. A mesh independence analysis was considered for the purposes of quality, accuracy and convergence. Five meshes were generated ranging from 205240 to 21266811 elements (Table 9.1). A mesh of 1065044 elements was considered appropriate for the purposes of the simulations based on the fact that further refinement was not giving additional benefit to the simulations (Figure 9.1). The mesh consisted mainly of tetrahedral elements for the pump regions. Prism elements were used for the boundary layers of the inflow and outflow graft wall (Figure 9.2).

Table 9.1 Data for mesh independence analysis

Elements	**Maximum Velocity Value (m/s)**
205240	2.42897
684503	2.44985
842178	2.9209
3335126	3.05376
21266811	2.9509

Blood was modelled as an incompressible, Newtonian fluid with density ρ = 1060 kg/m^3 and viscosity μ = 0.0035 *kg/m – s*. This is an appropriate assumption considering that the shear-thinning behaviour of blood becomes negligible at high shear rate (> 100 s^{-1}). The simulations were initially developed with the laminar model as ideal baseline conditions.

Subsequently, the shear stress transport (SST) k-ω model was considered for comparison purposes.

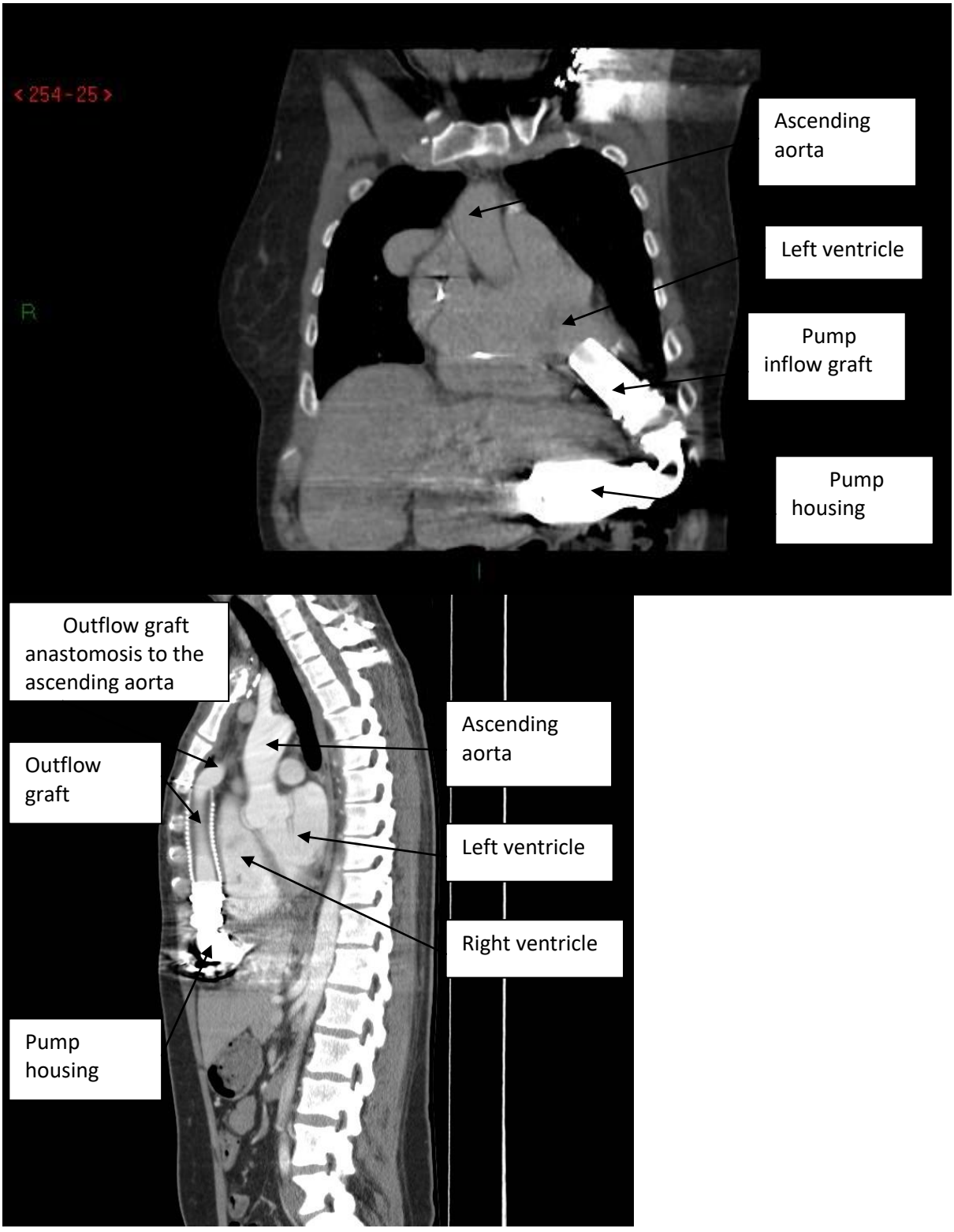

Figure 9.0 CT-scan images from DICOM series used for the 3D reconstruction of the HeartMate II.

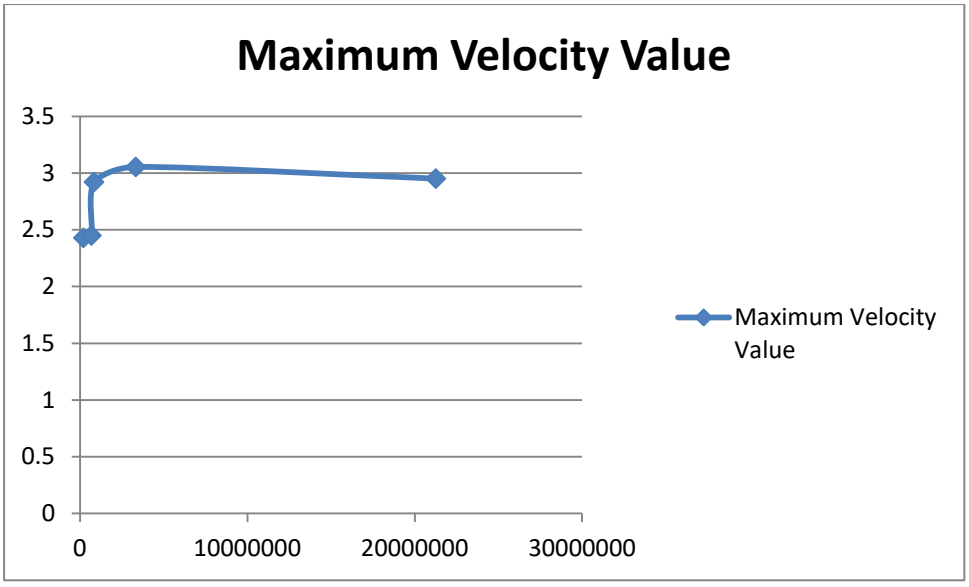

Figure 9.1 The maximum velocity value (y axis) is plotted as a function of the number of mesh elements (x axis).

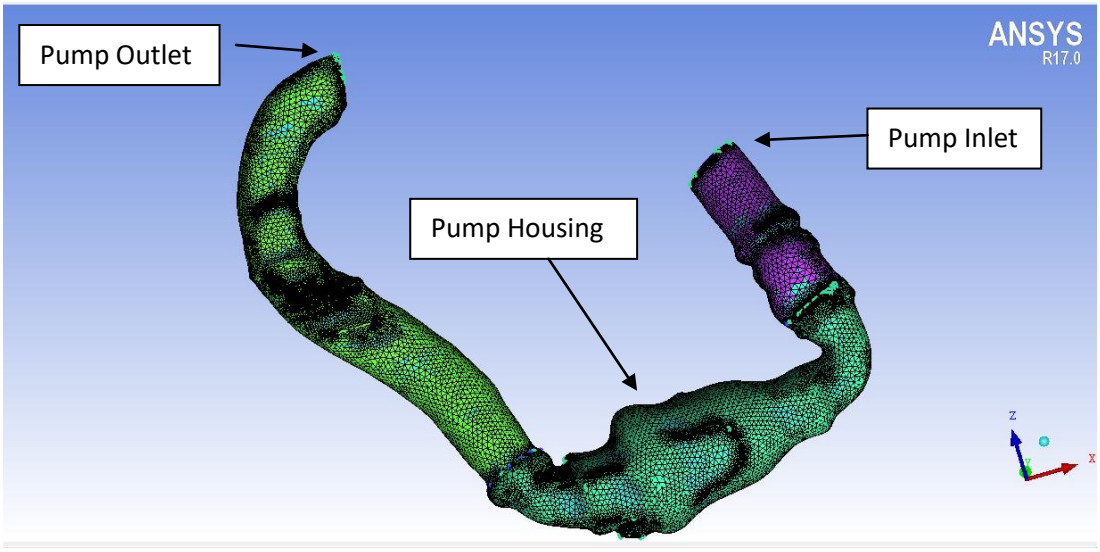

Figure 9.2 Mesh used for all the simulations. The HeartMate II consists of the pump (blue), the inflow graft (lilac) and the outflow graft (green).

The k-ω SST model was a key choice in view of its low Reynolds number correction factor considering that rotary blood pumps run at the transition point between laminar and turbulent flow. Simulations were run in 3D, double precision, serial mode in Ansys Workbench. The solver was pressure-based with absolute velocity formulation either in steady state or transient conditions. Boundary conditions were set at a specific mass flow rate (inlet) and at a fixed steady pressure (outlet). A flow of 6 L/min corresponding to 0.105 kg/s was considered at the inlet. The total pressure was set to zero at the inlet and the static pressure was set to 100 mmHg

(13332.2 Pa) at the outlet to achieve an average pressure increase of 100 mmHg. A fixed rotational speed of 9500 rpm for the impeller was considered in line with the range used in clinical practice for the HeartMate II. Pressure-velocity coupling was based on the coupled scheme. Spatial discretisation consisted of least squares cell based for the gradient; second order or PRESTO! for the pressure; second order upwind for the momentum, turbulent kinetic energy and turbulent dissipation rate. The PRESTO! scheme is well suited for steep pressure gradients involved in rotating flows. It provides improved pressure interpolation in situations where large body forces or strong pressure variations are present as in swirling flows. The pseudo transient algorithm and the warped-face gradient correction were also used to add an unsteady term to the solution equations with the aim to improve stability and enhance convergence. Walls were assumed rigid with no-slip boundary condition. The rotation of the impeller was simulated according to the moving reference frame (MRF) approach, which is a steady-state method available in Ansys Fluent for the the flow analysis of rotating parts. The equations of motion are modified with additional acceleration terms to account for the non-inertial motion of the moving frame. Boundary conditions are also defined in relation to the moving zone. Solutions become steady with respect to the moving reference frame and can be coupled with stationary domains through interfaces. The advantage of using a moving reference frame is that a flow field which is unsteady when viewed from the stationary frame becomes steady in the moving reference frame. Adjacent zones can be coupled to the moving zones through grid interfaces to create a simplified model of a complex moving zone system. A steady-state problem is desirable because it is easier and less computationally expensive to solve; boundary conditions are simpler; it is more straightforward to post-process and analyse. A “stationary wall” condition implies that the wall is stationary with respect to the adjacent cell zone. Therefore, in the case of a rotating reference frame, a stationary wall is actually rotating with respect to the absolute reference frame. To specify a non-rotating wall, selection of “moving wall” is needed during the set up procedure specifying an absolute rotational speed of 0 rpm (i.e., moving with respect to the rotating reference frame). Therefore, the wall of the HeartMate II body was set to “moving wall” with a rotational speed of 0 rpm; the impeller zone was set to “moving wall” with a rotational speed of 9500 rpm. The rotational movement of the impeller would cause displacement of the fluid zone. For this reason, a rotational speed of 0 rpm for the fluid zone was required.

The use of the sliding mesh method was subsequently considered to take into account the unsteady interaction between the stationary and rotating part. Nevertheless, the MRF approach was preferred in view of its features as previously mentioned. Finally, a time scale factor of 1 s was considered with an imput of 1000 iterations. Both steady state and transient simulations were considered according to the approach used.

Streamlines and contours of velocity, pressure distribution, and wall shear stress were considered for the analysis of flow in the pump. The discrete phase model (DPM) was used to estimate the particle residence time in the pump. An injection of mass-less particles from the inlet surface was considered for this purpose. The discrete random walk model was enabled during the DPM setting to take into account the lateral diffusion effect of the particles due to turbulence.

9.2 Results

9.2.1 Laminar model with MRF approach and DPM model

Laminar flow conditions in the pump were initially assumed as an ideal case. The simulation setting consisted of the laminar model in steady state conditions. The MRF approach was considered for the rotating impeller. The DPM model was used for the analysis of the particles residence time. A pump rotational speed of 9500 rpm was considered. Boundary conditions included mass flow inlet of 6 L/min equivalent to 0.105 Kg/s and pressure outlet of 13332.2 Pa equivalent to 100 mmHg. A time scale factor of 1 s was considered with an input of 1000 iterations.

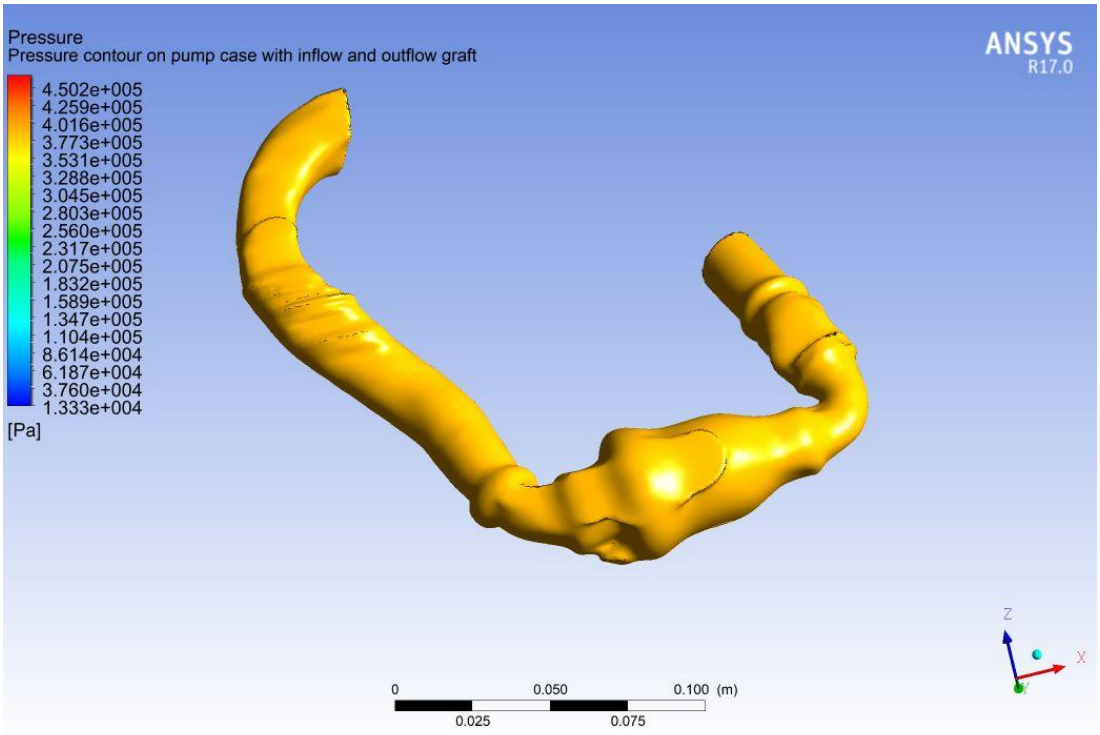

Figure 9.3 Uniform pressure distribution with values in the high spectrum in the inflow tract, pump case and outflow graft.

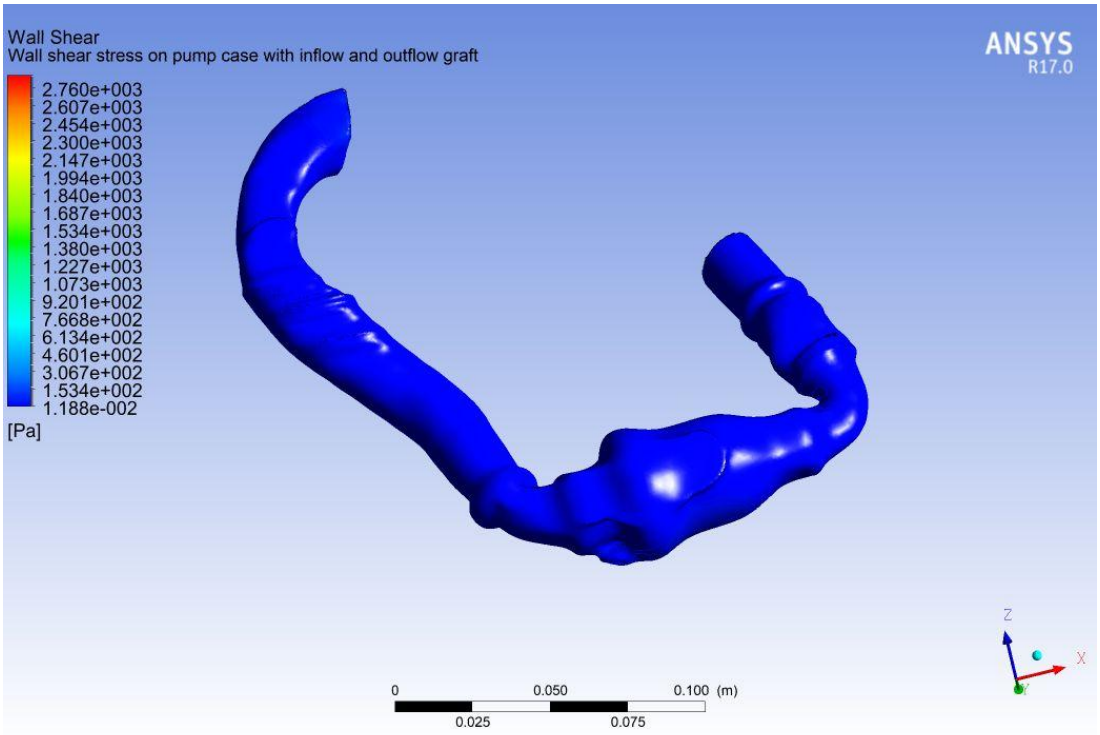

Figure 9.4 Uniform wall shear stress distribution with lower spectrum values in the inflow tract, pump case and outflow tract.

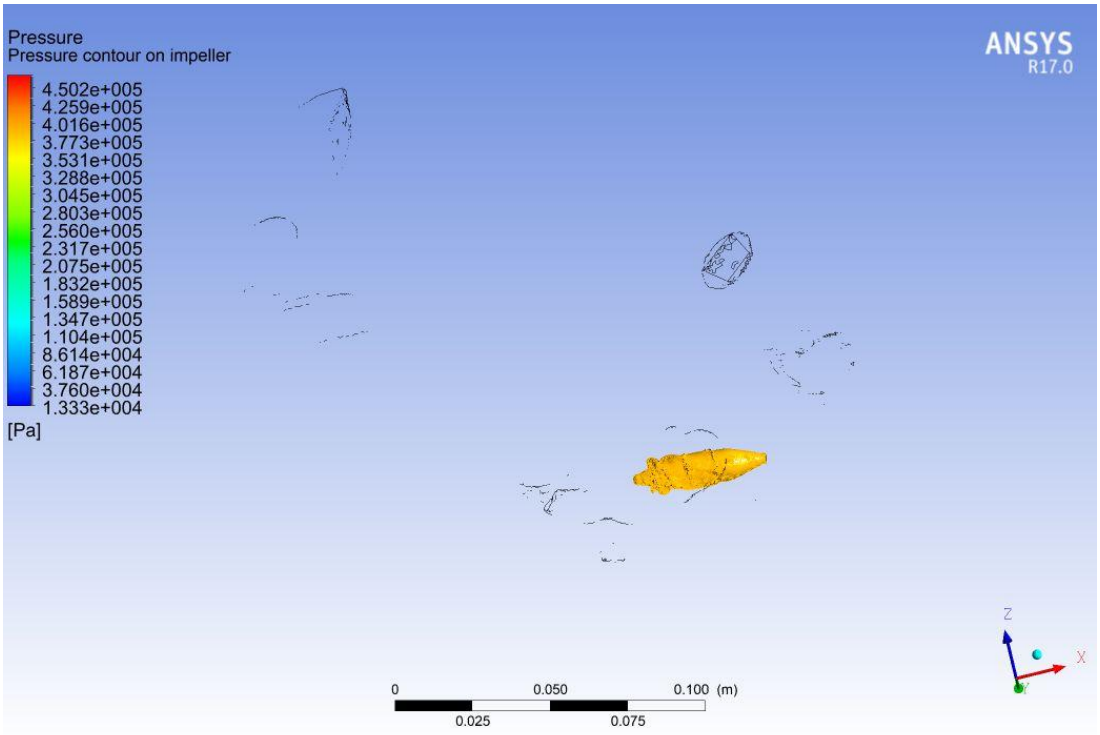

Figure 9.5 Uniform pressure distribution on the impeller with values in the higher spectrum.

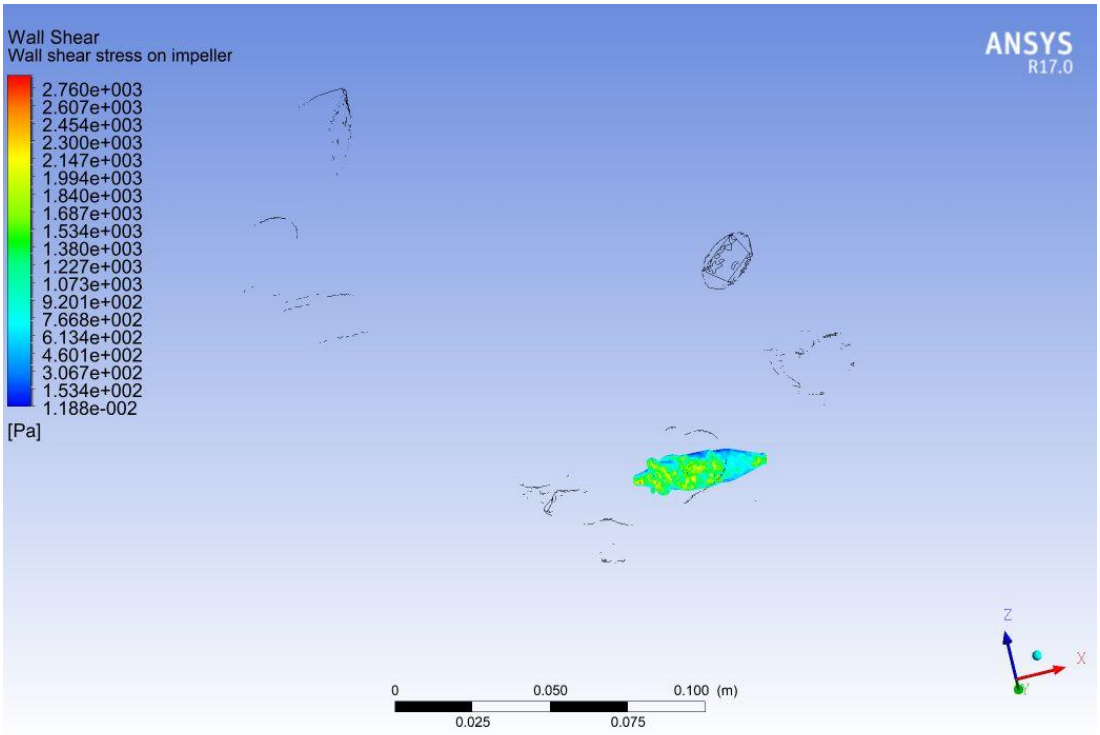

Figure 9.6 Wall shear stress distribution on the impeller with low values at the back and much higher values at the front.

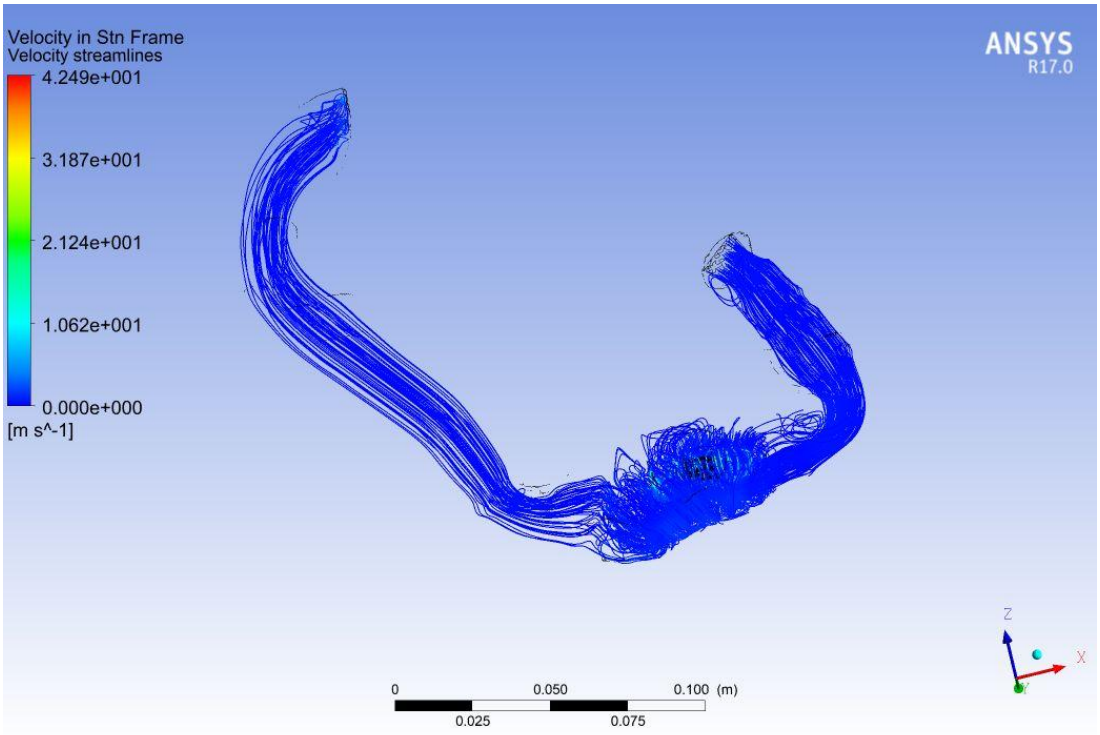

Figure 9.7 Uniform distribution of the velocity streamlines with values in the lower spectrum.

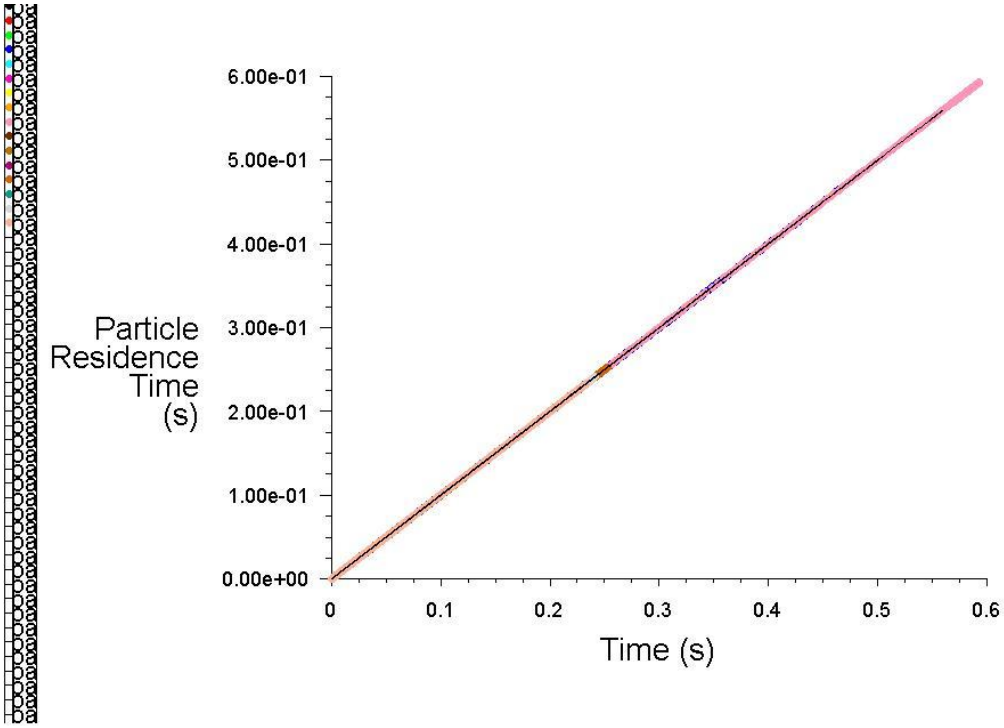

Figure 9.8 Laminar flow conditions show a particle residence time up to 0.6 s according to the DPM model in the context of the MRF approach.

9.2.2 k-ω SST model with MRF approach and DPM model

Subsequently, the k-ω SST model was used to account for the development of turbulence in the pump. Steady state conditions were considered and the MRF approach was implemented for the rotating impeller. The DPM model was used for the analysis of the particles residence time. A pump rotational speed of 9500 rpm was considered. Boundary conditions included mass flow inlet of 6 L/min equivalent to 0.105 Kg/s and pressure outlet of 13332.2 Pa equivalent to 100 mmHg. A time scale factor of 1 s was considered with an input of 1000 iterations.

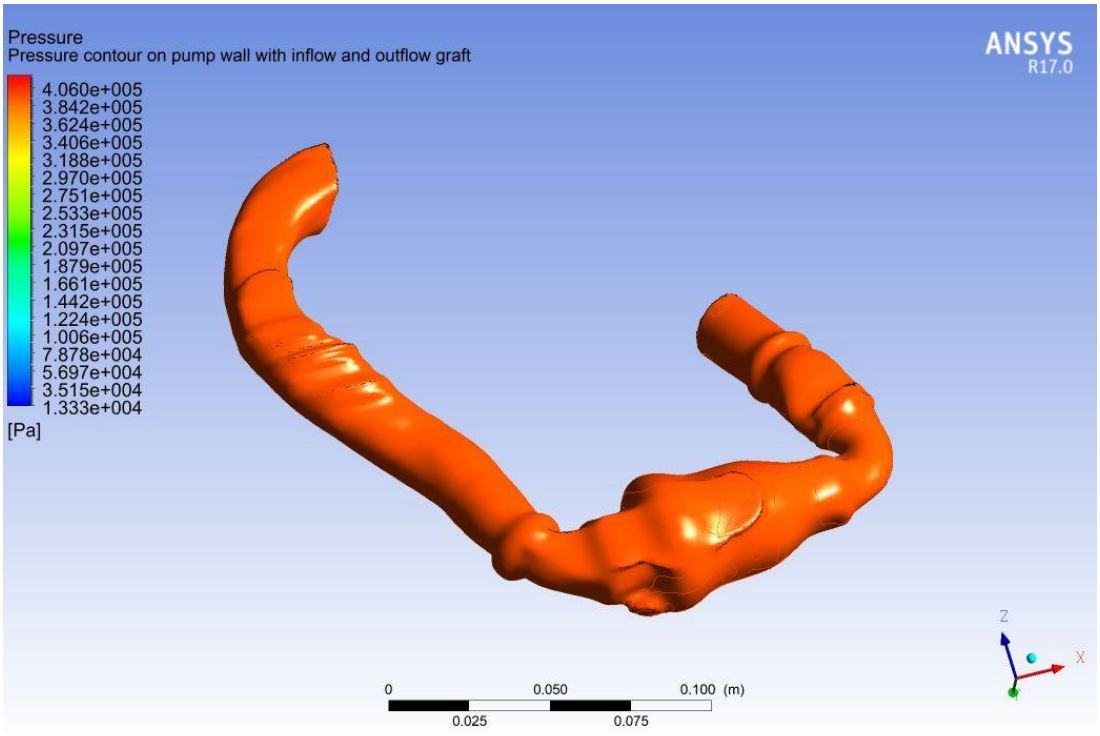

Figure 9.9 Uniform pressure distribution with higher spectrum values in the inflow graft, pump case and outflow graft.

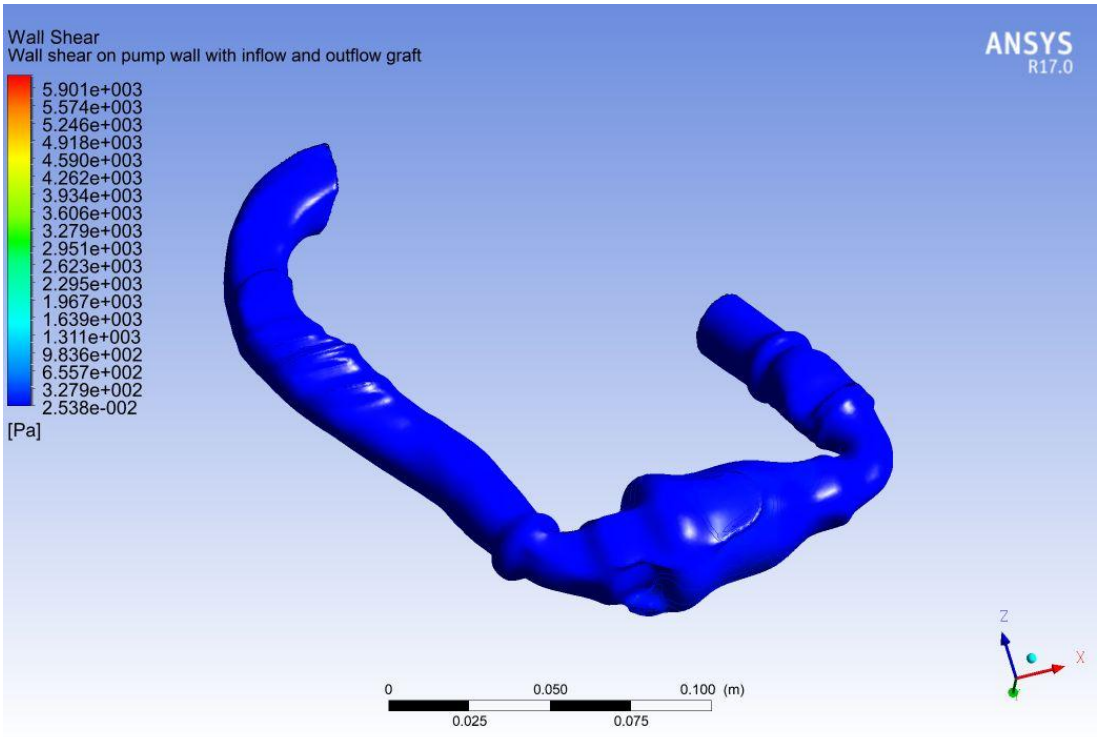

Figure 9.10 Uniform wall shear stress distribution with lower spectrum values in the inflow tract, pump case and outflow graft.

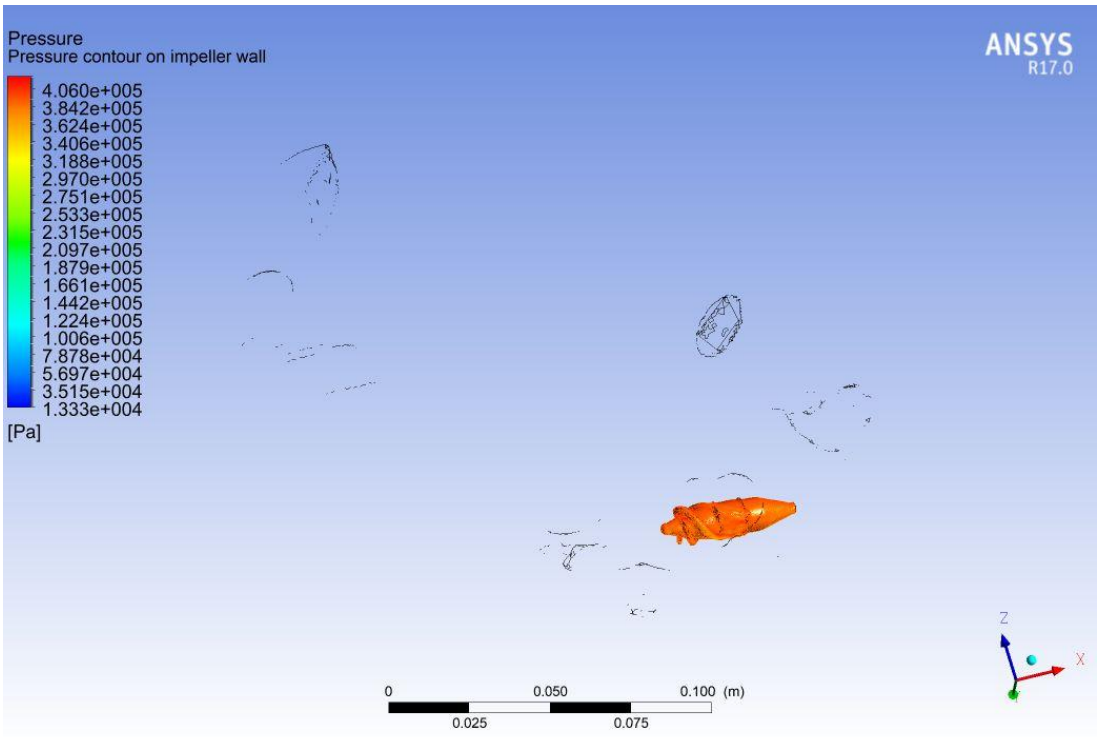

Figure 9.11 Uniform pressure distribution on the impeller with values in the higher spectrum.

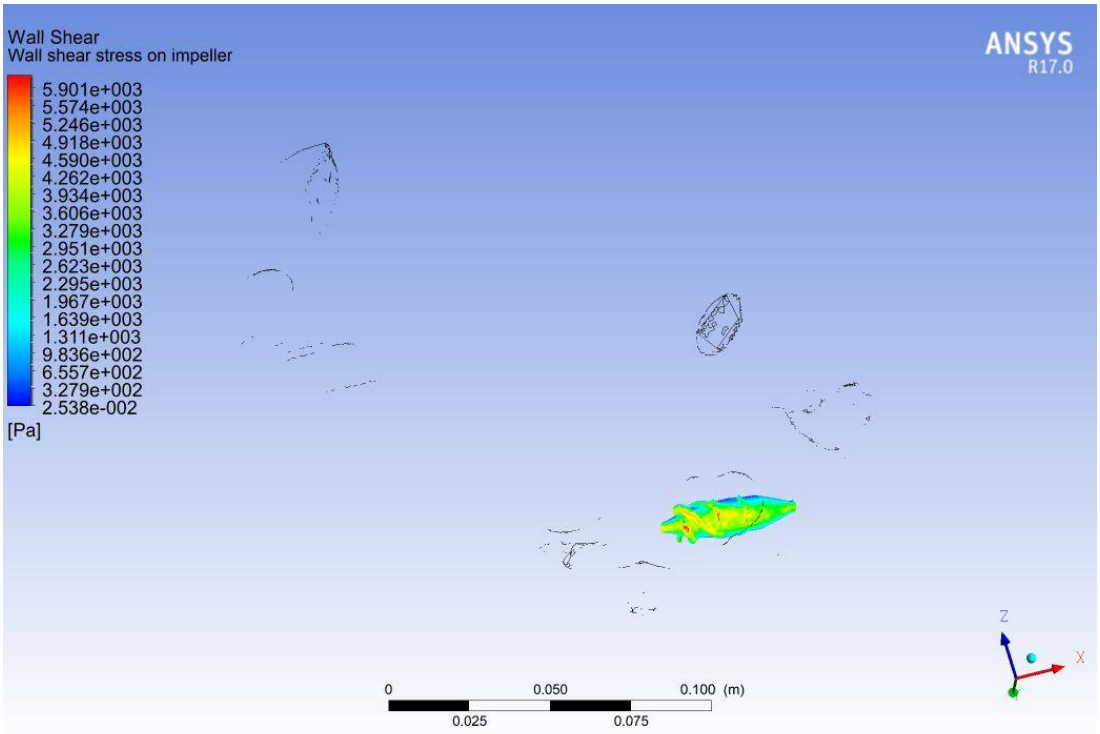

Figure 9.12 Wall shear stress distribution on the impeller with predominantly high spectrum values, particularly towards the front.

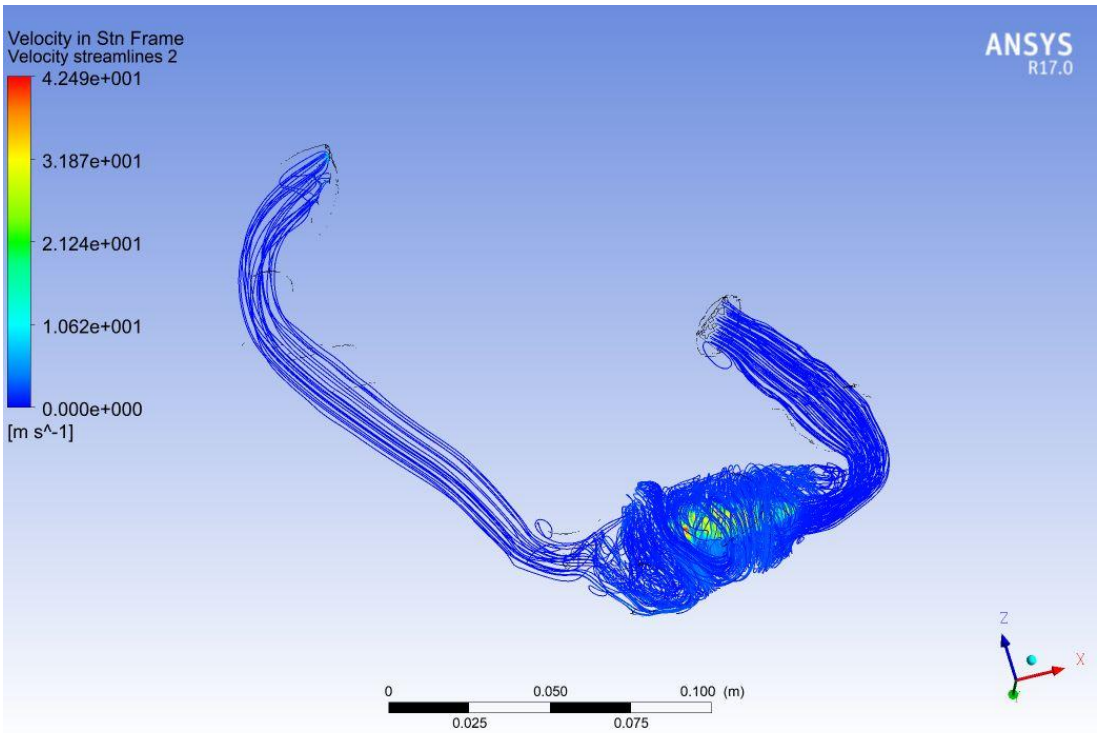

Figure 9.13 Uniform distribution of the velocity streamlines with values in the lower spectrum.

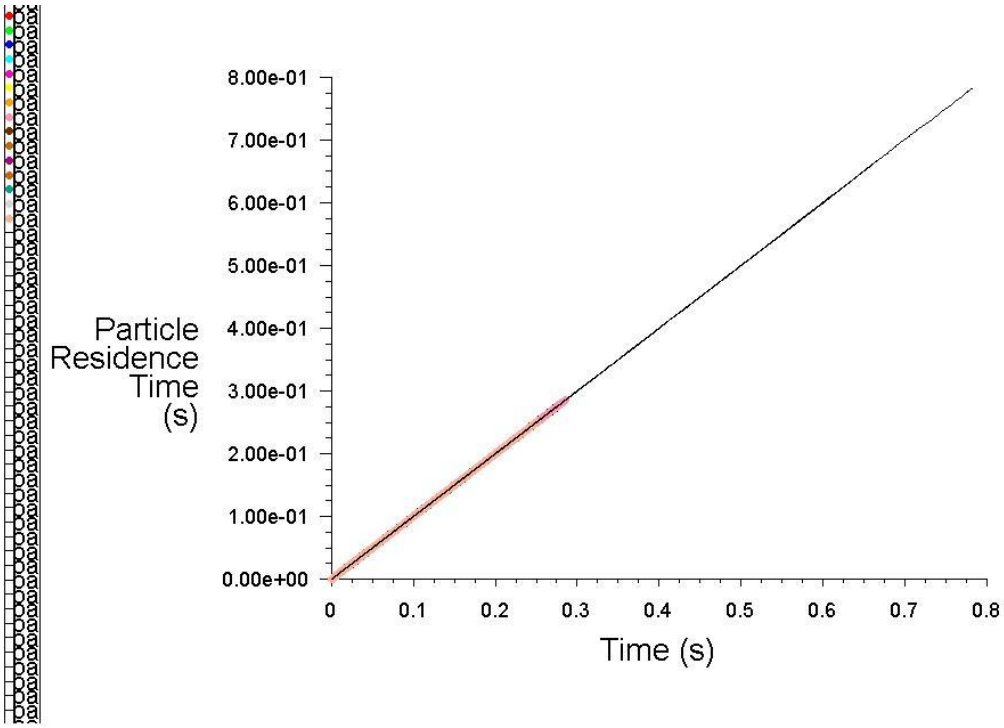

Figure 9.14 Onset of turbulent flow in the pump show a particle residence time up to 0.8 s according to the DPM model in the context of the MRF approach.

9.2.3 k-ω SST model with sliding mesh method and DPM model

Finally, the sliding mesh method was considered for comparison purposes in relation to accuracy of results. The k-ω SST model was used to account for the development of turbulence in the pump. A transient simulation was required. The DPM model was used for the analysis of the particles residence time. A pump rotational speed of 9500 rpm was considered. Boundary conditions included mass flow inlet of 6 L/min equivalent to 0.105 Kg/s and pressure outlet of 13332.2 Pa equivalent to 100 mmHg. A time scale factor of 1 s was considered with an input of 1000 iterations.

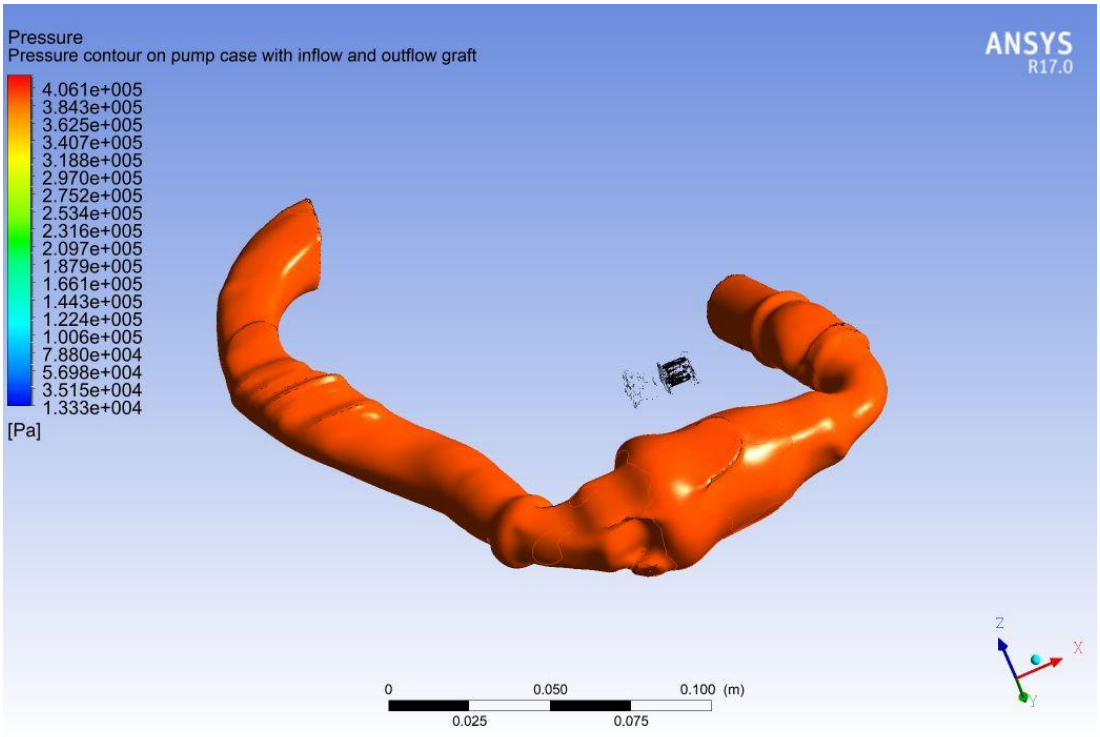

Figure 9.15 Uniform pressure distribution with high spectrum values in the inflow graft, pump case and outflow graft.

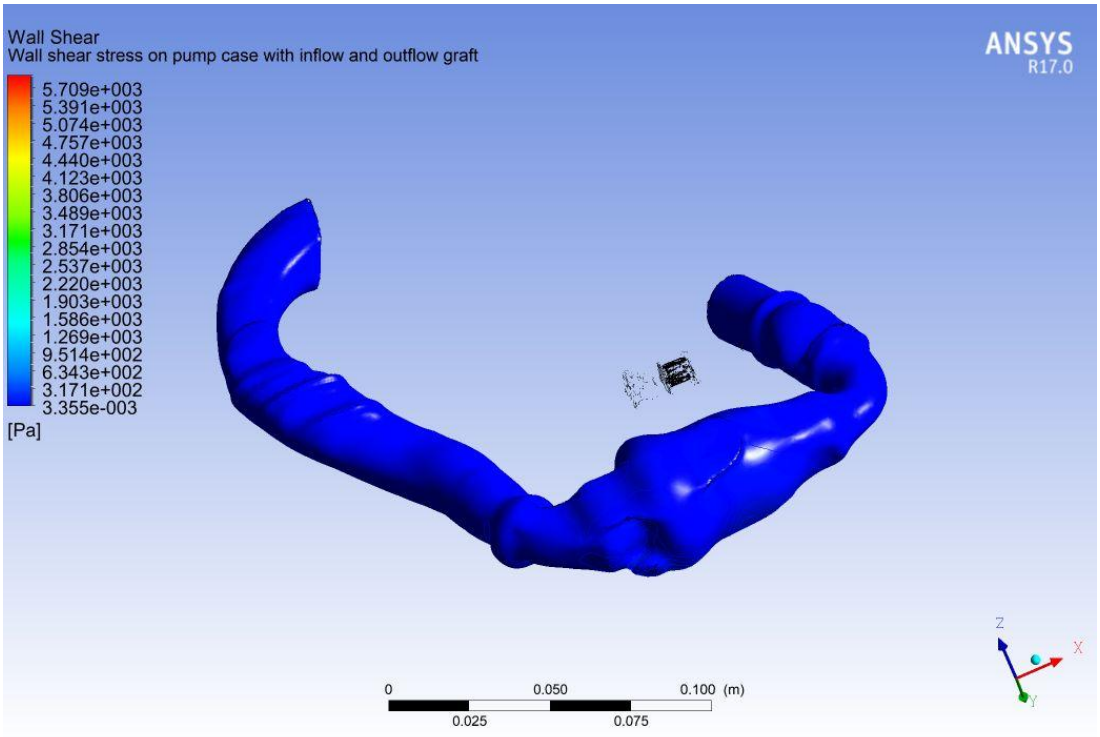

Figure 9.16 Uniform wall shear stress distribution with low spectrum values in the inflow graft, pump case and outflow graft.

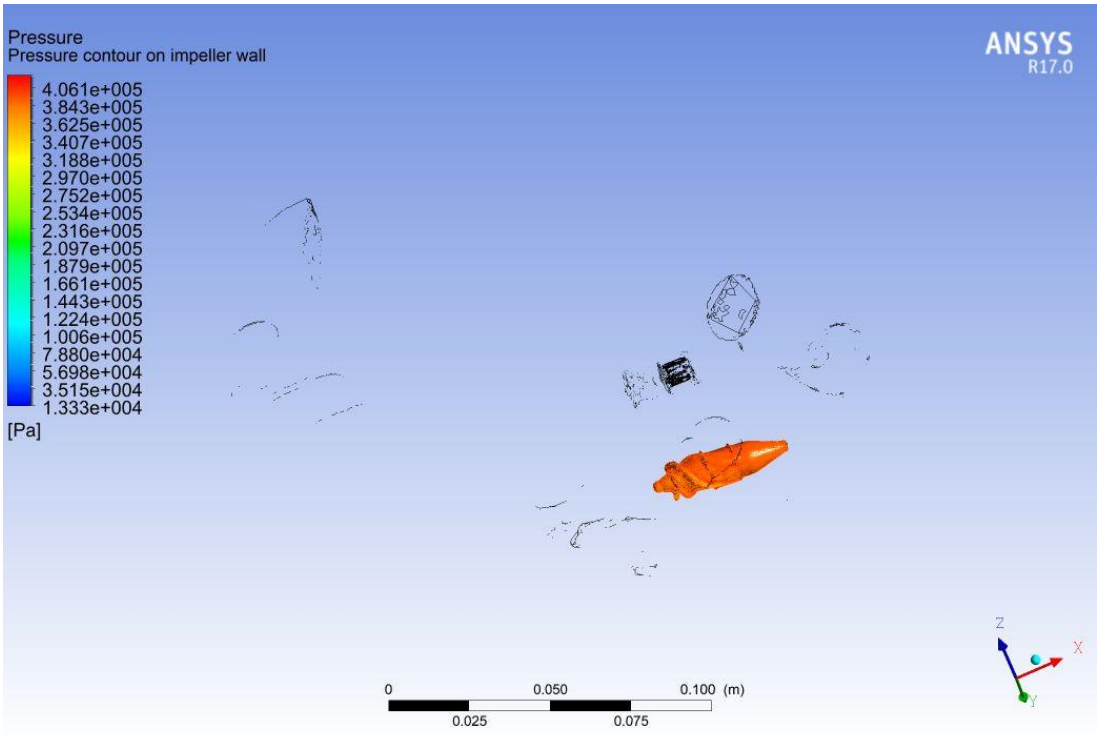

Figure 9.17 Uniform pressure distribution on the impeller with values in the high spectrum.

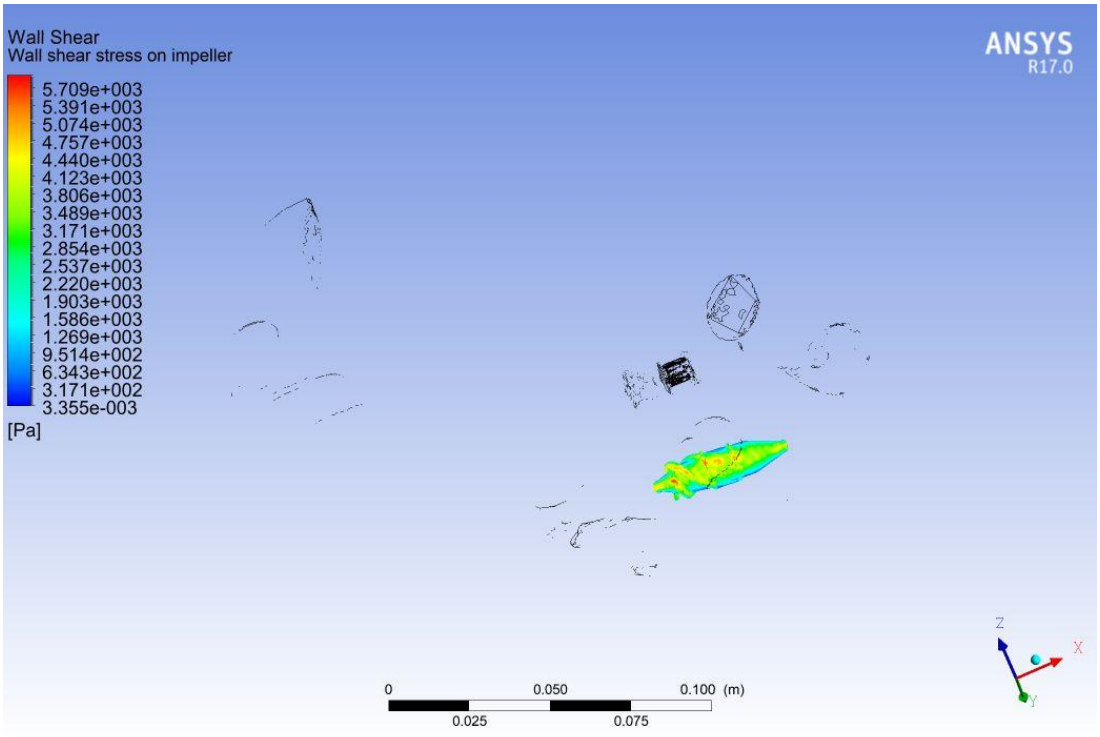

Figure 9.18 Wall shear stress distribution on the impeller with predominantly high spectrum values, particularly towards the front.

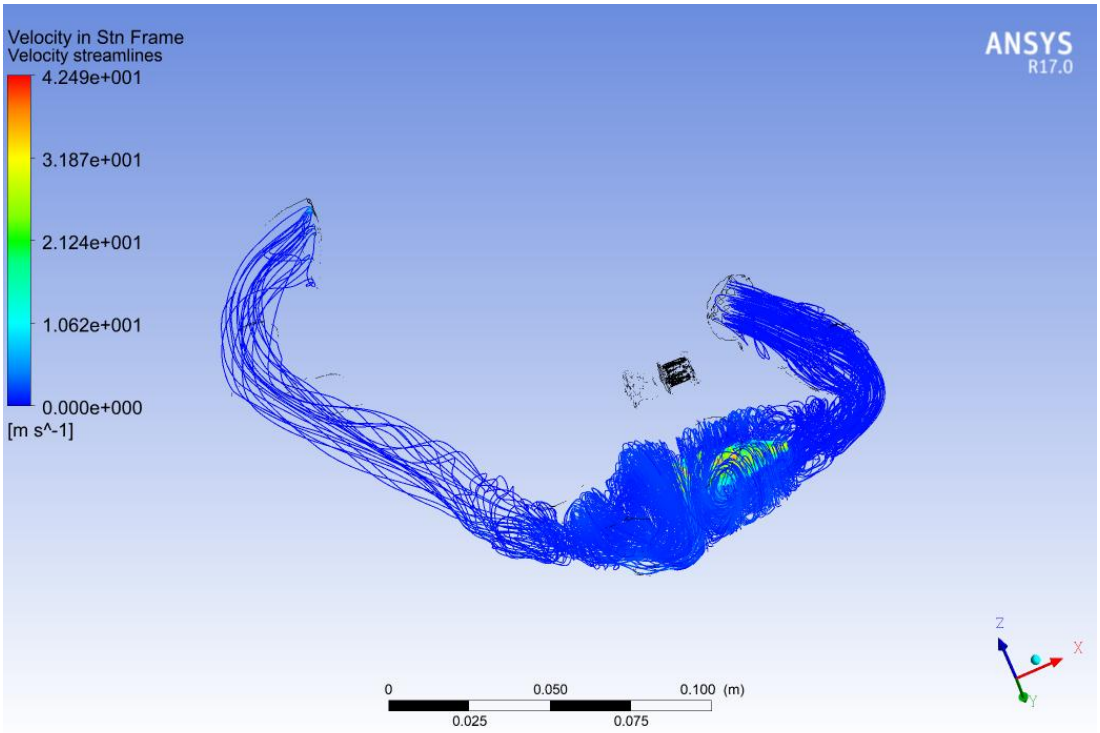

Figure 9.19 Velocity streamlines with dense distribution at the inflow graft and in the pump case.

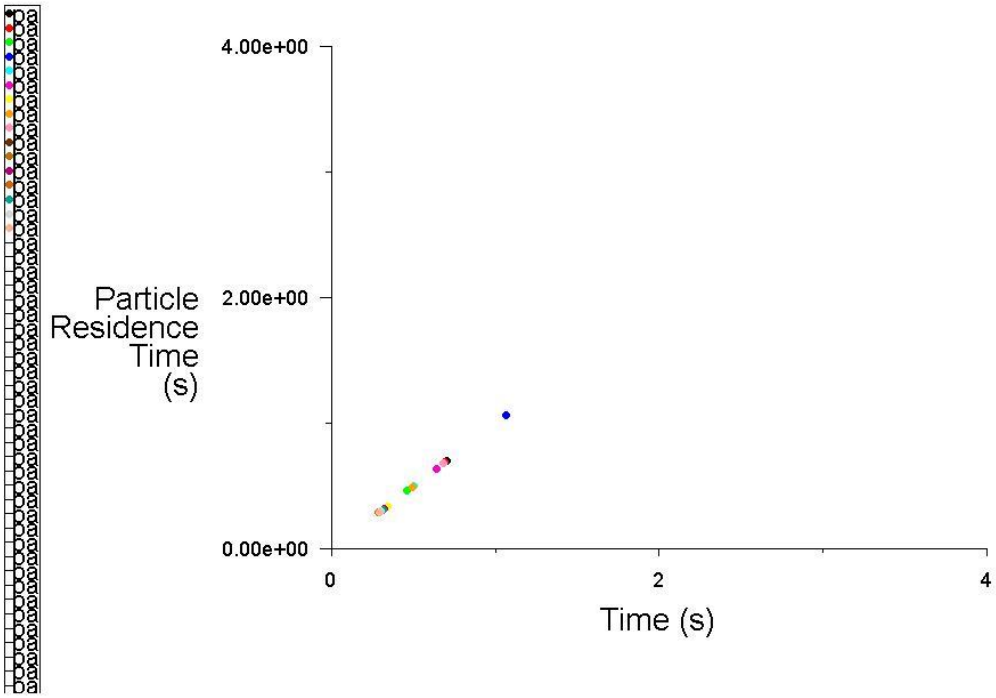

Figure 9.20 Onset of turbulent flow in the pump show a particle residence time up to 1 s according to the DPM model in the context of the sliding mesh method.

9.3 Discussion

The pressure distribution on the pump housing wall and inflow and outflow grafts of the HeartMate II was fairly consistent with high spectrum values (Fig. 9.3; Fig. 9.9; Fig. 9.15). The overall wall shear stress distribution on the body of the HeartMate II including inflow and outflow grafts was consistently in the lower scale values (Fig. 9.4; Fig. 9.10; Fig. 9.16). The pressure distribution on the impeller was consistently in the high scale values (Fig. 9.5; Fig. 9.11; Fig. 9.17). The wall shear stress distribution on the impeller was also quite consistent with high scale values towards the front. The velocity streamlines behaviour was consistent with lower scale values suggesting the potential for thrombus development in proximity of the anterior aspect around the ruby bearing as per my previous clinical experience (Capoccia, 2013). The particle residence time was between 0.6 s and 2 s. (Fig. 9.8; Fig. 9.14; Fig. 9.20). The duration of the simulations was in the order of hours, which would fit the time constraints of the clinical environment and be ready available before a planned MDT meeting.

Simulations based on the laminar model give initial information that could be discussed at a MDT meeting. The duration of the simulations remains within hours, which allows appropriate advanced planning in order to discuss an elective surgical procedure. Simulations based on the k-ω SST model take into account the transitional status from laminar to turbulent flow that is typical of rotary blood pumps. There are similar findings when using the laminar model and the k-omega SST in the context of the MRF approach and DPM model. Nevertheless, the use of the sliding mesh method seems to give slightly more accurate results although this is only an assumption in the absence of validation. Despite this limitation, it is reasonable to assume that an initial simulation based on the laminar model may be suitable for initial information that can be further refined according to the needs.

Chapter 10

Discussion and Future Perspectives

10 Discussion and Future Perspectives

10.1 Discussion

Ventricular assist devices (VADs) operate in a flow regime which has been difficult to simulate: the transitional region at the boundary of laminar and turbulent flow (Fraser, 2011).

The flow pattern in most regions of rotary blood pumps is turbulent because of the disturbance caused by the rotating impeller. The choice of a turbulence model is important for the outcome of the simulation but remains a controversial issue when applied to rotary blood pumps (Song, 2003a).

Two-equation turbulent models have been used to study the flow behaviour in rotary blood pumps. They allow the determination of a turbulent length and time scale by solving two separate transport equations. The standard k-ε turbulence model has been widely used in CFD simulations of rotary blood pumps (Chua, 2005; Anderson, 2000a; Anderson, 2000b; Song, 2004a; Miyazoe, 1999). The k-ε model is based on transport equations for the turbulence kinetic energy k and its dissipation rate ε. This is a semi empirical model where the transport equation for k is derived from the exact equation, while the transport equation for ε is obtained by physical reasoning. It is a popular turbulence model in view of its robustness, computational economy and sufficient accuracy for a wide range of flows in industrial applications. In contrast, it is based on the assumption that the flow is fully turbulent and the effects of molecular viscosity are negligible. Therefore, the standard k-ε model is valid only for high-Reynolds number turbulent flows (ANSYS Fluent Theory Guide, August 2016). In view of its weaknesses (Mizunuma, 2007), modifications have been introduced to improve its performance such as the RNG k-ε model (Yakhot, 1986; Yakhot, 1992) and the realizable k-ε model (Shih, 1995).

The standard k-ω model is based on the Wilcox k-ω model, which considers low-Reynolds number effects, compressibility and shear flow spreading (Wilcox, 1998). It is an empirical model based on transport equations for the turbulence kinetic energy k and the specific dissipation rate ω, which can be considered as the ratio of ε to k. Subsequent modifications have improved the accuracy of the model for predicting free shear flows (Wilcox, 2008). The shear-stress transport (SST) k-ω model (Menter, 1994) combines the robust and accurate formulation of the k-ω model in the near-wall region with the free-stream independence of the k-ε model in the far field. Turbulence models give more accurate results than the laminar model with k-ε RNG and Reynolds Stress (RSM) models being previously recommended for the study of flow behaviour in circulatory assist devices (Zhang, 2013), although this

seems to contradict the above considerations and my findings. In fact, my simulations have confirmed the suitability of the k-ω SST model for the Heart Ware HVAD and the HeartMate II continuous-flow devices but I am going to discuss this aspect later into more details.

My initial aim was to develop a simulation approach that may be applicable within the time constraints of the clinical environment with particular reference to multi-disciplinary team meetings (MDTs). This is an important aspect of patient care where treatment options are discussed with a view to offer the most suitable approach taking into account pros and cons, which may well affect outcome. Emotions may run high because of the desire to offer the best possible care to our patients and it is not uncommon to remain in disagreement about the approach to be used. Experience and clinical judgement still remain essential for this purpose where the clinician is the ultimate decision-maker. Nevertheless, the ability to make a final decision on a difficult case based on a simulation approach would be an attractive prospect. Although evidence based practice (EBP) seems the fashion at present where everything has to follow the outcome of rigorously designed randomised controlled clinical trials (RCTs), there will always be grey areas without clear answers or treatments that have shown their beneficial effect despite the absence of the required evidence. EBP is meant to provide a secure ground for clinical decision-making which may not be realistic. EBP seeks to address uncertainty but it cannot eliminate it. The results of trials are applicable in general but may not be completely suitable for a specific group of patients or even for the single patient. A limitation of the interpretation of RCTs is the apparent willingness to disregard the importance of the context and minimise the complexity of the individual patients involved (Baumann, 2010). As a clinician, I would like to have a solid ground for my decision-making but the reality is that this ground does not exist. A more personalised approach to treatment may add a different dimension with some potential advantages as long as it is considered in the appropriate context and not as a “magic bullet”.

The presence of non physiological flow patterns enhancing the haemostatic response is one of the major issues in blood re-circulating devices. The development of elevated flow stresses in the non physiological geometries of these devices is closely related to thrombus formation by chronic platelet activation. This, rather than haemolysis, seems the key aspect of blood trauma in blood re-circulating devices. The activation and sensitisation response of platelets in blood re-circulating devices is dependent on shear loading rate, shear stress magnitude and exposure time (Sheriff, 2013). The development of new methods may help with the optimisation of the

thrombogenic performance of these devices. The interaction between flow-induced stresses and blood components is related to the hypothesis that thrombo-embolism in blood re-circulating devices is initiated and maintained by the non-physiological flow patterns and stresses, which activate and enhance platelet aggregation (Bluestein, 2010). Platelet activation and thrombogenicity is probably the main point to focus on. Recognition that thrombosis rather than haemolysis is the primary clinical problem associated with blood re-circulating devices is critical for further progress. Different approaches have been considered for the study of device-induced thrombogenicity (Jesty, 2003), each of them with strengths and weaknesses that have been refined over the past years to increase accuracy and develop further understanding (Chiu, 2017; Chiu, 2019; Consolo, 2017; Selmi, 2019; Zhang, 2019; Ghodrati, 2020).

Vortex shedding is a major mechanism for the development of microemboli in blood re-circulating devices. Unsteady turbulent simulations (URANS) with the transient turbulence Wilcox k-ω model show the intricate dynamics of the shed vortices and quantify the stress history of platelets along pertinent trajectories (Bluestein, 2000; Bluestein, 2002).

The use of advanced approaches to turbulence modelling such as complex transient/turbulent simulations including a damage accumulation model has been successful (Alemu, 2007; Dumont, 2007). Interaction of activated platelets with blood field (Fogelson, 1996; Sorensen, 1999a; Sorensen, 1999b; Kuharsky, 2001; Affeld, 2004) and platelet deposition models have also been used (Reininger, 1999; Longest, 2003). A reliable method capable of delivering quantitatively accurate predictions of flow-induced blood haemostatic activation is essential in order to reduce thrombo-embolism in cardiovascular devices. Based on these considerations, I sought to investigate the role of laminar and k-ω SST models to determine patterns of flow behaviour that may help preoperative planning with a view to treatment optimisation and outcome prediction. The ability to model and simulate the effect of device implantation with reference to key elements and discuss the findings during a MDT meeting would allow visualisation of the intended therapeutic approach. Besides, the mapping of certain patterns of flow behaviour may also help identify potential problems during patients' follow up. I decided to apply this idea to a retrospective analysis of patients who underwent the insertion of the HeartWare HVAD (centrifugal) and the HeartMate II (axial) continuous-flow devices. A 3D reconstruction of the implanted devices from postoperative CT-scan imaging would allow visualisation of the relationship between the inflow cannula and the interventricular septum and the angle of the anastomosis between the

outflow graft and the ascending aorta. I also had separate CT-scan imaging of the impeller of the two devices, which I had previously explanted from two patients. This would allow a more detailed 3D reconstruction and assembly with the pump. The outcome was very successful for the HeartMate II impeller. Instead, the impeller of the HeartWare HVAD gave too many artefacts following CT-scanning. Therefore, I decided to reproduce the HVAD in Ansys Design Modeller and use it as a starting point for CFD analysis. Although not completely accurate and realistic, the application of the laminar model to my simulations was a good starting point with interesting results. The qualitative analysis was suggestive for critical areas at risk for thrombus formation in line with my clinical experience and findings following pump explantation. I have mainly concentrated my efforts on a qualitative analysis as an attempt to identify patterns of behaviour that may give a visual assessment for the purposes of clinical-decision making during a MDT meeting. Besides, the aim was the proposal of an approach based on easy understanding of basic principles considering that the majority of clinicians find quantitative assessment quite intimidating. Perhaps, a common language between biomedical engineers, clinicians and imaging experts would be the key starting point to build up a long-lasting co-operation where patients remain at the centre of what we do. Willingness to make this approach work remains a key element.

Steady state simulations and the use of multiple reference frame method (MRF), which involves a fixed evaluation frame (frozen rotor) without physical rotation of the impeller, are convenient approximations to reduce computing time but they do not take into account transient effects or other conditions (Gross-Hardt, 2019). This is the reason why I considered both steady state and transient simulations with variable pressure or pulsatile effect at the inlet as an attempt to create a more realistic simulation environment. Although it is important to maintain a critical approach and understand the limitations of CFD simulations (Malinauskas, 2017; Gross-Hardt, 2019), the potential of this method remains in my opinion quite attractive for clinical application. The outcome of the simulations performed for the HeartWare HVAD and the HeartMate II show the suitability of the k-ω SST model, which may be considered on a more routine basis for preoperative assessment, treatment optimisation and outcome prediction. The laminar model may still have a role to play as long as its limitations are taken into account.

10.2 Future Perspectives

Although continuous-flow LVADs have contributed significantly to the clinical management of advanced heart failure, some key issues remain to be addressed before their full potential can be achieved. Current available devices are persistently delivering a mid-term performance of 3-5 years. The next step is a consistent performance over 7-10 years. Further design improvement aimed at the reduction of shear stress and avoidance of stasis may address adverse events like bleeding, stroke and pump thrombosis. Cost-effectiveness should be considered in relation to availability of resources (Pinney, 2017). Recent reviews have highlighted the success and the limitations of current LVADs but also the potential for further developments that may consolidate their use on a more routine basis (Schumer, 2016; Pinney, 2017; Schmid Daners, 2017; Doost, 2017). Long-term, sustainable LVAD performance can be further improved by addressing key areas such as surface endothelialisation to reduce bleeding and pump thrombosis; improvement in haemocompatibility; CFD optimisation of devices aiming at further reduction of blood damage; full LVAD implantability with TETS technology. (Schmid Daners, 2017). Aortic regurgitation and exacerbation of right heart failure remain also unresolved issues following LVAD implantation with consequences on patient's outcome (Frazier, 2010; Soucy, 2013). Pump speed modulation based on physiological control systems generating a pulsatile-like arterial waveform may offer a potential solution for the prevention of these undesired effects (Soucy, 2015). The hybrid membrane VAD concept is a novel approach that may well lead to more haemocompatible devices (Ferrari, 2021). There are clear differences between axial and centrifugal flow design (Moazami, 2013). The recent trend has shifted towards the development of centrifugal continuous-flow devices in view of their higher flow pulsatility, improved estimate of flow accuracy, smaller size, lower inlet suction and equivalent adverse events rate for the HeartMate II and the HeartWare™ HVAD™ Pump (Pagani, 2009; Slaughter, 2013). The HeartMate III has these advantages including the option for physiological pulsatility, a bearingless pump rotor and an accurate flow estimator. The HeartWare™ MVAD™ Pump is an axial flow pump with some typical elements of a centrifugal design such as a rotor suspension, smaller size and an angled inlet port. The EVAHEART LVAS is another emergent hydraulically levitated centrifugal pump showing early promising results (Saito, 2014; Kashiyama, 2014).

The increasing number of patients in heart failure may lead to expansion of the indications for LVAD insertion. Treatment at an earlier stage is currently under investigation considering its potential for improved survival. LVAD treatment as destination therapy is likely to increase due to the growing

number of the elderly patient population with contraindication to transplantation. If indications for LVAD treatment are to be expanded, quality of life must remain the ultimate aim. For LVAD support to become an option for ambulatory heart failure patients, issues affecting quality of life improvement must be addressed. Further hospital admissions after LVAD insertion secondary to driveline infection, bleeding, pump thrombosis and recurrent heart failure is the most important factor to consider. The development of a trans-cutaneous energy transmission system (TETS) and improved blood-barrier interaction will play a key role in reducing and possibly eliminate these frequent and costly complications (Schumer, 2016).

Myocardial recovery in advanced heart failure patients on LVAD support is unusual except in particular reversible circumstances such as acute myocarditis, peripartum cardiomyopathy and toxic cardiomyopathy. This statement has been challenged more recently by the demonstration of a recovery pattern with clinical, molecular and genetic changes in the myocardium as a response to LVAD support (Pinney, 2017; Hall, 2011). Myocardial recovery may be more likely in younger patients with shorter duration of heart failure in a background of non-ischaemic cardiomyopathy (Birks, 2006; Birks, 2011). The RESTAGE-HF (Remission From Stage D Heart Failure) trial investigating LVAD support as bridge to recovery in patients with chronic non-ischaemic cardiomyopathy has shown feasibility and reproducibility leading to high rate of LVAD explantation following myocardial recovery (Birks, 2015; Birks, 2020). Although significant reverse remodelling is observed during LVAD support with near normalisation of cellular and structural abnormalities, this does not always translate into clinical myocardial recovery (Mann, 2012). Therefore, it is important to distinguish between myocardial remission (improved ventricular function requiring background supportive treatment) and myocardial recovery (complete normalisation without ongoing need for medical treatment). The optimal degree of unloading, differential effects on the unsupported left ventricle and surgical implantation technique may play a role in myocardial recovery. Earlier LVAD treatment using partial support, maintenance of cardiac architecture and attention to myocardial blood flow may be important elements to focus on to achieve further progress towards myocardial recovery (Pinney, 2017).

Despite the significant improvement in pump technology, the costs related to LVAD treatment remain high (Health Quality Ontario, 2004; Clegg, 2005; Health Quality Ontario, 2016). The evolution from pulsatile to continuous flow devices has reduced costs for implantation with improved long-term survival and greater functional status (Rogers, 2012) but the frequent need

for hospital admissions and high cost associated with in-patient and out-patient care still contribute to the low cost-effectiveness of LVAD support (Clarke, 2014; Health Quality Ontario, 2016). Therefore, despite the clear survival advantage, further reduction in adverse events as well as improvement in quality of life is needed to meet conventional cost-effectiveness thresholds (Pinney, 2017).

The significant advancement in numerical methods and 3-D imaging techniques has enabled quantification of cardiovascular mechanics in patient-specific anatomy and physiological models (Taylor, 2009). Image-based CFD simulations are at a stage to be soon translated into daily clinical application (Doost, 2016). An example is the assessment of the haemodynamic significance of coronary artery stenosis using fractional flow reserve (FFR) (Pijls, 1996), which is currently used in clinical practice to guide interventional or surgical revascularization (Tonino, 2009; Tonino, 2010; Fearon, 2010; De Bruyne, 2012). Although CTA has emerged as a non-invasive method for direct visualisation of coronary artery disease (Achenbach, 2001; Budoff, 2008; Min, 2010), its tendency to overestimate the degree of coronary stenosis still requires reliance on the more traditional invasive angiographic assessment (Goldstein, 2007; Meijboom, 2008; Nissen, 2008). Computational fluid dynamics allows calculation of coronary blood flow and pressure fields from anatomical image data (Kim, 2010; Taylor, 2010). Clinical evaluation based on CFD combined with CTA (Taylor, 2013) may become a daily approach for FFR calculation to guide therapeutic intervention through modelling and simulation. Patient-specific modelling and computational fluid dynamics have been applied extensively to the cardiovascular system with a varying degree of clinical impact. Although validation studies have confirmed agreement between simulations and *in vitro* models (Kung, 2011; Vukicevic, 2013), barriers to further clinical implementation include validation against *in vivo* data with uncertainty quantification, the need to show reliability with improved outcome and the need for more efficient modelling and simulation methods (Marsden, 2015). Computational cardiovascular modelling has the potential to enhance existing diagnostic procedures and treatment planning strategies although large-scale motion and deformation, fluid-structure interaction and a relatively high Reynolds number significantly increase the challenge for modelling and simulation. Computational cardiovascular modelling will have to include additional physics such as structural dynamics, acoustics, electro-mechanics and biochemistry to achieve its full potential in daily clinical applications (Mittal, 2016; Asner, 2017). Although there is wide recognition in the medical community and regulatory agencies of the significant potential

and benefit in using computational fluid dynamics (Morris, 2016), it is extremely important to be fully aware of the assumptions made and the limitations of the modelling approach in relation to application and interpretation of results (Bluestein, 2017; Pedrizzetti, 2015). Simulations should provide sufficiently accurate results clinicians can understand and use in daily clinical practice. Further understanding of the relative importance of physiological parameters is essential in order to establish those that play a key role and those that can be assumed or averaged leading to reduced model complexity and balancing speed versus accuracy (Morris, 2016). The large volume of clinical data stored in hospital systems would be of significant value for model development and validation and the VPH-Share project has already shown how anonymised patient-specific data can be shared securely (vph-share.eu. http://vph-share.eu). The clinical application of modelling approaches often used for device development or mainly for research purposes may give a different perspective. The coupling with 3D printing may add value to patient-specific modelling (Thaker, 2019). Finally, the medical community needs to raise the awareness and promote the appropriate education to allow further progress towards patient-specific modelling as a daily approach to guide therapeutic intervention and predict outcome.

Although there remain more questions than answers, I would like to think that at least two objectives may be achievable that is the feasibility of simulations within a time-frame compatible with daily clinical practice and the use of suitable CFD models.

I would like to think that this may be a prelude for further developments. I know that many clinicians are intimidated and reluctant to adopt a more quantitative approach as an aid during daily practice. Nevertheless, willingness, initiative and common sense may help with the development of a common language that may ease fears and help build more bridges towards better cooperation between clinicians and scientists.

10.3 Novelty and Contribution to the Field

The novelty lies in the use of both pressure-volume simulation analysis and 3D flow dynamics studies in VADs with a view to treatment optimisation and outcome prediction within the time constraints of a clinical setting in the context of a MDT meeting. The clinical significance and the contribution to the field is a more targeted approach for different groups of patients and a more quantitative evaluation in the clinical decision process based on a pro-active co-operation between clinicians and scientists reducing the potential

for “guess work”. The results of this thesis are a proof-of-concept as a prelude to a potential future implementation of patient-specific modelling within a clinical setting on a daily basis demonstrating a clear clinical significance and contribution to the field. The proposed approach does not consider modelling and simulation as a substitute for clinical experience but an additional tool to guide therapeutic intervention and complement the clinical decision process in which the clinician remains the ultimate decision-maker. Such an approach may well add a different dimension to the problem of heart failure with potential for high return in terms of patient’s outcome and long-term surveillance. The same principles would be applicable to other cardiovascular problems in line with the current concept of “Team Approach” such as the Heart Team, the Structural Heart Team or the Aortic Team. The present work has taken this concept closer to clinical delivery and has highlighted its potential but further work remains to be done in refining the technique.

Appendices

A1

Physics of VADS

A1 Physics of VADs

A1.1 Volume Displacement versus Rotary Blood Pumps

Volume displacement pumps drive blood forward by cyclically changing the internal volume of a pumping chamber. They generate pulsatile flow and require one-way valves. The output requirement for a pulsatile configuration consists of a flow rate of 5-10 *L/min* at a mean pressure of 100-150 *mmHg* and a rate less than 120 *bpm* with a mean filling pressure of about 20 *mmHg* (Antaki, 2006).

A compliance chamber is required to achieve volume compensation where an equivalent air or fluid volume must enter the non-blood side of the pump housing to prevent vacuum formation following blood ejection. The absence of volume compensation significantly increases the amount of energy consumed by the pump making it impractical (Szycher, 1986; Slaughter, 2010).

Rotary or turbo-dynamic blood pumps consist of a rotating component with one or more impellers supported by a bearing within the pump and powered through a spinning shaft or magnetic forces. The assembly of all rotating elements is the pump rotor (Antaki, 2006).

Volume displacement pumps generate pressure and flow in inverse proportion to vascular resistance: an increased resistance leads to increased cardiac work. In contrast, an increased resistance in rotary blood pumps leads to decreased work and therefore available power (Arnold, 2013).

Volume displacement pumps are suitable to generate pressure against resistance. In fact, they maintain a constant flow against an increasing resistance by generating a higher pressure at the expense of increased work and energy consumption. In the presence of very high resistance or flow stop, the pump fails. In contrast, rotary blood pumps generate flow according to the amount of pressure dependent on resistance to flow. If the outflow graft of the HeartMate II (axial) or the HeatWare HVAD (centrifugal) is clamped, the true electrical and mechanical work done by the pump decreases although in theory the impeller may be pushing against an infinite resistance. In a clinical setting this would be paradoxical because myocardial oxygen demand and wall stress increase dramatically following aortic cross-clamp. Rotary blood pumps consist of a motor turning an impeller, which rotates at high speed inside the pump housing. The impeller accelerates the fluid either forward (axial-flow pump) or outward (centrifugal-flow pump). The impeller's ability to generate flow depends on rotational

speed and blade features (radius, pitch and height) as described by Euler's pump theory.

The fluid is accelerated by the rotating impeller with the addition of mechanical energy to the kinetic component of flow. At the exit, the fluid decelerates shifting the added energy of flow back to pressure. This event depends on outflow resistance. At the inlet, suction occurs and power is consumed by the pump to produce hydraulic work and to overcome viscous friction. In the presence of an outflow obstruction leading to increased afterload in a rotary blood pump, the flow decreases and less work is done. The rotor spins at the same speed but the impeller contacts and thrusts less fluid resulting in less work with a decrease in energy demand. Therefore, clamping the outflow graft of a rotary blood pump leaves the impeller rotating in a swirling but static volume of fluid. At the point of no flow, total work decreases significantly and power consumption is entirely related to overcoming friction.

The main difference between the two pumps is that a rotary blood pump can handle a low/no flow event very well by reducing its workload rather than increasing it like a displacement pump does. On this occasion, the pump's behaviour is similar to a mixer: the impeller can contact, accelerate and do work only on the volume of fluid within the housing. During systole, the rotary pump work increases because of cardiac contraction with an increase in flow. The capacity of the pump is in excess of the physiologically supplied volumes and it can contact and accelerate more fluid. Therefore, more work is done and more power is required. The HeartMate II pulsatility index (PI) is based on this principle. The pump recognizes only the speed [*rpm*] and the power required to maintain a certain speed. There is no flow detector. In the presence of native cardiac ejection, power usage increases and the flow is higher. A lower PI relates to higher amount of support provided by the pump. A higher PI means more native heart ejection. The PI varies according to hydration status, contractility, right ventricular function and exercise. Troubleshooting becomes more intuitive. If the controller shows decreased power consumption with a stable rotor speed, it means decreased work and flow. This may be related to decreased inflow due to volume depletion or cannula malposition or to increased afterload following vasoconstriction, hypertension or cannula geometry. Echocardiographic assessment can differentiate between poor drainage and poor inflow due to volume depletion (Arnold, 2013).

Increased power consumption with increased PI suggests more native cardiac ejection due to myocardial recovery or volume repletion from a dehydrated status.

Thrombus formation affects the reported flow estimate by changing the relationship between speed, power and flow. Thrombus can cause increased power consumption if the main burden is on the bearings requiring more friction work leading to an increased flow. On the contrary, thrombus can cause decreased power consumption if flow is reduced due to the presence of clot in the housing inflow or outflow. The worst scenario is when both effects balance and power remains roughly the same with an occult reduction in flow and clinical evidence of low perfusion with poor ventricular drainage on echocardiographic assessment (Arnold, 2013).
In conclusion, rotary blood pumps are well suited for high-flow work with variable resistance. They are simple, durable and fundamentally different from volume displacement pumps in terms of hydrodynamics.

A1.2 Concepts of Pump Design

Rotary blood pumps can be described according to classical pump theory and Euler's equation. Although the small size of rotary blood pumps is a key feature for the purposes of implantation, a compromise is needed between exposure time in regions of high shear stress and the hydraulic efficiency of the pump. The presence of viscous boundary layers is more pronounced and challenging due to the small cross-sectional area for flow. The flow through the impeller can be described in terms of velocity triangles, which give the direction and magnitude of flow. The velocity triangles represent the different components of fluid velocity, namely tangential velocity, absolute velocity and relative velocity. Figure 2.1 shows the application of this method of analysis (Ingram, 2009). U is the impeller's tangential velocity whilst V is the absolute fluid's velocity compared to the surroundings. W is the relative fluid velocity compared to the rotating impeller. The angle between the absolute velocity and the axial direction is named α; the angle between the relative velocity and the axial direction is named β. The drawing of velocity triangles at the inlet and outlet allow performance analysis in relation to changes in pump speed or impeller diameter and width.

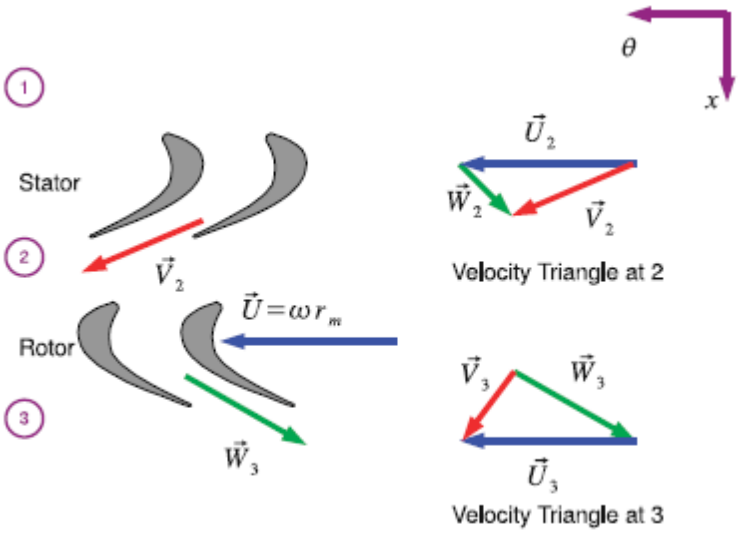

Figure A1.1 Velocity triangles method for pump performance analysis. From: Ingram G. *Basic Concepts in Turbomachinery*, Ventus Publishing ApS; 2009, pp 28-34.

The most important region of a continuous flow pump is the impeller, which defines the operating range of the pump. The impeller receives energy for rotation through the motor configuration and transfer energy to the fluid. The basic design formulae defining the shape and features of the impeller's blade follow Newton's second law of motion applied to a fluid traversing a rotating impeller (Wood, 2005). Rotary pumps spin a fluid to increase its momentum. From a thermodynamic point of view, the pump adds energy to the fluid. A simple control volume shows that the rate at which a pump adds energy to a fluid is:

$$\dot{W}^{g} = \frac{dV}{dt} \cdot \Delta P = Q \cdot \Delta P \qquad \text{(A1.1)}$$

Where $Q = dV/dt$ is the flow and ΔP is the pressure variation.
The efficiency of a pump (η_{Pump}) is defined as the ratio of the useful power output to the required power input ($\dot{W}_{IN}$):

$$\eta_{Pump} = \frac{Q \cdot \Delta P}{\dot{W}^{g}_{IN}} \qquad \dot{W}^{g}_{IN} = T \cdot \omega \qquad \Rightarrow \qquad \eta_{Pump} = \frac{Q \cdot \Delta P}{T \cdot \omega} \qquad \text{(A1.2)}$$

where ω is the rotational speed and T is the torque.

Considering $\Delta P = \rho \cdot g \cdot h_{Pump}$ where h_{Pump} is the pump head, ρ is the fluid density and g is the gravity acceleration, the pump efficiency equation becomes:

$$\eta_{Pump} = \frac{Q \cdot \rho \cdot g \cdot h_{Pump}}{T \cdot \omega} \tag{A1.3}$$

When the fluid thrust force does not act through the centre of gravity of a system, it generates a torque which produces rotational motion. In vector terms, the angular momentum vector $\boldsymbol{H}$ is the cross product of the position vector $\boldsymbol{r}$ of the force application point from a spatial coordinate origin times the momentum vector, which is the product of mass m times velocity vector $\boldsymbol{v}$ (Post, 2011):

$$\boldsymbol{H} = \boldsymbol{r} \times (m\boldsymbol{v}) \tag{A1.4}$$

For a fluid system defined within a control volume V, the total angular momentum is as follows:

$$\boldsymbol{H} = \int_V \rho \cdot (\boldsymbol{r} \times \boldsymbol{v})\, dV \tag{A1.5}$$

The rate of change of the angular momentum of a fluid system equals the rate of change of fluid angular momentum within the control volume plus any changes due to convective fluxes of angular momentum in or out of the surface (S) enclosing the control volume:

$$\frac{d\boldsymbol{H}}{dt} = \frac{\partial}{\partial t}\int_V \rho(\boldsymbol{r} \times \boldsymbol{v})\, dV + \int_S \rho(\boldsymbol{r} \times \boldsymbol{v})(\boldsymbol{v} \cdot d\boldsymbol{A}) \tag{A1.6}$$

where $d\boldsymbol{A}$ is the normal vector to the area element.

A torque produces a change in angular momentum. If we consider a right-hand coordinate system defined about an origin "*O*", the sum of any external torques $T_{O,i}$ on the system equals the total change in angular momentum according to the conservation law (Post, 2011). Therefore, the following general expression is obtained:

$$\sum_i \boldsymbol{T}_{O,i} = \frac{d\boldsymbol{H}}{dt} = \frac{\partial}{\partial t}\int_V \rho(\boldsymbol{r}\times\boldsymbol{v})\,dV + \int_S \rho(\boldsymbol{r}\times\boldsymbol{v})(\boldsymbol{v}\cdot d\boldsymbol{A}) \qquad \text{(A1.7)}$$

Newton's second law states that the torque on the impeller is equal to the rate of change of the angular momentum of fluid. Therefore:

$$T = m\cdot(v_{u2}\cdot r_2 - v_{u1}\cdot r_1) \qquad \text{(A1.8)}$$

Equation (2.8) defines the torque as a function of the mass, the radii (r_1 and r_2) and the tangential absolute velocities (v_{u1} and v_{u2}). According to Euler's velocity triangles, the absolute fluid velocity is the sum of the relative velocity of fluid with respect to the moving blade and the blade velocity. Figure 2.1 illustrates the corresponding velocity triangles at the inlet and outlet of a pump impeller blade.

The pump power ($\dot{W}_{Pump}$) is the product of torque and rotational speed in *radians/s*. Therefore:

$$\overset{g}{W}_{Pump} = \omega\cdot T = m\cdot(v_{u2}\cdot\omega\cdot r_2 - v_{u1}\cdot\omega\cdot r_1) = m\cdot(v_{u2}\cdot U_2 - v_{u1}\cdot U_1) \qquad \text{(A1.9)}$$

where $U_1=\omega\cdot r_1$ is the blade speed at the inlet and $U_2=\omega\cdot r_2$ is the blade speed at the outlet. Dividing Eq. (2.9) by $m\cdot g$, we obtain:

$$\frac{\overset{g}{W}_{Pump}}{m\cdot g} = \frac{1}{g}\cdot(v_{u2}\cdot U_2 - v_{u1}\cdot U_1) \qquad h_{Pump} = \frac{\overset{g}{W}_{Pump}}{m\cdot g}$$

$$h_{Pump} = \frac{1}{g}\cdot(v_{u2}\cdot U_2 - v_{u1}\cdot U_1) \;\Rightarrow\; g\cdot h_{Pump} = (v_{u2}\cdot U_2 - v_{u1}\cdot U_1) \qquad \text{(A1.10)}$$

Then, the efficiency of the pump can be written in a more generalized form:

$$\eta_{Pump} = \frac{\rho\cdot Q}{T\cdot\omega}\cdot(v_{u2}\cdot U_2 - v_{u1}\cdot U_1) \qquad \text{(A1.11)}$$

VADs are expected to perform over a range of operating conditions according to the patient's need; therefore, efficiency should vary minimally (Apel, 2001a). A reduced gap between the blade tip and the outer housing usually increases pressure head and efficiency although further reduction of

the tip clearance below a threshold value does not give any further increase in efficiency (Wu, 2010). Efficiency reduction with tip clearance is related to tip leakage flow escaping backwards around the blade through the clearance gap (Chua, 2007). Gap size reduction decreases leakage flow (Wu, 2010; Anderson, 2000a).

The fluid forces on the impeller are critical and can be calculated by integration over its surface area and used to determine the requirements of the bearing (Untaroiu, 2005).

The hydrodynamic performance of rotary blood pumps is measured in terms of head pressure, which is the difference in pressure between inlet and outlet. Pump head curves compare the relationship between pump flow and pressure at a specific operating pump speed. A centrifugal-flow pump has a flat head curve where it operates over a very wide range of flows for a very small change in pump head. This creates intrinsic high pump flow pulsatility in response to changing left ventricular pressure. Instead, an axial-flow pump has a steep head curve with a relatively linear relationship producing less flow pulsatility (Moazami, 2013). Figure 2.2 shows the features of the two types of rotary blood pump most frequently used in clinical practice. Both axial and centrifugal blood pumps have reduced preload sensitivity, which limits their ability of increased output in response to increased venous return. Centrifugal pump have also higher afterload sensitivity compared to axial pumps requiring the need for control of peripheral vascular resistance to maintain output.

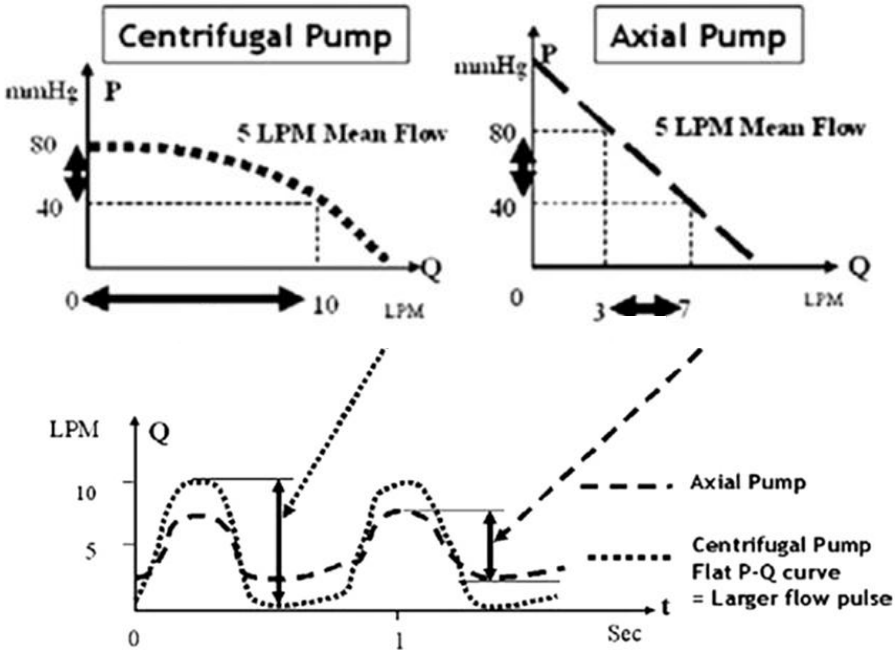

Figure A1.2 Comparison between centrifugal- and axial-flow rotary blood pumps. Modified from: Moazami et al. J Heart Lung Transplant 2013; 32(1): 1-11.

A1.3 Appendix 1 Summary

Volume displacement pumps generate pressure against resistance. They maintain a constant flow against an increasing resistance by generating a higher pressure at the expense of increased work and energy consumption. Rotary blood pumps generate flow according to the amount of pressure dependent on resistance to flow. The mechanical work produced by the pump decreases in the presence of high afterload leading to a reduction in energy demand. In other words, a rotary blood pump can handle a low or no flow event remarkably well by reducing its workload instead of increasing it like a volume displacement pump does. The hydrodynamic performance of rotary blood pumps is measured in terms of head pressure, which is the difference in pressure between inlet and outlet. A centrifugal-flow pump has a flat head curve where it operates over a very wide range of flows for a very small change in pump head. This creates intrinsic high pump flow pulsatility in response to changing left ventricular pressure. Instead, an axial-flow pump has a steep head curve with a relatively linear relationship producing less flow pulsatility.

References

A

Abraham F, Behr M, Heinkenschloss M. Shape optimization in steady blood flow: A numerical study of non-Newtonian effects. *Comp Meth Biomech Biomed Eng* 2005a; 8(2): 127-137.

Abraham F, Behr M, Heinkenschloss M. Shape optimization in unsteady blood flow: A numerical study of non-Newtonian effects. *Comp Meth Biomech Biomed Eng* 2005b; 8(3): 201-212.

Achenbach S, Daniel WG. Noninvasive coronary angiography – an acceptable alternative? *N Engl J Med* 2001; 345: 1909-1910.

Adatya S, Holley CT, Roy SS, Yarmohammadi H, Feng A, Eckman P, Colvin-Adams M, John R, Masri C. Echocardiographic Ramp Test for Continuous-Flow Left Ventricular Assist Devices. Do Loading Conditions Matter? *J Am Coll Cardiol* HF 2015; 3: 291-299.

Affeld K, Goubergrits L, Kertzscher U, Gadischke J, Reininger A. Mathematical model of platelet deposition under flow conditions. *Int J Artif Organs* 2004; 27(8): 699-708.

Aissaoui N, Morshuis M, Maoulida H, Salem J-E, Lebreton G, Brunn M, Chatellier G, Hagège A, Schoenbrodt M, Puymirat E, Latremouille C, Varnous S, Ouldamar S, Guillemain R, Diebold B, Guedeney P, Barreira M, Mutuon P, Guerot E, Paluszkiewicz L, Hakim-Meibodi K, Schulz U, Danchin N, Gummert J, Durand-Zaleski I, Leprince P, Fagon J-Y. Management of end-stage heart failure patients with or without ventricular assist device: an observational comparison of clinical and economic outcomes. *Eur J Cardiothorac Surg* 2018; 53: 170-177.

Alemu Y, Bluestein D. Flow-Induced Platelet Activation and Damage Accumulation in a Mechanical Heart Valve: Numerical Studies. *Artificial Organs* 2007; 31(9): 677-688.

Alemu Y, Girdhar G, Xenos M, Sheriff J, Jesty J, Einav S, Bluestein D. Design Optimization of a Mechanical Heart Valve for Reducing Valve Thrombogenicity – A Case Study with ATS Valve. *ASAIO J* 2010; 56: 389-396.

AlOmari A-HH, Savkin AV, Stevens M, Mason DG, Timms DL, Salamonsen RF, Lovell NH. Developments in control systems for rotary left ventricular assist devices for heart failure patients: a review. *Physiol Meas* 2013; 34: R1-R27.

Anand M, Kwack J, Masud A. A new generalized Oldroyd-B model for blood flow in complex geometries. *Int J Eng Sci* 2013; 72: 78-88.

Anand M, Rajagopal K, Rajagopal KR. A model for the formation and lysis of blood clots. *Pathophysiol Haemost Thromb* 2005; 34: 109-120.

Anand M, Rajagopal K, Rajagopal KR. A model for the formation, growth, and lysis of clots in quiescent plasma. A comparison between the effects of antithrombin III deficiency and protein C deficiency. *J Theor Biol* 2008; 253: 725-738.

Anderson JB, Wood HG, Allaire PE, Bearnson G, Khanwilkar P. Computational Flow Study of the Continuous Flow Ventricular Assist Device, Prototype Number 3 Blood Pump. *Artificial Organs* 2000a; 24: 377-385.

Anderson JB, Wood HG, Allaire PE, McDaniel JC, Olsen DB, Bearnson G. Numerical studies of blood shear and washing in a continuous flow ventricular assist device. *ASAIO J* 2000b; 46: 486-494.

ANSYS *Fluent Theory Guide*, Release 17.2, August 2016, pp 39-136.

ANSYS *Fluent User's Guide*, Release 17.2, August 2016, pp 751-826.

Antaki JF, Ghattas O, Burgreen GW, He B. Computational Flow Optimization of Rotary Blood Pump Components. *Artificial Organs* 1995; 19(7): 608-615.

Antaki JF, Poirier V, Pagani FD. Engineering Concepts in the Design of Mechanical Circulatory Support. In: *Mechanical Circulatory Support*. Frazier OH, Kirklin JK ed.; ISHLT Monograph Series, New York, Elsevier; 2006, pp 33-52.

Antonini-Canterin F, Carerj S, Di Bello V, Di Salvo G, La Carrubba S, Vriz O, Pavan D, Balbarini A, Nicolosi GL. Arterial stiffness and ventricular stiffness: a couple of diseases or a coupling disease? A review from the cardiologist's point of view. *Eur J Echocardiogr* 2009; 10: 36–43.

Apel J, Neudel F, Reul H. Computational fluid dynamics and experimental validation of a microaxial blood pump. *ASAIO J* 2001a; 47: 552-558.

Apel J, Paul R, Klaus S, Siess T, Reul H. Assessment of haemolysis related quantities in a microaxial blood pump by computational fluid dynamics. *Artificial Organs* 2001b; 25: 341-347.

Arada N, Sequeira A. Strong Steady Solutions for a generalized Oldroyd-B Model with Shear-Dependent Viscosity in a Bounded Domain, *Math Models Methods Appl Sci*; 2003; 13(9): 1303-1323.

Arakawa M, Nishimura T, Takewa Y, Umeki A, Ando M, Kishimoto Y, Fujii Y, Kyo S, Adachi H, Tatsumi E. Novel control system to prevent right ventricular failure induced by rotary blood pump. *J Artificial Organs* 2014; 17: 135-141.

Argueta-Morales IR, Tran R, Ceballos A, Clark W, Osorio R, Divo EA, Kassab AJ, DeCampli WM. Mathematical Modelling of Patient-Specific Ventricular Assist Device Implantation to Reduce Particulate Embolization Rate to Cerebral Vessels. *J Biomech Eng* 2014; 136: 071008-1-071008-8.

Arnold WS, Bourque K. The engineer and the clinician: Understanding the work output and troubleshooting of the HeartMate II rotary flow pump. *J Thorac Cardiovasc Surg* 2013; 145: 32-36.

Arts T, Bovendeerd PHM, Prinzen FW, Reneman RS. Relation between left ventricular cavity pressure and volume and systolic fibre stress and strain in the wall. *Biophys J* 1991; 59: 93-102.

Arts T, Delhaas T, Bovendeerd P, Verbeek X, Prinzen FW. Adaptation to mechanical load determines shape and properties of heart and circulation: the circadapt model. *Am J Physiol Heart Circ Physiol* 2005; 288: H1943–H1954.

Arts T, Lumens J, Kroon W, Delhaas T. Control of whole heart geometry by intramyocardial mechano-feedback: a model study. *PLoS Comput Biol* 2012; 8: e1002369.

Arts T, Reesink K, Kroon W, Delhaas T. Simulation of adaptation of blood vessel geometry to flow and pressure: implications for arterio-venous impedance. *Mech Res Commun* 2011; 42: 15–21.

Arvand A, Hormes M, Reul H. A Validated Computational Fluid Dynamics Model to Estimate Haemolysis in a Rotary Blood Pump. *Artificial Organs* 2005; 29: 531-540.

Asanoi H, Sasayama S, Kameyama T. Ventriculoarterial Coupling in Normal and Failing Heart in Humans. *Circ Res* 1989; 65: 483-493.

Asner L, Hadjicharalambous M, Chabiniok R, Peressutti D, Sammut E, Wong J, Carr-White G, Razavi R, King AP, Smith N, Lee J, Nordsletten D. Patient-specific modelling for left ventricular mechanics using data-driven boundary energies. *Comput Methods Appl Mech Eng* 2017; 314: 269-295.

Ataullakhanov FI, Panteleev MA. Mathematical Modelling and Computer Simulation in Blood Coagulation. *Pathophysiol Haemost Thromb* 2005; 34: 60-70.

B

Babushkina ES, Bessonov NM, Ataullakhanov FI, Panteleev MA. Continuous Modeling of Arterial Platelet Thrombus Formation Using a Spatial Adsorption Equation. *PLoS ONE* 2015; 10(10): e0141068.

Baghai M, Heilmann C, Beyersdorf F, Nakamura L, Geisen U, Olschewski M, Zieger B. Platelets dysfunction and acquired von Willebrand syndrome in patients with left ventricular assist devices. *Eur J Cardiothorac Surg* 2015; 48: 421-427.

Bassingthwaighte J, Hunter P, Noble D. The cardiac physiome: perspectives for the future. *Exp Physiol* 2009; 94(5): 597–605.

Baumann SL. The Limitations of Evidence-Based Practice. *Nurs Sci Q* 2010; 23(3): 226-230.

Bazilevs Y, Gohean JR, Hughes TJR, Moser RD, Zhang Y. Patient-specific isogeometric fluid-structure interaction analysis of thoracic aortic blood flow due to implantation of the Jarvik 2000 left ventricular assist device. *Comput Methods Appl Mech Eng* 2009; 198: 3534-3550.

Bearnson GB, Jacobs GB, Kirk J, Khanwilkar PS, Nelson KE, Long JW. HeartQuest ventricular assist device magnetically levitated centrifugal blood pump. *Artif Organs* 2006; 30: 339-346.

Begent N, Born GV. Growth rate in vivo of platelet thrombi, produced by iontophoresis of ADP, as a function of mean blood flow velocity. *Nature* 1970; 227: 926 –930.

Behbahani M, Behr M, Hormes M, Steinseifer U, Arora D, Coronado O, Pasquali M. A review of computational fluid dynamics analysis of blood pumps. *Eur J Appl Math* 2009; 20: 363-397.

Belcher P, Boerboom LE, Olinger GN. Standardization of end-systolic pressure-volume relation in the dog. *Am J Physiol Heart Circ Physiol* 1985; 249(3): H547-H553.

Birks EJ, Drakos S, Selzman C, Starling R, Cunningham C, Slaughter M, Spevack DM, Salahuddin A, Alturi P, Lowes B, Patel S, Farrar D, Kallel F, Rame JE. Remission From Stage D Heart Failure (RESTAGE-HF): Early Results From a Prospective Multi-Centre Study of Myocardial Recovery. *J Heart Lung Transplant* 2015; 34(4) Supplement: S40-S41.

Birks EJ, Drakos SG, Patel SR, Lowes BD, Selzman CH, Starling RC, Trivedi J, Slaughter MS, Alturi P, Goldstein D, Maybaum S, Um JY, Margulies KB, Stehlik J, Cunningham C, Farrar DJ, Rame JE. Prospective Multicentre Study of Myocardial Recovery Using Left Ventricular Assist Devices (RESTAGE-HF [Remission from Stage D Heart Failure]). *Circulation* 2020; 142(21): 2016-2028.

Birks EJ, George RS, Hedger M, Bahrami T, Wilton P, Bowles CT, Webb C, Bougard R, Amrani M, Yacoub MH, Dreyfus G, Khaghani A. Left Ventricular Assist Device and Pharmacological Therapy. A Prospective Study. *Circulation* 2011; 123: 381-390.

Birks EJ, Tansley PD, Hardy J, George RS, Bowles CT, Burke M, Banner NR, Khaghani A, Yacoub MH. Left Ventricular Assist Device and Drug Therapy for the Reversal of Heart Failure. *N Engl J Med* 2006; 355: 1873-1884.

Birks EJ, Tansley PD, Yacoub MH, Bowles CT, Hipkin M, Hardy J, Banner NR, Khaghani A. Incidence and Clinical Management of Life-Threatening Left Ventricular Assist Device Failure. *J Heart Lung Transplant* 2004; 23: 964-969.

Bishop CJ, Mason NO, Kfoury AG, Lux R, Stoker S, Horton K, Clayson SE, Rasmusson B, Reid BB. A novel non-invasive method to assess aortic valve opening in HeartMate II left ventricular assist device patients using a modified Karhunen-Loève transformation. *J Heart Lung Transplant* 2010; 29: 27-31.

Blanco PJ, Clausse A, Feijóo RA. Homogenization of the Navier–stokes equations by means of the multi-scale virtual power principle. *Comput Methods Appl Mech Eng* 2017; 315: 760–779.

Bluestein D, Chandran KB, Manning KB. Towards Non-thrombogenic Performance of Blood Recirculating Devices. *Ann Biomed Eng* 2010, 38(3): 1236-1256.

Bluestein D, Li YM, Krukenkamp IB. Free emboli formation in the wake of bileaflet mechanical heart valves and the effects of implantation techniques. *J Biomech* 2002, 35(12): 1533-1540.

Bluestein D, Rambod E, Gharib M. Vortex shedding as a mechanism for free emboli formation in mechanical heart valves. *J Biomech Eng* 2000, 122(2): 125-134.

Bluestein D. Research approaches for studying flow-induced thromboembolic complications in blood recirculating devices. *Expert Rev Medical Devices* 2004; 1(1): 65-80.

Bluestein D. Utilizing Computational Fluid Dynamics in Cardiovascular Engineering and Medicine – What You Need to Know. Its Translation to the Clinic/Bedside. *Artificial Organs* 2017; 41(2): 117-121.

Bodnár T. On the Eulerian formulation of a stress induced platelet activation function. *Mathematical Biosciences* 2014; 257: 91-95.

Bolno PB, Kresh JY. Physiologic and haemodynamic basis of ventricular assist devices. *Cardiol Clin* 2003; 21: 15-27.

Bonnemain J, Malossi ACI, Lesinigo M, Deparis S, Quarteroni A, von Segesser LK. Numerical simulation of left ventricular assist device implantations: Comparing the ascending and the descending aorta cannulations. *Med Eng Phys* 2013; 35: 1465-1475.

Borlaug BA, Kass DA. Ventricular-Vascular Interaction in Heart Failure. *Heart Fail Clin* 2008; 4(1): 23-36.

Bosco A, Reinartz B, Müller S. Differential Reynolds stress model and grid adaptation for hypersonic double wedge simulations. In: *Turbulence, Heat and Mass Transfer 6*. Hanjalić K, Nagano Y, Jakirlić S (Editors); Begell House Inc, 2009, pp 1-12.

Boston J, Antaki J, Simaan M. Hierarchical Control of Hearts Assist Devices. *IEEE Robot Autom Mag* 2003; 10(1): 54-64.

Bovendeerd PHM, Borsje P, Arts T, van De Vosse FN. Dependence of Intramyocardial Pressure and Coronary Flow on Ventricular Loading and Contractility: A Model Study. *Ann Biomed Eng* 2006; 34(12): 1833-1845.

Boyle AJ, Ascheim DD, Russo MJ, Kormos RL, John R, Naka Y, Gelijns AC, Hong KN, Teuteberg JJ. Clinical outcomes for continuous flow left ventricular assist device patients stratified by pre-operative INTERMACS classification. *J Heart Lung Transplant* 2011; 30(4): 402-407.

Bozkurt S, van de Vosse FN, Rutten MCM. Aortic Valve Function Under Support of a Left Ventricular Assist Device: Continuous vs. Dynamic Speed Support. *Ann Biomed Eng* 2015; 43(8): 1727-1737.

Bozkurt S, van de Vosse FN, Rutten MCM. Improving arterial pulsatility by feedback control of a continuous flow left ventricular assist device via in silico modelling. *Int J Artif Organs* 2014; 37(10): 773-785.

Brutsaert DL, Sys SU. Relaxation and diastole of the heart. *Physiol Rev* 1989; 69(4): 1228-1315.

Budoff MJ, Dowe D, Jollis JG, et al. Diagnostic performance of 64-multidetector row coronary computed tomographic angiography for evaluation of coronary artery stenosis in individuals without known coronary artery disease: results from the prospective multicenter ACCURACY (Assessment by Coronary Computed Tomographic Angiography of Individuals Undergoing Invasive Coronary Angiography) trial. *J Am Coll Cardiol* 2008; 52: 1724-1732.

Bungay SD, Gentry PA, Gentry RD. A mathematical model of lipid-mediated thrombin generation. *Math Med Biol*. 2003; 20: 105–129.

Burattini R, Gnudi G. Computer identification of models for the arterial tree input impedance: comparison between two new simple models and first experimental results. *Med Biol Eng Comput* 1982; 20: 134-144.

Burgreen GW, Antaki JF, Wu ZJ, Holmes AJ. Computational Fluid Dynamics as a Development Tool for Rotary Blood Pumps. *Artificial Organs* 2001; 25(5): 336-340.

Burgreen GW, Loree HM II, Bourque K, Dague C, Poirier VL, Farrar D, Hampton E, Wu ZJ, Gempp TM, Schöb R. Computational Fluid Dynamics Analysis of a Maglev Centrifugal Left Ventricular Assist Device. *Artificial Organs* 2004; 28(10): 874-880.

Burkhoff D. Mechanical Properties of the Heart and its Interaction with the Vascular System. A Basic Review of Pressure-Volume Relations. January 2011. From: *danielburkhoff.com* website.

Burkhoff D, Mirsky I, Suga H. Assessment of systolic and diastolic ventricular properties via pressure-volume analysis: a guide for clinical, translational, and basic researchers. *Am J Physiol Heart Circ Physiol* 2005; 289: H501-H512.

Burkhoff D, Sagawa K. Ventricular efficiency predicted by an analytical model. *Am J Physiol Regulatory Integrative Comp Physiol* 1986; 250: R1021-R1027.

Burkhoff D, Sugiura S, Yue DT, Sagawa K. Contractility-dependent curvilinearity of end-systolic pressure-volume relations. *Am J Physiol Heart Circ Physiol* 1987; 252: H1218-H1227.

Burkhoff D, Tyberg JV. Why does pulmonary venous pressure rise after onset of left ventricular dysfunction: a theoretical analysis. *Am J Physiol Heart Circ Physiol* 1993; 265: H1819–H1828.

C

Campbell KB, Kirkpatrick RD, Knowlen GG, Ringo JA. Late-Systolic Pumping Properties of the Left Ventricle. Deviation From Elastance-Resistance Behavior. *Circ Res* 1990; 66: 218-233.

Campbell KB, Ringo JA, Knowlen GG, Kirkpatrick RD, Schmidt SL. Validation of optional elastance-resistance left ventricle pump models. *Am J Physiol Heart Circ Physiol* 1986; 251: H382-H397.

Campbell KB, Ringo JA, Neti C, Alexander JE. Informational Analysis of Left-Ventricle/Systemic- Arterial Interaction. *Ann Biomed Eng* 1984; 12: 209-231.

Campbell KB, Ringo JA, Wakao Y, Klavano PA, Alexander JE. Internal capacitance and resistance allow prediction of right ventricle outflow. *Am J Physiol Heart Circ Physiol* 1982; 243(1): H99-H112.

Capoccia M, Bowles CT, Sabashnikov A, De Robertis F, Amrani M, Banner NR, Simon A. A UK single centre retrospective analysis of the relationship between haemodynamic changes and outcome in patients undergoing prolonged left ventricular assist device support. *Ann Thorac Cardiovasc Surg* 2015; 21: 151–156.

Capoccia M, Bowles CT, Sabashnikov A, Simon A. Recurrent Early Thrombus Formation in HeartMate II Left Ventricular Assist Device. *J Invest Med High Impact Case Rep* 2013; 1: 1-3.

Capoccia M, Marconi S and De Lazzari C. Decision-making in advanced heart failure patients requiring LVAD insertion: Can preoperative simulation become the way forward? A case study. *J Biomed Eng Inform* 2018a; 4(2).

Capoccia M, Marconi S, Singh SA, Pisanelli DM, De Lazzari C. Simulation as a preoperative planning approach in advanced heart failure patients. A retrospective clinical analysis. *BioMed Eng OnLine* 2018b; 17: 52.

Chatterjee MS, Purvis JE, Brass LF, Diamond SL. Pairwise agonist scanning predicts cellular signaling responses to combinatorial stimuli. *Nat Biotechnol*. 2010; 28 (7): 727–732.

Chen C-H, Fetics B, Nevo E, Rochitte CE, Chiou K-R, Ding PY-A, Kawaguchi M, Kass DA. Noninvasive Single-Beat Determination of Left Ventricular End-Systolic Elastance in Humans. *J Am Coll Cardiol* 2001; 38: 2028-2034.

Cheng A, Williamitis CA, Slaughter MS. Comparison of continuous-flow and pulsatile-flow left ventricular assist devices: is there an advantage to pulsatility? *Ann Cardiothorac Surg* 2014; 3(6): 573-581.

Chipongo K, Khiadani M, Lari KS. Comparison and verification of turbulence Reynolds-averaged Navier-Stokes closures to model spatially varied flows. *Scientific Reports* 2020 ; 10 : 19059.

Chirinos JA. Ventricular-arterial coupling: Invasive and non-invasive assessment. *Artery Res* 2013; 7(1): doi:10.1016/j.artres.2012.12.002.

Chirinos JA, Rietzschel ER, De Buyzere ML, De Bacquer D, Gillebert TC, Gupta AK, Segers P; on behalf of the Asklepios investigators. Arterial Load and Ventricular-Arterial Coupling. Physiologic Relations With Body Size and Effect of Obesity. *Hypertension* 2009; 54: 558-566.

Chirinos JA, Sweitzer N. Ventricular-Arterial Coupling in Chronic Heart Failure. *Card Fail Rev* 2017; 3(1): 12-18.

Chiu W-C, Alemu Y, McLarty AJ, Einav S, Slepian MJ, Bluestein D. Ventricular Assist Device implantation Configurations Impact Overall Mechanical Circulatory Support System Thrombogenic Potential. *ASAIO J* 2017; 63:285-292.

Chiu W-C, Slepian MJ, Bluestein D. Thrombus Formation Patterns in the HeartMate II Ventricular Assist Device: Clinical Observations Can Be Predicted by Numerical Simulations. *ASAIO J* 2014; 60: 237-240.

Chiu W-C, Tran PL, Khalpey Z, Lee E, Woo Y-R, Slepian MJ, Bluestein D. Device Thrombogenicity Emulation: An *In Silico* Predictor of *In Vitro* and *In Vivo* Ventricular Assist Device Thrombogenicity. *Scientific Reports* 2019; 9: 2946.

Cho YI, Kensey KR. Effects of the non-Newtonian viscosity of blood on flows in a diseased arterial vessel. Part I: Steady flows. *Biorheology* 1991; 28: 241-262.

Choi S, Boston JR, Antaki JF. An Investigation of the Pump Operating Characteristics as a Novel Control Index for LVAD Control. *Int J Control Autom Syst* 2005; 3(1): 100-108.

Choi S, Boston JR, Thomas D, Antaki JF. Modelling and Identification of an Axial Flow Pump. *Proceedings of the American Control Conference*, Albuquerque, New Mexico; 1997, 3714-3715.

Chow E, Farrar DJ. Right heart function during prosthetic left ventricular assistance in a porcine model of congestive heart failure. *J Thorac Cardiovasc Surg* 1992; 104: 569-578.

Chua LP, Ong KS, Song G. Study of Velocity and Shear Stress Distributions in the Impeller Passages and the Volute of a Bio-centrifugal Ventricular Assist Device. *Artificial Organs* 2008; 32(5): 376-387.

Chua LP, Song G, Yu SCM, Lim TM. Computational Fluid Dynamics of Gap Flow in a Biocentrifugal Blood Pump. *Artificial Organs* 2005; 29: 620-628.

Chua LP, Su B, Tau ML, Zhou T. Numerical Simulation of an Axial Blood Pump. *Artificial Organs* 2007; 31: 560-570.

Chung DC, Niranjan SC, Clark JW Jr, Bidani A, Johnston WE, Zwischenberger JB, Traber DL. A dynamic model of ventricular interaction and pericardial influence. *Am J Physiol Heart Circ Physiol* 1997; 272: H2942–H2962.

Claessens TE, Georgakopoulos D, Afanasyeva M, Vermeersch SJ, Millar HD, Stergiopulos N, Westerhof N, Verdonck PR, Segers P. Nonlinear isochrones in murine left ventricular pressure-volume loops: how well does the time-varying elastance concept hold? *Am J Physiol Heart Circ Physiol* 2006; 290: H1474-H1483.

Clarke A, Pulikottil-Jacob R, Connock M, Suri G, Kandala NB, Maheswaran H, Banner NR, Sutcliffe P. Cost-effectiveness of left ventricular assist devices (LVADs) for patients with advanced heart failure: analysis of the British NHS bridge to transplant (BTT) program. *Int J Cardiol* 2014; 171(3): 338-45.

Clegg AJ, Scott DA, Loveman E, Colquitt J, Hutchinson J, Royle P, Bryant J. The clinical and cost-effectiveness of left ventricular assist devices for end-stage heart failure: a systematic review and economic evaluation. *Health Technol Assess* 2005; 9(45): 1-132.

Consolo F, Sheriff J, Gorla S, Magri N, Bluestein D, Pappalardo F, Slepian MJ, Fiore GB, Redaelli A. High Frequency Components of Hemodynamic Shear Stress Profiles are a Major Determinant of Shear-Mediated Platelet Activation in Therapeutic Blood Recirculating Devices. *Sci Rep* 2017; 7: 4994.

Cox LGE, Loerakker S, Rutten MCM, de Mol BAJM, van de Vosse FN. A Mathematical Model to Evaluate Control Strategies for Mechanical Circulatory Support. *Artificial Organs* 2009; 33: 593-603.

Crow S, Chen D, Milano C, Thomas W, Joyce L, Piacentino V 3rd, Sharma R, Wu J, Arepally G, Bowles D, Rogers J, Villamizar-Ortiz N. Acquired von Willebrand Syndrome in Continuous-Flow Ventricular Assist Device Recipients. *Ann Thorac Surg* 2010a; 90(4): 1263-1269.

Crow S, Milano C, Joyce L, Chen D, Arepally G, Bowles D, Thomas W, Villamizar-Ortiz N. Comparative Analysis of von Willebrand Factor Profiles in Pulsatile and Continuous Left Ventricular Assist Device Recipients. *ASAIO J* 2010b; 56(5): 441-445.

D

Dang NC, Topkara VK, Mercando M, Kay J, Kruger KH, Aboodi MS, Oz MC, Naka Y. Right Heart Failure After Left Ventricular Assist Device Implantation in Patients With Chronic Congestive Heart Failure. *J Heart Lung Transplant* 2006; 25: 1-6.

Darowski M, De Lazzari C, Ferrari G, Clemente F, Guaragno M. The influence of simultaneous intra-aortic balloon pumping and mechanical ventilation on hemodynamic parameters—numerical simulation. *Front Med Biol Eng* 1999; 9(2): 155–174.

Day SW, McDaniel JC, Wood HG, Allaire PE, Landrot N, Curtas A. Particle Image Velocimetry Measurements of Blood Velocity in a Continuous Flow Ventricular Assist Device. *ASAIO J* 2001; 47(4): 406-411.

Day SW, McDaniel JC, Wood HG, Allaire PE, Song X, Lemire PP, Miles SD. A Prototype HeartQuest Ventricular Assist Device for Particle Image Velocimetry Measurements. *Artificial Organs* 2002; 26(11): 1002-1005.

de Biasi AR, Manning KB, Salemi A. Science for surgeons: Understanding pump thrombogenesis in continuous-flow left ventricular assist devices. *J Thorac Cardiovasc Surg* 2015; 149: 667-673.

De Bruyne B, Pijls NH, Kalesan B, et al. Fractional flow reserve-guided PCI versus medical therapy in stable coronary disease. *N Engl J Med* 2012; 367: 991-1001.

De Lazzari C. Interaction between the septum and the left (right) ventricular free wall in order to evaluate the effects on coronary blood flow: numerical simulation. Comput Methods *Biomech Biomed Eng* 2012; 15(12): 1359–1368.

De Lazzari C, Capoccia M, Marconi S. How can LVAD support influence ventricular energetics parameters in advanced heart failure patients? A retrospective study. *Comput Methods Programs Biomed* 2019a; 172: 117-126.

De Lazzari C, D'Ambrosi A, Tufano F, Fresiello L, Garante M, Sergiacomi R, Stagnitti F, Caldarera CM, Alessandri N. Cardiac resynchronization therapy: could a numerical simulator be a useful tool in order to predict the response of the biventricular pacemaker synchronization? *Eur Rev Med Pharmacol Sci* 2010; 14(11): 969–78.

De Lazzari C, Darowski M, Ferrari G, Clemente F. The influence of left ventricle assist device and ventilatory support on energy-related cardiovascular variables. *Medical Eng Phys* 1998; 20(2): 83–91.

De Lazzari C, Darowski M, Ferrari G, Clemente F, Guaragno M. Ventricular energetics during mechanical ventilation and intra-aortic balloon pumping-computer simulation. *J Med Eng Technol* 2001; 25(3): 103–111.

De Lazzari C, Darowski M, Ferrari G, Pisanelli DM, Tosti G. Modelling in the study of interaction of Hemopump device and artificial ventilation. *Comput Biol Med* 2006b; 36(11): 1235-1251.

De Lazzari C, Darowski M, Ferrari G, Pisanelli DM, Tosti G. The impact of rotary blood pump in conjunction with mechanical ventilation on ventricular energetic parameters: numerical simulation. *Methods Inf Med* 2006a; 45: 574–583.

De Lazzari C, Darowski M, Wolski P, Ferrari G, Tosti G. In vivo and simulation study of artificial ventilation effects on energetic variables in cardiosurgical patients. *Methods Inf Med* 2005; 44: 98–105

De Lazzari C, De Lazzari B, Iacovoni A, Marconi S, Papa S, Capoccia M, Badagliacca R, Vizza CD. Intra-aortic balloon counterpulsation timing: A new numerical model for programming and training in the clinical environment. *Comput Methods Progr Biomed* 2020; 194: 105537.

De Lazzari C, Genuini I, Pisanelli DM, D'Ambrosi A, Fedele F. Interactive simulator for e-Learning environments: a teaching software for health care professionals. *BioMed Eng OnLine* 2014; 13: 172.

De Lazzari B, Iacovoni A, Mottaghy K, Capoccia M, Badagliacca R, Vizza CD, De Lazzari C. ECMO Assistance during Mechanical Ventilation: Effects Induced on Energetic and Haemodynamic Variables. *Comput Methods Progr Biomed* 2021; 202: 106003.

De Lazzari B, Iacovoni A, Capoccia M, Papa S, Badagliacca R, Filomena D, De Lazzari C. Ventricular and Atrial Pressure-Volume Loops: Analysis of the Effects Induced by Right Centrifugal Pump Assistance. *Comput Methods Progr Biomed* 2022; 9: 181.

De Lazzari C, Pirckhalava M, editors. Cardiovascular and pulmonary artificial organs: educational training simulators. Rome: Consiglio Nazionale delle Ricerche (CNR) Press; 2017.

De Lazzari C, Quatember B. Cardiac energetics in presence of lung assist devices: in silico study. *Model Num Sim Mater Sci* 2016; 6:41–57.

De Lazzari C, Saltarocchi S, Genuini I, Capoccia M. Clinical Applications. In: Capoccia M, De Lazzari C. Concepts, Mathematical Modelling and Applications in Heart Failure, 2019, Nova Science Publishers.

De Lazzari C, Stalteri D. CARDIOSIM cardiovascular software simulator. http://cardi osim.dsb.cnr.it/.

De Tombe PP, Jones S, Burkhoff D, Hunter WC, Kass DA. Ventricular stroke work and efficiency both remain nearly optimal despite altered vascular loading. *Am J Physiol Heart Circ Physiol* 1993; 264: H1817-H1824.

Diamond G, Forrester JS, Hargis J, Parmley WW, Danzig R, Swan HJ. Diastolic pressure-volume relationship in the canine left ventricle. *Circ Res* 1971; 29: 267-275.

Diamond SL. System Analysis of Thrombus Formation. *Circ Res* 2016; 118: 1348-1362.

Doost SN, Ghista D, Su B, Zhong L, Morsi YS. Heart blood flow simulation: a perspective review. *BioMed Eng OnLine* 2016; 15: 101.

Doost SN, Zhong L, Morsi YS. Ventricular Assist Devices: Current State and Challenges. *J Med Devices* 2017; 11: 040801-1-040801-11.

Doshi D, Burkhoff D. Cardiovascular Simulation of Heart Failure. Pathophysiology and Therapeutics. *J Cardiac Fail* 2016; 22: 303-311.

Drzewiecki GM, Karam E, Welkowitz W. Physiological basis for mechanical time-variance in the heart: special consideration of non-linear function. *J Theor Biol* 1989; 139(4): 465-486.

Du VX, Huskens D, Maas C, Al Dieri R, de Groot PG, de Laat B. New Insights into the Role of Erythrocytes in Thrombus Formation. *Semin Thromb Hemost* 2014; 40: 72-80.

Duanmu Z, Yin M, Fan X, Yang X, Luo X. A patient-specific lumped-parameter model of coronary circulation. *Sci Rep* 2018; 8: 874.

E

Eckman PM, John R. Bleeding and Thrombosis in Patients With Continuous-Flow Ventricular Assist Devices. *Circulation* 2012; 125: 3038-3047.

Egorov Y, Menter FR, Cokljat D. Scale-Adaptive Simulation Method for Unsteady Flow Predictions. Part 2: Application to Aerodynamic Flows", *J Flow Turb Combust* 2010; 85(1): 139-165.

Elbeery JR, Owen CH, Savitt MA, Davis JW, Feneley MP, Rankin JS, VanTrigt P. Effects of the left ventricular assist device on right ventricular function. *J Thorac Cardiovasc Surg* 1990; 99: 809-816.

Elzinga G, Westerhof N. The Pumping Ability of the Left Heart and the Effect of Coronary Occlusion. *Circ Res* 1976; 38: 297-302.

Elzinga G, Westerhof N. The Effect of an Increase in Inotropic State and End-Diastolic Volume on the Pumping Ability of the Feline Left Heart. *Circ Res* 1978; 42(5): 620-628.

Emergy RW, Joyce LD. Directions in cardiac assistance. *J Card Surg* 1991; 6: 400-414.

F

Fager AM, Wood JP, Bouchard BA, Feng P, Tracy PB. Properties of procoagulant platelets: defining and characterizing the subpopulation binding a functional prothrombinase. *Arterioscler Thromb Vasc Biol* 2010; 30(12): 2400-2407.

Farrar DJ, Chow E, Compton PG, Foppiano L, Woodard J, Hill JD. Effects of acute right ventricular ischemia on ventricular interactions during prosthetic left ventricular support. *J Thorac Cardiovasc Surg* 1991; 102: 588-595.

Farrar DJ, Compton PG, Dajee H, Fonger JD, Hill JD. Right heart function during left heart assist and the effects of volume loading in a canine preparation. *Circulation* 1984; 70: 708-716.

Farrar DJ, Compton PG, Hershon JJ, Fonger JD, Hill JD. Right Heart Interaction with the Mechanically Assisted Left Heart. *World J Surg* 1985a; 9: 89-102.

Farrar DJ, Compton PG, Hershon JJ, Hill JD. Right ventricular function in an operating room model of mechanical left ventricular assistance and its effects in patients with depressed left ventricular function. *Circulation* 1985b; 72: 1279-1285.

Farrar DJ, Hill JD, Pennington DG, McBride LR, Holman WL, Kormos RL, Esmore D, Gray LA Jr, Seifert PE, Schoettle GP, Moore CH, Hendry PJ, Bhayana JN. Preoperative and Postoperative Comparison of Patients with Univentricular and Biventricular Support with the Thoratec Ventricular Assist Device as a Bridge to Cardiac Transplantation. *J Thorac Cardiovasc Surg* 1997; 113: 202-209.

Farrar DJ, Holman WR, McBride LR, Kormos RL, Icenogle TB, Hendry PJ, Moore CH, Loisance DY, El-Banayosy A, Frazier H. Long-Term Follow-up of Thoratec Ventricular Assist Device Bridge-to-Recovery Patients Successfully Removed From Support After Recovery of Ventricular Function. *J Heart Lung Transplant* 2002; 21: 516-521.

Farrar DJ. Ventricular interaction during mechanical circulatory support. *Semin Thorac Cardiovasc Surg* 1994; 6: 163-168.

Fearon WF, Bornschein B, Tonino PA, et al. Economic evaluation of fractional flow reserve-guided percutaneous coronary intervention in patients with multivessel disease. *Circulation* 2010; 122: 2545-2550.

Fedosov DA, Caswell B, Karniadakis GE. A multiscale red blood cell model with accurate mechanics, rheology, and dynamics. *Biophys J* 2010; 98: 2215-2225.

Fedosov DA, Lei H, Caswell B, Suresh S, Karniadakis GE. Multiscale modeling of red blood cell mechanics and blood flow in malaria. *PLoS Comput Biol* 2011; 7(12): e1002270.

Fedosov DA, Noguchi H, Gompper G. Multiscale modelling of blood flow: from single cells to blood rheology. *Biomech Model Mechan* 2014; 13: 239-258.

Ferrari A, Giampietro C, Bachmann B, Bernardi L, Bezuidenhhout D, Ermanni P, Hopf R, Kitz S, Kress G, Loosli C, Marina V, Meboldt M, Pellegrini G, Poulikakos D, Rebholz M, Schmid Daners M, Schmidt T, Starck C, Stefopoulos G, Sündermann S, Thamsen B, Zilla P, Potapov E, Falk V, Mazza E. A Novel Hybrid Membrane VAD as First Step toward Haemocompatible Blood Propulsion. *Ann Biomed Eng* 2021; 49(2): 716-731.

Ferrari G, De Lazzari C, Mimmo R, Tosti G, Ambrosi D. A modular numerical model of the cardiovascular system for studying and training in the field of cardiovascular physiopathology. *J Biomed Eng* 1992; 14: 91–107.

Ferrari G, Di Molfetta A, Zieliński K, Fresiello L. Circulatory modelling as a clinical decision support and an educational tool. *Biomed Data J* 2015; 1 (3): 45–50.

Ferrari M, Kadipasaoglu KA, Croitoru M, Conger J, Myers T, Gregoric I, Radovancevic B, Letsou GV, Frazier OH. Evaluation of Myocardial Function in Patients With End-Stage Heart Failure During Support With the Jarvik 2000 Left Ventricular Assist Device. *J Heart Lung Transplant* 2005; 24: 226-228.

Ferreira A, Chen S, Simaan M, Boston J, Antaki J. A discriminant-analysis based suction detection system for rotary blood pumps. Proceedings of 28th *IEEE Annual International Conference of Engineering in Medicine and Biology*, New York, NY; 2006, 5382-5385.

Filipovic N, Kojic M, Tsuda A. Modelling thrombosis using dissipative particle dynamics method. *Philos Trans A Math Phys Eng Sci* 2008; 366: 3265-3279.

Flamm MH, Diamond SL. Multiscale Systems Biology and Physics of Thrombosis Under Flow. *Ann Biomed Eng* 2012; 40(11): 2355-2364.

Fogelson AL, Guy RD. Immersed-boundary-type models of intravascular platelet aggregation Comput Methods. *Appl Mech Eng* 2008; 197: 2087–2104.

Fogelson AL, Hussain YH, Leiderman K. Blood clot formation under flow: the importance of factor XI depends strongly on platelet count. *Biophys J* 2012; 102: 10-18.

Fogelson AL, Keener JP. Toward an understanding of fibrin branching structure. *Phys Rev E Stat Nonlin Soft Matter Phys.* 2010; 81: 051922.

Fogelson AL, Tania N. Coagulation under flow: the influence of flow-mediated transport on the initiation and inhibition of coagulation. *Pathophysiol Haemost Thromb*. 2005; 34: 91–108.

Fogelson AL, Wang NT. Platelet dense-granule centralization and the persistence of ADP secretion. *Am J Physiol* 1996; 270(3 Pt 2): H1131-H1140.

Fogelson AL. A mathematical model and numerical method for studying platelet adhesion and aggregation during blood clotting. *J Comput Phys* 1984; 56: 111-134.

Fraser KH, Taskin ME, Griffith BP, Wu ZJ. The use of computational fluid dynamics in the development of ventricular assist devices. *Med Eng Phys* 2011; 33: 263-280.

Frazier OH. Unforeseen consequences of therapy with continuous-flow pumps. *Circ Heart Fail* 2010; 3: 647-649.

Fresiello L, Ferrari G, Di Molfetta A, Zieliński K, Tzallas A, Jacobs S, Darowski M, Kozarski M, Meyns B, Katertsidis NS, Karvounis EC, Tsipouras MG, Trivella MG. A cardiovascular simulator tailored for training and clinical uses. *J Biomed Inform* 2015; 57: 100–112.

Fukamachi K, Asou T, Nakamura Y, Toshima Y, Oe M, Mitani A, Sakamoto M, Kishizaki K, Sunagawa K, Tokunaga K. Effects of left heart bypass on right ventricular performance. Evaluation of the right ventricular end-systolic and end-diastolic pressure-volume relation in the in situ normal canine heart. *J Thorac Cardiovasc Surg* 1990; 99: 725-734.

Furie B, Furie BC. Mechanisms of Thrombus Formation. *N Engl J Med* 2008; 359: 938-949.

G

Gaddum NR, Stevens M, Lim E, Fraser J, Lovell N, Mason D, Timms D, Salamonsen R. Starling-Like Flow Control of a Left Ventricular Assist Device: In Vitro Validation. *Artificial Organs* 2014; 38(3): E46-E56.

Garcia S, Kandar F, Boyle A, Colvin-Adams M, Lliao K, Joyce L, John R. Effects of Pulsatile- and Continuous-flow Left Ventricular Assist Devices on Left Ventricular Unloading. *J Heart Lung Transplant* 2008; 27(3): 261-267.

Geisen U, Heilmann C, Beyersdorf F, Benk C, Berchtold-Herz M, Schlensak C, Budde U, Zieger B. Non-surgical bleeding in patients with ventricular assist devices could be explained by acquired von Willebrand disease. *Eur J Cardiothorac Surg* 2008; 33(4): 679-684.

Gharaie SH, Mosadegh B, Morsi Y. Towards computational prediction of flow-induced damage of blood cells using a time-accumulated model. *J Biomech Sci Eng* 2017; 12(4): DOI: 10.1299/jbse.17-00168.

Ghodrati M, Maurer A, Schlöglhofer T, Khienwald T, Zimpfer D, Beitzke D, Zonta F, Moscato F, Schima H, Aigner P. The influence of left ventricular assist device inflow cannula position on thrombosis risk. *Artif Organs* 2020; 44: 939-946.

Gibbins JM. Platelet adhesion signalling and the regulation of thrombus formation. *J Cell Sci*. 2004; 117: 3415–3425.

Giersiepen M, Wurzinger LJ, Opitz R, Reul H. Estimation of shear stress-related blood damage in heart valve prosthesis-in vitro comparison of 25 aortic valves. *Int J Artif Organs* 1990; 13: 300-306.

Gilbert JC, Glantz SA. Determinants of Left Ventricular Filling and of the Diastolic Pressure-Volume Relation. *Circ Res* 1989; 64: 827-852.

Girdhar G, Xenos M, Alemu Y, Chiu W-C, Lynch BE, Jesty J, Einav S, Slepian MJ, Bluestein D. Device Thrombogenicity Emulation: A Novel Method for Optimizing Mechanical Circulatory Support Device Thromboresistance. *PLoS ONE* 2012; 7(3): e32463. DOI:10.1371/journal.pone.0032463.

Giridharan GA, Skliar M, Olsen DB, Pantalos GM. Modelling and Control of a Brushless DC Axial Flow Ventricular Assist Device. *ASAIO J* 2002; 48: 272-289.
Glantz SA, Kernoff RS. Muscle stiffness determined from canine left ventricular pressure-volume curves. *Circ Res* 1975; 37: 787-794.
Glantz SA, Parmley WW. Factors which affect the diastolic pressure-volume curve. *Circ Res* 1978; 42: 171-180.

Glower DD, Spratt JA, Snow ND, Kabas JS, Davis JW, Olsen CO, Tyson GS, Sabiston DC Jr, Rankin JS. Linearity of the Frank-Starling relationship in the intact heart: the concept of preload recruitable stroke work. *Circulation* 1985; 71: 994-1009.

Goldstein JA, Gallagher MJ, O'Neill WW, Ross MA, O'Neil BJ, Raff GL. A randomized controlled trial of multi-slice coronary computed tomography for evaluation of acute chest pain. *J Am Coll Cardiol* 2007; 49: 863-871.

Goodman PD, Barlow ET, Crapo PM, Mohammad SF, Solen KA. Computational model of device-induced thrombosis and thrombo-embolism. *Ann Biomed Eng* 2005; 33: 780-797.

Govindarajan V, Rakesh V, Reifman J, Mitrophanov AY. Computational study of thrombus formation and clotting factor effects under venous flow conditions. *Biophys J* 2016; 110: 1869-1885.

Granegger M, Moscato F, Casas F, Wieselthaler G, Schima H. Development of a Pump Flow Estimator for Rotary Blood Pumps to Enhance Monitoring of Ventricular Function. *Artif Organs* 2012; 36: 691-699.

Gray RA, Pathmanathan P. Patient-Specific Cardiovascular Computational Modelling: Diversity of Personalisation and Challenges. *J Cardiovasc Transl Res* 2018; 11: 80-88.

Griffith BP, Kormos RL, Borovetz HS, Litwak K, Antaki JF, Poirier VL, Butler KC. HeartMate II Left Ventricular Assist System: From Concept to First Clinical Use. *Ann Thorac Surg* 2001; 71: S116-S120.

Grigioni M, Daniele C, Morbiducci U, D'Avenio G, Di Benedetto G, Barbaro V. The power-law mathematical model for blood damage prediction: analytical developments and physical inconsistencies. *Artificial Organs* 2004; 28(5): 467-475.

Grigioni M, Morbiducci U, D'Avenio G, Di Benedetto G, Del Gaudio C. A novel formulation for blood trauma prediction by a modified power-law mathematical model. *Biomech Model Mechanobiol* 2005; 4(4): 249-260.

Grinstein J, Rodgers D, Kalantari S, Sayer G, Kim GH, Sarswat N, Adatya S, Ota T, Jeevanandam V, Burkhoff D, Uriel N. HVAD Waveform Analysis as a Noninvasive Marker of Pulmonary Capillary Wedge Pressure: A First Step Toward the Development of a Smart Left Ventricular Assist Device Pump. *ASAIO J* 2018; 64(1): 10-15.

Groot RD, Warren PB. Dissipative particle dynamics: Bridging the gap between atomistic and mesoscopic simulation. *J Chem Phys* 1997; 107: 4423-4435.

Gross-Hardt SH, Sonntag SJ, Boehning F, Steinseifer U, Schmitz-Rode T, Kaufmann TAS. Crucial Aspects for Using Computational Fluid Dynamics as a Predictive Evaluation Tool for Blood Pumps. *ASAIO J* 2019; 65: 864-873.

Grossi EA, Connolly MW, Krieger KH, Nathan IM, Hunter CE, Colvin SB, Baumann FG, Spencer FC. Quantification of pulsatile flow during cardiopulmonary bypass to permit direct comparison of the effectiveness of various types of "pulsatile" and "nonpulsatile" flow. *Surgery* 1985; 98(3): 547-554.

Gwak K-W, Ricci M, Snyder S, Paden BE, Boston JR, Simaan MA, Antaki JF. *In Vitro* Evaluation of Multiobjective Hemodynamic Control of a Heart-Assist Pump. *ASAIO J* 2005; 51: 329-335.

H

Hall JL, Fermin DR, Birks EJ, Barton PJR, Slaughter M, Eckman P, Baba HA, Wohlschlaeger J, Miller LW. Clinical, Molecular, and Genomic Changes in Response to a Left Ventricular Assist Device. *J Am Coll Cardiol* 2011; 57(6): 641-652.

Hariharan P, D'Souza GA, Horner M, Morrison TM, Malinauskas RA, Myers MR. Use of the FDA nozzle model to illustrate validation techniques in computational fluid dynamics (CFD) simulations. *PLoS ONE* 2017; 12(6): e0178749.

Harvi. Interactive software simulator of cardiovascular physiology http://www.pvloo ps.com/.

Health Quality Ontario. Left Ventricular Assist Devices for Destination Therapy: A Health Technology Assessment. *Ontario Health Technol Assess Series* 2016; 8; 16(3): 1-60.

Health Quality Ontario. Left ventricular assist devices: an evidence-based analysis. *Ontario Health Technol Assess Series* 2004; 4(3): 1-69.

Heatley G, Sood P, Goldstein D, Uriel N, Cleveland J, Middlebrook D, Mehra MR and on behalf of the MOMENTUM 3 Investigators. Clinical trial design and rationale of the Multicenter Study of MagLev Technology in Patients Undergoing Mechanical Circulatory Support Therapy With HeartMate 3 (MOMENTUM 3) investigational device exemption clinical study protocol. *J Heart Lung Transplant* 2016; 35: 528-536.

Hellums JD. 1993 Whitaker Lecture: biorheology in thrombosis research. *Ann Biomed Eng* 1994; 22: 445-455.

HeMoLab (Hemodynamics Modelling Laboratory) http://hemol ab.lncc.br/.

Hockin M, Jones K, Mann KG. A model for the stoichiometric regulation of blood coagulation. *J Biol Chem*. 2002;277:18322–18333.

Holman WL, Naftel DC, Eckert CE, Kormos RL, Goldstein DJ, Kirklin JK. Durability of left ventricular assist devices: Interagency Registry for Mechanically Assisted Circulatory Support (INTERMACS) 2006 to 2011. *J Thorac Cardiovasc Surg* 2013; 146: 437-441.

Hunter WC. End-Systolic Pressure As a Balance Between Opposing Effects of Ejection. *Circ Res* 1989; 64: 265-275.

Hunter WC, Janicki JS, Weber KT, Noordergraaf A. Flow pulse response: a new method for the characterization of ventricular mechanics. *Am J Physiol Heart Circ Physiol* 1979; 237: H282-H292.

Hunter WC, Janicki JS, Weber KT, Noordergraaf A. Systolic Mechanical Properties of the Left Ventricle. Effects of Volume and Contractile State. *Circ Res* 1983; 52: 319-327.

I

Ingels NB Jr, Daughters GT, Nikolic SD, DeAnda A, Moon MR, Bolger AF, Komeda M, Derby GC, Yellin EL, Miller DC. Left ventricular diastolic suction with zero left atrial pressure in open-chest dogs. *Am J Physiol Heart Circ Physiol* 1996; 270: H1217-H1224.

Ingram G. *Basic Concepts in Turbomachinery*, Ventus Publishing ApS; 2009, pp 28-34.

J

Janicki JS, Weber KT. The pericardium and ventricular interaction, distensibility, and function. *Am J Physiol Heart Circ Physiol* 1980; 238: H494-H503.

Janz RF, Grimm AF. Deformation of the diastolic left ventricle. Nonlinear elastic effects. *Biophys J* 1973; 13: 689-704.

Jesty J, Bluestein D. Acetylated prothrombin as a substrate in the measurement of the procoagulant activity of platelets: elimination of the feedback activation of platelets by thrombin. *Anal Biochem* 1999; 272: 64-70.

Jesty J, Yin W, Perrotta P, Bluestein D. Platelet activation in a circulating flow loop: combined effects of shear stress and exposure time. *Platelets* 2003, 14(3): 143-149.

John R, Mantz K, Eckman P, Rose A, May-Newman K. Aortic valve pathophysiology during left ventricular assist device support. *J Heart Lung Transplant* 2010; 29: 1321-1329.

John R. Implantation of Continuous-Flow Ventricular Assist Devices: Technical Considerations. *Oper Tech Thorac Cardiovasc Surg* 2012; 17(2): 143-153.

Jones KC, Mann KG. A model for the tissue factor pathway to thrombin: II: a mathematical simulation. *J Biol Chem*. 1994; 269: 23367–23373.

Jorde UP, Aaronson KD, Najjar SS, Pagani FD, Hayward C, Zimpfer D, Schlöglhofer T, Goldstein DJ, Leadley K, Chow M-J, Brown MC, Uriel N. Identification and Management of Pump Thrombus in the HeartWare Left Ventricular Assist Device System. A Novel Approach Using Log File Analysis. *J Am Coll Cardiol HF* 2015; 3: 849-856.

Jung MH, Hassager C, Balling L, Russell SD, Boesgaard S, Gustafsson F. Relation between pressure and volume unloading during ramp testing in patients supported with a continuous-flow left ventricular assist device. *ASAIO J* 2015; 61(3): 307-312.

K

Kalitzin G, Medic G. Iaccarino G, Durbin P. Near-wall Behaviour of RANS Turbulence Models and Implications for Wall Functions. *J Comput Phys 2005; 204: 265-291*.

Kapur NK, Vest AR, Cook J, Kiernan MS. Pump Thrombosis: A Limitation of Contemporary Left Ventricular Assist Devices. *Curr Probl Cardiol* 2015; 40: 511-540.

Karšaj I, Humphrey JD. A mathematical model of evolving mechanical properties of intraluminal thrombus. *Biorheology* 2009; 46(6): 509-527.

Kashiyama N, Toda K, Miyagawa S, Nishi H, Yoshikawa Y, Fukushima S, Yoshioka D, Saito T, Sawa Y. Initial experience of EVAHEART explantation after continuous flow LVAD off test with percutaneous occlusion balloon. *J Artif Organs* 2014; 17: 366-369.

Kasirajan V, Fukamachi K, Kondo H, Massiello A, Chen J-F, Smedira N, McCarthy P. In Vitro Hemodynamic and Echocardiographic Effect of LVAD Valve Regurgitation. *ASAIO J* 1997; 43(2): 50.

Kass DA, Beyar R, Lankford E, Heard M, Maughan WL, Sagawa K. Influence of contractile state on curvilinearity of in situ end-systolic pressure-volume relations. *Circulation* 1989; 79: 167-178.

Kass DA, Beyar R. Evaluation of contractile state by maximal ventricular power divided by the square of end-diastolic volume. *Circulation* 1991; 84: 1698-1708.

Kass DA, Kelly RP. Ventriculo-Arterial Coupling: Concepts, Assumptions, and Applications. *Ann Biomed Eng* 1992; 20: 41-62.

Kass DA, Maughan WL, Guo ZM, Kono A, Sunagawa K, Sagawa K. Comparative influence of load versus inotropic states on indexes of ventricular contractility: experimental and theoretical analysis based on pressure-volume relationships. *Circulation* 1987; 76: 1422-1436.

Kass DA, Maughan WL. From "E_{max}" to pressure-volume relations: a broader view. *Circulation* 1988; 77: 1203-1212.

Kassis H, Cherukuri, K, Agarwal R, Kanwar M, Elapavaluru S, Sokos GG, Moraca RJ, Bailey SH, Murali S, Benza RL, Raina A. Significance of Residual Mitral Regurgitation After Continuous Flow Left Ventricular Assist Device Implantation. *J Am Coll Cardiol HF* 2017; 5(2): 81-88.

Kaufmann F, Hörmandinger C, Stepanenko A, Kretzschmar A, Soltani S, Krabatsch T, Potapov E, Hetzer R. Acoustic Spectral Analysis for Determining Pump Thrombosis in Rotary Blood Pumps. *ASAIO J 2014; 60: 502-507*.

Kavarana MN, Pessin-Minsley MS, Urtecho J, Catanese KA, Flannery M, Oz MC, Naka Y. Right Ventricular Dysfunction and Organ Failure in Left Ventricular Assist Device Recipients: A Continuing Problem. *Ann Thorac Surg* 2002; 73: 745-750.

Kawahito S, Nakata K, Nonaka K, Sato T, Yoshikawa M, Takano T, Maeda T, Linneweber J, Schulte-Eistrup S, Flowers D, Glueck J, Nosé Y, Analysis of the Arterial Blood Pressure Waveform Using Fast Fourier Transform Technique During Left Ventricular Nonpulsatile Assistance: In Vitro Study. *Artificial Organs* 2000b; 24: 580-583.

Kawahito S, Takano T, Nakata K, Maeda T, Nonaka K, Linneweber J, Schulte-Eistrup S, Sato T, Mikami M, Glueck J, Nosé Y. Analysis of the

Arterial Blood Pressure Waveform During Left Ventricular Nonpulsatile Assistance in Animal Models. *Artificial Organs* 2000a; 24(10): 816-820.

Kelly NS, Gill HS, Cookson AN, Fraser KH. Influence of Shear-Thinning Blood Rheology on the Laminar-Turbulent Transition over a Backward Facing Step. *Fluids* 2020; 5: 57.

Kelly RP, Ting CT, Yang TM, Liu CP, Maughan WL, Chang MS, Kass DA. Effective arterial elastance as index of arterial vascular load in humans. *Circulation* 1992; 86: 513–521.

Kim E-J, Capoccia M. Mechano-electric effect and a heart assist device in the synergistic model of cardiac function. *Math Biosci Eng* 2020; 17(5): 5212-5233.

Kim E-J, Capoccia M. Synergistic Model of Cardiac Function with a Heart Assist Device *Bioengineering* 2019; 7(1): 1.

Kim HJ, Vignon-Clementel IE, Coogan JS, Figueroa CA, Jansen KE, Taylor CA. Patient-specific modelling of blood flow and pressure in human coronary arteries. *Ann Biomed Eng* 2010; 38: 3195-3209.

Kim S-E, Choudhury D, Patel B. Computations of Complex Turbulent Flows Using the Commercial Code ANSYS Fluent. In: *Proceedings of the ICASE/LaRC/AFOSR Symposium on Modelling Complex Turbulent Flows*, Hampton, Virginia, 1997.

Kim YS, Kim E-H, Kim H-G, Shim EB, Song K-S, Lim KM. Mathematical analysis of the effects of valvular regurgitation on the pumping efficacy of continuous and pulsatile left ventricular assist devices. *Integr Med Res* 2016; 5: 22-29.

Kirklin JK, Naftel DC, Kormos RL, Stevenson LW, Pagani FD, Miller MA, Baldwin JT, Young JB. Fifth INTERMACS annual report: Risk factor analysis from more than 6,000 mechanical circulatory support patients. *J Heart Lung Transplant* 2013; 32: 141-156.

Kirklin JK, Naftel DC, Pagani FD, Kormos RL, Myers S, Acker MA, Rogers J, Slaughter MS, Stevenson LW. Pump thrombosis in the Thoratec HeartMate II device: An update analysis of the INTERMACS Registry. *J Heart Lung Transplant* 2015a; 34: 1515-1526.

Kirklin JK, Naftel DC, Pagani FD, Kormos RL, Stevenson L, Miller M, Young JB. Long-term mechanical circulatory support (destination therapy): On track to compete with heart transplantation? *J Thorac Cardiovasc Surg* 2012; 144: 584-603.

Kirklin JK, Naftel DC, Pagani FD, Kormos RL, Stevenson LW, Blume ED, Myers SL, Miller MA, Baldwin JT, Young JB. Seven INTERMACS annual report: 15,000 patients and counting. *J Heart Lung Transplant* 2015; 34(12): 1495-1504.

Kirklin JK, Pagani FD, Kormos RL, Stevenson LW, Blume ED, Myers SL, Miller MA, Baldwin JT, Young JB, Naftel DC. Eighth annual INTERMACS report: Special focus on framing the impact of adverse events. *J Heart Lung Transplant* 2017; 36(10): 1080-1086.

Kishimoto Y, Takewa Y, Arakawa M, Umeki A, Ando M, Nishimura T, Fujii Y, Mizuno T, Nishimura M, Tatsumi E. Development of a novel drive mode to prevent aortic insufficiency during continuous-flow LVAD support by synchronizing rotational speed with heartbeat. *J Artif Organs* 2013; 16: 129-137.

Konig CS, Clark C, Mokhtarzadeh-Dehghan MR. Comparison of flow in numerical and physical models of a ventricular assist device using low- and high-viscosity fluids. *Proc IMechE Part H: J Eng Med* 1999; 213: 423-432.

Korakianitis T, Shi Y. A concentrated parameter model for the human cardiovascular system including heart valve dynamics and atrioventricular interaction. *Med Eng Phys* 2006a; 28: 613-628.

Korakianitis T, Shi Y. Numerical simulation of cardiovascular dynamics with healthy and diseased heart valves. *J Biomech* 2006b; 39: 1964-1982.

Kozarski M, Ferrari G, Zieliński K, Górczyńska K, Palko KJ, Tokarz A, Darowski M. Open loop hybrid circulatory model: the effect of the arterial lumped parameter loading structure on selected ventricular and circulatory variables. *Biocybernet Biomed Eng* 2008; 28(1): 17–27.

Krukenkamp IB, Silverman NA, Pridjian A, Levitsky S. Correlation between the linearized Frank-Starling relationship and myocardial energetics in the ejecting heart. Afterload independence and sensitivity to inotropic state. *J Thorac Cardiovasc Surg* 1987; 93: 728-740.

Kuharsky AL, Fogelson AL. Surface-mediated control of blood coagulation: the role of binding site densities and platelet deposition. *Biophys J* 2001; 80(3): 1050-1074.

Kumar DR, Hanlin E, Glurich I, Mazza JJ, Yale SH. Virchow's Contribution to the Understanding of Thrombosis and Cellular Biology. *Clin Med Res* 2010; 8(3-4): 168-172.

Kumar P, Antony N. Designing and Modelling a Ventricular Assist Device. *IOSR J Electrical Electronics Eng* 2016; 11(2): 7-13.

Kung E, Les A. Figueroa C, Medina F, Arcaute K, Wicker R, McConnell M, Taylor C. In Vitro Validation of Finite Element Analysis of Blood Flow in Deformable Models. *Ann Biomed Eng* 2011; 39(7): 1947-1960.

L

Lankhaar JW, Rövekamp FA, Steendijk P, Faes TJC, Westerhof BE, Kind T, Vonk-Noordegraaf A, Westerhof N. Modeling the Instantaneous Pressure-

Volume Relation of the Left Ventricle: A Comparison of Six Models. *Ann Biomed Eng* 2009; 37: 1710-1726.

Larrabide I, Blanco PJ, Urquiza SA, Dari EA, Vénere MJ, de Souza e Silva NA, Feijóo RA. HeMoLab—Haemodynamics Modelling Laboratory: an application for modelling the human cardiovascular system. *Comput Biol Med* 2012; 42: 993–1004.

Launder BE, Spalding DB. *Lectures in Mathematical Models of Turbulence*. Academic Press, London, England, 1972.

Launder BE, Spalding DB. The Numerical Computation of Turbulent Flows. *Computer Methods in Applied Mechanics and Engineering* 1974; 3: 269-289.

Laurenzi IJ, Diamond SL. Monte Carlo simulation of the heterotypic aggregation kinetics of platelets and neutrophils. *Biophys J*. 1999; 77: 1733–1746.

Lawson JH, Kalafatis M, Stram S, Mann KG. A model for the tissue factor pathway to thrombin: I: an empirical study. *J Biol Chem*. 1994; 269:23357–23366.

Leiderman K, Fogelson A. An overview of mathematical modelling of thrombus formation. *Thromb Res* 2014; 133: S12-S14.

Leiderman K, Fogelson AL. Grow with the flow: a spatial-temporal model of platelet deposition and blood coagulation under flow. *Math Med Biol* 2011; 28: 47-84.

Leiderman K, Fogelson AL. The influence of hindered transport on the development of platelet thrombi under flow. *Bull Math Biol* 2013; 75: 1255-1283.

Leverett LB, Hellums JD, Alfrey CP, Lynch EC. Red blood cell damage by shear stress. *Biophys J* 1972; 12: 257-272.

Li Z, Yazdani A, Tartakovsky A, Karniadakis GE. Transport dissipative particle dynamics model for mesoscopic advection-diffusion reaction problems. *J Chem Phys* 2015; 143: 014101.

Lim E, Dokos S, Cloherty SL, Salamonsen RF, Mason DG, Reizes JA, Lovell NH. Parameter-Optimized Model of Cardiovascular – Rotary Blood Pump Interactions. *IEEE Trans Biomed Eng* 2010; 57(2): 254-266.

Lim E, Dokos S, Salamonsen RF, Rosenfeldt FL, Ayre PJ, Lovell NH. Effect of Parameter Variations on the Hemodynamic Response Under Rotary Blood Pump Assistance. *Artificial Organs* 2012b; 36(5): E125-E137.

Lim E, Dokos S, Salamonsen RF, Rosenfeldt FL, Ayre PJ, Lovell NH. Numerical Optimization Studies of Cardiovascular-Rotary Blood Pump Interaction. *Artificial Organs* 2012a; 36(5): E110-E124.

Lim KM, Costantino J, Gurev V, Zhu R, Shim EB, Trayanova NA. Comparison of the effects of continuous and pulsatile left ventricular assist devices on ventricular unloading using a cardiac electromechanics model. *J Physiol Sci* 2012; 62: 11-19.

Lim KM, Hong S-B, Lee BK, Shim EB, Trayanova N. Computational analysis of the effect of valvular regurgitation on ventricular mechanics using a 3D electromechanics model. *J Physiol Sci* 2015; 65: 159-164.

Lim KM, Kim IS, Choi SW, Min BG, Won YS, Kim HY, Shim EB. Computational analysis of the effect of the type of LVAD flow on coronary perfusion and ventricular afterload. *J Physiol Sci* 2009; 59: 307-316.

Lisy O, Redfield MM, Jovanovic S, Jougasaki M, Jovanovic A, Leskinen H, Terzic A, Burnett JC Jr. Mechanical Unloading Versus Neurohumoral Stimulation on Myocardial Structure and Endocrine Function In Vivo. *Circulation* 2000; 102: 338-343.

Little WC, Cheng CP, Peterson T, Vinten-Johansen J. Response of the left ventricular end-systolic pressure volume relation in conscious dogs to a wide range of contractile states. *Circulation* 1988; 78: 736-745.

Little WC, Freeman GL. Description of LV pressure-volume relations by time-varying elastance and source resistance. *Am J Physiol Heart Circ Physiol* 1987; 253: H83-H90.

Little WC. The left ventricular dP/dt_{max}-end-diastolic volume relation in closed-chest dog. *Circ Res* 1985; 56: 808-815.

Liu MB, Liu GR, Zhou LW, Chang JZ. Dissipative Particle Dynamics (DPD): An Overview and Recent Developments. *Arch Computat Methods Eng* 2015; 22: 529-556.

Lloyd WF. The Specific Heat of Human Blood. *British Medical Journal* 1897; October 16: 1072.

Lo K, Denney WS, Diamond SL. Stochastic modeling of blood coagulation initiation. *Pathophysiol Haemost Thromb*. 2005; 34: 80 –90.

Lobanov AI, Starozhilova TK. The effect of convective flows on blood coagulation processes. *Pathophysiol Haemost Thromb*. 2005; 34: 121–134.

Longest PW, Kleinstreuer C. Comparison of blood particle deposition models for non-parallel flow domains. *J Biomech* 2003; 36: 421-430.

Lopes G Jr, Bock E, Gómez L. Numerical Analyses for Low Reynolds Flow in a Ventricular Assist Device. *Artificial Organs* 2017; 41(6): E30-E40.

Lorenz R, Benk C, Bock J, Stalder AF, Korvink JG, Hennig J, Markl M. Closed Circuit MR Compatible Pulsatile Pump System Using a Ventricular

Assist Device and Pressure Control Unit. *Magnetic Res Med* 2012; 67: 258-268.

Luan D, Zai M, Varner JD. Computationally derived points of fragility of a human cascade are consistent with current therapeutic strategies. *PLoS Comput Biol*. 2007; 3: 1347–1359.

Lumens J. Creating your own virtual patient with circadapt simulator. *Eur Heart* J 2014; 35: 335–337.

Lumens J, Arts T, Marcus JT, Vonk-Noordegraaf A, Delhaas T. Early-diastolic left ventricular lengthening implies pulmonary hypertension-induced right ventricular decompensation. *Cardiovasc Res* 2012b; 96: 286–295.

Lumens J, Delhaas T. Cardiovascular modelling in pulmonary arterial hypertension: focus on mechanisms and treatment of right heart failure using the circadapt model. *Am J Cardiol* 2012; 110: 39S–48S.

Lumens J, Delhaas T, Kirn B, Arts T. Three-wall segment (triseg) model describing mechanics and hemodynamics of ventricular interaction. *Ann Biomed Eng* 2009; 37: 2234–2255.

Lumens J, Leenders GE, Cramer MJ, De Boeck BW, Doevendans PA, Prinzen FW, Delhaas T. Mechanistic evaluation of echocardiographic dyssynchrony indices: patient data combined with multiscale computer simulations. *Circ Cardiovasc Imaging* 2012; 5: 491–499.

Lumens J, Ploux S, Strik M, Gorcsan J 3rd, Cochet H, Derval N, Strom M, Ramanathan C, Ritter P, Haissaguerre M, Jais P, Arts T, Delhaas T, Prinzen FW, Bordachar P. Comparative electromechanical and hemodynamic effects of left ventricular and biventricular pacing in dyssynchronous heart failure: electrical resynchronization versus left–right ventricular interaction. *J Am Coll Cardiol* 2013; 62: 2395–2403.

Luo C, Ramachandran D, Ware DL, Ma TS, Clark JW. Modelling left ventricular diastolic dysfunction: classification and key indicators. *Theor Biol Med Model* 2011; 8: 14.

Luo C, Ware DL, Zwischenberger JB, Clark JW. A mechanical model of the human heart relating septal function to myocardial work and energy. *Cardiovasc Eng* 2008; 8: 174–184.

M

Malehsa D, Meyer AL, Bara C, Strüber M. Acquired von Willebrand syndrome after exchange of the HeartMate XVE to the HeartMate II ventricular assist device. *Eur J Cardiothorac Surg* 2009; 35(6): 1091-1093.

Malinauskas RA, Hariharan P, Day SW, Herbertson LH, Buesen M, Steinseifer U, Aycock KI, Good BC, Deutsch S, Manning KB, Craven BA. FDA Benchmark Medical Device Flow Models for CFD Validation. *ASAIO J* 2017; 63: 150-160.

Mancini DM, Beniaminovitz A, Levin H, Catanese K, Flannery M, Di Tullio M, Savin S, Cordisco ME, Rose E, Oz M. Low Incidence of Myocardial Recovery After Left Ventricular Assist Device Implantation in Patients With Chronic Heart Failure. *Circulation* 1998; 98: 2383-2389.

Mann DL, Barger PM, Burkhoff D. Myocardial Recovery and the Failing Heart. Myth, Magic, or Molecular Target? *J Am Coll Cardiol* 2012; 60(24): 2465-2472.

Mansouri M, Gregory SD, Salamonsen RF, Lovell NH, Stevens MC, Pauls JP, Akmeliawati R, Lim E. Preoad-based Starling-like control of rotary blood pumps: An *in-vitro* evaluation. *PLoS ONE* 2017; 12(2): e0172393

Mansouri M, Salamonsen RF, Lim E, Akmeliawati R, Lovell NH. Preload-Based Starling-Like Control for Rotary Blood Pumps: Numerical Comparison with Pulsatility Control and Constant Speed Operation. *PLoS ONE* 2015; 10(4): e0121413.

Mariscalco G, Wozniak MJ, Dawson AG, Serraino GF, Porter R, Nath M, Klersy C, Kumar T, Murphy GJ. Body mass index and mortality among adults undergoing cardiac surgery. a nationwide study with a systematic review and meta-analysis. *Circulation* 2017; 135: 850–863.

Markl M, Benk C, Klausmann D, Stalder AF, Frydrychowicz A, Hennig J, Beyersdorf F. Three-dimensional magnetic resonance flow analysis in a ventricular assist device. *J Thorac Cardiovasc Surg* 2007; 134: 1471-1476.

Marsden AL, Bazilevs Y, Long CC, Behr M. Recent advances in computational methodology for simulation of mechanical circulatory assist devices. *Wiley Interdiscip Rev Syst Biol Med 2014; 6(2): 169-188*.

Marsden AL, Esmaily-Moghadam M. Multiscale Modelling of Cardiovascular Flows for Clinical Decision Support. *Appl Mech Rev* 2015; 67: 030804-1-030804-11.

Martina JR, Westerhof BE, de Jonge N, van Goudoever J, Westers P, Chamuleau S, van Dijk D, Rodermans BFM, de Mol BAJM, Lahpor JR. Noninvasive Arterial Blood Pressure Waveforms in Patients with Continuous-Flow Left Ventricular Assist Devices. *ASAIO J* 2014; 60: 154-161.

Marx G. Simulating fibrin clotting time. *Med Biol Eng & Comput* 2006; 44: 79-85.

Mason DT. Usefulness and limitations of the rate of rise of the intraventricular pressure (dp/dt) in the evaluation of myocardial contractility in man. *Am J Cardiol* 1969; 23: 516-527.

Maughan WL, Shoukas AA, Sagawa K, Weisfeldt ML. Instantaneous pressure-volume relationship of the canine right ventricle. *Circ Res* 1979; 44: 309-315.

Maughan WL, Sunagawa K, Burkhoff D, Sagawa K. Effect of arterial impedance changes on the end-systolic pressure-volume relation. *Circ Res* 1984; 54: 595-602.

Maughan WL, Sunagawa K, Sagawa K. Ventricular systolic interdependence: volume elastance model in isolated canine hearts. *Am J Physiol Heart Circ Physiol* 1987; 253: H1381-H1390.

Maybaum S, Epstein S, Beniaminovitz A, Oz M, Bergmann S, Mancini D. Resting myocardial blood flow and metabolism predicts improved native left ventricular output and the ability to exercise with weaning in patients with the TCI HeartMate left ventricular assist device. *J Heart Lung Transplant* 1999; 18(1): 62 (abstract 118).

Maybaum S, Williams M, Barbone A, Levin H, Oz M, Mancini D. Assessment of Synchrony Relationships Between the Native Left Ventricle and the HeartMate Left Ventricular Assist Device. *J Heart Lung Transplant* 2002; 21: 509-515.

McCarthy PM. Hemodynamic and physiologic changes during support with an implantable left ventricular assist device. *J Thorac Cardiovasc Surg* 1995; 109: 409-418.

McConnell PI, Del Rio CL, Kwiatkowski P, Farrar DJ, Sun BC. Assessment of Cardiac Function During Axial-flow Left Ventricular Assist Device Support Using a Left Ventricular Pressure-derived Relationship: Comparison With Pre-load Recruitable Stroke Work. *J Heart Lung Transplant* 2007; 26: 159-166.

McConnell PI, Sun BC. Pressure-Volume Analysis During Axial Flow Ventricular Assist Device Support. *J Heart Lung Transplant* 2006; 25: 256-257.

Medvitz RB, Kreider JW, Manning KB, Fontaine AA, Deutsch S, Paterson EG. Development and Validation of a Computational Fluid Dynamics Methodology for Simulation of Pulsatile Left Ventricular Assist Devices. *ASAIO J* 2007; 53(2): 122-131.

Mehra MR, Goldstein DJ, Uriel N, Cleveland JC, Yuzefpolskaya M, Salerno C, Walsh MN, Milano CA, Patel CB, Ewald GA, Itoh A, Dean D et al. Two-Year Outcomes with a Magnetically Levitated Cardiac Pump in Heart Failure. *N Engl J Med* 2018; 378: 1386-1395.

Mehra MR, Naka Y, Uriel N, Goldstein DJ, Cleveland JC, Colombo PC, Walsh MN, Milano CA, Patel CB, Jorde UP, Pagani FD, Aaronson KD, Dean DA, McCants K, Itoh A, Ewald GA, Horstmanshof D, Long JW, Salerno C et al. A Fully Magnetically Levitated Circulatory Pump for Advanced Heart Failure. *N Engl J Med* 2017; 376: 440-450.

Mehra MR, Salerno C, Cleveland JC, Pinney S, Yuzefpolskaya M, Milano CA, Itoh A, Goldstein DJ, Uriel N, Gulati S, Pagani FD, John R, Adamson R,

Bogaev R, Thohan V, Chuang J, Sood P, Goates S, Silvestry SC. Healthcare Resource Use and Cost Implications in the MOMENTUM 3 Long-Term Outcome Study. Randomised Controlled Trial of a Magnetically Levitated Cardiac Pump in Advanced Heart Failure. *Circulation* 2018a; 138: 1923-1934.

Mehra MR, Stewart GC, Uber PA. The vexing problem of thrombosis in long-term mechanical circulatory support. *J Heart Lung Transplant* 2014; 33: 1-11.

Mehra MR, Uriel N, Naka Y, Cleveland JC Jr, Yuzefpolskaya M, Salerno CT, Walsh MN, Milano CA, Patel CB, Hutchins SW, Ransom J, Ewald GA, Itoh A, Raval NY, Silvestry SC, Cogswell R, John R, Bhimaraj A, Bruckner BA, Lowes BD, Um JY, Jeevanandam V, Sayer G, Mangi AA, Molina EJ, Sheikh F, Aaronson K, Pagani FD, Cotts WG, Tatooles AJ, Babu A, Chomsky D, Katz JN, Tessmann PB, Dean D, Krishnamoorthy A, Chuang J, Topuria I, Sood P, Goldstein DJ for the MOMENTUM 3 Investigators. A Fully Magnetically Levitated Left Ventricular Assist Device – Final Report. *N Engl J Med* 2019; 380: 1618-1627.

Meijboom WB, Van Mieghem CA, van Pelt N, et al. Comprehensive assessment of coronary artery stenoses: computed tomography coronary angiography versus conventional coronary angiography and correlation with fractional flow reserve in patients with stable angina. *J Am Coll Cardiol* 2008; 52: 636-643.

Menter FR, Egorov Y. Scale-Adaptive Simulation Method for Unsteady Flow Predictions. Part 1: Theory and Model Description. *J Flow Turb Combust* 2010; 85(1): 113-138.

Menter FR, Langtry R, Völker S. Transition Modeling for General Purpose Codes. *J Flow Turb Combust* 2006; 77(1-4): 277-303.

Menter FR. Best Practice: Scale-Resolving Simulations in ANSYS CFD Version 2.00. Technical Paper from ANSYS, *www.ansys.com*, 2015.

Menter FR. Influence of Freestream Values on k-ω Turbulence Model Predictions. *AIAA J* 1992; 30(6): 1657-1659.

Menter FR. Review of the shear-stress transport turbulence model experience from an industrial perspective. *Int J Comp Fluid Dyn* 2009; 23(4): 305-316.

Menter FR. Turbulence Modelling for Engineering Flows. Technical Paper from ANSYS, *www.ansys.com*, 2011.

Menter FR. Two-Equation Eddy-Viscosity Turbulence Models for Engineering Applications. *AIAA J* 1994; 32(8): 1598-1605.

Meyer AL, Kuehn C, Weidemann J, Malehsa D, Bara C, Fischer S, Haverich A, Strüber M. Thrombus formation in a HeartMate II left ventricular assist device. *J Thorac Cardiovasc Surg* 2008; 135: 203-204.

Milano CA , Rogers JG , Tatooles AJ , Bhat G , Slaughter MS , Birks EJ , et al. HVAD: the ENDURANCE supplemental trial. *JACC Heart Fail* 2018; 6(9): 792 – 802.

Miller LW, Pagani FD, Russell SD, John R, Boyle AJ, Aaronson KD, Conte JV, Naka Y, Mancini D, Delgado RM, MacGillivray TE, Farrar DJ, Frazier OH; HeartMate II Clinical Investigators. Use of a Continuous-Flow Device in Patients Awaiting Heart Transplantation. *N Engl J Med* 2007; 357(9): 885-896.

Min JK, Shaw LJ, Berman DS. The present state of coronary computed tomography angiography: a process in evolution. *J Am Coll Cardiol* 2010; 55: 957-965.

Mirsky I, Tajimi T, Peterson KL. The development of the entire end-systolic pressure-volume and ejection fraction-afterload relations: a new concept of systolic myocardial stiffness. *Circulation* 1987; 76(2): 343-356.

Mittal R, Seo JH, Vedula V, Choi YJ, Liu H, Huang HH, Jain S, Younes L, Abraham T, George RT. Computational Modelling of Cardiac Haemodynamics: Current Status and Future Outlook. *J Comput Phys* 2016; 305: 1065-1082.

Miyamoto AT, Tanaka S, Matloff JM. Right ventricular function during left heart bypass. *J Thorac Cardiovasc Surg* 1983; 85: 49-53.

Miyazoe Y, Sawairi T, Ito K, Konishi Y, Yamane T, Nishida M, Asztalos B, Masuzawa T, Tsukiya T, Endo S, Taenaka Y. Computational Fluid Dynamics Analysis to Establish the Design Process of a Centrifugal Blood Pump: Second Report. *Artificial Organs* 1999; 23(8): 762-768.

Mizunuma H, Nakajima R. Experimental Study on the Shear Stress Distributions in a Centrifugal Blood Pump. *Artificial Organs* 2007; 31: 550-559.

Moazami N, Fukamachi K, Kobayashi M, Smedira NG, Hoercher KJ, Massiello A, Lee S, Horvath DJ, Starling RC. Axial and centrifugal continuous-flow rotary pumps: a translation from pump mechanics to clinical practice. *J Heart Lung Transplant* 2013; 32(1): 1-11.

Mody NA, King MR. Platelet adhesive dynamics part II: high shear-induced transient aggregation via GPIba-vWF-GPIba bridging. *Biophys J* 2008b; 95:2556 –2574.

Mody NA, King MR. Platelet adhesive dynamics: part I: characterization of platelet hydrodynamic collisions and wall effects. *Biophys J*. 2008a; 95: 2539–2555.

Mody NA, King MR. Three-dimensional simulations of a platelet-shaped spheroid near a wall in shear flow. *Phys Fluids.* 2005a; 17:113302-113301–113302-12.

Mody NA, Lomakin O, Doggett TA, Diacovo TG, King MR. Mechanics of transient platelet adhesion to von Willebrand factor under flow. *Biophys J*. 2005b; 88: 1432–1443.

Moeendarbary E, Ng T, Zangeneh M. Dissipative particle dynamics: introduction, methodology and complex fluid applications – a review. *Int J Appl Mech* 2009; 1(04): 737-763.

Moiseyev G, Bar-Yoseph PZ. Computational modelling of thrombosis as a tool in the design and optimization of vascular implants. *J Biomech* 2013; 46: 248-252.

Mokadam NA, Andrus S, Ungerleider A. Thrombus formation in a HeartMate II. *Eur J Cardio-thorac Surg* 2011; 39: 414.

Monroe DM, Hoffman M, Roberts HR. Platelets and Thrombin Generation. *Arterioscler Thromb Vasc Biol* 2002; 22: 1381-1389.

Moon MR, Castro LJ, DeAnda A, Tomizawa Y, Daughters GT, Ingels NB, Miller DC. Right ventricular dynamics during left ventricular assistance in closed-chest dogs. *Ann Thorac Surg* 1993; 56: 54-67.

Moreno N, Vignal P, Li J, Calo VM. Multiscale modelling of blood flow: coupling finite elements with smoothed dissipative particle dynamics. *Procedia Comput Sci* 2013; 18: 2565-2574.

Mori D, Yano K, Tsubota K, Ishikawa T, Wada S, Yamaguchi T. Simulation of platelet adhesion and aggregation regulated by fibrinogen and von Willebrand factor. *Thromb Haemost*. 2008; 99:108 –115.

Morris PD, Narracott A, von Tengg-Kobligk H, Silva Soto DA, Hsiao S, Lungu A, Evans P, Bressloff NW, Lawford PV, Hose DR, Gunn JP. Computational fluid dynamics modelling in cardiovascular medicine. *Heart* 2016; 102: 18-28.

Morshuis M, El-Banayosy A, Arusoglu L, Koerfer R, Hetzer R, Wieselthaler G, Pavie A, Nojiri C. European experience of Duraheart^{TM} magnetically levitated centrifugal left ventricular assist system. *Eur J Cardiothorac Surg* 2009; 35: 1020-1028.

Moscato F, Danieli GA, Schima H. Dynamic modelling and identification of an axial flow ventricular assist device. *Int J Artif Organs* 2009; 32: 336-343.

Moscato F, Vollkron M, Bergmeister H, Wieselthaler G, Leonard E, Schima H. Left Ventricular Pressure-Volume Loop Analysis During Continuous Cardiac Assist in Acute Animal Trials. *Artificial Organs* 2007; 31: 369-376.

Moser RD, Kim J, Mansour NN. Direct numerical simulation of turbulent channel flow up to Re_τ = 590. *Phys Fluids* 1999; 11(4): 943-945.

Munnix ICA, Cosemans JMEM, Auger JM, Heemskerk JWM. Platelet response heterogeneity in thrombus formation. *Thromb Haemost* 2009; 102: 1149-1156.

N

Naiyanetr P, Moscato F, Vollkron M, Zimpfer D, Wieselthaler G, Schima H. Continuous assessment of cardiac function during rotary blood pump support: A contractility index derived from pump flow. *J Heart Lung Transplant* 2010; 29: 37-44.

Najjar SS, Slaughter MS, Pagani FD, Starling RC, McGee EC, Eckman P, Tatooles AJ, Moazami N, Kormos RL, Hathaway DR, Najarian KB, Bhat G, Aaronson KD, Boyce SW and for the HVAD Bridge to Transplant ADVANCE Trial Investigators. An Analysis of pump thrombus events in patients in the HeartWare ADVANCE bridge to transplant and continued access protocol trial. *J Heart Lung Transplant 2014; 33: 23-34*.

Negroni JA, Lascano EC. Concentration and elongation of attached cross-bridges as pressure determinants in a ventricular model. *J Mol Cell Cardiol* 1999; 31(8): 1509–1526.

Nerem R. *Structure and Function of the Circulation*. New York: Plenum Press; 1981.

Nesbitt WS, Westein E, Tovar-Lopez FJ, Tolouei E, Mitchell A, Fu J, Carberry J, Fouras A, Jackson SP. A shear gradient– dependent platelet aggregation mechanism drives thrombus formation. *Nat Med*. 2009;15: 665–675.

Netuka I, Sood P, Pya Y, Zimpfer D, Krabatsch T, Garbade J, Rao V, Morshuis M, Marasco S, Beyersdorf F, Damme L, Schmitto JD. Fully Magnetically Levitated Left Ventricular Assist System for Treating Advanced HF. A Multicenter Study. *J Am Coll Cardiol* 2015; 66: 2579-2589.

Nishida M, Yamane T, Tsukamoto Y, Ito K, Konishi Y, Masuzawa T, Tsukiya T. Shear Evaluation by Quantitative Flow Visualization Near the Casing Surface of a Centrifugal Blood Pump. *JSME Int J Series C* 2002; 45(4): 981-988.

Nishigaki K, Matsuda H, Hirose H, Nakano S, Ohtani M, Ohkubo N, Matsuwaka R, Kawashima Y. The Effect of Left Ventricular Bypass on the Right Ventricular Function: Experimental Analysis of the Effects of Ischemic Injuries to the Right Ventricular Free Wall and Interventricular Septum. *Artificial Organs* 1990; 14: 218-223.

Nissen SE. Limitations of computed tomography coronary angiography. *J Am Coll Cardiol* 2008; 52: 2145-2147.

Noailly J, Van Oosterwyck H, Wilson W, Quinn TM, Ito K. A poroviscoelastic description of fibrin gels. *J Biomech* 2008; 41: 3265-3269.

Nobili M, Sheriff J, Morbiducci U, Redaelli A, Bluestein D. Platelet Activation Due to Haemodynamic Shear Stresses: Damage Accumulation Model and Comparison to *In Vitro* Measurements. *ASAIO J* 2008; 54(1): 64-72.

O

Ochsner G, Wilhelm MJ, Amacher R, Petrou A, Cesarovic N, Staufert S, Röhrnbauer B, Maisano F, Hierold C, Meboldt M, Schmid Daners M. *In Vivo* Evaluation of Physiologic Control Algorithms for Left Ventricular Assist Devices Based on Left Ventricular Volume or Pressure. *ASAIO J* 2017; 63: 568-577.

Olansen JB, Clark JW, Khoury D, Ghorbel F, Bidani A. A closed-loop model of the canine cardiovascular system that includes ventricular interaction. *Comput Biomed Res* 2000; 33: 260–295.

Olsen D. The History of Continuous-Flow Blood Pumps. *Artificial Organs* 2000; 24(6): 401-404.

P

Pagani FD, Long JW, Dembitsky WP, Joyce LD, Miller LW. Improved Mechanical Reliability of the HeartMate XVE Left Ventricular Assist System. *Ann Thorac Surg* 2006; 82: 1413-1418.

Pagani FD, Miller LW, Russell SD, Aaronson KD, John R, Boyle AJ, Conte JV, Bogaev RC, MacGillivray TE, Naka Y, Mancini D, Massey HT, Chen L, Klodell CT, Aranda JM, Moazami N, Ewald GA, Farrar DJ, Frazier OH; HeartMate II Investigators. Extended Mechanical Circulatory Support With a Continuous-Flow Rotary Left Ventricular Assist Device. *J Am Coll Cardiol* 2009; 54: 312-321.

Park RC, Little WC, O'Rourke RA. Effect of alteration of left ventricular activation sequence on the left ventricular end-systolic pressure-volume relation in closed-chest dogs. *Circ Res* 1985; 57(5): 706-717.

Park SJ, Tector A, Piccioni W, Raines E, Gelijns A, Moskowitz A, Rose E, Holman W, Furukawa S, Frazier OH, Dembitsky W. Left ventricular assist devices as destination therapy: A new look at survival. *J Thorac Cardiovasc Surg* 2005; 129: 9-17.

Pedrizzetti G, Domenichini F. Left Ventricular Fluid Mechanics: The Long Way from Theoretical Models to Clinical Applications. *Ann Biomed Eng* 2015; 43(1): 26-40.

Peiró J, Veneziani A. Reduced models of the cardiovascular system. In: *Cardiovascular Mathematics. Modelling and simulation of the cardiovascular system*. Formaggia L, Quarteroni A, Veneziani A eds. Springer-Verlag Milano; 2009, pp 347-394.

Petrou A, Monn M, Meboldt M, Schmid Daners M. A Novel Multi-objective Physiological Control System for Rotary Left Ventricular Assist Devices. *Ann Biomed Eng* 2017; 45(12): 2899-2910.

Pijls NH, De Bruyne B, Peels K, et al. Measurement of fractional flow reserve to assess the functional severity of coronary-artery stenoses. *N Engl J Med* 1996; 334: 1703-1708.

Pillay P, Krishnan R. Modeling, simulation, and analysis of permanent-magnet motor drives, Part I: the permanent-magnet synchronous motor drive. *IEEE Trans Ind Appl* 1989; 25(2): 265-273.

Pinney SP, Anyanwu AC, Lala A, Teuteberg JJ, Uriel N, Mehra MR. Left Ventricular Assist Devices for Lifelong Support. *J Am Coll Cardiol* 2017; 69(23): 2845-2861.

Pirbodaghi T, Axiak S, Weber A, Gempp T, Vandenberghe S. Pulsatile control of rotary blood pumps: Does the waveform modulation matter ? *J Thorac Cardiovasc Surg* 2012; 144: 970-977.

Pirbodaghi T, Weber A, Axiak S, Carrel T, Vandenberghe S. Asymmetric speed modulation of a rotary blood pump affects ventricular unloading. *Eur J Cardiothorac Surg* 2013; 43: 383-388.

Pirbodaghi T, Weber A, Carrel T, Vandenberghe S. Effect of Pulsatility on the Mathematical Modelling of Rotary Blood Pumps. *Artificial Organs* 2011; 35(8): 825-832.

Pirbodaghi T. Mathematical Modelling of Rotary Blood Pumps in a Pulsatile In Vitro Flow Environment. *Artificial Organs* 2017; 41(8): 710-716.

Pironet A, Desaive T, Kosta S, Lucas A, Paeme S, Collet A, Pretty CG, Kolh P, Dauby PC. A multi-scale cardiovascular system model can account for the load-dependence of the end-systolic pressure–volume relationship. *Biomed Eng OnLine* 2013; 12: 8.

Pivkin IV, Richardson PD, Karniadakis G. Blood flow velocity effects and role of activation delay time on growth and form of platelet thrombi. *Proc Natl Acad Sci U S A*. 2006;103:17164 –17169.

Ponder E. The Coefficient of Thermal Conductivity of Blood and of Various Tissues. *J Gen Physiol* 1962; 45: 545-551.

Popovac M, Hanjalic K. Compound Wall Treatment for RANS Computation of Complex Turbulent Flows and Heat Transfer. *J Flow Turbulence and Combustion 2007; 78(2): 177-202*.

Post S. *Applied and Computational Fluid Mechanics*. Jones and Bartlett Publishers; 2011, pp 81-155.

Potapov EV, Loebe M, Nasseri BA, Sinawski H, Koster A, Kuppe H, Noon GP, DeBakey ME, Hetzer R. Pulsatile Flow in Patients with a Novel

Nonpulsatile Implantable Ventricular Assist Device. *Circulation* 2000; 102(Suppl III): III-183-III-187.

Purvis JE, Chatterjee MS, Brass LF, Diamond SL. A molecular signalling model of platelet phosphoinositide and calcium regulation during homeostasis and P2Y1 activation. *Blood*. 2008; 112(10): 4069–4079.

Purvis JE, Radhakrishnan R, Diamond SL. Steady-state kinetic modelling constrains cellular resting states and dynamic behavior. *PLoS Comput Biol*. 2009; 5:1–9.

R

Rao MA (2014) Flow and Functional Models for Rheological Properties of Fluid Foods. In: *Rheology of Fluid, Semisolid, and Solid Foods. Principles and Applications* (Rao MA, ed), pp 27-36. New York: Springer Science + Business Media.

Ratcliffe MB, Bavaria JE, Wenger RK, Bogen DK, Edmunds LH. Left ventricular mechanics of ejecting, postischemic hearts during left ventricular circulatory assistance. *J Thorac Cardiovasc Surg* 1991; 101: 245-255.

Redfield MM, Jacobsen SJ, Borlaug BA, Rodeheffer RJ, Kass DA. Age- and Gender-Related Ventricular-Vascular Stiffening. A Community-Based Study. *Circulation* 2005; 112(15): 2254-2262.

Reininger CB, Lasser R, Rumitz M, Boger C, Schweiberer L. Computational analysis of platelet adhesion and aggregation under stagnation point flow conditions. *Comput Biol Med* 1999, 29(1): 1-18.

Reynolds WC. Fundamentals of turbulence for turbulence modelling and simulation. *Lecture Notes for Von Karman Institute*, Agard Report No. 755, 1987.

Rezaienia MA, Paul G, Avital E, Rahideh A, Rothman MT, Korakianitis T. In-vitro investigation of cerebral-perfusion effects of a rotary blood pump installed in the descending aorta. *J Biomech* 2016; 49: 1865-1872.

Rezaienia MA, Paul G, Avital EJ, Mozafari S, Rothman M, Korakianitis T. In-vitro investigation of the hemodynamic responses of the cerebral, coronary and renal circulations with a rotary blood pump installed in the descending aorta. *Med Eng Phys* 2017; 40: 2-10.

Rezaienia MA, Rahideh A, Hamedani A, Bosak DEM, Zustiak S, Korakianitis T. Numerical and In Vitro Investigation of a Novel Mechanical Circulatory Support Device Installed in the Descending Aorta. *Artificial Organs* 2015; 39(6): 502-513.

Rezaienia MA, Rahideh A, Rothman MT, Sell SA, Mitchell K, Korakianitis T. In Vitro Comparison of Two Different Mechanical Circulatory Support Devices installed in Series and in Parallel. *Artificial Organs* 2014; 38(9): 800-809.

Robertson AM, Sequeira A, Owens RG. Rheological models for blood. In: *Cardiovascular Mathematics. Modelling and simulation of the circulatory system*. Formaggia L, Quarteroni A, Veneziani A eds.; Milano, Springer-Verlag Italia; 2009, pp 211-241.

Rogers JG, Bostic RR, Tong KB, Adamson R, Russo M, Slaughter MS. Cost-effectiveness analysis of continuous-flow left ventricular assist devices as destination therapy. *Circ Heart Fail* 2012; 5(1): 10-16.

Rogers JG, Pagani FD, Tatooles AJ, Bhat G, Slaughter MS, Birks EJ, Boyce SW, Najjar SS, Jeevanandam V, Anderson AS, Gregoric ID, Mallidi H, Leadley K, Aaronson KD, Frazier OH, Milano CA. Intrapericardial Left Ventricular Assist Device for Advanced Heart Failure. *N Engl J Med* 2017; 376: 451-460.

Romano MA, Haft J, Pagani FD. HeartWare HVAD: Principles and Techniques for Implantation. *Oper Tech Thorac Cardiovasc Surg* 2013; 18(3): 230-238.

Rose EA, Gelijns AC, Moskowitz AJ, Heitjan DF, Stevenson LW, Dembitsky W, Long JW, Ascheim DD, Tierney AR, Levitan RG, Watson JT, Meier P, for the Randomized Evaluation of Mechanical Assistance for the Treatment of Congestive Heart Failure (REMATCH) Study Group. Long-Term Use of A Left Ventricular Assist Device For End-Stage Heart Failure. *N Engl J Med* 2001; 345(20): 1435-1443.

Rotta JC.*Turbulente Strömumgen*. 1972, BG Teubner Stuttgart.

Rudman M, Blackburn HM. Direct numerical simulation of turbulent non-Newtonian flow using a spectral element method. *Appl Math Model 2006; 30: 1229-1248*.

Rukhlenko OS, Dudchenko OA, Zlobina KE, Guria GT. Mathematical Modelling of Intravascular Blood Coagulation under Wall Shear Stress. *PLoS One* 2015; 10(7): e0134028.

Rushmer RF, Crystal DK, Wagner C. The functional anatomy of ventricular contraction. *Circ Res* 1953; 1: 162-170.

S

Sagawa K. The Ventricular Pressure-Volume Diagram Revisited. *Circ Res* 1978; 43: 677-687.

Sagawa K. The End-Systolic Pressure-Volume Relation of the Ventricle: Definition, Modifications and Clinical Use. *Circulation* 1981; 63: 1223-1227.

Sagawa K, Maughan L, Suga H, Sunagawa K. Cardiac Contraction and the Pressure-Volume Relationships. Oxford University Press, New York; 1988.

Sagawa K, Suga H, Shoukas AA, Bakalar KM. End-systolic pressure/volume ratio: a new index of ventricular contractility. *Am J Cardiol* 1977; 40: 748-753.

Saito A, Shiono M, Orime Y, Yagi S, Nakata K, Eda K, Hattori T, Funahashi M, Taniguchi Y, Negishi N, Sezai Y. Effects of Left Ventricular Assist Device on Cardiac Function: Experimental Study of Relationship between Pump Flow and Left Ventricular Diastolic Function. *Artificial Organs* 2001; 25: 728-732.

Saito S, Westaby S, Piggot D, Dudnikov S, Robson D, Catarino PA, Clelland C, Nojiri C. End-Organ Function During Chronic Nonpulsatile Circulation. *Ann Thorac Surg* 2002; 74: 1080-1085.

Saito S, Yamazaki K, Nishinaka T, Ichihara Y, Ono M, Kyo S, Nishimura T, Nakatani T, Toda K, Sawa Y, Tominaga R, Tanoue T, Saiki Y, Matsui Y, Takemura T, Niinami H, Matsumiya G; J-MACS Research Group. Post-approval study of a highly pulsed, low-shear-rate, continuous-flow, left ventricular assist device, EVAHEART: a Japanese multicenter study using J-MACS. *J Heart Lung Transplant* 2014; 33: 599-608.

Salamonsen RF, Lim E, Gaddum N, AlOmari A-HH, Gregory SD, Stevens M, Mason DG, Fraser JF, Timms D, Karunanithi MK, Lovell NH. Theoretical Foundations of a Starling-Like Controller for Rotary Blood Pumps. *Artif Organs* 2012; 36(9): 787-796.

Salamonsen RF, Lim E, Mason DG. Applied Physiology of Rotary Blood Pumps: How Robust is the Relationship between Left Ventricular Stroke Work and Speed Pulsatility of the Ventrassist Rotary Blood Pump? *Artificial Organs* 2009; 33: A82.

Salamonsen RF, Mason DG, Ayre PJ. Response of Rotary Blood Pumps to Changes in Preload and Afterload at a Fixed Speed Setting Are Unphysiological When Compared With the Natural Heart. *Artificial Organs 2*011; 35(3): E47-E53.

Saltarocchi S. Simulation in Advanced Heart Failure with a View to Selection and Optimization of Device Therapy. MD Thesis, 2018. Sapienza University, Rome.

Santamore WP, Burkhoff D. Haemodynamic consequences of ventricular interaction as assessed by model analysis. *Am J Physiol Heart Circ Physiol* 1991; 260: H146–H157.

Santamore WP, Gray LA Jr. Left Ventricular Contributions to Right Ventricular Systolic Function During LVAD Support. *Ann Thorac Surg* 1996; 61: 350-356.

Santamore WP, Meier GD, Bove AA. Effects of hemodynamic alterations on wall motion in the canine right ventricle. *Am J Physiol Heart Circ Physiol* 1979; 236: H254-H262.

Sarnoff SJ, Mitchell JH. The regulation of the performance of the heart. *Am J Med* 1961; 30: 747-771.

Sato T, Shishido T, Kawada T, Miyano H, Miyashita H, Inagaki M, Sugimachi M, Sunagawa K. ESPVR of in situ rat left ventricle shows contractility-dependent curvilinearity. *Am J Physiol* 1998; 274(5): H1429-H1434.

Schima H, Trubel W, Moritz A, Wieselthaler G, Stohr HG, Thoma H, Losert U, Wolner E. Noninvasive Monitoring of Rotary Blood Pumps: Necessity, Possibilities and Limitations. *Artificial Organs* 1992; 16(2): 195-202.

Schlendorf K, Patel CB, Gehrig T, Kiefer TL, Felker GM, Hernandez AF, Blue LJ, Milano CA, Rogers JG. Thrombolytic Therapy for Thrombosis of Continuous Flow Ventricular Assist Devices. *J Cardiac Fail* 2014; 20: 91-97.

Schmid Daners M, Kaufmann F, Amacher R, Ochsner G, Wilhelm MJ, Ferrari A, Mazza E, Poulikakos D, Meboldt M, Falk V. Left Ventricular Assist Devices: Challenges Toward Sustaining Long-Term Patient Care. *Ann Biomed Eng* 2017; 45(8): 1836-1851.

Schumer EM, Black MC, Monreal G, Slaughter MS. Left ventricular assist devices: current controversies and future directions. *Eur Heart J* 2016; 37: 3434-3439.

Segers P, Steendijk P, Stergiopulos N, Westerhof N. Predicting systolic and diastolic aortic pressure and stroke volume in the intact sheep. *J Biomech* 2001; 34: 41-50.

Segers P, Stergiopulos N, Westerhof N. Quantification of the contribution of cardiac and arterial remodeling to hypertension. *Hypertension* 2000; 36: 760-765.

Selmi M, Chiu W-C, Chivukula VK, Melisurgo G, Beckman JA, Mahr C, Aliseda A, Votta E, Redaelli A, Slepian MJ, Bluestein D, Pappalardo F, Consolo F. Blood damage in Left Ventricular Assist Devices: Pump thrombosis or system thrombosis? *Int J Artif Organs* 2019; 42(3): 113-124.

Senzaki H, Chen C-H, Kass DA. Single-Beat Estimation of End-Systolic Pressure-Volume Relation in Humans. A New Method With the Potential for Noninvasive Application. *Circulation* 1996; 94: 2497-2506.

Sequeira A, Janela J. An Overview of Some Mathematical Models of Blood Rheology. In: *A Portrait of State-of-the-Art Research at the Technical University of Lisbon*. Pereira MS ed.; Springer; 2007a, pp 65-87.

Sequeira A, Janela JP. A note on computational blood rheology. *Proc Appl Math Mech* 2007b; 7: 1101207-1101208.

Sequeira A, Santos RF, Bodnar T. Blood coagulation dynamics: mathematical modelling and stability results. *Math Biosc Eng* 2011; 8(2): 425-43.

Sharp M, Mohammad F. Scaling of haemolysis in needles and catheters. *Ann Biomed Eng* 1998; 26: 788-797.

Sheikh FH, Russell SD. HeartMate II continuous-flow left ventricular assist system. *Expert Rev Med Devices* 2011; 8: 11-21.

Shepard RB, Simpson DC, Sharp JF. Energy equivalent pressure. *Arch Surg* 1966; 93: 730-740.

Sheriff J, Soares JS, Xenos M, Jesty J, Bluestein D. Evaluation of Shear-Induced Platelet Activation Models Under Constant and Dynamic Shear Stress Loading Conditions Relevant to Devices. *Ann Biomed Eng* 2013; 41(6): 1279-1296.

Sheriff J, Soares JS, Xenos M, Jesty J, Bluestein D. Evaluation of Shear-Induced Platelet Activation Models Under Constant and Dynamic Shear Stress Loading Conditions Relevant to Devices. *Annals of Biomedical Engineering 2013; 41(6): 1279-1296*.

Sheriff JF. Shear-Induced Platelet Sensitization and the Development of an Activation Model. *PhD Thesis,* Stony Brook University, December 2010.

Shi Y, Brown AG, Lawford PV, Arndt A, Nuesser P, Hose DR. Computational modelling and evaluation of cardiovascular response under pulsatile impeller pump support. *Interface Focus* 2011a; 1: 320-337.

Shi Y, Brown1 AG, Lawford PV, Arndt A, Nuesser P, Hose D. Computational modelling and evaluation of cardiovascular response under pulsatile impeller pump support. *Interface Focus* 2011; 1: 320-337.

Shi Y, Korakianitis T, Bowles C. Numerical simulation of cardiovascular dynamics with different types of VAD assistance. *J Biomech* 2007; 40: 2919-2933.

Shi Y, Korakianitis T. Impeller-pump model derived from conservation laws applied to the simulation of the cardiovascular system coupled to heart-assist pumps. *Comput Biol Med* 2018; 93: 127-138.

Shi Y, Korakianitis T. Numerical Simulation of Cardiovascular Dynamics With Left Heart Failure and In-series Pulsatile Ventricular Assist Device. *Artificial Organs* 2006; 30(12): 929-948.

Shi Y, Lawford PV, Hose DR. Numerical Modeling of Hemodynamics with Pulsatile Impeller Pump Support. *Ann Biomed Eng* 2010; 38(8): 2621-2634.

Shi Y, Lawford P, Hose R. Review of zero-D and 1-D models of blood flow in the cardiovascular system. *BioMed Eng OnLine* 2011; 10: 33.

Shi Y, Shi Y, Korakianitis T. Physiological control of an in-series connected pulsatile VAD: numerical simulation study. *Comput Methods Biomech Biomed Eng* 2011b; 14(11): 995-1007.

Shibeshi SS and Collins WE. The Rheology of Blood Flow in a Branched Arterial System. *Appl Rheol 2005; 15(6): 398-405.*

Shih TH, Liou WW, Shabbir A, Yang Z, Zhu J. A New *k-ε* Eddy-Viscosity Model for High Reynolds Number Turbulent Flows - Model Development and Validation. *Comput Fluids* 1995; 24(3): 227-238.

Shroff SG, Janicki JS, Weber KT. Left ventricular systolic dynamics in terms of its chamber mechanical properties. *Am J Physiol Heart Circ Physiol* 1983; 245(1): H110-H124.

Shroff SG, Janicki JS, Weber KT. Evidence and quantitation of left ventricular systolic resistance. *Am J Physiol Heart Circ Physiol* 1985; 249: H358-H370.

Shu F, Vandenberghe S, Antaki F. The Importance of dQ/dt on the Flow Field in a Turbodynamic Pump With Pulsatile Flow. *Artificial Organs* 2009; 33(9): 757-762.

Sidhu K, Lam PH, Mehra MR. Evolving trends in mechanical circulatory support: Clinical development of a fully magnetically levitated durable ventricular assist device. *Trends Cardiovasc Med* 2020; 30: 223-229.

Siess T, Reul H. Basic Design Criteria for Rotary Blood Pumps. In: *Rotary Blood Pumps. New Developments and Current Applications*. Matsuda H ed.; Tokyo, Springer-Verlag; 2000, pp 69-83.

Simaan MA, Ferreira A, Chen S, Antaki J, Galati D. A Dynamical State-Space Representation and Performance Analysis of A Feedback-Controlled Rotary Left Ventricular Assist Device. *IEEE Trans Control Syst Technol* 2009; 17(1): 15-28.

Slaughter MS, Myers TJ. Transcutaneous Energy Transmission for Mechanical Circulatory Support Systems: History, Current Status, and Future Prospects. *J Card Surg* 2010; 25: 484-489.

Slaughter MS, Pagani FD, McGee EC, Birks EJ, Cotts WG, Gregoric I, Frazier OH, Icenogle T, Najjar SS, Boyce SW, Acker MA, John R, Hathaway DR, Najarian KB, Aaronson KD; HeartWare Bridge to Transplant ADVANCE Trial Investigators. HeartWare ventricular assist system for bridge to transplant: combined results of the bridge to transplant and continued access protocol trial. *J Heart Lung Transplant* 2013; 32: 675-683.

Slaughter MS, Rogers JG, Milano CA, Russell SD, Conte JV, Feldman D, Sun B, Tatooles AJ, Delgado RM III, Long JW, Wozniak TC, Ghumman W, Farrar DJ, Frazier OH et al. Advanced Heart Failure Treated with Continuous-Flow Left Ventricular Assist Device. *N Engl J Med* 2009; 361: 2241-2251.

Slaughter MS, Silver MA, Farrar DJ, Tatooles AJ, Pappas PS. A New Method of Monitoring Recovery and Weaning the Thoratec Left Ventricular Assist Device. *Ann Thorac Surg* 2001; 71: 215-218.

Smagorinsky J. General Circulation Experiments with the Primitive Equations. *Monthly Weather Review* 1963; 91: 99–165.

Smirnov PE, Menter FR. Sensitization of the SST Turbulence Model to Rotation and Curvature by Applying the Spalart-Shur Correction Term. *J Turbomachinery* 2009; 131: 041010-1 – 041010-8.

Smith BW, Chase JG, Nokes RI, Shaw GM, David T. Velocity profile method for time varying resistance in minimal cardiovascular system models. *Phys Med Biol* 2003; 48: 3375–3387.

Smith BW, Chase JG, Nokes RI, Shaw GM, Wake G. Minimal haemodynamic system model including ventricular interaction and valve dynamics. *Med Eng Phys* 2004; 26: 131–139.

Soares JS, Pasta S, Vorp DA, Moore JE Jr. Modelling in cardiovascular biomechanics. *Int J Eng Science* 2010; 48: 1563-1575.

Song X, Throckmorton AL, Wood HG, Allaire PE, Olsen DB. Transient and Quasi-Steady Computational Fluid Dynamics Study of a Left Ventricular Assist Device. *ASAIO J* 2004a; 50: 410-417.

Song X, Untaroiu A, Wood HG, Allaire PE, Throckmorton AL, Day SW, Olsen DB. Design and Transient Computational Fluid Dynamics Study of a Continuous Flow Ventricular Assist Device. *ASAIO J* 2004b; 50: 215-224.

Song X, Wood HG, Day SW, Olsen DB. Studies of Turbulence Models in a Computational Fluid Dynamics Model of a Blood Pump. *Artificial Organs* 2003a; 27(10): 935-937.

Song X, Wood HG, Olsen DB. Transient Computational Fluid Dynamics Study of an Axial Blood Pump. *ASAIO J* 2003b; 49: 144.

Sonnenblick EH. Force-velocity relations in mammalian heart muscle. *Am J Physiol* 1962; 202(5): 931-939.

Sorensen EN, Burgreen GW, Wagner WR, Antaki JF. Computational simulation of platelet deposition and activation: I. Model development and properties. *Ann Biomed Eng* 1999a, 27(4): 436-448.

Sorensen EN, Burgreen GW, Wagner WR, Antaki JF. Computational simulation of platelet deposition and activation: II. Results for Poiseuille flow over collagen. *Ann Biomed Eng* 1999b, 27(4): 449-458.

Soucy KG, Giridharan GA, Choi Y, Sobieski MA, Monreal G, Cheng A, Schumer E, Slaughter MS, Koenig SC. Rotary pump speed modulation for generating pulsatile flow and phasic left ventricular volume unloading in a bovine model of chronic ischemic heart failure. *J Heart Lung Transplant* 2015; 34: 122-131.

Soucy KG, Koenig SC, Giridharan GA, Sobieski MA, Slaughter MS. Rotary pumps and diminished pulsatility: do we need a pulse? *ASAIO J* 2013; 59: 355-366.

Spalart PR. Strategies for turbulence modelling and simulations. *Int J Heat Fluid Flow* 2000; 21: 2.

Spronk HMH, Govers-Riemslag JWP, ten Cate H. The blood coagulation system as a molecular machine. *BioEssays* 2003; 25: 1220-1228.

Starling RC, Moazami N, Silvestry SC, Ewald G, Rogers JG, Milano CA, Rame JE, Acker MA, Blackstone EH, Ehrlinger J, Thuita L, Mountis MM, Soltesz EG, Lytle BW, Smedira NG. Unexpected Abrupt Increase in Left Ventricular Assist Device Thrombosis. *N Engl J Med 2014; 370: 33-40*.

Stephens AF, Stevens MC, Gregory SD, Kleinheyer M, Salamonsen RF. In Vitro Evaluation of an Immediate Response Starling-Like Controller for Dual Rotary Blood Pumps. *Artificial Organs* 2017; 41(10): 911-922.

Stergiopulos N, Meister JJ, Westerhof N. Determinants of stroke volume and systolic and diastolic aortic pressure. *Am J Physiol Heart Circ Physiol* 1996; 270: H2050-H2059.

Stewart SFC, Day S, Burgreen GW, Paterson EG, Manning KB, Hariharan P, Deutsch S, Giarra M, Cheek C, Reddy V, Berman MR, Myers MR, Malinauskas RA. Preliminary Results of FDA'S "Critical Path" Project to Validate Computational Fluid Dynamic Methods used in Medical Device Evaluation. *ASAIO J* 2009; 55(2): 173.

Storm C, Pastore JJ, MacKintosh FC, Lubensky TC, Janmey PA. Nonlinear elasticity in biological gels. *Nature* 2005; 435: 191-194.

Strueber M, O'Driscoll G, Jansz P, Khaghani A, Levy WC, Wieselthaler GM et al. Multicenter Evaluation of an Intrapericardial Left Ventricular Assist System. *J Am Coll Cardiol* 2011; 57: 1375-1382.

Stulak JM, Sharma S, Maltais S. Management of Pump Thrombosis in Patients with Left Ventricular Assist Devices. *Am J Cardiovasc Drugs* 2015; 15(2): 89-94.

Su JB, Crozatier B. Preload-induced curvilinearity of left ventricular end-systolic pressure-volume relations. Effects on derived indexes in closed-chest dogs. *Circulation* 1989; 79: 431-440.

Suga H. Theoretical Analysis of a Left-Ventricular Pumping Model Based on the Systolic Time-Varying Pressure/Volume Ratio. *IEEE Trans Biomed Eng* 1971; 18(1): 47-55.

Suga H, Hayashi T, Shirahata M, Ninomiya I. Critical Evaluation of Left Ventricular Systolic Pressure Volume Area as Predictor of Oxygen Consumption Rate. *Jpn J Physiol* 1980b; 30: 907-919.

Suga H, Hisano R, Goto Y, Yamada O. Normalization of end-systolic pressure-volume relation and E_{max} of different sized hearts. *Jpn Circ J* 1984; 48: 136-143.

Suga H, Hisano R, Goto Y, Yamada O, Igarashi Y. Effect of Positive Inotropic Agents on the Relation between Oxygen Consumption and Systolic Pressure Volume Area in Canine Left Ventricle. *Circ Res* 1983; 53: 306-318.
Suga H, Kitabatake A, Sagawa K. End-systolic pressure determines stroke volume from fixed end-diastolic volume in the isolated canine left ventricle under a constant contractile state. *Circ Res* 1979; 44: 238-249.

Suga H, Sagawa K. Mathematical interrelationship between instantaneous ventricular pressure–volume ratio and myocardial force–velocity relation. *Ann Biomed Eng* 1972; 1: 160–181.

Suga H, Sagawa K, Demer L. Determinants of Instantaneous Pressure in Canine Left Ventricle. Time and Volume Specification. *Circ Res* 1980a; 46: 256-263.

Suga H, Sagawa K, Kostiuk DP. Controls of ventricular contractility assessed by pressure-volume ratio, E_{max}. *Cardiovasc Res* 1976; 10: 582-592.

Suga H, Sagawa K, Shoukas AA. Load Independence of the Instantaneous Pressure-Volume Ratio of the Canine Left Ventricle and Effects of Epinephrine and Heart Rate on the Ratio. *Circ Res* 1973; 32: 314-322.

Suga H, Sagawa K. Instantaneous Pressure-Volume Relationships and Their Ratio in the Excised, Supported Canine Left Ventricle. *Circ Res* 1974; 35: 117-126.

Suga H, Yamada O, Goto Y, Igarashi Y. Peak isovolumic pressure-volume relation of puppy left ventricle. *Am J Physiol* 1986; 250(2): H167-H172.

Suga H, Yamakoshi K-I. Effects of Stroke Volume and Velocity of Ejection on End-Systolic Pressure of Canine Left Ventricle. End-Systolic Volume Clamping. *Circ Res* 1977; 40: 445-450.

Suga H. Cardiac energetics: from $E_{(max)}$ to pressure-volume area. *Clin Exp Pharmacol Physiol* 2003; 30: 580-585.

Sun Y. Modeling the dynamic interaction between left ventricle and intra-aortic balloon pump. *Am J Physiol Heart Circ Physiol* 1991; 261: H1300-H1311.

Sunagawa K, Burkhoff D, Lim KO, Sagawa K. Impedance loading servo pump system for excised canine ventricle. *Am J Physiol Heart Circ Physiol* 1982; 243: H346-H350.

Sunagawa K, Maughan WL, Burkhoff D, Sagawa K. Left ventricular interaction with arterial load studied in isolated canine ventricle. *Am J Physiol Heart Circ Physiol* 1983; 245: H773-H780.

Sunagawa K, Maughan WL, Sagawa K. Optimal arterial resistance for the maximal stroke work studied in isolated canine left ventricle. *Circ Res* 1985; 56(4): 586-595.

Sunagawa K, Sagawa K, Maughan WL. Ventricular Interaction with the Loading System. *Ann Biomed Eng* 1984; 12: 163-189.

Sutton JP, Ho SY, Anderson RH. The forgotten interleaflet triangles: a review of the surgical anatomy of the aortic valve. *Ann Thorac Surg* 1995; 59(2): 419-427.

Szycher M, Clay W, Gernes D, Sherman C. Thermedics' Approach to Ventricular Support Systems. *J Biomater Appl* 1986; 1: 39-105.

T

Takeuchi M, Igarashi Y, Tomimoto S, Odake M, Hayashi T, Tsukamoto T, Hata K, Takaoka H, Fukuzaki H. Single-beat estimation of the slope of the end-systolic pressure-volume relation in the human left ventricle. *Circulation* 1991; 83: 202-212.

Taylor CA, Figueroa CA. Patient-specific Modelling of Cardiovascular Mechanics. *Annu Rev Biomed Eng* 2009; 11: 109-134.

Taylor CA, Fonte TA, Min JK. Computational Fluid Dynamics Applied to Cardiac Computed Tomography for Noninvasive Quantification of Fractional Flow Reserve. *J Am Coll Cardiol* 2013; 61(22): 2233-2241.

Taylor CA, Steinman DA. Image-based modeling of blood flow and vessel wall dynamics: applications, methods and future directions. *Ann Biomed Eng* 2010; 38: 1188-1203.

Taylor JO, Witmer KP, Neuberger T, Craven BA, Meyer RS, Deutsch S, Manning KB. In Vitro Quantification of Time Dependent Thrombus Size Using Magnetic Resonance Imaging and Computational Simulations of Thrombus Surface Shear Stresses. *J Biomech Eng* 2014; 136: 071012-1-071012-11.

Tchantchaleishvili V, Luc JGY, Cohan CM, Phan K, Hübbert L, Day SW, Massey HT. Clinical Implications of Physiologic Flow Adjustment in Continuous-Flow Left Ventricular Assist Devices. *ASAIO J* 2017; 63: 240-250.

Thaker R, Araujo-Gutierrez R, Marcos-Abdala HG, Agrawal T, Fida N, Kassi M. Innovative Modelling Techniques and 3D Printing in Patients with Left Ventricular Assist Devices: A Bridge from Bench to Clinical Practice. *J Clin Med* 2019; 8: 635: 1-9.

Throckmorton AL, Tahir SA, Lopes SP, Rangus OM, Sciolino MG. Steady and Transient Flow Analysis of a Magnetically Levitated Pediatric VAD: Time Varying Boundary Conditions. *Int J Artif Organs* 2013; 36(10): 693-699.

Throckmorton AL, Untaroiu A. CFD analysis of a mag-lev ventricular assist device for infants and children: fourth generation design. *ASAIO J* 2008; 54: 423-431.

Tokarev AA, Butylin AA, Ataullakhanov FI. Platelet Adhesion from Shear Blood Flow Is Controlled by Near-Wall Rebounding Collisions with Erythrocytes. *Biophys J* 2011a; 100: 799-808.

Tokarev AA, Butylin AA, Ermakova EA, Shnol EE, Panasenko GP, Ataullakhanov FI. Finte Platelet Size Could Be Responsible for Platelet Margination Effect. *Biophys J* 2011b; 101: 1835-1843.

Tonino PA, De Bruyne B, Pijls NH, et al. Fractional flow reserve versus angiography for guiding percutaneous coronary intervention. *N Engl J Med* 2009; 360: 213-224.

Tonino PA, Fearon WF, De Bruyne B, et al. Angiographic versus functional severity of coronary artery stenoses in the FAME study: Fractional Flow Reserve Versus Angiography in Multivessel Evaluation. *J Am Coll Cardiol* 2010; 55: 2816-21.

Topper SR, Navitsky MA, Medvitz RB, Paterson EG, Siedlecki CA, Slattery MJ, Deutsch S, Rosenberg G, Manning KB. The Use of Fluid Mechanics to Predict Regions of Microscopic Thrombus Formation in Pulsatile VADs. *Cardiovasc Eng Technol* 2014; 5(1): 54-69.

Tosenberger A, Ataullakhanov F, Bessonov N, Panteleev M, Tokarev A, Volpert V. Modelling of thrombus growth and growth stop in flow by the method of dissipative particle dynamics. *Russian J Num Analysis Math Model* 2012; 27: 507-522.

Tosenberger A, Ataullakhanov F, Bessonov N, Panteleev M, Tokarev A, Volpert V. Modelling of thrombus growth in flow with DPD-PDE method. *J Theor Biol* 2013; 337: 30-41.

Tosenberger A, Ataullakhanov F, Bessonov N, Panteleev M, Tokarev A, Volpert V. Modelling of platelet-fibrin clot formation in flow with a DPD-PDE method. *J Math Biol* 2016; 72(3): 649-681.

Tosenberger A, Bessonov N, Volpert V. Influence of fibrinogen deficiency on clot formation in flow by hybrid model. *Math Model Nat Phenomena* 2015; 10: 36-47.

Triep M, Brücker C, Schröeder W, Siess T. Computational Fluid Dynamics and Digital Particle Image Velocimetry Study of the Flow Through an Optimized Micro-axial Blood Pump. *Artificial Organs* 2006; 30(5): 384-391.

Truskey GA, Yuan F, Katz DF (2010) Conservation Relations for Fluid Transport, Dimensional Analysis, and Scaling. In: *Transport Phenomena in Biological Systems* (Truskey GA, Yuan F, Katz DF, eds), pp 146-195. New Jersey: Pearson Education, Inc.

Tuzun E, Roberts K, Cohn WE, Sargin M, Gemmato CJ, Radovancevic B, Frazier OH. In Vivo Evaluation of the HeartWare Centrifugal Ventricular Assist Device. *Tex Heart Inst J* 2007; 34: 406-411.

U

Ündar A, Eichstaedt HC, Masai T, Yang S-Q, Bigley JE, McGarry MC, Mueller M, Vaughn WK, Fraser CD. Comparison of six pediatric cardiopulmonary bypass pumps during pulsatile and nonpulsatile perfusion. *J Thorac Cardiovasc Surg* 2001; 122: 827-829.

Ündar A, Frazier OH, Fraser CD Jr. Defining pulsatile perfusion: quantification in terms of energy equivalent pressure. *Artificial Organs* 1999; 23: 712-716.

Ündar A, Myers JL. Arterial pressure and pump flow rate during chronic pulsatile and non-pulsatile cardiac support. *Ann Thorac Surg* 2005b; 79(3): 1093-1094.

Ündar A, Zapanta CM, Reibson JD, Souba M, Lukic B, Weiss WJ, Snyder AJ, Kunselman AR, Pierce WS, Rosenberg G, Myers JL. Precise Quantification of Pressure Flow Waveforms of a Pulsatile Ventricular Assist Device. *ASAIO J* 2005a; 51: 56-59.

Ündar A. Fundamentals of pulsatile versus nonpulsatile flow during chronic support. *ASAIO J* 2003; 49: 139-140.

Ündar A. Myths and Truths of Pulsatile and Nonpulsatile Perfusion During Acute and Chronic Cardiac Support. *Artificial Organs* 2004; 28(5): 439-443.

Ündar A. The ABCs of research on pulsatile versus nonpulsatile perfusion during cardiopulmonary bypass. *Med Sci Monit* 2002; 8: ED21-ED24.

Untaroiu A, Wood HG, Allaire PE, Throckmorton AL, Day S, Patel SM, Ellman P, Tribble C, Olsen DB. Computational design and experimental testing of a novel axial flow LVAD. *ASAIO J* 2005; 51: 702-710.

Uriel N, Colombo PC, Cleveland JC, Long JW, Salerno C, Goldstein DJ, Patel CB, Ewald GA, Tatooles AJ, Silvestry SC, John R, Caldeira C, Jeevanandam V, Boyle AJ, Sundareswaran KS, Sood P, Mehra MR. Hemocompatibility-Related Outcomes in the MOMENTUM 3 Trial at 6 Months. A randomized Controlled Study of a Fully Magnetically Levitated Pump in Advanced Heart Failure. *Circulation* 2017; 135: 2003-2012.

Uriel N, Morrison KA, Garan AR, Kato TS, Yuzefpolskaya M, Latif F, Restaino SW, Mancini DM, Flannery M, Takayama H, John R, Colombo PC, Naka Y, Jorde UP. Development of a Novel Echocardiography Ramp Test for Speed Optimisation and Diagnosis of Device Thrombosis in Continuous-Flow Left Ventricular Assist Devices: The Columbia Ramp Study. *J Am Coll Cardiol* 2012; 60(18): 1764-1775.

Ursino M. Interaction between carotid baroregulation and the pulsating heart: a mathematical model. *Am J Physiol* 1998; 275: 1733-1747.

Usik TP, Mazhari R, McCulloch AD. Effect of Laminar Orthotropic Myofibre Architecture on Regional Stress and Strain in the Canine Left Ventricle. *J Elasticity* 2000; 61: 143-164.

V

van den Horn GJ, Westerhof N, Elzinga G. Interaction of heart and arterial system. *Ann Biomed Eng* 1984; 12: 151-162.

van den Horn GJ, Westerhof N, Elzinga G. Optimal Power Generation by the Left Ventricle. A Study in the Anesthetized Open Thorax Cat. *Circ Res* 1985; 56: 252-261.

van den Horn GJ, Westerhof N, Elzinga G. Feline left ventricle does not always operate at optimum power output. *Am J Physiol Heart Circ Physiol* 1986; 250: H961-H967.

van der Velde ET, Burkhoff D, Steendijk P, Karsdon J, Sagawa K, Baan J. Nonlinearity and load sensitivity of end-systolic pressure-volume relation of canine left ventricle in vivo. *Circulation* 1991; 83: 315-327.

Van Roon AM, Mulder LJM, Althaus M, Mulder G. Introducing a baroreflex model for studying cardiovascular effects on mental workload. *Psychophysiology* 2004; 41: 961-981.

Vandenberghe S, Segers P, Antaki JF, Meyns B, Verdonck PR. Haemodynamic Modes of Ventricular Assist with a Rotary Blood Pump: Continuous, Pulsatile and Failure. *ASAIO J* 2005; 51: 711-718.

Vandenberghe S, Segers P, Meyns B, Verdonck PR. Effect of Rotary Blood Pump Failure on Left Ventricular Energetics Assessed by Mathematical Modelling. *Artificial Organs* 2002; 26(12): 1032-1039.

Vandenberghe S, Segers P, Meyns B, Verdonck PR. Unloading Effect of a Rotary Blood Pump Assessed by Mathematical Modelling. *Artificial Organs* 2003; 27(12): 1094-1101.

Vandenberghe S, Segers P, Steendijk P, Meyns B, Dion RAE, Antaki JF, Verdonck P. Modeling Ventricular Function during Cardiac Assist: Does Time-Varying Elastance Work? *ASAIO J* 2006; 52: 4-8.

Vandenberghe S, Segers P, Verdonck P. Mathematical Modelling of Ventricular Assist Devices. In: *Cardiac Perfusion and Pumping Engineering*. Ghista DN, Ng EY-K eds. World Scientific Publishing Co. Pte. Ltd. Singapore; 2007, pp 419-475.

Versteeg HK, Malalasekera W. *An Introduction to Computational Fluid Dynamics. The Finite Volume Method*. Pearson Education Limited; 2007, pp 285-303.

Vlachopoulos C, Mcdonald P, Spratt P, O'Rourke M. Pulse Wave Analysis in the Assessment of Patients with Left Ventricular Assist Device. *J Heart Lung Transplant* 2001; 20: 98-102.

Vollkron M, Schima H, Huber L, Benkowski R, Morello G, Wieselthaler G. Advanced Suction Detection for an Axial Flow Pump. *Artificial Organs* 2006; 30(9): 665-670.

Vollkron M, Schima H, Huber L, Wieselthaler G. Interaction of the cardiovascular system with an implanted rotary assist device: simulation study with a refined computer model. *Artificial Organs* 2002; 26: 349-359.

Voronov RS, Stalker TJ, Brass LF, Diamond SL. Simulation of Intrathrombus Fluid and Solute Transport Using *In Vivo* Clot Structures with Single Platelet Resolution. *Ann Biomed Eng* 2013; 41(6): 1297-1307.

Vreman AW, Kuerten JGM. Comparison of direct numerical simulation databases of turbulent channel flow at Re_τ = 180. *Phys Fluids* 2014; 26: 015102.

Vukicevic M, Chiulli JA, Conover T, Pennati G, Hsia TY, Figliola RS. Mock Circulatory System of the Fontan Circulation to Study Respiration Effects on Venous Flow Behavior. *Comput Methods Appl Mech Eng* 2013; 59(3): 253-260.

W

Wallin S, Johansson AV. An explicit algebraic Reynolds stress model for incompressible and compressible turbulent flows. *J Fluid Mech* 2000; 403: 89-132.

Wang J, Slattery MJ, Hoskins MH, Liang S, Dong C, Du Q. Monte Carlo simulation of heterotypic cell aggregation in nonlinear shear flow. *Math Biosci Eng*. 2006; 3: 683– 696.

Wang W, King MR. Multiscale Modeling of Platelet Adhesion and Thrombus Growth. *Ann Biomed Eng* 2012; 40(11): 2345-2354.

Wang Y, Loghmanpour N, Vandenberghe S, Ferreira A, Keller B, Gorcsan J, Antaki J. Simulation of dilated heart failure with continuous flow circulatory support. *PLoS ONE* 2014; 9(1): e85234.

Weber KT, Janicki JS, Reeves RC, Hefner LL, Reeves TJ. Determinants of stroke volume in the isolated canine heart. *J Appl Physiol* 1974; 37(5): 742-747.

Weisel JW, Nagaswami C. Computer modelling of fibrin polymerisation kinetics correlated with electron microscope and turbidity observations: clot structure and assembly are kinetically controlled. *Biophys J* 1992; 63: 111-128.

Weisel JW. Biomechanics in hemostasis and thrombosis. *J Thrombosis Haemostasis* 2010; 8: 1027-1029.

Westerhof N, Stergiopulos N, Noble MIM. Snapshots of Hemodynamics. An Aid for Clinical Research and Graduate Education. Second Edition, Springer; 2010.

Wiegmann L, Boës S, de Zélicourt D, Thamsen B, Schmid Daners M, Meboldt M, Kurtcuoglu V. Blood Pump Design Variations and Their Influence on Hydraulic Performance and Indicators of Hemocompatibility. *Ann Biomed Eng* 2018; 46(3): 417-428.

Wieselthaler GM, O'Driscoll G, Jansz P, Khaghani A, Strueber M et al. Initial clinical experience with a novel left ventricular assist device with a magnetically levitated rotor in a multi-institutional trial. *J Heart Lung Transplant* 2010; 29: 1218-1225.

Wilcox DC. Formulation of the k-omega Turbulence Model Revisited. *AIAA J* 2008; 46(11): 2823-2838.

Wilcox DC. *Turbulence modelling for CFD*. DCW Industries, Inc. La Canada, California; 1998.

Wilson SR, Givertz MM, Stewart GC, Mudge GH Jr. Ventricular Assist Devices. The Challenges of Outpatient Management. *J Am Coll Cardiol* 2009; 54: 1647-1659.

Withington PS, Graham TR, Allan A, Marrinan MT, Lewis CT. In vitro evaluation of an implantable left ventricular assist device. *J Med Eng Technol* 1991; 15: 68-71.

Wood HG, Throckmortom AL, Untaroiu A, Song X. The medical physics of ventricular assist devices. *Rep Prog Phys* 2005; 68: 545-576.

Wright G. Hemodynamic analysis could resolve the pulsatile blood flow controversy. *Ann Thorac Surg* 1994; 58: 1199-1204.

Wright G. Mechanical simulation of cardiac function by means of pulsatile blood pumps. *J Cardiothorac Vasc Anesth* 1997; 11: 299-309.

Wu J, Antaki JF, Wagner WR, Snyder TA, Paden BE, Borovetz HS. Elimination of Adverse Leakage Flow in a Miniature Pediatric Centrifugal Blood Pump by Computational Fluid Dynamics-Based Design Optimization. *ASAIO J* 2005; 51(5): 636-643.

Wu J, Paden BE, Borovetz HS, Antaki JF. Computational Fluid Dynamics Analysis of Blade Tip Clearances on Haemodynamic Performance and Blood Damage in a Centrifugal Ventricular Assist Device. *Artif Organs* 2010; 34: 402-411.

Wu J, Yun BM, Fallon AM, Hanson SR, Aidun CK, Yoganathan AP. Numerical Investigation of the Effects of Channel Geometry on Platelet Activation and Blood Damage. *Ann Biomed Eng* 2011; 39(2): 897-910.

Wu W-T, Jamiolkowski MA, Wagner WR, Aubry N, Massoudi M, Antaki JF. Multi-Constituents Simulation of Thrombus Deposition. *Sci Rep* 2017; 7: 42720 DOI: 10.1038/srep42720.

Wu W-T, Yang F, Wu J, Aubry N, Massoudi M, Antaki JF. High fidelity computational simulation of thrombus formation in Thoratec HeartMate II continuous flow ventricular assist device. *Sci Rep* 2016; 6: 38025 DOI: 10.1038/srep38025.

Wu Z, Xu Z, Kim O, Alber M. Three-dimensional multi-scale model of deformable platelets adhesion to vessel wall in blood flow. *Phil Trans R Soc A* 2014; 372: 201300380.

Wu ZJ, Gottlieb RK, Burgreen GW, Holmes JA, Borzelleca DC, Kameneva MV, Griffith BP, Antaki JF. Investigation of fluid dynamics within a miniature mixed flow blood pump. *Exp Fluids* 2001; 31(6): 615-629.

X

Xenos M, Girdhar G, Alemu Y, Jesty J, Slepian M, Einav S, Bluestein D. Device Thrombogenicity Emulator (DTE) – Design optimization methodology for cardiovascular devices: A study in two bileaflet MHV designs *J Biomech* 2010; 43: 2400-2409.

Xu Z, Chen N, Kamocka MM, Rosen ED, Alber M. A multiscale model of thrombus development. *J Royal Soc Interface* 2008; 5: 705-722.

Xu Z, Chen N, Shadden SC, Marsden JE, Kamocka MM, Rosen ED, Alber M. Study of blood flow impact on growth of thrombi using a multiscale model. *Soft Matter* 2009; 5: 769-779.

Xu Z, Christley S, Lioi J, Kim O, Harvey C, Sun W, Rosen ED, Alber M. Multiscale model of fibrin accumulation on the blood clot surface and platelet dynamics. *Methods Cell Biol* 2012; 110: 367-388.

Xu Z, Kamocka M, Alber M, Rosen ED. Computational Approaches to Studying Thrombus Development. *Arterioscler Thromb Vasc Biol* 2011; 31: 500-505.

Xu Z, Kim O, Kamocka M, Rosen ED, Alber M. Multiscale models of Thrombogenesis. *WIREs Syst Biol Med* 2012; doi: 10.1002/wsbm.116.

Xu Z, Lioi J, Mu J, Kamocka MM, Liu X, Chen DZ, Rosen ED, Alber M. A multiscale model of venous thrombus formation with surface-mediated control of blood coagulation cascade. *Biophys J* 2010; 98: 1723-1732.

Y

Yakhot V, Orszag SA, Thangam S, Gatski TB, Speziale CG. Development of turbulence models for shear flows by a double expansion technique. *Phys Fluids A* 1992; 4(7): 1510-1520.

Yakhot V, Orszag SA. Renormalization Group Analysis of Turbulence I Basic Theory. *J Sci Comput* 1986; 1(1): 1-51.

Yamaguchi T, Ishikawa T, Imai Y, Matsuki N, Xenos M, Deng Y, Bluestein D. Particle-Based Methods for Multiscale Modelling of Blood Flow in the Circulation and in Devices: Challenges and Future Directions. *Ann Biomed Eng* 2010; 38(3): 1225-1235.

Yang F, Kormos RL, Antaki JF. High-speed visualization of disturbed pathlines in axial flow ventricular assist device under pulsatile conditions. *J Thorac Cardiovasc Surg* 2015; 150: 938-944.

Yang Z, Mochalkin I, Doolittle RF. A model of fibrin formation based on crystal structures of fibrinogen and fibrin fragments complexed with synthetic peptides. *Proc Natl Acad Sci U S A*. 2000; 97: 14156 –14161.

Yang Q, Zimmerman J, Steinfeld A, Carey L, Antaki JF. Investigating the heart pump implant decision process: opportunities for decision support tools to help. *ACM Trans Comput Hum Interact* 2016; 2016: 4477–4488.

Yazdani A, Li H, Humphrey JD, Karniadakis GE. A General Shear-Dependent Model for Thrombus Formation. *PLOS Comput Biol* 2017; 13(1): e1005291. DOI:10.1371/journal.pcbi.1005291.

Yellin EL, Hori M, Yoran C, Sonnenblick EH, Gabbay S, Frater RW. Left ventricular relaxation in the filling and nonfilling intact canine heart. *Am J Physiol* 1986; 250(4): H620-H629.

Yoganathan AP, He Z, Casey JS. Fluid mechanics of heart valves. *Annu Rev Biomed Eng* 2004; 6: 331-362.

Yu H, Engel S, Janiga G, Thévenin D. A Review of Hemolysis Prediction Models for Computational Fluid Dynamics. *Artificial Organs* 2017; 41(7): 603-621.

Yuhki A, Hatoh E, Nogawa M, Miura M, Shimazaki Y, Takatani S. Detection of Suction and Regurgitation of the Implantable Centrifugal Pump Based on the Motor Current Waveform Analysis and its Application to Optimization of the Pump Flow. *Artificial Organs* 1999; 23: 532-537.

Z

Zhang J, Zhang P, Fraser KH, Griffith BP, Wu ZJ. Comparison of Fluid Dynamic Numerical Models for a Clinical Ventricular Assist Device and Experimental Validation. *Artificial Organs* 2013; 37(4): 380-389.

Zhang P, Zhang L, Slepian MJ, Deng Y, Bluestein D. A multiscale biomechanical model of platelets: Correlating with in-vitro results. *J Biomech* 2017; 50: 26-33.

Zhang PH, Tkatch C, Newman R, Grimme W, Vainchtein D, Kresh JY. The mechanics of spiral flow: Enhanced washout and transport. *Artif Organs* 2019; 43: 1144-1153.

Zhou J, Armstrong GP, Medvedev AL, Smith WA, Golding LAR, Thomas JD. Numeric Modelling of the Cardiovascular System with a Left Ventricular Assist Device. *ASAIO J* 1999; 45: 83-89.

Ziff RM. Kinetics of polymerisation. *J Stat Phys*. 1980; 23:241–263.

Ziff RM, Stell G. Kinetics of polymer gelation. *J Chem Phys*. 1980; 73: 3492–3499.